

Universität Stuttgart

DISSERTATION

Nonlinear phenomena in stochastic thermodynamics

From optimal protocols to criticality

Von der Fakultät Mathematik und Physik der Universität Stuttgart
zur Erlangung der Würde eines Doktors der Naturwissenschaften
(Dr. rer. nat.) genehmigte Abhandlung

Vorgelegt von

BENEDIKT REMLEIN

aus Lohr am Main

Hauptbericht: Prof. Dr. Udo Seifert
Mitbericht: Prof. Dr. Thomas Speck
Prüfungsvorsitz: Prof. Dr. Ronny Nawrodt

Tag der Einreichung: 28. Februar 2024
Tag der mündlichen Prüfung: 15. April 2024

II. Institut für Theoretische Physik

2024

CONTENTS

Zusammenfassung	vii
Abstract	xii
Publications	xix
1 Introduction	1
2 Stochastic thermodynamics on discrete state space	5
2.1 Introductory remarks	5
2.2 Equilibrium system in contact with a heat bath	5
2.3 Open system in contact with heat bath, particle and work reservoirs	9
2.4 Stochastic energetics and entropy along a single trajectory	11
2.4.1 Stochastic energetics: the first law	11
2.4.2 Entropy along a stochastic trajectory	12
2.4.3 Ensemble averages	14
2.5 Finite-time thermodynamics and optimal protocols	15
2.5.1 Finite-time protocols	15
2.5.2 Minimizing entropy production in continuous state space	16
2.5.3 Optimal protocols on discrete state space	18
2.6 Stochastic thermodynamics of chemical reaction networks	21
2.6.1 Introductory remarks	21
2.6.2 Closed systems and the chemical master equation	21
2.6.3 Open chemical reaction network and entropy	24
2.6.4 Simulating the dynamics: Gillespie's direct method	26
2.7 Approximate methods for Markov jump processes – the weak-noise limit	28
2.7.1 Approximating the master equation	28
2.7.2 Van Kampen's system-size expansion	29
2.7.3 Chemical Langevin equation	31
2.7.4 Rate equation	34
2.7.5 WKB method	35
2.8 Characterization of nonequilibrium dynamical systems	36
2.8.1 Critical behavior and scaling form	36
2.8.2 Bifurcation theory	39
2.8.3 Supercritical Hopf bifurcation	41

2.8.4	Coherent oscillations	44
3	Optimality of non-conservative driving for finite-time processes with discrete states	47
3.1	Introduction	47
3.2	Optimal control of Markov jump processes	48
3.2.1	Set-up	48
3.2.2	Optimality of non-conservative driving	50
3.2.3	Bound on the optimal cycle affinity	51
3.2.4	Configurations that tend to saturate the affinity bound	52
3.2.5	Generalization to rates including a structural parameter	55
3.2.6	Recovering the optimal protocol for Langevin systems in the continuum limit	55
3.3	Conclusion	56
4	Coherence of oscillations in the weak-noise limit	57
4.1	Introduction	57
4.2	Coherence of oscillations	59
4.3	One-dimensional Fokker-Planck systems in the weak-noise limit	60
4.3.1	Quality factor	60
4.3.2	Bound on the quality factor	63
4.3.3	Proof of entropic bound in the weak-noise limit	64
4.3.4	A specific example	66
4.4	Planar oscillations in the weak-noise limit	67
4.5	Cubic normal form for a Hopf bifurcation	71
4.5.1	Stuart-Landau oscillator	71
4.5.2	Effective diffusion coefficient	72
4.6	Brusselator	76
4.7	Discussion and conclusion	79
5	Nonequilibrium fluctuations of chemical reaction networks at criticality – The Schlögl model as paradigmatic case	81
5.1	Introduction	81
5.2	Schlögl model	82
5.3	Along the critical line	85
5.3.1	Numerical data	85
5.3.2	Rate equation and mean flux	88
5.3.3	Diffusion approximation and diffusion coefficient	89

5.4	Along the pitchfork bifurcation	96
5.4.1	Numerical data	96
5.4.2	In the monostable regime and at the critical point	99
5.4.3	Bistable regime and two-state approximation	100
5.5	Scaling form	102
5.5.1	General monostable pathway	102
5.5.2	Change of coordinates	103
5.5.3	Scaling form for the particle flux	104
5.5.4	Scaling form for the diffusion coefficient	105
5.6	Discussion and conclusion	106
6	Nonequilibrium fluctuations of chemical reaction networks at criticality – The Brusselator model as paradigmatic case	109
6.1	Introduction	109
6.2	The thermodynamic consistent Brusselator model	110
6.3	Numerical data	112
6.4	Rate equation, mean flux and normal form mapping	114
6.4.1	Rate equation	114
6.4.2	Normal form mapping	115
6.5	Discontinuous diffusion coefficient	119
6.5.1	System-size expansion	119
6.5.2	Cubic normal form model	123
6.5.3	Integration of van Kampen’s approximation	124
6.5.4	Chemical Langevin equation	126
6.5.5	Discussion of the different approximations	126
6.6	Conclusion	128
7	Concluding remarks	131
A	Optimality of non-conservative driving for finite-time processes with discrete states	135
A.1	Comment on Eq. (3.11) of the main text	135
A.2	Improved bound for symmetric rates	136
A.2.1	Local extrema	137
A.2.2	Extrema on the boundary	139
A.2.3	Concluding remark	142
A.3	Numerical scheme	143
A.4	Randomly generated configurations	144

A.5	Affinity bound for nonsymmetrical splitting	144
A.6	Continuum limit for nonsymmetrical splitting	146
B	Coherence of oscillations in the weak-noise limit	149
B.1	Irrelevance of the second solution of the one-dimensional Fokker-Planck system	149
B.2	Method introduced in [45]	149
C	Nonequilibrium fluctuations of chemical reaction networks at criticality – The Schlögl model as paradigmatic case	153
C.1	Phase diagram in the $c_A - c_B$ -plane	153
C.2	Diffusion coefficient in linear system	154
	List of Figures	169
	List of Tables	170
	Erklärung	171

ZUSAMMENFASSUNG

Biochemische Prozesse benötigen typischerweise eine konstante Energiezufuhr. Sie sind daher nicht im thermodynamischen Gleichgewicht. Zumeist laufen solche Prozesse in einer Umgebung ab, deren thermische Energie mit der des Systems vergleichbar ist, sodass Fluktuationen eine wichtige Rolle spielen. Eine physikalische Theorie, welche derartige Systeme beschreiben möchte, muss daher diese Aspekte berücksichtigen. Stochastische Thermodynamik hat sich über die letzten Jahrzehnte zu einer umfassenden Theorie entwickelt, fluktuierende Systeme unter Nichtgleichgewichtsbedingungen zu betrachten. Die Identifikation thermodynamischer Größen wie Arbeit und Entropie entlang einer Trajektorie ermöglicht die systematische Untersuchung sogenannter mesoskopischer Systeme, d.h., Systeme, in welchen Fluktuationen nicht ignoriert werden dürfen.

Bringt man ein System in endlicher Zeit von einem gegebenen Anfangs- in einen gegebenen Endzustand, wird unweigerlich Entropie produziert. Das externe Protokoll, welches diese Transformation mit minimalem entropischen Aufwand durchführt, heißt optimales Protokoll. Für Systeme mit diskreten Zuständen konvergiert das optimale Protokoll im Kontinuumslimit gegen jenes, welches im kontinuierlichen Zustandsraum die gesamte, produzierte Entropie minimiert. Das optimale Treiben in derartigen Systemen ist konservativ, d.h., es kann von einem Potential abgeleitet werden. Für Systeme mit diskretem Zustandsraum steht eine derartige Charakterisierung des optimalen Treibens noch aus. Wir schließen diese Lücke in dieser Arbeit. Wir beweisen, dass das optimale Protokoll für eine Transformation über einem diskreten Zustandsraum nicht konservativ ist, d.h., es gibt eine Affinität, welche nicht durch Differenzen der freien Energien der jeweiligen Zustände dargestellt werden kann. Zudem zeigen wir, dass die optimale Affinität durch die Anzahl der Zustände in einem Zyklus beschränkt ist.

Unser zweites Hauptaugenmerk liegt auf nichtlinearen Phänomenen im Grenzfall schwachen Rauschens. Chemische Reaktionsnetzwerke (CRN) können in diesem Grenzfall verschiedene, nicht-triviale Effekte wie Bifurkationen und Grenzzyklen aufzeigen. Die Oszillationen dieser Grenzzyklen sind verrauscht, weshalb sie nach einer gewissen Zeit ihre Präzision verlieren. Dieser Verlust der Kohärenz wird durch die Güte eines Oszillators charakterisiert. Wir untersuchen diese Kenngröße für eine eindimensionale Bewegung auf einem periodischen Ring und leiten einen analytischen Ausdruck für die Güte des Oszillators im

Grenzfall schwachen Rauschens her. Mit diesem Ausdruck beweisen wir kontinuierliche Versionen thermodynamischer Schranken an die Güte eines Oszillators, welche ursprünglich für Markovnetzwerke vermutet wurden. Außerdem parametrisieren wir zweidimensionale, stochastische Oszillatoren entlang deren Bogenlänge, sodass wir eine effektiv eindimensionale Bewegung erhalten. Mit dem analytischen Ausdruck der Güte eines eindimensionalen Oszillators leiten wir eine Formel für diese approximative Beschreibung her. Wir wenden dieses Vorgehen auf zwei Beispielsysteme an, welche stochastische Grenzzyklen aufzeigen.

Neben dem Phänomen der Kohärenz eines Grenzzyklus beschäftigen wir uns mit dem Entstehen eines solchen durch einen kontinuierlichen Phasenübergang. Als Musterbeispiel eines univarianten Systems, welches einen kontinuierlichen Nichtgleichgewichtsphasenübergang aufweist, betrachten wir das Schlögl Modell. Wir zeigen numerisch und analytisch, dass sich der Teilchenfluss, welcher in die Chemostaten hinein und heraus strömt, und dessen zugeordneter Diffusionskoeffizient in der Umgebung des kritischen Punktes durch Skalenformen darstellen lassen. Als weiteres Beispiel für einen kontinuierlichen Nichtgleichgewichtsphasenübergang untersuchen wir die Hopf-Bifurkation im thermodynamisch-konsistenten Brüsselator. Wir finden numerisch und theoretisch, dass der Teilchenfluss aus und in die chemischen Reservoirs nicht differenzierbar vom Kontrollparameter abhängt. Die Fluktuationen des Stroms, welche durch den Diffusionskoeffizienten charakterisiert werden, erfüllen im Regime oberhalb der Bifurkation eine Skalenform. Nähert man sich der Bifurkation von unten, ist der Diffusionskoeffizient eine unstetige Funktion des Kontrollparameters.

Diese Dissertation ist aufgebaut wie folgt. In Kapitel 1 motivieren wir das Thema und geben eine kurze Einführung. In Kapitel 2 erläutern wir die theoretischen Grundlagen, welche zum Verständnis der nachfolgenden Kapitel nötig sind. Wir diskutieren unsere ersten Hauptergebnisse bezüglich optimaler Protokolle auf diskreten Zustandsräumen in Kapitel 3. Dieses Kapitel basiert auf Ref. [1]. Wir präsentieren unsere Resultate bezüglich der Kohärenz von Oszillatoren in Kapitel 4, welches auf Ref. [2] basiert. In Kapitel 5, welches auf Ref. [3] beruht, untersuchen wir den Nichtgleichgewichtsphasenübergang im Schlögl Modell und in Kapitel 6 den thermodynamisch-konsistenten Brüsselator. Wir schließen in Kapitel 7. Im Folgenden geben wir eine Zusammenfassung der Kapitel 2 bis 6.

KAPITEL 2: STOCHASTISCHE THERMODYNAMIK FÜR SYSTEME MIT DISKRE- TEN ZUSTÄNDEN

Wir führen die grundlegenden Prinzipien stochastischer Thermodynamik für Systeme mit diskreten Zuständen ein und diskutieren Anwendungen, welche in dieser Dissertation

untersucht werden. Wir betrachten ein geschlossenes System von Mikrozuständen, welches in Kontakt mit einem Wärmebad ist, und wiederholen das kanonische Ensemble aus der statistischen Mechanik. Wir wechseln in ein vergrößertes Bild von Mesozuständen und führen thermodynamische Potentiale ein. Unter der Annahme, dass Übergänge innerhalb eines Mesozustands schneller stattfinden als zwischen verschiedenen Mesozuständen, erhalten wir eine Markovsche Dynamik auf dem Level des vergrößerten Systems. Wir diskutieren die lokale, detaillierte Gleichgewichtsbedingung ("local detailed balance"), welche die Sprungraten mit freien Energiedifferenzen der verschiedenen Zustände in Verbindung bringt. Wir öffnen das System und erlauben den Austausch von chemischer Energie oder Abfuhr von Arbeit, indem wir es an Teilchen- und Arbeitsreservoirs koppeln. In einer derartigen Nichtgleichgewichtssituation erreicht das System einen stationären Nichtgleichgewichtszustand, in welchem konstant Entropie produziert wird. Anschließend definieren wir physikalische Größen wie innere Energie, Arbeit und Entropie entlang dieser verrauschten Trajektorie auf thermodynamisch konsistente Art und Weise. Zuletzt zeigen wir, dass diese Definitionen in Einklang mit Gleichgewichtsthermodynamik sind, indem wir deren Ensemblemittelwert bestimmen.

Weiterhin betrachten wir Transformationen eines Systems mit endlicher Übergangszeit von einem gegebenen Anfangs- zu einem Endzustand. Wir erläutern die wichtigsten Ergebnisse für Systeme mit kontinuierlichem Zustandsraum und zeigen, dass ein Treiben, welches eine derartige Transformation mit minimalem entropischen Aufwand durchführt, von einem Potential abgeleitet werden kann. Für Systeme mit diskreten Zuständen formulieren wir das Optimierungsproblem, in welchem die totale Entropieproduktion während der Transformation minimiert wird. Wir wiederholen den Kontinuumlimes und zeigen, dass das optimale Protokoll in diesem Grenzfall gegen jenes mit kontinuierlichem Zustandsraum konvergiert.

Koppeln wir ein System diskreter Zustände an mehrere Teilchenreservoirs, bezeichnen wir es als chemisches Reaktionsnetzwerk (CRN). Wir führen die grundlegenden Notationen und thermodynamischen Größen für geschlossene und offene CRN ein. Wir fokussieren uns auf Systeme mit Chemostaten. Ein Chemostat ist ein Teilchenreservoir, welches derart reguliert ist, dass die Konzentration der zur Verfügung gestellten Teilchen im System konstant gehalten wird. Der Teilchenstrom aus bzw. in den Chemostat ist daher unmittelbar mit Entropieproduktion verbunden. Zuletzt diskutieren wir eine Methode, die Dynamik eines CRN numerisch zu simulieren.

Im Allgemeinen kann die Bewegungsgleichung der Wahrscheinlichkeitsverteilung eines CRN aufgrund von Nichtlinearitäten nicht analytisch gelöst werden, weshalb Näherungs-

methoden nötig sind. Wir diskutieren die Entwicklung der Mastergleichung für große Reaktionsvolumen nach van Kampen und Gillespies chemische Langevin-Gleichung. Diese Methoden approximieren die Dynamik als Diffusionsprozess. Im Grenzfall großer Systeme kann die Teilchenzahl durch deren Dichte ersetzt werden, was zu Fokker-Planck Gleichungen führt, deren Lösungen durch eine WKB-Methode bestimmt werden können. Lässt man die Systemgröße ins unendliche wachsen, wird das Rauschen unterdrückt und man erhält die chemischen Ratengleichungen.

Im Limes großer Systeme zeigen chemische Reaktionsnetzwerke verschiedene nicht-triviale Phänomene, wie z.B. Grenzzyklen oder Phasenübergänge. Wir wiederholen kritisches Verhalten bei Gleichgewichtsphasenübergängen und diskutieren es im Kontext von Bifurkationstheorie. Wir illustrieren verschiedene Bifurkation durch ein eindimensionales, dynamisches System und betrachten die kubische Normalform für eine Hopf-Bifurkation als Musterbeispiel für ein zweidimensionales System, welches einen kontinuierlichen Nichtgleichgewichtsphasenübergang vorweist. Zuletzt erörtern wir die Güte eines verrauschten Oszillators als Maß seiner Kohärenz. Diese Kenngröße ist definiert durch das Verhältnis des Imaginär- und Realteils des ersten nicht-trivialen Eigenwerts der zugrundeliegenden Dynamik. Abschließend gehen wir darauf ein, wie die Güte eines Oszillators mit physikalischen Größen, wie Entropieproduktion oder dem thermodynamischen Treiben entlang eines periodischen Markovnetzwerkes, zusammenhängt.

KAPITEL 3: OPTIMALITÄT DES NICHT-KONSERVATIVEN TREIBENS IN ENDLICHER ZEIT FÜR PROZESSE MIT DISKRETEN ZUSTÄNDEN

Wir betrachten ein Optimierungsproblem auf diskreten Zuständen. Ein optimaler Prozess mit endlicher Übergangszeit transformiert eine gegebene Anfangsverteilung in eine Endverteilung in einer vorgegebenen Zeit und verursacht währenddessen minimale thermodynamische Kosten, welche durch die totale Entropieproduktion gegeben sind. Wir beweisen, dass das optimale Protokoll für ein System mit diskreten Zuständen nicht konservativ ist, d.h., das optimale Treiben ist im Allgemeinen durch eine Affinität gegeben. Dieser Befund steht im Kontrast zu Systemen mit kontinuierlichem Zustandsraum. Weiterhin zeigen wir, dass die optimale Affinität durch die Anzahl der Zustände in einem Zyklus beschränkt ist. Numerische Befunde legen nahe, dass diese Schranke durch kurze Übergangszeiten oder Konfigurationen mit großen Differenzen zwischen Anfangs- und Endverteilung gesättigt wird. Wir verallgemeinern unsere Resultate auf Transformationen, welche die Vorwärts- und Rückrichtung eines Übergangs unterschiedlich beeinflussen. Zuletzt zeigen wir, dass

wir im Grenzfall eines verschwindenden Gitterabstands das Ergebnis eines optimalen, konservativen Treibens reproduzieren.

KAPITEL 4: KOHÄRENTE OSZILLATIONEN IM LIMES VERSCHWINDENDEN RAUSCHENS

Die Kohärenz eines verrauschten Oszillators wird durch dessen Güte beschrieben. Wir berechnen diese Kenngröße für eine Oszillation, welche durch eine getriebene Fokker-Planck Dynamik entlang eines eindimensionalen, periodischen Potentials beschrieben wird, im Grenzfall schwachen Rauschens mittels der WKB-Methode. Dieser analytische Ausdruck erlaubt es uns, eine kontinuierliche Version einer Schranke an die Güte der Oszillation herzuleiten und zu beweisen, welche ursprünglich für Markovnetzwerke vermutet wurde [4]. Im Limes verschwindenden Rauschens gleicht diese einer anderen vermuteten Schranke, welche die totale Entropieproduktion während einer Periode beinhaltet [5]. Wir projizieren eine verrauschte, zweidimensionale Bewegung auf deren Bogenlänge und erhalten einen approximativen Ausdruck für die Güte eines ebenen Oszillators. Diese Approximationsmethode wenden wir auf den verrauschten Stuart-Landau Oszillator an. Wir evaluieren die Gültigkeit unserer Methode numerisch, indem wir mit einem allgemeinen Ausdruck vergleichen, welcher mit Techniken aus der Hamilton-Jacobi Theorie hergeleitet wurde. Wir finden eine Diskrepanz für Systeme mit starker Kopplung zwischen dem normalen und tangentialen Freiheitsgrad. Für dieses spezielle Modell finden wir eine Variation unseres Approximationsschemas, welche numerisch mit dem Hamilton-Jacobi Ausdruck übereinstimmt. Als zweite Fallstudie betrachten wir den thermodynamisch-konsistenten Brusselator, welcher ein Modell für eine chemische Uhr darstellt. Unsere Arbeit trägt somit zum intuitiven Verständnis kohärenter Oszillation bei und ergänzt die bisherigen, komplexen Resultate, welche auf Hamilton-Jacobi Theorie basieren.

KAPITEL 5: NICHTGLEICHGEWICHTSFLUKTUATIONEN KRITISCHER REAKTIONSNETZWERKE – DAS SCHLÖGL MODELL ALS MUSTERBEISPIEL

Wir betrachten den kontinuierlichen Nichtgleichgewichtsphasenübergang im Schlögl Modell und untersuchen den Teilchenfluss, welcher aus den Chemostaten heraus oder hinein strömt, und dessen Fluktuationen. Dieser Teilchenfluss ist proportional zur Entropieproduktion. Numerische Simulationen zeigen, dass der Diffusionskoeffizient, welcher die Fluktuationen des Flusses beschreibt, am kritischen Punkt mit der Systemgröße divergiert. In der Umgebung

des kritischen Punktes erfüllt er eine Skalenform. Im monostabilen Regime untersuchen wir dieses Phänomen analytisch mittels der chemischen Langevin-Gleichung und der Entwicklung nach van Kampen. Wir leiten die entsprechenden kritischen Exponenten her. Im bistabilen Regime approximieren wir das System als Markovnetzwerk mit zwei Zuständen. Nachdem vorherige Studien Fluktuationen während des Phasenübergangs erster Ordnung im Schlögl Modell untersucht haben, vervollständigen wir somit das thermodynamische Verständnis der Nichtgleichgewichtsfluktuationen in diesem Mustersystem.

KAPITEL 6: NICHTGLEICHGEWICHTSFLUKTUATIONEN KRITISCHER REAKTIONSNETZWERKE – DER BRÜSSELATOR ALS MUSTERBEISPIEL

Der thermodynamisch-konsistente Brüsselator ist ein Musterbeispiel für eine chemische Uhr. Wir untersuchen den Teilchenstrom aus und in die Chemostate und dessen Fluktuationen während der Hopf-Bifurkation des Systems. Numerische Berechnungen zeigen, dass der Teilchenfluss nicht differenzierbar vom Kontrollparameter abhängt. Wir erklären dieses Verhalten mittels einer Abbildung auf die kubische Normalform für eine Hopf-Bifurkation. Weitere numerische Simulationen zeigen, dass der Diffusionskoeffizient, welcher dem Fluss zugeordnet ist, an der Bifurkation mit der Systemgröße divergiert. Oberhalb der Bifurkation erfüllt er eine Skalenform und wir extrahieren kritische Exponenten. Unterhalb der Bifurkation zeigt der Diffusionskoeffizient ein unstetiges Verhalten als Funktion des Kontrollparameters. Weitere numerische Untersuchungen mittels der chemischen Langevin-Gleichung und van Kampens Entwicklung bestätigen diesen Befund. Wir leiten einen Ausdruck für den Diffusionskoeffizienten her, welchen wir nicht weiter analytisch untersuchen können. Daher bleibt die analytische Bestimmung der kritischen Exponenten und eine theoretische Erklärung für das unstetige Verhalten als Frage offen.

ABSTRACT

Biochemical processes typically operate on energy-scales comparable with the thermal energy of their environment. Additionally, these processes rely on the constant consumption of energy, i.e., work under nonequilibrium conditions. Thus, any physical theory aiming to describe those systems needs to incorporate fluctuations into a general nonequilibrium setting. Over the last decades, stochastic thermodynamics has been developed as a comprehensive framework to study those fluctuating systems that are far from equilibrium.

The identification of physical quantities like work and entropy along a single trajectory allows a systematic thermodynamic treatment of mesoscopic systems where fluctuations cannot be ignored.

The transformation of a system from a given initial to a final state within finite-time comes with an inevitable thermodynamic cost. For a system with discrete state space, the optimal protocol that performs this transformation with minimal entropic cost reduces to the continuum one in the appropriate limit. For systems with continuous state space, the optimal transformation is achieved by applying a gradient force, i.e., a conservative force. However, for systems with discrete state space this characterization is still pending. In this thesis, we close this gap and prove that for a system with discrete states the optimal process involves non-conservative driving, i.e., a genuine driving affinity. Furthermore, in a multicyclic network, the optimal driving affinity is bounded by the number of states within each cycle.

The second main objective of this thesis is the treatment of nonlinear phenomena in the weak-noise limit. In this limit, chemical reaction networks (CRNs) show a variety of non-trivial behaviors like bifurcations and noisy limit cycles. Since those oscillators behave stochastic, they lose their precision after some time. This loss is characterized by the quality factor. We study this quantity for a one-dimensional motion along a periodic ring and obtain an analytical expression for the quality factor in the weak-noise limit. Using this expression, we derive and prove continuous versions of thermodynamic bounds on the quality factor which have been conjectured for Markov networks. Furthermore, we describe noisy planar oscillations as effective, one-dimensional motion along the arc-length and apply our expression to two paradigmatic systems exhibiting limit cycle oscillations.

Besides the coherence of noisy limit cycle oscillations, we also focus on their emergence through a continuous phase transition. We study the Schlögl model as a paradigmatic univariate model undergoing a continuous nonequilibrium phase transition. We numerically and analytically show that the particle flux in and out the chemostats and its associated diffusion coefficient obey a scaling form in the vicinity of the critical point. As second paradigmatic example of a continuous nonequilibrium phase transition, we study the thermodynamically consistent Brusselator model undergoing a Hopf bifurcation. We numerically and theoretically find that the particle flux depends non-differentiable on the control parameter. The fluctuations quantified through the associated diffusion coefficient follow a scaling form above the bifurcation. However, approaching the bifurcation from below, the diffusion coefficient develops a discontinuous dependence on the control parameter.

This dissertation is structured as follows. In Chapter 1, we motivate and introduce the topic. We present the theoretical basics for this thesis in Chapter 2. In Chapter 3, we present the first main results regarding optimal protocols on discrete state space. This chapter is based on Ref. [1]. We discuss our results about the coherence of noisy oscillations in Chapter 4, which is based on Ref. [2]. In Chapter 5, which is based on Ref. [3], we present our discussion about the continuous phase transition in the Schlögl model, and in Chapter 6 about the thermodynamically consistent Brusselator model. We conclude in Chapter 7. In the following, we give a summary of Chapters 2 to 6.

CHAPTER 2: STOCHASTIC THERMODYNAMICS ON DISCRETE STATE SPACE

We discuss the basic concepts and applications of stochastic thermodynamics on discrete state space that are needed throughout this thesis. We recapitulate the canonical ensemble of statistical mechanics considering a closed system of microstates in contact with a heat reservoir. We coarse-grain those states into mesostates and introduce thermodynamic potentials. Under the assumption that the time-scale of transitions within mesostates is much faster than transitions between different mesostates, we obtain a Markovian dynamics for the coarse-grained states. We briefly discuss the local detailed balance condition that connects the transition rates between the states with their free energy. Coupling the system to external particle and work reservoirs, we allow the exchange of chemical energy or extraction of work, i.e., we obtain a genuine nonequilibrium situation. In this set-up, the Markovian dynamics allows for a nonequilibrium steady-state (NESS), i.e., a stationary state with constant rate of entropy production. Considering a single trajectory following this Markovian dynamics, we define physical quantities like internal energy, work and entropy in a thermodynamic consistent way. We further show that these definitions are consistent with equilibrium thermodynamics by evaluating their ensemble average.

For a finite-time transformation of a system from a given initial to a final state, we briefly discuss the essential results for continuous state space and show that the optimal protocol that performs such a transformation with minimal entropic cost is given by a potential force. Considering a system with discrete state space, we discuss the variational problem for minimizing the total entropy production with dynamical constraints. We further recapitulate the continuum limit. In that limit, the optimization problem converges towards the continuum one.

If a system is coupled to a heat and several particle reservoirs, we denote it as chemical reaction network (CRN). We introduce the basic notions for closed and open systems with

focus on chemostatted networks. In those networks, the reservoirs are externally controlled such that the concentration of their particle species in the system is kept constant. Thus, the particle flux in and out of those reservoirs is directly linked to the entropy produced in the system. Furthermore, we introduce the Gillespie algorithm to simulate the dynamics of a CRN.

The dynamics of a CRN is in general not analytically solvable due to nonlinearities, thus, approximate methods are needed. We discuss van Kampen's system-size expansion and the chemical Langevin equation (CLE) as diffusion approximations of the master equation. These approaches have in common that they describe a CRN using the continuous particle density which approximates a system well in the limit of increasing system-size, i.e., in the weak-noise limit. In this limit, all approximation schemes lead to Fokker-Planck equations that can be solved using the WKB-method. In the limit of infinite system-size, we recover the chemical rate equations.

In the limit of increasing system-size, CRN exhibit various non-trivial phenomena like noisy limit cycle oscillations and bifurcations respectively phase transition. We briefly review critical behavior from equilibrium statistical mechanics and discuss it in the context of bifurcation theory by considering an one-dimensional dynamical system. We further introduce the normal form for a Hopf bifurcation as an example for a two-dimensional system undergoing a nonequilibrium phase transition. Finally, we discuss the quality factor of a noisy oscillator as a measure of its coherence, i.e., a qualitative measure for keeping the precision. The quality factor is determined through the ratio of the imaginary and real part of the first non-trivial eigenvalue of the underlying dynamics. Furthermore, we discuss the relation of this measure to thermodynamic quantities as entropy production and the driving affinity along a unicyclic network.

CHAPTER 3: OPTIMALITY OF NON-CONSERVATIVE DRIVING FOR FINITE-TIME PROCESSES WITH DISCRETE STATES

We study an optimal control problem on discrete state space. An optimal finite-time process drives a given initial distribution to a given final one in a given time at lowest cost as quantified by total entropy production. We prove that the optimal protocol for a system with discrete states involves a genuine driving affinity, i.e., is non-conservative. This finding is in contrast to the case of a system with continuous states. We further show that the optimal driving affinity is bounded by the number of states within a cycle. Numerical simulations show that the derived bound tends to be saturated for short allocated times or

configurations that need to transport large densities. We generalize our findings to drivings that affect forward and backward rates nonsymmetrically. Finally, we recover the result for continuous state space in the limit of vanishing lattice spacing.

CHAPTER 4: COHERENCE OF OSCILLATIONS IN THE WEAK-NOISE LIMIT

The coherence of a noisy oscillator is measured by the quality factor. Using a WKB-ansatz, we determine this quantity for oscillations arising from a driven Fokker-Planck dynamics along a periodic one-dimensional potential analytically in the weak-noise limit. With this expression, we derive and prove for this continuum model the analog of an upper bound on the quality factor that has been conjectured for the coherence of oscillations in discrete Markov networks [4]. Furthermore, in the weak-noise limit, we show that this bound is equivalent to another conjectured bound which includes the total entropy produced during one period [5]. We adapt this one-dimensional approach to motion along a noisy two-dimensional oscillator by projecting it onto the arc-length, thus, by introducing an effective one-dimensional parameterization of this planar motion. We apply our scheme to the noisy Stuart-Landau oscillator and discuss its range of validity. Comparing numerically with a general framework based on techniques from Hamilton-Jacobi theory, we find a discrepancy for systems with a strong coupling between the radial and angular degree of freedom. For this specific example, we adjust our projection method such that the quality factor numerically agrees with the full theory. As second example, we study the thermodynamically consistent Brusselator as a simple model for a chemical clock. Our approach thus complements the fairly sophisticated extant general framework based on techniques from Hamilton-Jacobi theory.

CHAPTER 5: NONEQUILIBRIUM FLUCTUATIONS OF CHEMICAL REACTION NETWORKS AT CRITICALITY – THE SCHLÖGL MODEL AS PARADIGMATIC CASE

We study the continuous nonequilibrium phase transition in the Schlögl model. We investigate the flux in the chemostats that is proportional to the entropy production and its critical fluctuations. Numerical simulations show that the corresponding diffusion coefficient diverges at the critical point as a function of system size. In the vicinity of the critical point, the diffusion coefficient follows a scaling form. We develop an analytical approach based on the chemical Langevin equation and van Kampen's system size expansion that

yields the corresponding exponents in the monostable regime. In the bistable regime, we rely on a two-state approximation in order to analytically describe the critical behavior. Our work complements previous studies that considered the fluctuations of the particle flux during the first order phase transition within the Schlögl model. Thus, we complete the thermodynamic understanding of nonequilibrium fluctuations in this paradigmatic model.

CHAPTER 6: NONEQUILIBRIUM FLUCTUATIONS OF CHEMICAL REACTION NETWORKS AT CRITICALITY – THE BRUSSELATOR MODEL AS PARADIGMATIC CASE

The thermodynamically consistent Brusselator model is a prime example for a chemical clock. We study the flux in and out of the chemostats and its fluctuations while the system undergoes a Hopf bifurcation. We numerically show that the particle flux depends non-differentiable on the control parameter. This finding is rationalized using a mapping onto the cubic normal form for a Hopf bifurcation. Furthermore, numerical simulations show that the diffusion coefficient associated with this flux diverges with the system-size at the bifurcation. Approaching the bifurcation from above, the diffusion coefficient obeys a scaling form and we obtain critical exponents. However, approaching the bifurcation from below, the fluctuations develop a discontinuous dependence on the control parameter. This finding is supported through numerical simulations using van Kampen's system-size expansion and the chemical Langevin equation (CLE). We derive an expression for the diffusion coefficient which we cannot further treat analytically. Thus, we leave the theoretical description of the discontinuity and the extraction of scaling exponents as an open problem.

PUBLICATIONS

Parts of this thesis have been published in:

- [1] Remlein, B. & Seifert, U. *Optimality of nonconservative driving for finite-time processes with discrete states*. *Phys. Rev. E* **103**, L050105 (2021)

© 2021 American Physical Society.

Chapter 3 and Appendix A are based on this publication.

Author contributions: U.S. conceived the project. B.R. developed the mathematical framework and performed numerical calculations. B.R. wrote the original draft of the manuscript. B.R. and U.S. reviewed and edited it.

- [2] Remlein, B., Weissmann, V. & Seifert, U. *Coherence of oscillations in the weak-noise limit*. *Phys. Rev. E* **105**, 064101 (2022)

© 2022 American Physical Society.

Chapter 4 and Appendix B are based on this publication.

Author contributions: B.R. and U.S. conceived the project. B.R. developed the mathematical framework. B.R. and V.W. performed numerical calculations and developed further conceptual ideas through many discussions. B.R. wrote the original draft of the manuscript. B.R. and U.S. reviewed and edited it. Part of this work was presented in the master thesis by V. Weissmann supervised by U. Seifert and co-supervised by B. Remlein.

- [3] Remlein, B. & Seifert, U. *Nonequilibrium fluctuations of chemical reaction networks at criticality: The Schlögl model as paradigmatic case*. arXiv: 2402.13168 (2024)

Chapter 5 and Appendix C are based on this publication.

Author contributions: B.R. and U.S. conceived the project. B.R. developed the mathematical framework and performed numerical calculations. B.R. wrote the original draft of the manuscript. B.R. and U.S. reviewed and edited it.

INTRODUCTION

Life comes with a cost. As we experience this fact on a daily basis, the statement is not less true regarding any physical model aiming to describe a genuine living system, for instance, a cell or molecular motor. While we presumably think at first about money that we need to pay our rent or food, from a physical point of view, the latter would be a more reasonable choice. Through the consumption of food, we supply energy to our body, thus, provide the possibility to perform work. In terms of physics, the budget that keeps track of the cost of living is manifested in the first and second law of thermodynamics.

The very beginning of thermodynamics are the attempts to phenomenologically describe steam engines and their efficiency [6]. The rigorous, statistical foundation of equilibrium thermodynamics was later initiated by Boltzmann [7] and continued by Gibbs [8]. In order to derive macroscopic, thermodynamic laws from an underlying microscopic description, a key concept is the thermodynamic limit where the number of particles in a system grows to infinity. While this is certainly a good assumption in order to describe the mean behavior of a gas enclosed in a vessel, it fails when describing the energy budget of a single molecular motor.

As the experimental capabilities to resolve distances on the scale of μm and beyond grew over the last decades, it became possible to observe single molecules embedded in an aqueous solution. The development of optical tweezers even allowed to trap single particles and manipulate them [9, 10]. On these short length-scales, the motion of a molecule becomes noisy as collisions with constituents of the surrounding liquid become important. Thus, fluctuations need to be incorporated in order to successfully describe such an erratic motion.

The probably most prominent example of a theoretical description of such an erratic motion is due to Einstein. In his seminal work [11], Einstein examined the motion of a Brownian particle immersed in a liquid. He derived the probability distribution for the particle's velocity in order to understand the noisy motion. Furthermore, he established a relation between the diffusion coefficient of the particle and the temperature and viscosity of the liquid. Thus, he successfully connected a dynamical quantity of the particle with characteristic parameters of the surrounding medium.

In a more general setting, stochastic thermodynamics has been developed as a framework to study small, fluctuating systems in contact with external reservoirs possibly driving them out of equilibrium [12, 13]. It allows for a systematic thermodynamic treatment based on a fluctuating trajectory and its underlying probability distribution [14, 15]. Early results include various fluctuations theorems for the work [16] or entropy production [15, 17, 18], thus, refining the second law of thermodynamics by incorporating its fluctuating nature. Recent developments include the thermodynamic uncertainty relation (TUR) conjectured by Barato & Seifert [19] and proven by Horowitz & Gingrich [20]. This relation bounds the total entropy production of a Markov process through the mean value and fluctuations of any time anti-symmetric flux in a nonequilibrium stationary state. Thus, the TUR provides a further refinement of the second law for systems following a Markovian dynamics.

In this thesis, we use the framework of stochastic thermodynamics to study various nonlinear phenomena. This dissertation is structured as follows. The basic concepts of the theory are established in Chapter 2. We introduce the basic notions and provide background of the applications that will be discussed in detail in the subsequent chapters. As all examined phenomena are motivated by biological systems, we will briefly formulate the core ideas by considering such as examples.

In order to perform different tasks, a cell needs to change its shape or constituents. Thus, it needs to transform from the present state to a predetermined final one within finite-time. In Chapter 3, we study such transformations regarding the minimization of its inevitable thermodynamic cost in terms of optimal control theory. We prove that the transformation of a system with discrete state space that minimizes the total entropy in general includes a non-conservative force.

Inside a cell, there is a biochemical process that serves as an inner clock. The ability to keep track of time of a noisy self-sustained oscillator is quantified by the quality factor. We examine this quantity for various one- and two-dimensional stochastic clocks in Chapter 4. We derive a novel, transparent formula for the quality factor of a one-dimensional motion on a ring. Using this formula, we derive and prove continuous versions of thermodynamic bounds on the the quality factor. Furthermore, we approximate a planar oscillator as one-dimensional motion along the arc-length and obtain an expression for the quality factor of a two-dimensional oscillator. We apply this result to the noisy Stuart-Landau oscillator and Brusselator model and discuss the validity of our approximation.

While a cell changes its shape, it varies its mechanical properties, e.g., from being rigid to visco-elastic, i.e., it undergoes a phase transition. In Chapter 5, we consider the Schlögl model as a generic, univariate system that undergoes a continuous phase

transition. We numerically and analytically show that the diffusion coefficient associated with the thermodynamic flux diverges at the critical point and obtain scaling exponents. We develop a theory that reproduces the numerically observed behavior based on the chemical Langevin equation, van Kampen's system-size expansion and a coarse-graining into a two-state system. We summarize our results by deriving a scaling form for the particle flux and the diffusion coefficient.

In Chapter 6, we study the thermodynamic flux of the Brusselator model while undergoing a Hopf bifurcation. We numerically find that the derivative of the thermodynamic flux develops a jump in the vicinity of the bifurcation. We analytically explain this behavior using a mapping of the system to the normal form for a Hopf bifurcation. Furthermore, at the transition, we find that the diffusion coefficient associated with this flux diverges with system-size. Above the bifurcation, the diffusion coefficient follows a scaling-form. Approaching the bifurcation from below, we numerically find a discontinuous jump in the diffusion coefficient. We approximate the system through a chemical Langevin equation and van Kampen's system-size expansion and obtain an equation which we cannot further simplify. Studying the corresponding equations numerically supports the finding of a discontinuous behavior of the diffusion coefficient. We leave the analytical explanation as open problem. We conclude in Chapter 7

STOCHASTIC THERMODYNAMICS ON DISCRETE STATE SPACE

2.1 INTRODUCTORY REMARKS

Stochastic thermodynamics is a theory that applies to small systems in contact with reservoirs driving them out of equilibrium. A prominent example is a molecular motor that constantly consumes energy in order to perform work. As such a motor is constantly subject to fluctuations, its motion will be noisy. In this chapter, we discuss the basic concepts of thermodynamics in order to understand what a noisy motion is and how physical observables like work or entropy can be identified along such a trajectory.

We start by briefly reviewing the basic notion of the canonical ensemble in statistical mechanics, closely following Ref. [21, 22]. Afterwards, we formulate the first law along a single trajectory, commonly referred to as stochastic energetics, before we introduce entropy and discuss the second law.

Having established the basic thermodynamic notion, in Sec. 2.5, we briefly discuss optimal control theory for continuous state space before we introduce the optimization problem for Markov jump networks. As another broad class of systems with discrete state space, chemical reaction networks and its thermodynamic description will be addressed in Sec. 2.6. In Sec. 2.7, we discuss approximate methods for the dynamics of such reaction networks focusing on the so called weak-noise limit. In this limit, non-trivial effects like coherent oscillations and phase transitions can emerge which will be the topic of the last section, Sec. 2.8.

2.2 EQUILIBRIUM SYSTEM IN CONTACT WITH A HEAT BATH

We consider the canonical ensemble of statistical mechanics, i.e., a closed equilibrium system consistent of microstates $\{\xi\}$ in contact with a heat bath at inverse temperature β .

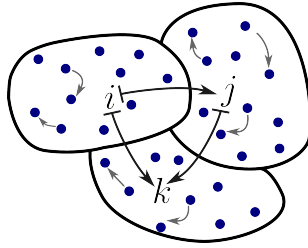


Figure 2.1: Sketch of the coarse-graining procedure. Microstates (blue dots) are combined into mesostates i , j and k (black areas). Fast transitions between microstates are indicated by thin gray arrows, slow transitions between mesostates by black ones with a line as foot.

Furthermore, we assume that every microstate ξ has an energy $H(\xi)$. The free energy of the system is given by

$$\mathcal{F} \equiv -\frac{1}{\beta} \ln \left(\sum_{\xi} e^{-\beta H(\xi)} \right). \quad (2.1)$$

Through this thermodynamic potential, the internal energy and entropy are obtained as

$$U = \partial_{\beta}(\beta\mathcal{F}) \quad (2.2)$$

$$S = \beta^2 \partial_{\beta} \mathcal{F} = \beta(U - \mathcal{F}). \quad (2.3)$$

The dynamics of each microstate is often not traceable, e.g., because the dynamics is too fast or there are too many degrees of freedom. Thus, we group several microstates together into one observable mesostate i , see Fig. 2.1. While coarse-graining the set of microstates $\{\xi\}$ into a set of mesostates $\{i\}$, we assume that each microstate ξ is uniquely assigned to one and only one mesostate i . In equilibrium, the probability for the system to be in mesostate i is

$$p_i^{eq} = \sum_{\xi \in i} \exp[-\beta(H(\xi) - \mathcal{F})] \equiv \exp[-\beta(\mathcal{F}_i - \mathcal{F})], \quad (2.4)$$

where the free energy of state i is defined as

$$\mathcal{F}_i \equiv \sum_{\xi \in i} \exp[-\beta H(\xi)]. \quad (2.5)$$

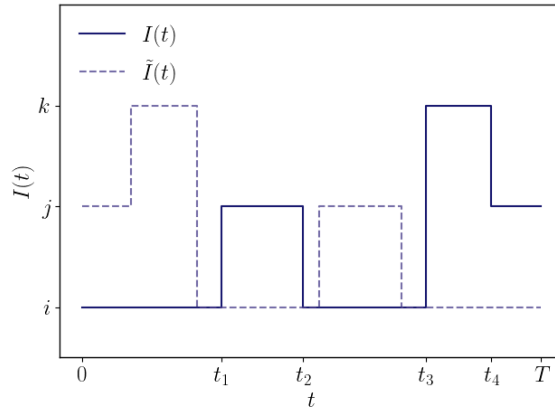


Figure 2.2: Trajectory $I(t)$ and time-versed one $\tilde{I}(t) \equiv I(T - t)$ of length T over the states i , j and k . For times $t_i < t < t_{i+1}$ the system rests in the corresponding state. For $t = t_i$ a jump from one mesostate to another takes place.

The internal energy of mesostate i follows as

$$U_i = \partial_\beta(\beta\mathcal{F}_i) = \sum_{\xi \in i} p(\xi|i)H(\xi) \quad (2.6)$$

with the conditional probability of microstate ξ given mesostate i ,

$$p(\xi|i) \equiv \exp\{-\beta[H(\xi) - \mathcal{F}_i]\} . \quad (2.7)$$

The intrinsic entropy of mesostate i is obtained through the Shannon entropy of the conditional probabilities,

$$S_i \equiv \beta^2 \partial_\beta \mathcal{F}_i = - \sum_{\xi \in i} p(\xi|i) \ln p(\xi|i) . \quad (2.8)$$

This quantity is a measure for the number of microstates ξ that contribute to mesostate i .

We now consider a trajectory $I(t) \equiv \{I_t\}_{0 \leq t \leq T}$ of length T that visits various mesostates $I_t \in \{i\}$ over the course of time, see Fig. 2.2. If we assume that the dynamics of the microstates within a mesostate is much faster than the one between mesostates, the motion of the mesostates becomes memoryless, i.e., a transition from present state i to j does not depend on the history of the trajectory. Thus, given that the trajectory is in state i at time t' , the probability to visit mesostate j after some time interval δt satisfies

$$p(j, t' + \delta t | \{I_t\}_{0 \leq t \leq t'}) = p(j, t' + \delta t | i, t') , \quad (2.9)$$

which is denoted as the Markov property. In the limit of a vanishing time interval δt , we get the rate for a transition from state i to j

$$k_{ij} \equiv \lim_{\delta t \rightarrow 0} \frac{1}{\delta t} p(j, t' + \delta t | i, t'). \quad (2.10)$$

Due to time translational invariance in equilibrium, k_{ij} does not depend on t' .

In an equilibrium system, there is no arrow of time, thus, it is equally likely to observe trajectory $I(t)$ and its time reversed one $\tilde{I}(t)$, i.e.,

$$p[I(t)] = p[\tilde{I}(t)] , \quad (2.11)$$

where time-reversal on this coarse level is defined as $\tilde{I}(t) \equiv I(T - t)$, see Fig. 2.2. This leads to a balance condition for the transitions between two mesostates,

$$k_{ij} p_j^{eq} = k_{ji} p_i^{eq} , \quad (2.12)$$

i.e., any jump from state i to j is on average balanced by a transition in the reversed direction. Plugging the equilibrium distribution, Eq. (2.4), into Eq. (2.12), we obtain the local detailed balance condition

$$\frac{k_{ij}}{k_{ji}} = \exp[-\beta(\mathcal{F}_i - \mathcal{F}_j)] = \exp[-\beta(U_i - U_j) + (S_i - S_j)] , \quad (2.13)$$

which sets thermodynamic constraints onto the transition rates between arbitrary states i and j . Furthermore, the Markovian dynamics of the mesostates $\{i\}$ is governed by a master equation

$$\partial_t p_i(t) = \sum_j [k_{ij} p_j(t) - k_{ji} p_i(t)] \equiv - \sum_j j_{ij}(t) , \quad (2.14)$$

where $p_i(t)$ denotes the probability to find the system in state i at time t and we introduced the probability current $j_{ij}(t)$ between state i and j . This dynamics leaves the equilibrium distribution p_i^{eq} , Eq. (2.4), invariant. Assuming that every mesostate j can be reached from any other state i , any initial distribution p_i^0 converges towards the equilibrium one in the course of time. Furthermore, the local detailed balance condition, Eq. (2.13), leads to vanishing net fluxes $j_{ij}(t)$ between any states i and j .

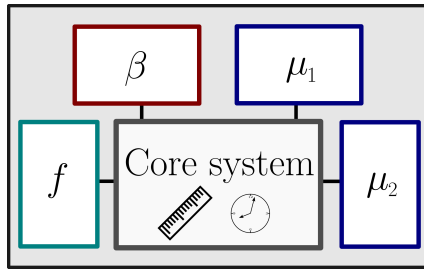


Figure 2.3: Schematic partition of the supersystem (black box) into work (green), heat (red) and several particle (blue) reservoirs. In the core system (gray box) measurements, e.g., length or time, take place.

The assumption of timescale separation does not necessarily imply equilibrium. In the next section, we consider a Markovian system coupled to external reservoirs, thus, breaking detailed balance, Eq. (2.12), allowing energy and particle exchange.

2.3 OPEN SYSTEM IN CONTACT WITH HEAT BATH, PARTICLE AND WORK RESERVOIRS

So far, we considered closed systems in contact with a heat bath which will ultimately reach thermal equilibrium. In this section, we partition the closed system into different segments, i.e., we divide the closed supersystem into a core system and reservoirs providing energy and particles, see Fig. 2.3. The core system is the system of interest where we can perform measurements.

Following the coarse-graining procedure discussed in the previous section, we split the free energy of the super system into those of the core system and the reservoirs. This leads to the extended local detailed balance condition

$$\frac{k_{ij}}{k_{ji}} = \exp \left[-\beta \left(\mathcal{F}_i - \mathcal{F}_j - \sum_{\alpha} d_{ij}^{\alpha} \mu_{\alpha} + l_{ij} f \right) \right] \equiv \exp[-\beta(\Delta_{ij}\mathcal{F} + A_{ij})]. \quad (2.15)$$

We identify three contributions. First, the change of free energy in the core system $\Delta_{ij}\mathcal{F} \equiv \mathcal{F}_i - \mathcal{F}_j$. Second, the work done on the system by the particle reservoirs during the transition $i \rightarrow j$ of the core system,

$$\mathcal{W}_{ij}^{\text{chem}} \equiv \sum_{\alpha} d_{ij}^{\alpha} \mu_{\alpha}. \quad (2.16)$$

Their free energy changes by providing $d_{ij}^\alpha > 0$ or consuming $d_{ij}^\alpha < 0$ particles of species α at chemical potential μ_α . Third, the mechanical work that can be extracted in a step of length l_{ij} while working against an external force f ,

$$\mathcal{W}_{ij}^{\text{mech}} \equiv l_{ij} f . \quad (2.17)$$

Due to the coupling to the external reservoirs, the core system can be considered as a driven open system. The nonequilibrium driving along a transition $i \rightarrow j$ is given by the free energy difference of the reservoirs,

$$A_{ij} \equiv \mathcal{W}_{ij}^{\text{chem}} - \mathcal{W}_{ij}^{\text{mech}} = -A_{ji}. \quad (2.18)$$

This quantity is also called driving affinity for that respective transition.

The above considerations apply also for time-dependent driving, e.g., chemical potentials which can change according to an externally applied protocol λ_t . Through the local detailed balance condition, Eq. (2.15), this leads to time-dependent transition rates,

$$k_{ij} = k_{ij}(\lambda_t) . \quad (2.19)$$

Thus, the time-evolution of the core-system, Eq. (2.14), generalizes to

$$\partial_t p_i(t) = \sum_j [k_{ij}(\lambda_t) p_j(t) - k_{ji}(\lambda_t) p_i(t)] \equiv \sum_j \mathcal{L}_{ij}(\lambda_t) p_j(t) , \quad (2.20)$$

where we introduced the generator $\mathcal{L}_{ij}(\lambda_t)$ of the stochastic dynamics.

In the following, we focus on two special classes of processes with a constant protocol $\lambda_t = \lambda$. The stationary solution of Eq. (2.20) is defined by

$$\mathcal{L}(\lambda) \mathbf{p}^s(\lambda) = 0 , \quad (2.21)$$

with the vector of probabilities $\mathbf{p}^s(\lambda) \equiv \{p_i^s\}$ and the generator matrix $\mathcal{L}(\lambda)$ with entries $\mathcal{L}_{ij}(\lambda)$. For vanishing affinities, i.e., $A_{ij} = 0$, we recover the equilibrium situation of the previous section. Thus, the stationary solution will be the equilibrium one,

$$p_i^{\text{eq}} = \exp[-\beta(\mathcal{F}_i - \mathcal{F})] . \quad (2.22)$$

In a genuine nonequilibrium situation with constant driving, Eq. (2.20) admits a stationary solution with non-vanishing probability currents $j_{ij}^s(\lambda) \neq 0$, thus, breaking the detailed

balance condition, Eq. (2.12). This solution is denoted as nonequilibrium steady-state (NESS) with probability p_i^s to find the core system in mesostate i .

The local detailed balance condition, Eq. (2.15), connects the dynamical picture of a system evolving according to a master equation with thermodynamic quantities such as entropy, internal energy and work. In the following sections, we explain how these physical objects can be defined along a stochastic trajectory $I(t)$.

2.4 STOCHASTIC ENERGETICS AND ENTROPY ALONG A SINGLE TRAJECTORY

2.4.1 Stochastic energetics: the first law

We consider a stochastic trajectory $I(t)$ of length T over the discrete set of mesostates, compare Fig. 2.2. Stochastic thermodynamics sets the framework to identify physical observables like internal energy, heat and work along such fluctuating paths. Thus, these quantities become stochastic variables. The internal energy at time t along the trajectory is given by

$$U_{I_t}(\lambda_t) \equiv \sum_j \delta_{I_t,j} U_j(\lambda_t) , \quad (2.23)$$

where $U_j(\lambda_t)$ denotes the internal energy of mesostate j , I_t is the state of the trajectory at time t and $\delta_{i,j}$ the Kronecker-delta. The rate of change of the internal energy is

$$\frac{d}{dt} U_{I_t}(\lambda_t) = \sum_j \left[\dot{\delta}_{I_t,j} U_j(\lambda_t) + \delta_{I_t,j} \dot{\lambda}_t \partial_\lambda U_j(\lambda) |_{\lambda=\lambda_t} \right] , \quad (2.24)$$

where $\dot{\delta}_{I_t,j}$ denotes the time derivative of the Kronecker-delta and $\dot{\lambda}_t$ the one of the protocol. A formal definition of $\dot{\delta}_{I_t,j}$ is given below, Eq. (2.26). All in all, the change of internal energy originates from a jump between mesostates and the external driving.

The change of the work along the trajectory also has two contributions,

$$\frac{d}{dt} \mathcal{W}_{I_t}(\lambda_t) \equiv \sum_{i,j} [\dot{n}_{ij}(t) A_{ij}(\lambda_t)] + \dot{\lambda}_t \partial_\lambda \mathcal{F}_{I_t}(\lambda) |_{\lambda=\lambda_t} , \quad (2.25)$$

one coming from the nonequilibrium driving along a transition, Eq. (2.18), and the other due to the external protocol λ_t . Here, $n_{ij}(t)$ denotes the number of transitions from state i

to j along the trajectory $I(t)$ up to time t . For the derivative of this quantity the following relation holds

$$\dot{\delta}_{I_t,j} = - \sum_j [\dot{n}_{ij}(t) - \dot{n}_{ji}(t)] , \quad (2.26)$$

essentially defining the derivative of the Kronecker-delta.

Imposing the first law of thermodynamics to hold along the trajectory,

$$\frac{d}{dt}U_{I_t}(\lambda_t) = \frac{d}{dt}\mathcal{W}_{I_t}(\lambda_t) - \frac{d}{dt}Q_{I_t}(\lambda_t) , \quad (2.27)$$

and using Eq. (2.26), we obtain the rate of dissipated heat as

$$\begin{aligned} \frac{d}{dt}Q_{I_t}(\lambda_t) &\equiv \sum_{i,j} \dot{n}_{ij}(t) [A_{ij}(\lambda_t) + \Delta_{ij}\mathcal{F}(\lambda_t)] - \frac{1}{\beta} \frac{d}{dt}S_{I_t}(\lambda_t) \\ &= \sum_{i,j} \dot{n}_{ij}(t) \ln \frac{k_{ij}(\lambda_t)}{k_{ji}(\lambda_t)} - \frac{1}{\beta} \frac{d}{dt}S_{I_t}(\lambda_t) , \end{aligned} \quad (2.28)$$

where we inserted the local detailed balance condition, Eq. (2.15), in the last step and identified the change of intrinsic entropy using Eq. (2.3),

$$\frac{d}{dt}S_{I_t}(\lambda_t) \equiv \sum_j [\dot{\delta}_{I_t,j} S_j(\lambda_t)] + \dot{\lambda}_t \partial_\lambda S_{I_t}(\lambda)|_{\lambda=\lambda_t} . \quad (2.29)$$

Due to the dependence of the intrinsic entropy on the external protocol λ_t and Eq. (2.28), we find that heat is even dissipated when the system stays in the same state and not only through transitions between mesostates.

2.4.2 Entropy along a stochastic trajectory

Along a trajectory, the entropy of the system at time t is given by

$$S(\lambda_t) \equiv S_{I_t}(\lambda_t) + S_{\text{sto}}(\lambda_t) , \quad (2.30)$$

where we introduced the stochastic entropy [15]

$$S_{\text{sto}}(\lambda_t) \equiv - \ln p_{I_t}(t) = - \sum_j \delta_{I_t,j} \ln p_j(t) , \quad (2.31)$$

with the solution $p_j(t)$ of the master equation (2.20). The entropy of the surrounding medium is defined through the dissipated heat,

$$S_{\text{med}}(\lambda_t) \equiv \beta Q_{I_t}(\lambda_t) . \quad (2.32)$$

The total entropy production rate along the trajectory is given by

$$\frac{d}{dt} S_{\text{tot}}(\lambda_t) \equiv \frac{d}{dt} S_{\text{med}} + \frac{d}{dt} S(\lambda_t) . \quad (2.33)$$

The time derivative of the entropy of the system reads

$$\begin{aligned} \frac{d}{dt} S(\lambda_t) &= \frac{d}{dt} S_{I_t}(\lambda_t) - \sum_j \left[\delta_{I_t,j} \frac{\dot{p}_j(t)}{p_j(t)} + \delta_{I_t,j} \ln p_j(t) \right] \\ &= \frac{d}{dt} S_{I_t}(\lambda_t) - \sum_j \delta_{I_t,j} \frac{\dot{p}_j(t)}{p_j(t)} - \sum_{i,j} \dot{n}_{ij}(t) \ln \frac{p_j(t)}{p_i(t)} , \end{aligned} \quad (2.34)$$

where the last equality follows from Eq. (2.26). Using the derivative of the entropy of the system and the definition of the dissipated heat, Eq. (2.28), the total entropy production rate becomes

$$\frac{d}{dt} S_{\text{tot}}(\lambda_t) = \sum_{i,j} \dot{n}_{ij}(t) \ln \frac{p_i(t) k_{ij}(\lambda_t)}{p_j(t) k_{ji}(\lambda_t)} - \sum_j \delta_{I_t,j} \frac{\dot{p}_j(t)}{p_j(t)} . \quad (2.35)$$

The total entropy produced along a trajectory $I(t)$ of length T is then given by

$$\Delta S_{\text{tot}}[I(t)] \equiv \int_0^T dt \frac{d}{dt} S_{\text{tot}}(\lambda_t) . \quad (2.36)$$

In a NESS with constant external driving λ , time derivatives of the probabilities $p_i(t)$ and the protocol vanish. Thus, Eq. (2.35) simplifies to

$$\frac{d}{dt} S_{\text{tot}}(\lambda_t) = \sum_{i,j} \dot{n}_{ij}(t) \ln \frac{k_{ij}(\lambda)}{k_{ji}(\lambda)} . \quad (2.37)$$

So far, we considered the definition of thermodynamic observables along a single trajectory. In the next section, we consider the ensemble average of these objects.

2.4.3 Ensemble averages

In laboratory situations, the motion of a tracer particle is in general noisy. Thus, it is impossible to predict the future behavior of such an object. However, the motion is well characterized by mean values with respect to the underlying probability distribution. These mean values are the ensemble average which we denote by $\langle \dots \rangle$. The following identification will be useful in the upcoming calculations,

$$\langle \delta_{I_t, j} \rangle = p_j(t), \quad (2.38)$$

$$\langle \dot{n}_{ij}(t) \rangle = p_i(t)k_{ij}(\lambda_t). \quad (2.39)$$

With this preliminary considerations, we start with the internal energy, Eq. (2.23).

The average value of internal energy simplifies to

$$\langle U_{I_t}(\lambda_t) \rangle = \sum_j p_j(t)U_j(\lambda_t). \quad (2.40)$$

The mean total change of internal energy along a trajectory $I(t)$ of length T is then

$$\langle \Delta U[I(t)] \rangle = \sum_j [p_j(T)U_j(\lambda_T) - p_j(0)U_j(\lambda_0)]. \quad (2.41)$$

Integration of Eq. (2.25) and taking the ensemble-average yields the mean work along the trajectory

$$\langle \mathcal{W}[I(t)] \rangle = \int_0^T dt \left(\sum_{i < j} j_{ij}(t)A_{ij}(\lambda_t) + \sum_j p_j(t)\dot{\lambda}_t \partial_\lambda \mathcal{F}_j(\lambda)|_{\lambda=\lambda_t} \right). \quad (2.42)$$

Similar calculations using Eq.(2.28) lead to the mean dissipated heat

$$\langle Q[I(t)] \rangle = \int_0^T dt \sum_{i < j} j_{ij}(t) \ln \frac{k_{ij}(\lambda_t)}{k_{ji}(\lambda_t)} - \frac{1}{\beta} \sum_j [p_j(T)S_j(\lambda_T) - p_j(0)S_j(\lambda_0)]. \quad (2.43)$$

Also on the ensemble level, we find the first law of thermodynamics

$$\langle U_{I_t}(\lambda_t) \rangle = \langle \mathcal{W}[I(t)] \rangle - \langle Q[I(t)] \rangle, \quad (2.44)$$

which we had implemented on the trajectory level.

Concerning the entropy production rate, Eq.(2.35), the mean value is given by

$$\sigma(t) \equiv \left\langle \frac{d}{dt} S_{\text{tot}}(\lambda_t) \right\rangle = \sum_{i<j} [p_i(t)k_{ij}(\lambda_t) - p_j(t)k_{ji}(\lambda_t)] \ln \frac{p_i(t)k_{ij}(\lambda_t)}{p_j(t)k_{ji}(\lambda_t)} \geq 0. \quad (2.45)$$

The mean entropy production rate is non-negative which follows from the inequality $(x - y) \ln(x/y) \geq 0$ for non-negative x and y . The total entropy production is

$$\langle \Delta S_{\text{tot}}[I(t)] \rangle = \int_0^T dt \sigma(t) \geq 0. \quad (2.46)$$

Thus, the definition of total entropy production rate, Eq. (2.35), is consistent with the second law of thermodynamics.

The intrinsic $S_i(\lambda_t)$ and stochastic entropy $S_{\text{sto}}(\lambda_t)$ are variables that are not extensive in time. Thus, in a steady-state with constant external protocol λ , only the entropy rate of the surrounding medium contributes to the total entropy production rate. Averaging Eq.(2.28) and using the definition of the medium entropy, Eq.(2.32), the mean entropy production rate becomes

$$\sigma^s = \sum_{i<j} j_{ij}^s(\lambda) \ln \frac{k_{ij}(\lambda)}{k_{ji}(\lambda)} = \sum_{i<j} j_{ij}^s(\lambda) A_{ij}(\lambda). \quad (2.47)$$

With a consistent thermodynamic theory at hand, we apply these concepts to several applications. We start with finite-time transformations in the next section.

2.5 FINITE-TIME THERMODYNAMICS AND OPTIMAL PROTOCOLS

2.5.1 *Finite-time protocols*

We consider a transformation of a system during a finite time T from a given initial state to a finale one, see Fig. 2.4. The requirement of finite time leads to an inevitable entropic cost, hence, making the transformation nonequilibrium. An obvious question is how such a transformation can be optimized regarding the thermodynamic cost. When dealing with macroscopic systems, this field is denoted as finite-time thermodynamics [23].

The application of these optimization techniques to fluctuating systems is a recent development. The first systematic study examined a moving harmonic trap in contact with

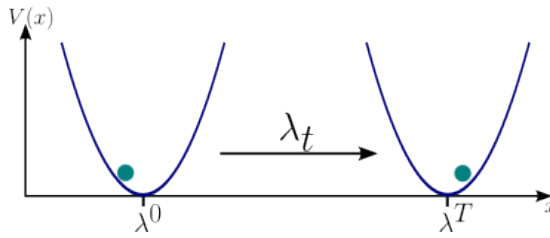


Figure 2.4: Brownian particle (green dot) trapped in a harmonic potential. The external protocol λ_t transforms the trap initially located at λ^0 to λ^T within finite time T .

a heat reservoir [24], see Fig. 2.4. The authors have found that the optimal transformation minimizing the work includes discontinuous jumps at the beginning and end of the process. This behavior turned out to be generic.

From a more technical and applied point of view, the minimization of released heat during a process is of particular interest as it leads to a refined second law of thermodynamics or Landauer-principle [25–27]. This will be the setting for the rest of this section and Chapter 3.

Recent studies connect the optimization problem to geometric quantities like the Wasserstein distance [26, 28]. This link to information geometry ultimately led to the unification of thermodynamic optimization for Markov jump processes, Langevin dynamics and quantum systems [29, 30].

2.5.2 *Minimizing entropy production in continuous state space*

In this section, we introduce the optimization problem for Fokker-Planck systems and highlight the most important results in relation to Chapter 3. For simplicity and clarity of arguments, we discuss a one-dimensional motion. The generalization to more dimensions is straight forward.

We consider a system with continuous state space following a Fokker-Planck dynamics. The equation of motion for the systems probability distribution reads

$$\partial_t p(x, t) = -\partial_x [F(x, t, \lambda_t) p(x, t) - D \partial_x p(x, t)] \equiv -\partial_x [\nu(x, t) p(x, t)] , \quad (2.48)$$

where $\nu(x, t)$ denotes the local mean velocity, D the diffusion constant and $F(x, t, \lambda_t)$ the force driving the system depending on an externally controlled protocol λ_t . Total entropy production rate for the Fokker-Planck dynamics is given by [12]

$$\sigma^{\text{cont}}(t) = \frac{1}{D} \langle \nu(x, t)^2 \rangle . \quad (2.49)$$

This expression can for example be obtained by performing the continuum limit of the discrete one, Eq. (2.45). The total entropy production for a process of duration T is then

$$\Delta S_{\text{tot}} \equiv \int_0^T dt \sigma^{\text{cont}}(t) . \quad (2.50)$$

Since the Fokker-Planck equation (2.48) and the total entropy production, Eq. (2.50), depend only on the probability $p(x, t)$ and local mean velocity $\nu(x, t)$, we treat them as free parameters for the optimization.

Assuming that the system is initially prepared according to $p^0(x)$, we ask for the protocol $\nu^*(x, t)$ to transform the system into a given final state $p^T(x)$ in finite time T . This transformation should be done with minimal entropic cost. The requirement for a finite time T is crucial since any quasi-static, i.e., infinitely slow transformation comes with vanishing entropy production. The optimization problem is given by

$$\min_{\{p(x,t), \nu(x,t), \eta(x,t)\}} \Delta S[p(x, t), \nu(x, t), \eta(x, t)] \quad (2.51)$$

with the functional

$$\Delta S[p(x, t), \nu(x, t), \eta(x, t)] \equiv \frac{1}{D} \int_0^T dt \int dx \left(\nu(x, t)^2 p(x, t) + \eta(x, t) \{ \partial_t p(x, t) + \partial_x [\nu(x, t) p(x, t)] \} \right) , \quad (2.52)$$

where we introduced a Lagrangian multiplier $\eta(x, t)$ to incorporate the constraint that the dynamics should be governed by a Fokker-Planck equation. The protocol $\nu^*(x, t)$ which solves the minimization problem is termed optimal protocol.

Variation of Eq. (2.52) with respect of $\eta(x, t)$ reproduces the Fokker-Planck equation (2.48). The remaining equations are equivalent to

$$\nu^*(x, t) = -\frac{1}{2} \partial_x \eta(x, t) . \quad (2.53)$$

and

$$\partial_t \nu^*(x, t) = -\nu^*(x, t) \partial_x \nu^*(x, t) . \quad (2.54)$$

Thus, $\nu^*(x, t)$ satisfies the inviscid Burgers equation [31]. Furthermore, the optimal protocol is a total differential, Eq. (2.53), hence, for a transformation of a system from initial state $p^0(x)$ to $p^T(x)$ during a finite time T only conservative forces are necessary [25, 26]. A further noteworthy property of the solution to the optimization problem, Eq. (2.51), is that it is the shortest connection between $p^0(x)$ and $p^T(x)$ in the space of probability distributions. Thus, the optimal protocol establishes a connection to information geometry [28–30].

2.5.3 Optimal protocols on discrete state space

We consider a system with discrete but finite state space. The dynamics is governed by a master equation,

$$\partial_t p_i(t) = - \sum_j [k_{ji}(\lambda_t) p_i(t) - k_{ij}(\lambda_t) p_j(t)] , \quad (2.55)$$

where the rates $k_{ij}(\lambda_t)$ can be externally controlled and $p_i(t)$ denotes the probability to find the system at time t in state i .

The optimization problem is similar to the continuous case discussed above. We assume that the system is initially prepared according to $\{p_i^0\}$ and should be transformed into $\{p_i^T\}$ with minimal entropic cost. In order to formulate the minimization problem and most important results, we closely follow Ref. [27] but use a slightly altered notation.

It is convenient to parameterize the probabilities as

$$\phi_i(t) \equiv \sqrt{p_i(t)} . \quad (2.56)$$

The transition rates can be written as

$$k_{ij}(\lambda_t) = \kappa_{ij}(t) e^{A_{ij}(t)/2} , \quad (2.57)$$

with symmetric $\kappa_{ij}(t) = \kappa_{ji}(t)$ and anti-symmetric part $A_{ij}(t) = -A_{ji}(t)$. As a simultaneous variation of both parts would lead to a trivial problem, we keep κ_{ij} constant, hence, setting

a typical time-scale for the transition from state i to j . Thus, the $\{A_{ij}(t)\}$ remain as the externally controlled protocols. We further introduce the driving between two states

$$\varphi_{ij}(t) \equiv A_{ij}(t) + 2 \ln \frac{\phi_i(t)}{\phi_j(t)}. \quad (2.58)$$

With these quantities the master equation becomes

$$\partial_t \phi_i(t) = - \sum_{j \neq i} \kappa_{ij} \phi_j \sinh \frac{\varphi_{ij}(t)}{2}. \quad (2.59)$$

The entropy production rate, Eq. (2.45), reads

$$\sigma(t) = 2 \sum_{i < j} \kappa_{ij} \phi_i(t) \phi_j(t) \varphi_{ij}(t) \sinh \frac{\varphi_{ij}(t)}{2}. \quad (2.60)$$

Since the dynamical equation and entropy production rate only depend on $\{\phi_i(t), \varphi_{ij}(t)\}$, we treat them as free parameters for the optimization. Introducing Lagrange multipliers $\{\eta_i(t)\}$ to enforce the master dynamics, the full functional is given by

$$\begin{aligned} \Delta S[\{\phi_i(t), \varphi_{ij}(t), \eta_i(t)\}] \equiv & \int_0^T dt \left\{ 2 \sum_{i < j} \kappa_{ij} \phi_i(t) \phi_j(t) \varphi_{ij}(t) \sinh \frac{\varphi_{ij}(t)}{2} \right. \\ & \left. + \sum_i \eta_i(t) \left(\partial_t \phi_i(t) + \sum_{j \neq i} \kappa_{ij} \phi_j(t) \sinh \frac{\varphi_{ij}(t)}{2} \right) \right\}. \end{aligned} \quad (2.61)$$

Variation leads to the Euler-Lagrange equations

$$0 = \eta_i(t) \phi_j(t) - \eta_j(t) \phi_i(t) + 4 \phi_i(t) \phi_j(t) \left[\tanh \frac{\varphi_{ij}(t)}{2} + \frac{\varphi_{ij}(t)}{2} \right], \quad (2.62)$$

$$\partial_t \phi_i(t) = - \sum_{j \neq i} \kappa_{ij} \phi_j(t) \sinh \frac{\varphi_{ij}(t)}{2}, \quad (2.63)$$

$$\partial_t \eta_i(t) = \sum_{j \neq i} \kappa_{ij} [2 \phi_j(t) \varphi_{ij}(t) - \eta_j(t)] \sinh \frac{\varphi_{ij}(t)}{2}. \quad (2.64)$$

Taking the time derivative of Eq. (2.62) and plugging in Eq. (2.63) and (2.64) results in the equation of motion for the driving function,

$$\begin{aligned} \partial_t \varphi_{ij}(t) &= \frac{1}{1 - \frac{1}{2} \tanh^2 \frac{\varphi_{ij}(t)}{2}} \\ &\times \sum_k \left[\kappa_{ik} \frac{\phi_k(t)}{\phi_i(t)} \sinh \frac{\varphi_{ik}(t)}{2} \tanh \frac{\varphi_{ik}(t)}{2} - \kappa_{jk} \frac{\phi_k(t)}{\phi_j(t)} \sinh \frac{\varphi_{jk}(t)}{2} \tanh \frac{\varphi_{jk}(t)}{2} \right]. \end{aligned} \quad (2.65)$$

In order to perform a continuum-limit, we define

$$v(x, t) dx \equiv \varphi_{x, x+dx}(t) = -\varphi_{x+dx, x}(t) \quad (2.66)$$

and introduce

$$v(x, t) \equiv \varphi'_{x,x}(t), \quad (2.67)$$

where a prime denotes the derivative with respect to the second index. Furthermore, we assume a unicyclic network structure with overall constant symmetric parts, i.e., $\kappa_{ij} \equiv \kappa$. Moreover, we relabel the states as $i \rightarrow x$ with $i \pm 1 \rightarrow x \pm dx$ to make the lattice spacing explicit. We further introduce a time-scale

$$\tau_0 \equiv \frac{2}{\kappa dx^2}, \quad (2.68)$$

which is assumed to be finite in the limit of vanishing lattice-spacing, i.e., $dx \rightarrow 0$. In that limit, Eq. (2.65) reduces in leading order to

$$\partial_t v(x, t) dx = -\frac{\kappa}{2} v(x, t) \partial_x v(x, t) dx^3 + \mathcal{O}(dx^4). \quad (2.69)$$

Thus, we recover the inviscid Burgers equation in the continuum limit,

$$\tau_0 \partial_t v(x, t) + v(x, t) \partial_x v(x, t) = 0. \quad (2.70)$$

In summary, the minimization problem over discrete state space reduces to the Fokker-Planck one, see Sec. 2.5.2, in the limit of small lattice spacing. However, it is not clear whether or not the optimal protocol is conservative. In Chapter 3, we will define what a

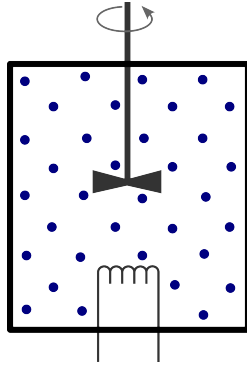


Figure 2.5: Sketch of a tank filled with a reaction species (blue dots) surrounded by a dilute solution. The temperature of the liquid is controlled through the immersion heater at the bottom. Due to a constant motion of the rotor, we obtain a well-stirred mixture.

conservative protocol is for a system with discrete state space and address this question in detail.

2.6 STOCHASTIC THERMODYNAMICS OF CHEMICAL REACTION NETWORKS

2.6.1 *Introductory remarks*

The basic thermodynamic notion of an open system in contact with a heat bath and several particle reservoirs has already been introduced in Sec. 2.4. In this section, we focus on the thermodynamics of chemical reaction networks (CRN). We start with a closed, equilibrium system to establish the notation and discuss the dynamics. In the second part, we consider open CRN supplied by chemostats, i.e., particle reservoirs that keep the concentration of certain particle species constant. For such systems, non-vanishing particle fluxes are possible that are ultimately related to entropy production. This section is based on Ref. [32–34].

2.6.2 *Closed systems and the chemical master equation*

We consider a closed system of volume Ω containing molecules of s different species X_i , $i = 1, \dots, s$. We assume that the molecules form a well-stirred mixture in a dilute solution, i.e., all molecules are entirely surrounded by the solvent and homogeneously distributed over the volume. We further assume that the system is contact with a heat bath at temperature

β . A possible experimental setting would be a continuously stirred tank reactor, see Fig. 2.5.

We denote the number of molecules of species X_i with a non-negative integer $n_i \in \mathbb{N}_0$. The interactions of the species are described through a network of reactions



where $\rho \in \{1, 2, \dots, r\}$ denotes the reaction channel. We assume that each reaction is associated with a reversed one such that each reaction channel ρ consists of two processes that could in principle balance each other. The change in the population of species X_i during a transition through channel ρ is given through the stoichiometric coefficients

$$\nu_{\rho}^i \equiv \nu_{-\rho}^i - \nu_{+\rho}^i. \quad (2.72)$$

We denote the vector of the number of molecules as

$$\mathbf{n} \equiv \{n_i\}_{i=1}^s. \quad (2.73)$$

The vector of stoichiometric coefficients for the forward (+) respectively backward (−) reaction of channel ρ is defined as

$$\boldsymbol{\nu}_{\rho}^{\pm} \equiv \{\pm \nu_{\rho}^i\}_{i=1}^s. \quad (2.74)$$

The change in the number of population of species during a forward respectively backward reaction through channel ρ becomes

$$\mathbf{n} \rightarrow \mathbf{n}' \equiv \mathbf{n} + \boldsymbol{\nu}_{\rho}^{\pm}. \quad (2.75)$$

The dynamics of a CRN is determined through the transition rates of the different reactions,

$$\begin{aligned} W_{\rho}^{+}(\mathbf{n}) &= \Omega k_{\rho}^{+} \prod_{i=1}^s \prod_{m=1}^{\nu_{+\rho}^i} \frac{n_i - m + 1}{\Omega}, \\ W_{\rho}^{-}(\mathbf{n}) &= \Omega k_{\rho}^{-} \prod_{i=1}^s \prod_{m=1}^{\nu_{-\rho}^i} \frac{n_i - m + 1}{\Omega}. \end{aligned} \quad (2.76)$$

These are given through the molecular rate constant k_ρ^\pm and the probability for the necessary number of particles to collide as specified in the reaction scheme. For example, in the forward reaction of channel ρ , $\nu_{+\rho}^i$ particles of species X_i have to collide in order for the reaction to take place. This leads to the product expression in Eq.(2.76).

The dynamics of this reactive stochastic process is governed by the chemical master equation

$$\partial_t p(\mathbf{n}, t) = \sum_{\rho=1}^s \sum_{\chi=\pm} [W_\rho^\chi(\mathbf{n} - \boldsymbol{\nu}_\rho^\chi) p(\mathbf{n} - \boldsymbol{\nu}_\rho^\chi, t) - W_\rho^\chi(\mathbf{n}) p(\mathbf{n}, t)] , \quad (2.77)$$

where the probability is normalized over all possible states,

$$\sum_{\mathbf{n}} p(\mathbf{n}, t) = 1 . \quad (2.78)$$

The connection to the master equation introduced in Eq. (2.14) becomes obvious when we rewrite Eq.(2.77) as

$$\partial_t p(\mathbf{n}, t) = \sum_{\mathbf{n}'} [w(\mathbf{n}'|\mathbf{n}) p(\mathbf{n}', t) - w(\mathbf{n}|\mathbf{n}') p(\mathbf{n}, t)] , \quad (2.79)$$

with transition rates

$$w(\mathbf{n}'|\mathbf{n}) \equiv \sum_{\rho} \sum_{\chi=\pm} W_\rho^\chi(\mathbf{n}') \delta_{\mathbf{n}', \mathbf{n} - \boldsymbol{\nu}_\rho^\chi} . \quad (2.80)$$

In analogy to the probability flux, the reaction flow is defined as

$$j_\rho(\mathbf{n}, t) \equiv j_\rho^+(\mathbf{n}, t) - j_\rho^-(\mathbf{n}, t) , \quad (2.81)$$

where

$$j_\rho^\pm(\mathbf{n}, t) \equiv W_\rho^\pm(\mathbf{n} - \boldsymbol{\nu}_\rho^\pm) p(\mathbf{n} - \boldsymbol{\nu}_\rho^\pm, t) - W_\rho^\pm(\mathbf{n}) p(\mathbf{n}, t) . \quad (2.82)$$

In an equilibrium stationary state, no net fluxes are present. Thus, the detailed balance condition, Eq. (2.12), reduces to

$$j_\rho^{\pm s}(\mathbf{n}) \equiv 0 , \quad (2.83)$$

for all $\rho = 1, 2, \dots, r$. Every closed CRN will eventually reach its equilibrium state.

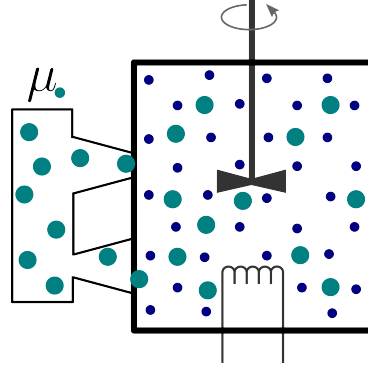
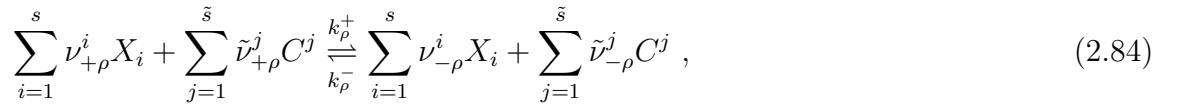


Figure 2.6: Reaction tank as described in Fig. 2.5. We allow a chemostatted species (green dots) to be exchanged with a particle reservoir. Through the upper channel the chemostatted species gets into the tank, whereas through the lower one, particles can be extracted.

If the system is open and in contact with chemostats, this flux balance can be broken due to nonequilibrium boundary conditions. We consider this situation in the next section.

2.6.3 Open chemical reaction network and entropy

We bring the chemical reaction network in contact with external particle reservoirs, thus, allowing exchange of matter, see Fig. 2.6. We assume the reservoirs regulate the system such that the concentration of certain species are kept constant. These reservoirs are called chemostats and the controlled species are said to be chemostatted. The reaction scheme reads



with in total \tilde{s} chemostatted species C^j . We denote the concentration of the externally controlled species as c_j .

The transition rates become

$$W_{\rho}^{\pm}(\mathbf{n}, \mathbf{c}) = \Omega k_{\rho}^{\pm} \prod_{i=1}^s \prod_{m=1}^{\nu_{\pm\rho}^i} \frac{n_i - m + 1}{\Omega} \prod_{j=1}^{\tilde{s}} c_j^{\tilde{\nu}_{\pm\rho}^j}. \quad (2.85)$$

In order for the transition to happen, the probability of a collision with a chemostatted species needs to be included. Here, $\mathbf{c} \equiv \{c_j\}_{j=1}^{\tilde{s}}$ denotes the vector of concentrations of the regulated species. The dynamics is still governed by the chemical master equation (2.77)

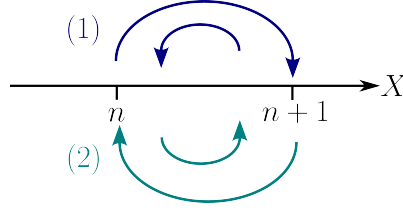


Figure 2.7: Closed pathways for the one-dimensional chemical reaction network with two reaction channels, (1) $A \rightleftharpoons X$ and (2) $X \rightleftharpoons B$. Starting in state n , the system can leave through channel (1), consuming a molecule A , and return through channel (2) while producing a B molecule. The opposite cycle is shown when starting in state n and leaving through channel (2) while consuming a B molecule. Returning through channel (1), i.e., producing an A molecule, leaves the X state invariant. The cycle affinity, Eq. (2.87), compares the thermodynamic weight of both pathways.

but with rates that depend on the concentrations \mathbf{c} . Due to the externally imposed particle flux, the master equation (2.77) admits solutions that can break detailed balance. An example would be the transport of a molecule from one chemostat to another. A stationary solution with non-vanishing fluxes is again termed nonequilibrium steady-state (NESS).

In a NESS, a cycle flux $j_{\mathcal{C}}$ between chemostats can emerge, i.e., a constant flux along a closed reaction pathway \mathcal{C} , see Fig. 2.7. Such a path goes back to the initial state of internal species X_i , leaving their state unchanged. However, particles are exchanged with the chemostats along the way. Thus, an exchange of energy occurs during a completed cycle. By the local detailed balance condition, Eq. (2.15), the rates along the path \mathcal{C} are connected with the chemical potential of the reservoirs,

$$\mu_j = \mu_0 + \frac{1}{\beta} \ln \frac{c_j}{c_0}, \quad (2.86)$$

where μ_0 and c_0 are reference values and β denotes the inverse temperature. For a cycle \mathcal{C} between the reservoirs of species C^i and C^j , thermodynamic consistency requires

$$\beta(\mu_i - \mu_j) = \prod_{\rho \in \mathcal{C}} \ln \frac{W_{\rho}^{+}(\mathbf{n}, \mathbf{c})}{W_{\rho}^{-}(\mathbf{n}, \mathbf{c})} \equiv A_{\mathcal{C}}, \quad (2.87)$$

where we introduced the affinity $A_{\mathcal{C}}$ along the cycle \mathcal{C} . This quantity is a measure for the thermodynamic driving along the cycle, i.e., the entropy produced when passing through the cycle. Using Eq. (2.47), the mean steady-state entropy production rate reads

$$\sigma^s = \sum_{\mathcal{C}} j_{\mathcal{C}} A_{\mathcal{C}}. \quad (2.88)$$

Another way of expressing the steady-state entropy production rate of a chemostatted CRN is given by [34]

$$\sigma^s = \sum_{j=1}^{\tilde{s}} j_j \mu_j , \quad (2.89)$$

where j_j denotes the mean particle flux provided by the reservoir associated with species C^j .

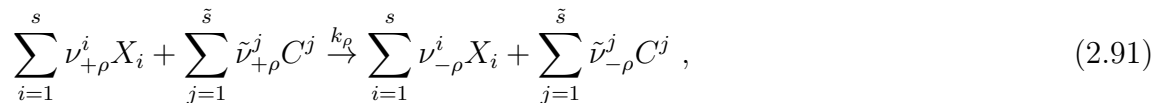
For schemes involving potential nonlinear reactions, it is in general not even possible to obtain an explicit, analytical expression for the stationary solution. Thus, in order to examine such systems, numerical and approximate methods are needed. Before we discuss diffusion approximations of the master equation, we introduce in the next section the stochastic sampling algorithm [35], a numerical scheme to generate trajectories whose statistics exactly satisfy the master equation.

2.6.4 *Simulating the dynamics: Gillespie's direct method*

Thermodynamic consistency requires that every reaction can also occur in the reversed direction. Thus, in the previous sections, we combined forward and backward transitions into one reaction channel. For the purpose of this section, we treat every reaction separately, i.e., we consider reaction ρ out of all possible reactions R where

$$R \equiv \{+1, -1, +2, -2, \dots, +r, -r\} . \quad (2.90)$$

The reaction scheme for reaction ρ reads



with reaction rates

$$W_\rho(\mathbf{n}) = \Omega k_\rho \prod_{i=1}^s \prod_{m=1}^{\nu_{+\rho}^i} \frac{n_i - m + 1}{\Omega} \prod_{j=1}^r c_j^{\tilde{\nu}_{+\rho}^j} . \quad (2.92)$$

The vector of stoichiometric coefficients is

$$\boldsymbol{\nu}_\rho \equiv \boldsymbol{\nu}_\rho^- - \boldsymbol{\nu}_\rho^+ . \quad (2.93)$$

The stochastic sampling algorithm proposed by Gillespie [35] is a numerical scheme to generate a trajectory $\mathbf{I}(t)$ that obeys the reaction scheme, Eq. (2.91). The probability distribution of an ensemble of such trajectories, i.e., $p(\mathbf{n}, t) \equiv \langle \delta_{\mathbf{I}(t), \mathbf{n}} \rangle$, satisfies the master equation, Eq. (2.77). Assuming the system is in state \mathbf{n} , the core ingredient of Gillespie's scheme is the exact sampling of the waiting time τ_W for the next reaction to occur and to decide which reaction ρ_0 takes place.

In a Markov network, the waiting time for a reaction to take place is exponentially distributed. This can be seen from the survival probability of a given state \mathbf{n} . Assuming the system is in state \mathbf{n} , the probability $\mathfrak{s}_\rho(t|\mathbf{n})$ to not leave that state through reaction ρ satisfies the differential equation

$$\frac{d}{dt} \mathfrak{s}_\rho(t|\mathbf{n}) = -W_\rho(\mathbf{n}) \mathfrak{s}_\rho(t|\mathbf{n}) , \quad \mathfrak{s}_\rho(0|\mathbf{n}) = 1 . \quad (2.94)$$

Since the transition rates are time-independent, the solution reads

$$\mathfrak{s}_\rho(t|\mathbf{n}) = e^{-W_\rho(\mathbf{n})t} . \quad (2.95)$$

The overall survival probability of state \mathbf{n} is then the product over all possible ways to leave the state,

$$\mathfrak{s}(t|\mathbf{n}) = \prod_{\rho} \mathfrak{s}_\rho(t|\mathbf{n}) = e^{-W_{\text{tot}}(\mathbf{n})t} , \quad (2.96)$$

with

$$W_{\text{tot}}(\mathbf{n}) \equiv \sum_{\rho} W_\rho(\mathbf{n}) . \quad (2.97)$$

The waiting time distribution follows as

$$\mathfrak{w}(t|\mathbf{n}) \equiv \frac{d}{dt} [1 - \mathfrak{s}(t|\mathbf{n})] = W_{\text{tot}}(\mathbf{n}) e^{-W_{\text{tot}}(\mathbf{n})t} . \quad (2.98)$$

Assuming that some reaction takes place to leave state \mathbf{n} , the probability for reaction ρ to occur is

$$\mathfrak{p}_\rho(\mathbf{n}) \equiv \frac{W_\rho(\mathbf{n})}{W_{\text{tot}}(\mathbf{n})} . \quad (2.99)$$

All in all, we can now formulate Gillespie's direct method [35]. The reaction scheme is summarized in the following steps.

1. At time t , the trajectory $\mathbf{I}(t)$ is in state \mathbf{n} , i.e., $\mathbf{I}(t) = \mathbf{n}$.
2. Calculate the propensities $W_\rho(\mathbf{n})$ and $W_{\text{tot}}(\mathbf{n})$, Eq. (2.97).
3. Draw a random number r_1 from a uniform distribution over the interval $[0, 1)$ and calculate the waiting time τ_W for the next reaction to take place,

$$\tau_W \equiv -\frac{1}{W_{\text{tot}}(\mathbf{n})} \ln(1 - r_1) , \quad (2.100)$$

satisfying Eq. (2.98).

4. Using Eq. (2.99) and another random number r_2 drawn from a uniform distribution over the interval $[0, 1)$, determine which reaction takes place, i.e., find ρ_0 such that

$$\sum_{\rho=0}^{\rho_0-1} \mathfrak{p}_\rho(\mathbf{n}) < r_2 \leq \sum_{\rho=0}^{\rho_0} \mathfrak{p}_\rho(\mathbf{n}) . \quad (2.101)$$

5. Update the time and population,

$$t \rightarrow t + \tau_W , \quad \mathbf{I}(t + \tau_W) = \mathbf{n} + \boldsymbol{\nu}_{\rho_0} . \quad (2.102)$$

6. Repeat step 1.-5. until the final time is reached.

Finally, we note that Gillespie's direct method is not only applicable to CRN as it has been discussed in this section. The stochastic simulation algorithm extends to any system that is described by a master equation. For instance, a physical system evolving over a set of discrete mesostates, compare Sec. 2.3.

2.7 APPROXIMATE METHODS FOR MARKOV JUMP PROCESSES – THE WEAK-NOISE LIMIT

2.7.1 *Approximating the master equation*

The master equation is in general difficult to solve analytically. Furthermore, the exact numerical scheme, see Sec. 2.6.4, becomes computationally inefficient for large system-sizes Ω . Thus, approximate methods are needed.

In this section, we discuss schemes to solve master equations by approximating them as diffusion processes. These methods have in common that they change from the description using the number of particles \mathbf{n} towards the corresponding concentrations \mathbf{x} . The basic assumption for a description of the system by concentrations is that the volume Ω of the system is sufficiently large. Thus, we consider the limit $\Omega \rightarrow \infty$ which is termed the weak-noise limit or thermodynamic limit. In the limit of infinite system-size, the system is described by the deterministic rate equation. The weak-noise limit considers the leading-order stochastic corrections to that macroscopic motion.

We briefly discuss the most important approximation schemes. The resulting Fokker-Planck equations admit stationary solutions which obey a large deviation principle [36]. The special case of WKB solutions are discussed in the last section. For simplicity and clarity of arguments, we consider one-dimensional systems. More-dimensional systems are a straightforward generalization. The starting point of this section is the following master equation,

$$\partial_t p(n, t) = \sum_{n'} \left[w(n'|n)p(n', t) - w(n|n')p(n, t) \right]. \quad (2.103)$$

2.7.2 Van Kampen's system-size expansion

A first step towards a systematic expansion of the chemical master equation is the system-size expansion due to van Kampen [37]. The main assumption is that the dynamics of the system becomes deterministic with weak fluctuations in the limit of large system-size Ω . This leads to the ansatz

$$n(t) = \Omega \hat{x}(t) + \sqrt{\Omega} \zeta(t), \quad (2.104)$$

where $\hat{x}(t)$ denotes the deterministic variable and $\zeta(t)$ the fluctuations. An expansion of the chemical master equation (2.103) for large Ω using van Kampen's ansatz, Eq. (2.104), yields the equation of motion for the deterministic $\hat{x}(t)$ and the dynamical equation for the probability distribution of the fluctuations ζ .

Through the transformation rule of probability densities, the distribution of the fluctuations is given by

$$\pi(\zeta, t) \equiv \sqrt{\Omega} p\left(\Omega \hat{x}(t) + \sqrt{\Omega} \zeta, t\right). \quad (2.105)$$

The dynamics is obtained as

$$\partial_t \pi(\zeta, t) = \frac{d}{dt} \left[\sqrt{\Omega} p[\Omega \hat{x}(t) + \sqrt{\Omega} \zeta, t] \right] = \underbrace{\sqrt{\Omega} \partial_t p(n, t)}_i + \underbrace{\sqrt{\Omega} \partial_\zeta \pi(\zeta, t) \partial_t \hat{x}}_{ii} . \quad (2.106)$$

Term i can be evaluated with the Kramers-Moyal expansion [38, 39] which yields

$$\partial_t p(n, t) = \sum_{l=1}^{\infty} \frac{(-1)^l}{l! \Omega^{(l-1)/2}} \partial_\zeta^l \left[\tilde{\alpha}_l \left(\hat{x}(t) + \zeta(t)/\sqrt{\Omega} \right) \pi(\zeta, t) \right] , \quad (2.107)$$

with rescaled jump moments,

$$\tilde{\alpha}_l(x, t) \equiv \lim_{\Omega \rightarrow \infty} \alpha_l(\Omega x)/\Omega , \quad l = 1, 2, \dots , \quad (2.108)$$

and

$$\alpha_l(n, t) \equiv \sum_{n'} (n' - n)^l w(n'|n) . \quad (2.109)$$

The transition rates $w(n'|n)$ are possibly time-dependent, e.g., through an external driving protocol λ_t . A Taylor expansion of the rescaled jump-moments in Eq. (2.107) for $\Omega \gg 1$ gives

$$\tilde{\alpha}_l \left(\hat{x}(t) + \xi(t)/\sqrt{\Omega} \right) = \tilde{\alpha}_l(\hat{x}(t)) + \frac{1}{\sqrt{\Omega}} \alpha'_l(\hat{x}(t)) \zeta(t) + \mathcal{O}(1/\Omega) . \quad (2.110)$$

Comparing orders of Ω in term i and ii of Eq. (2.106) together with Eq. (2.110) yields the dynamical equations. In $\mathcal{O}(1)$,

$$\frac{d}{dt} \hat{x}(t) = \tilde{\alpha}_1(\hat{x}(t)) , \quad (2.111)$$

and in $\mathcal{O}(1/\sqrt{\Omega})$,

$$\partial_t \pi(\zeta, t) = -\partial_\zeta [\tilde{\alpha}'_1(\hat{x}(t)) \xi \pi(\zeta, t)] + \frac{1}{2} \tilde{\alpha}_2(\hat{x}(t)) \partial_\zeta^2 \pi(\zeta, t) . \quad (2.112)$$

This constitutes van Kampen's system-size expansion.

The deterministic equation (2.111) is in general a nonlinear ordinary differential equation. It is often called macroscopic law for the mean or mean-field equation since it is also obtained when simply ignoring all fluctuations in the system, i.e., when approximating

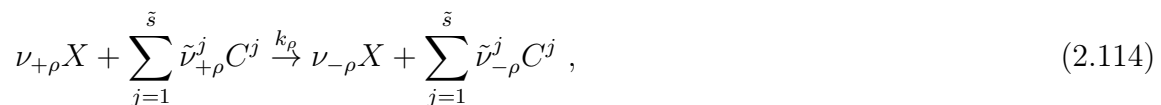
$$\frac{d}{dt} \langle x(t) \rangle = \langle \tilde{\alpha}_1(x(t)) \rangle \approx \tilde{\alpha}_1(\langle x(t) \rangle) . \quad (2.113)$$

Thus, $\hat{x}(t)$ is often interpreted as mean concentration $\langle x(t) \rangle$ and the Ω -expansion as systematic tool in order to derive a mean-field law. However, this interpretation is sometimes misleading and one should consider $\hat{x}(t)$ as the most probable value instead.

The above described system-size expansion needs to be slightly altered if the derivative $\tilde{\alpha}'_1(\hat{x}(t))$ in Eq. (2.112) vanishes. We will encounter this situation in Chapter 5. Nevertheless, the basic idea of the system-size expansion as presented in this section can still be applied. Given that the derivative is non-vanishing, the above expansion is also termed linear-noise approximation.

2.7.3 Chemical Langevin equation

Even though, van Kampen's system-size expansion is a systematic expansion of the master equation (2.103), its range of applicability relies on the validity of the interpretation of the motion as a deterministic, mean-field description with weak fluctuations, Eq. (2.104). To overcome this limitations, Gillespie proposed to describe a given reaction scheme through a Langevin equation [40]. For the purpose of this section, we consider the setting of Sec. 2.6.4 and refer to that section for the necessary definitions. The reaction scheme involving only one internal species X reads



where $\rho \in R \equiv \{-1, +1, -2, +2, \dots, +s, -s\}$ denotes the reaction that takes place. The number of molecules of species X is denoted as n . Imposing two conditions on the transition rates $W_\rho(n)$, the time-evolution of a trajectory can be approximated through a Langevin equation which is denoted chemical Langevin equation (CLE). These constraints on the propensity functions are termed leap conditions.

The first leap condition requires the existence of a leap time τ that is small enough such that the internal state of the system does not change during that time. Given that a system is in state n at time t , this conditions constrains the propensity function to satisfy

$$W_\rho(n_{t'}) \simeq W_\rho(n), \quad \forall t' \in [t, t + \tau], \quad \forall \rho, \quad (2.115)$$

where $n_{t'}$ denotes the state of the system at time t' . Since the reactions that occur during time interval $[t, t + \tau]$ do not change the transition rates $W_\rho(n)$, all reaction events during that time will be independent of each other. With the interpretation of the propensity functions as [40]

$$\begin{aligned} W_\rho(n)dt &\equiv \text{probability that one reaction through channel } \rho \text{ will occur} \\ &\quad \text{somewhere in the volume } \Omega \text{ within the time interval } [t, t + dt) \\ &\quad \text{given that at time } t \text{ the number of the species is } n, \end{aligned} \quad (2.116)$$

the first leap condition leads to the existence of independent Poisson variables $\mathcal{P}_\rho(W_\rho(n_t), \tau)$ such that the dynamics of a trajectory can be approximated as

$$n_{t+\tau} = n_t + \sum_{\rho} \nu_{\rho}^i \mathcal{P}_\rho(W_\rho(n_t), \tau), \quad (2.117)$$

with $\tau \ll 1$. The mean values of these variables are given as

$$\left\langle \mathcal{P}_\rho(W_\rho(n_t), \tau) \right\rangle = W_\rho(n_t)\tau, \quad \rho = 1, 2, \dots. \quad (2.118)$$

The second leap condition concerns this mean value. The leap time τ should be big enough that the following holds,

$$\langle \mathcal{P}_\rho(W_\rho(n_t), \tau) \rangle = W_\rho(n_t)\tau \gg 1, \quad \rho = 1, 2, \dots. \quad (2.119)$$

Before we address the seeming contradiction to the first leap condition, Eq. (2.115), we evaluate on the consequences. If Eq. (2.119) holds, the central limit theorem can be applied to approximate the Poisson as Gaussian variables, i.e.,

$$\mathcal{P}_\rho(W_\rho(n_t), \tau) \approx \mathcal{N}_\rho(W_\rho(n_t)\tau, W_\rho(n_t)\tau), \quad (2.120)$$

where $\mathcal{N}_\rho(\mathbf{m}, \mathbf{v})$ denotes a Gaussian variable with mean \mathbf{m} and variance \mathbf{v} . Thus, using normal distributed variables, the approximate dynamics is given by

$$n_{t+\tau} = n_t + \tau \sum_{\rho} \nu_{\rho} W_{\rho}(n_t) + \sqrt{\tau} \sum_{\rho} \nu_{\rho} [W_{\rho}(n_t)]^{1/2} \mathcal{N}_{\rho}(0, 1) . \quad (2.121)$$

Assuming that τ satisfies both leap conditions, i.e., Eq. (2.115) and (2.119), and is macroscopic infinitesimal compared to t , the chemical Langevin equation (CLE) is obtained as

$$\frac{d}{dt} n(t) = \sum_{\rho} \nu_{\rho} W_{\rho}(n(t)) + \sum_{\rho} \nu_{\rho} [W_{\rho}(n(t))]^{1/2} \xi_{\rho}(t) , \quad (2.122)$$

with Gaussian white-noise $\langle \xi_{\alpha}(t) \xi_{\beta}(t') \rangle = \delta_{\alpha\beta} \delta(t - t')$. In terms of stochastic calculus, this equation needs to be interpreted in the sense of Ito [38].

We need to address two points in the derivation of the CLE. First, the second leap condition, Eq. (2.119), justifies the usage of the central limit theorem. By doing so, we transition from a discrete state variable $n \in \mathbb{N}_0$ towards a continuous $n \in \mathbb{R}_{\geq 0}$. Thus, at this stage of approximation, it is justified to use the concentration in order to describe the system. The CLE for the concentration $x \equiv n/\Omega$ reads

$$\frac{d}{dt} x(t) = \sum_{\rho} \nu_{\rho} w_{\rho}(x(t)) + \frac{1}{\sqrt{\Omega}} \sum_{\rho} \nu_{\rho} [w_{\rho}(x(t))]^{1/2} \xi_{\rho}(t) , \quad (2.123)$$

where we introduced the rescaled transition rates,

$$w_{\rho}(x) \equiv \lim_{\Omega \rightarrow \infty} W_{\rho}(\Omega x) / \Omega . \quad (2.124)$$

These are related to the rescaled jump moments of the previous section, Eq. (2.108), as

$$\tilde{\alpha}_1(x) = \sum_{\rho} \nu_{\rho} w_{\rho}(x) \quad \text{and} \quad \tilde{\alpha}_2(x) = \sum_{\rho} \nu_{\rho}^2 w_{\rho}(x) . \quad (2.125)$$

The CLE (2.123) is equivalent to a Fokker-Planck equation, sometimes called chemical Fokker-Planck equation,

$$\partial_t p(x, t) = -\partial_x \left[\left(\sum_{\rho} \nu_{\rho} w_{\rho}(x) \right) p(x, t) \right] + \frac{1}{2\Omega} \partial_x^2 \left[\left(\sum_{\rho} \nu_{\rho}^2 w_{\rho}(x) \right) p(x, t) \right] . \quad (2.126)$$

The linear noise approximation is obtained by plugging van Kampen's ansatz, Eq. (2.104), into that Fokker-Planck equation and expanding for large system-size Ω . Identifying the jump moments according to Eq. (2.125) yields Eq. (2.112).

The second point which we need to address is the seeming contradiction between the first and second leap condition. This is closely related to the interpretation of τ as infinitesimally in order to derive the white-noise CLE. The resolution of this conflict is the limit of large system-sizes Ω or large numbers of molecules. In the limit of a large population, both leap conditions can always be satisfied, especially, it holds that $\tau \ll 1$ [41]. Thus, in the thermodynamic limit, i.e., $\Omega \gg 1$ with finite concentrations x , the chemical master equation (2.103) is well approximated by the CLE (2.123).

2.7.4 Rate equation

In the limit of infinite system-size Ω , the stochasticity of the chemical master equation (2.103) becomes less and less dominant leading to a deterministic motion. Setting the Ω -dependent terms in Eq. (2.126) to zero yields

$$\partial_t p(x, t) = -\partial_x \left[\left(\sum_{\rho} \nu_{\rho} w_{\rho}(x) \right) p(x, t) \right]. \quad (2.127)$$

The parameterized solution satisfies the following ordinary differential equation,

$$\frac{d}{dt} x(t) = \sum_{\rho} \nu_{\rho} w_{\rho}(x(t)), \quad (2.128)$$

which is called the rate equation. The same equation is obtained by considering only the Ω -independent terms in van Kampen's system-size expansion, Eq. (2.112), using the identification Eq. (2.125). In fact, the rate equation is exactly the mean-field law derived in Eq. (2.111).

2.7.5 WKB method

In the previous sections, we have derived diffusion approximations for the chemical master equation (2.103). The resulting Fokker-Planck equations, Eq. (2.112) and (2.126), are both of the type,

$$\partial_t p(x, t) = -\partial_x \left[F(x)p(x, t) - \frac{1}{\Omega} \partial_x \left(Q(x)p(x, t) \right) \right], \quad (2.129)$$

with an amplitude $1/\Omega$ in front of the highest derivative that becomes small in the limit of large system-sizes. In the previous section, we have seen that neglecting the second derivative leads to a deterministic motion. In this section, we discuss the WKB method – a systematic way to examine Eq. (2.129) without neglecting the small term.

The main idea of the WKB method is to identify a small parameter and to develop a perturbation theory in that smallness-parameter. This procedure is named after Gregor Wentzel, Hendrik Anthony Kramers and Léon Brillouin. In the weak-noise limit, the small parameter is the inverse system-size. Hence, the WKB ansatz is [39]

$$p(x, t) \propto \exp[-\Omega\phi(x, t)], \quad (2.130)$$

i.e., the solution is assumed to satisfy a large deviation principle [36, 42–44]. Plugging Eq. (2.130) into the Fokker-Planck equation (2.129) yields in leading order,

$$\begin{aligned} \partial_t \phi(x, t) &= -F(x)\partial_x \phi(x, t) - Q(x)[\partial_x \phi(x, t)]^2 + \mathcal{O}\left(\frac{1}{\Omega}\right) \\ &\equiv H\left(x, \partial_x \phi(x, t)\right). \end{aligned} \quad (2.131)$$

This is a Hamilton-Jacobi equation for the quasi-potential $\phi(x, t)$ with the Hamiltonian

$$H(x, p) \equiv Q(x)p^2 + F(x)p. \quad (2.132)$$

Depending on the situation, Eq. (2.131) can be easier to analyze than the full Fokker-Planck problem. The stationary solution of Eq. (2.131), i.e.,

$$0 = H\left(x, \partial_x \phi^s(x)\right), \quad (2.133)$$

is equivalent to the zero energy solution of the dynamical system

$$\dot{x}(t) = \frac{\partial H}{\partial p} \left(x(t), p(t) \right), \quad (2.134)$$

$$\dot{p}(t) = -\frac{\partial H}{\partial x} \left(x(t), p(t) \right). \quad (2.135)$$

This equivalence is the main concept to understand the coherence of a noisy clock as reported in Ref. [45, 46] and summarized in Appendix B. Furthermore, Eq. (2.131) will be the starting point of Chapter 4.

2.8 CHARACTERIZATION OF NONEQUILIBRIUM DYNAMICAL SYSTEMS

2.8.1 *Critical behavior and scaling form*

We briefly recap the basic notion of a continuous equilibrium phase transition. As illustrative example, we consider the one-dimensional Ising model for ferromagnetism. This section is based on the textbook [47].

We consider a system of spins $\{\sigma_i = \pm 1\}$ at each site $i = 1, 2, \dots, N$ of a one-dimensional lattice with periodic boundary conditions, i.e., we identify $\sigma_{N+1} = \sigma_1$. The energy is given by the Hamiltonian

$$H(\{\sigma_i\}) \equiv -\frac{J}{2} \sum_{i=1}^N \sigma_i \sigma_{i+1} - h \sum_{i=1}^N \sigma_i, \quad (2.136)$$

with free parameters J and h . In order to study the magnetic behavior of the system, we introduce the mean magnetization per site

$$m \equiv \frac{1}{N} \sum_{i=1}^N \langle \sigma_i \rangle = \langle \sigma_1 \rangle, \quad (2.137)$$

where we used the translational invariance of the system in the last step. If $m = 0$, there is no magnetic order in the system, whereas for $m \neq 0$, there is a preferred direction for the spins to align. Thus, the mean magnetization serves as an order-parameter of the Ising model, i.e., it indicates whether the system is in the ordered or disordered phase.

If we consider a single site i , the spin sitting there experiences a field

$$h_i \equiv h + \frac{J}{2}(\sigma_{i-1} + \sigma_{i+1}) , \quad (2.138)$$

with an average contribution

$$\langle h_i \rangle = h + Jm . \quad (2.139)$$

Furthermore, ignoring higher-order fluctuations, we replace

$$\sigma_i \sigma_{i+1} \rightarrow m(\sigma_i + \sigma_{i+1}) - m^2 . \quad (2.140)$$

Everything together, we obtain the mean-field Hamiltonian for the Ising model

$$H_{\text{MF}}(\{\sigma_i\}) \equiv \frac{J}{2} N m^2 - \sum_{i=1}^N (h + Jm) \sigma_i . \quad (2.141)$$

The free-energy is then given by

$$\mathcal{F} \equiv -\frac{1}{\beta} \ln \sum_{\{\sigma_i\}} e^{-\beta H_{\text{MF}}(\{\sigma_i\})} = -\frac{1}{\beta} \ln \left[e^{-\frac{\beta J}{2} m^2} 2 \cosh \beta(h + Jm) \right]^N , \quad (2.142)$$

compare also Sec. 2.2. Differentiation with respect to the external field h leads to the state equation for the mean magnetization

$$m = \tanh \beta(Jm + h) . \quad (2.143)$$

Thus, we find that the mean magnetization is a function of the external parameters J and h . Depending on the value of these parameters, the average magnetization per site behaves differently. Hence, J and h are called control parameters of the Ising model. For convenience we introduce the reduced and critical temperature

$$\tau \equiv \beta_c / \beta - 1 \quad \text{and} \quad \beta_c = 1/J . \quad (2.144)$$

In the limit of a small h and τ , a Taylor-expansion of Eq. (2.143) leads to the state of equation of magnetism

$$\beta_c h = \tau m + \frac{1}{3} m^3 . \quad (2.145)$$

For the special case of a vanishing external field, i.e., $h = 0$, we find the solution

$$m = 0 , \tag{2.146}$$

for $\tau > 0$ and

$$m = \pm\sqrt{3}(-\tau)^{1/2} , \tag{2.147}$$

for $\tau < 0$. Thus, β_c is the temperature for which the system smoothly transitions from one solution of the mean magnetization, Eq. (2.146), to the other, Eq. (2.147).

In the regime below τ_c , Eq. (2.146) is still a valid solution. However, the free energy evaluated at the solution of Eq. (2.147) is lower than the one of vanishing magnetization. Thus, Eq. (2.147) is the thermodynamically relevant solution for $\tau < \tau_c$.

We consider another special case for $\tau = \tau_c \equiv 0$. The solution of Eq. (2.145) satisfies

$$m \propto h^{1/3} . \tag{2.148}$$

Like in Eq. (2.147), we find a power-law dependence of the order-parameter on the control parameter. This behavior is a trade-mark for continuous phase transitions.

In general, the solution of Eq. (2.145) satisfies the scaling form

$$m = m(\tau, h) = |\tau|^{1/2} m_{\pm} \left(\frac{h}{|\tau|^{3/2}} \right) , \tag{2.149}$$

where $m_{\pm}(x)$ denotes the solution depending on the sign of τ . This scaling representation is generic for a continuous phase transition, i.e., any order parameter m depending on the control parameters τ and h satisfies in the vicinity of the critical point the scaling form

$$m(\tau, h) = |\tau|^{\beta} m_{\pm} \left(\frac{h}{|\tau|^{\delta\beta}} \right) , \tag{2.150}$$

with critical exponents β and δ and the $m_{\pm}(x)$ are denoted as scaling functions. For the mean-field Ising model, the exponents are $\beta = 1/2$ and $\delta = 3$, compare Eq. (2.149). This power-law behavior also effects physical quantities that are derived from the order parameter, thus, leading to further exponents and scaling relations between them. A set of critical exponents characterizes a continuous phase transition and defines its universality class. For example, any system undergoing a continuous phase transition exhibiting the same critical exponents as the Ising model is said to belong to the Ising universality class.

There are in general several more aspects regarding continuous phase transitions which would be indispensable to consider in a comprehensive review. However, the above mentioned concepts are the key ingredients for the discussions in Chapter 5 and Chapter 6. Thus, we now turn to the dynamical point of view on phase transitions.

2.8.2 Bifurcation theory

In the context of dynamical systems, phase transitions are known as bifurcations [48]. As this dynamical picture is not restricted to equilibrium systems, bifurcation theory is the natural framework to study nonequilibrium transitions. An intuitive picture for a bifurcation is drawn by a particle moving in a potential. While externally varying the energy landscape, the potential minimum can change its position or more minima can emerge. Thus, depending on the external parameter, the particle could end up in a different minimum in the long-time limit. This behavior is called bifurcation.

We consider a dynamical system,

$$\dot{x}(t) = -\partial_x V(x, \rho, h) , \quad (2.151)$$

with potential

$$V(x, \rho, h) \equiv \frac{1}{4}x^4 - \frac{\rho}{2}x^2 - hx , \quad (2.152)$$

where h and ρ are externally controlled. For $\rho_c = h_c \equiv 0$, this system exhibits a critical point, i.e., the fixed point x^* of the dynamics is not linearly stable. In the following, we consider two special pathways in the $\rho - h$ -plane through the critical point $x_c \equiv 0$.

For $\rho = 0$ and varying h ,

$$V(x, 0, h) \equiv \frac{1}{4}x^4 - hx , \quad (2.153)$$

there is always a unique minimum x^* , see Fig. 2.8,

$$x^*(h) = \text{sign}(h)|h|^{1/3} , \quad (2.154)$$

that is linearly stable, i.e., $\partial_x^2 V(x^*) > 0$ except for $h = h_c$. At the critical point h_c , the stability stems from the higher order derivative, i.e., $\partial_x^4 V(x^*) > 0$, whereas $\partial_x V(x^*) =$

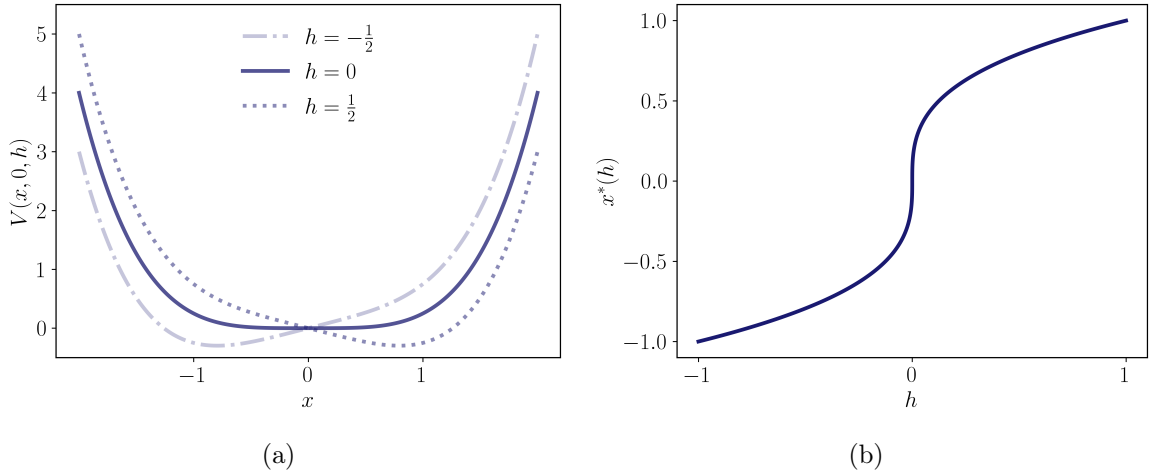


Figure 2.8: Characterization of the transition along the $\rho = 0$ -line. (a) Potential landscape, Eq. (2.153), for various h . (b) Parameterized minimum of the potential $x^*(h)$ as a function of the control parameter h .

$\partial_x^2 V(x^*) = \partial_x^3 V(x^*) = 0$. In this example, we find power-law scaling, i.e., $x^* \propto |h|^{1/3}$, compare Eq. (2.148).

The second path is given through a vanishing parameter h , i.e., $h = 0$, while varying ρ with potential

$$V(x, \rho, 0) \equiv \frac{1}{4}x^4 - \frac{\rho}{2}x^2, \quad (2.155)$$

see Fig. 2.9. For negative ρ , there exists only one unique, stable minimum $x^* = x_0 \equiv 0$. For $\rho > 0$, the potential exhibits two stable minima at $x_{\pm}(\rho) = \pm\rho^{1/2}$ with an unstable maximum at $x_0 = 0$ in between, compare Eq. (2.147). Thus, the system is called bistable and the transition is denoted as transition into bistability or supercritical pitchfork bifurcation.

The above discussed systems are called normal forms for the respective bifurcations. This means any system that undergoes a certain bifurcation can be brought into the corresponding normal form through a series of transformations. In that sense, the above obtained scaling exponents define universality classes as discussed in the previous section. In Chapter 5, we will discuss these two paths for a CRN and evaluate the thermodynamic flux and its fluctuations in the vicinity of the critical point.

So far, we only considered systems with one degree of freedom. In the next section, we discuss a two-dimensional system that undergoes a continuous phase transition.

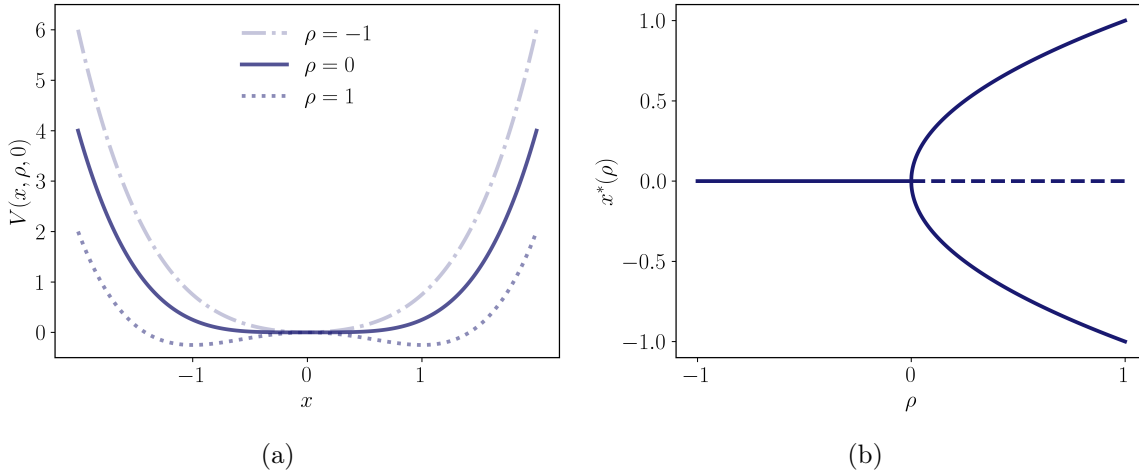


Figure 2.9: Characteristics of a pitchfork bifurcation. (a) Potential landscape, Eq. (2.155), for various value of the control parameter ρ . (b) Bifurcation diagram of the fixed points of the dynamical system Eq. (2.151). A solid line denotes a stable, a dashed line an unstable fixed point.

2.8.3 Supercritical Hopf bifurcation

We consider a system of two continuous degrees of freedom denoted as (x, y) . We further assume that the system shows exponentially damped oscillations towards a fixed point (x^*, y^*) with a damping rate that is given by an external parameter ρ . Thus, any deviations from the fixed point will be suppressed over the course of time, see Fig. 2.10a. If we decrease the damping and switch sign of ρ , the fixed point loses stability and all deviations will grow, hence, leading to oscillations around the fixed point, see Fig. 2.10c. This type of transition is termed supercritical Hopf bifurcation [48].

The dynamical system,

$$\begin{pmatrix} \dot{x}(t) \\ \dot{y}(t) \end{pmatrix} = \begin{pmatrix} \rho & -\omega \\ \omega & \rho \end{pmatrix} \begin{pmatrix} x(t) \\ y(t) \end{pmatrix} + [x(t)^2 + y(t)^2] \begin{pmatrix} a & -b \\ b & a \end{pmatrix} \begin{pmatrix} x(t) \\ y(t) \end{pmatrix} \equiv F_{CNF}[x(t), y(t)] \quad (2.156)$$

is denoted the cubic normal form for a Hopf bifurcation or Stuart-Landau oscillator. For $\rho < 0$, the above dynamical systems converges to the fixed point $(x^*, y^*) = (0, 0)$ in the limit of $t \rightarrow \infty$, see Fig. 2.10a and 2.10b. For positive ρ , the system admits a stable

closed loop in phase space denoted as limit cycle, see Fig. 2.10d. The dynamics can be parameterized in the long time limit as

$$\begin{pmatrix} x_{LC}(t) \\ y_{LC}(t) \end{pmatrix} = \sqrt{\frac{\rho}{a}} \begin{pmatrix} \cos[(\omega + b\frac{\rho}{a})t] \\ \sin[(\omega + b\frac{\rho}{a})t] \end{pmatrix}. \quad (2.157)$$

For a general vector field $F(x, y)$ with fixed point (x^*, y^*) , this type of bifurcation is characterized through the eigenvalues λ_{\pm} of the Jacobian $DF(x^*, y^*)$ evaluated at the fixed point, i.e.,

$$\lambda_{\pm} = \Re[\lambda](\rho) \pm i \Im[\lambda](\rho). \quad (2.158)$$

The bifurcation takes place for a control parameter value ρ_c that is determined by the following conditions

$$\Re[\lambda](\rho_c) = 0, \quad \frac{d\Re[\lambda]}{d\rho}(\rho_c) \neq 0, \quad \text{and} \quad \Im[\lambda](\rho_c) \neq 0, \quad (2.159)$$

i.e., crossing the imaginary axis away from the origin with non-vanishing velocity. For the vector field of the cubic normal form, Eq. (2.156), the eigenvalue is

$$\lambda_{\pm} = \rho \pm i\omega. \quad (2.160)$$

Thus, the bifurcation takes place for $\rho = \rho_c \equiv 0$.

A self-sustained oscillator like a limit cycle is a prime nonequilibrium phenomenon and often used to model chemical clocks [46, 49]. The oscillations are not externally driven but need a non-potential force, thus, are out of equilibrium. The supercritical Hopf bifurcation is therefore often denoted as continuous nonequilibrium phase transition.

The vector field, Eq. (2.156), is termed normal form since any system undergoing such a bifurcation can be brought into that form through a series of transformations. In Chapter 6, we will explain this transformation scheme and apply it to the rate equations of a nonlinear CRN.

In the next section, we discuss oscillations that emerge in stochastic systems and how to characterize them.

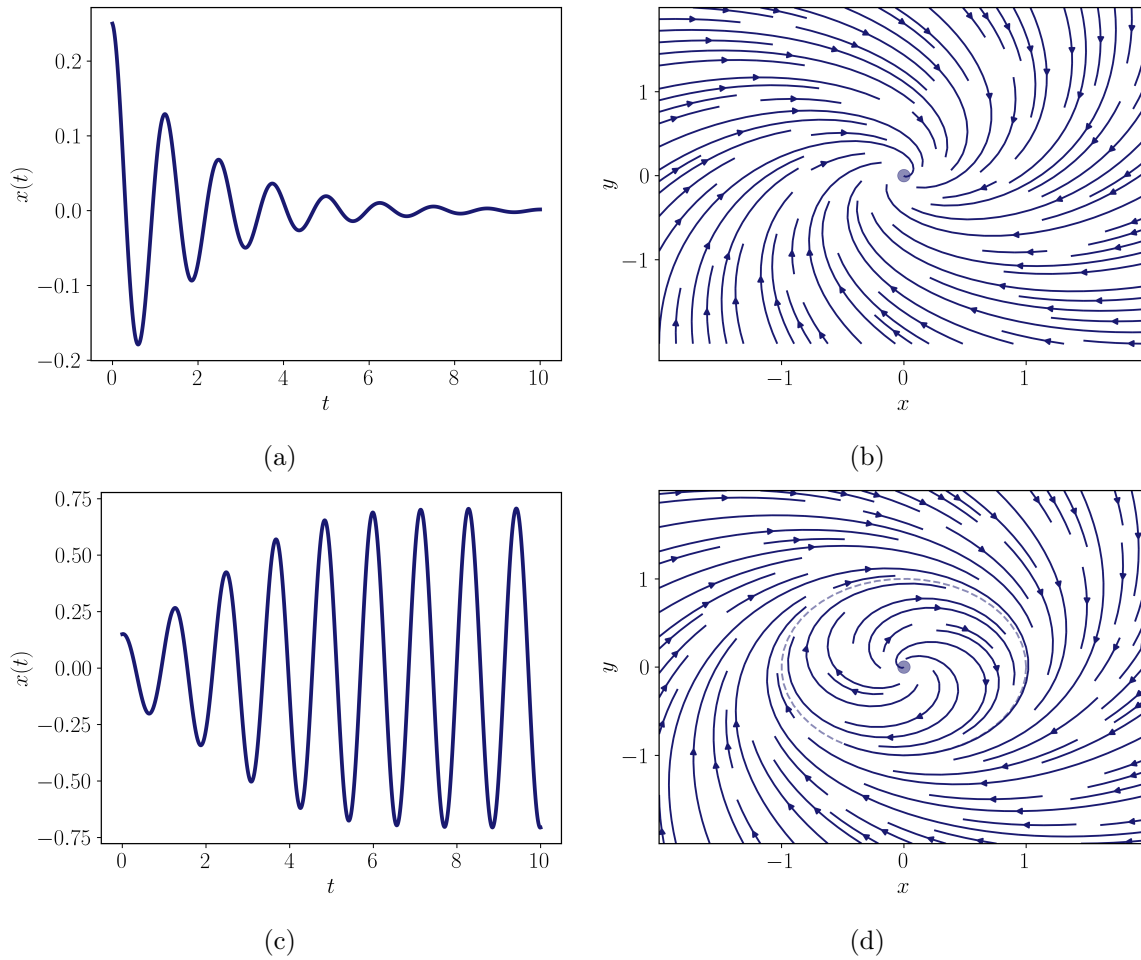


Figure 2.10: Different scenarios for a Hopf bifurcation. (a) Dynamics of $x(t)$, Eq. (2.156), in the fixed point regime of the cubic normal form. (b) Vector field $F_{CNF}(x, y)$, Eq. (2.156), for $\rho = \omega = a = b = -1$ displaying a fixed point behavior. A dot denotes the fixed point. (c) $x(t)$ dynamics in the oscillatory regime of the cubic normal form starting close to the fixed point. (d) $F_{CNF}(x, y)$ above the bifurcation exhibiting a stable limit cycle (dashed line) around the fixed point (dot).

2.8.4 *Coherent oscillations*

We consider noisy self-sustained oscillations, e.g., a CRN or a vector field perturbed by weak noise exhibiting a limit cycle. Such oscillations are characterized through their quality factor \mathcal{R} . If the system does not oscillate, \mathcal{R} vanishes. Thus, this quantity can serve as order parameter for an oscillating system.

The quality factor is defined through the eigenvalues of the underlying dynamics,

$$\mathcal{L}_x v_n(x) = \lambda_n v_n(x) , \quad (2.161)$$

where \mathcal{L}_x denotes the generator of the dynamics, e.g., a Fokker-Planck or master equation, λ_n the eigenvalues and $v_n(x)$ the corresponding eigenfunctions.

The stationary solution corresponds to the vanishing eigenvalue, i.e.,

$$p^s(x) = v_0(x), \quad \lambda_0 = 0 . \quad (2.162)$$

If we consider a system following a master equation, the Perron-Frobenius theorem implies a hierarchy on the eigenvalues,

$$0 = \lambda_0 > \Re \lambda_1 \geq \Re \lambda_2 \geq \dots . \quad (2.163)$$

For a Fokker-Planck equation, a similar theorem only holds for equilibrium systems [39]. Thus, the general solution for the probability density is given by

$$p(t) = \sum_n c_n e^{\lambda_n t} v_n(x) . \quad (2.164)$$

In the long time limit, the slowest decay mode dominates the relaxation into the stationary state. Hence, the dynamic of the system is characterized by

$$\lambda_1 \equiv -\frac{1}{\tau} \pm i \omega \quad (2.165)$$

The ratio of real and imaginary part of this eigenvalue defines the quality factor,

$$\mathcal{R} \equiv \omega \tau. \quad (2.166)$$

This quantity is closely related to the number of coherent oscillations

$$\mathcal{N} \equiv \frac{1}{2\pi} \mathcal{R} , \quad (2.167)$$

i.e., the number of oscillations before the initial amplitude has decayed by a factor of $1/e$. Thus, the higher the quality factor, the more oscillations without loss of coherence occur.

From an experimental or numerical point of view, the quality factor can be obtained through the correlation function of an observable O ,

$$C_O(t) \equiv \langle O(t)O(0) \rangle = \sum_n o_n \exp(\lambda_n t) . \quad (2.168)$$

In the long-time limit, the dynamics of the correlation function is dominated by the slowest decay rate, i.e., $C_O(t)$ describes a damped oscillation with the real part of the first non-trivial eigenvalue as decay rate and with frequency given by its imaginary part [46].

The quality factor is closely related to thermodynamic quantities. For a uni-cyclic network the quality factor is bounded through the number of states N and driving along the cycle \mathcal{A} as

$$\mathcal{R} \leq \cot \frac{\pi}{N} \tanh \frac{\mathcal{A}}{2N} . \quad (2.169)$$

This relation has been conjectured by Barato and Seifert in a more general setting based on strong numerical evidence [4] and proven by Ohga and co-workers [50].

Furthermore, Oberreiter and co-workers conjectured that the quality factor respectively the number of coherent oscillations gives a lower bound on the total entropy production per period that is needed to maintain the oscillations [5],

$$\Delta S_{\text{tot}} \geq 4\pi^2 \mathcal{N} . \quad (2.170)$$

In Chapter 4 we will derive and proof Eq. (2.169) and (2.170) for a periodic one-dimensional system with continuous state space.

OPTIMALITY OF NON-CONSERVATIVE DRIVING FOR FINITE-TIME PROCESSES WITH DISCRETE STATES

3.1 INTRODUCTION

In thermodynamics, a finite-time process transforms a given initial state into a given final one in a given finite time. This process is optimal if it comes at the lowest cost, i.e., at the lowest entropy production. The condition of a finite time is crucial, since quasi-static processes, which require infinitely slow driving, do not generate entropy at all. For macroscopic systems, such processes have been studied under the label of finite-time thermodynamics [23]. For small systems in contact with a thermal environment and thus following a stochastic dynamics, optimal finite-time processes were shown to have an inevitable thermodynamic cost that scales asymptotically like the inverse of the allocated time [24, 51]. This scaling was later shown to be the exact minimal entropy production for any finite time for an underlying Langevin dynamics [26, 52], see also [53]. For system with discrete state space undergoing a master equation dynamics, this scaling holds asymptotically as several case studies have shown [54–56]. In the linear response regime, an appealing systematic theory for the optimal driving involves geometric concepts like the thermodynamic length [57–62]; see [63] for a brief review. A complementary aspect of this optimization concerns the derivation of speed limits for transformations between an initial and final distribution [64]. For an effective two-state system, a prominent experimental application of optimal protocols is the minimal cost of erasing a bit in a finite-time extension of the Landauer bound [65–69].

A fundamental distinction for any non-equilibrium process is whether or not the driving is conservative, i.e., whether or not it arises from a time-dependent potential. The former case applies *inter alia* to single molecules manipulated with optical tweezers [70, 71], to colloidal particles in time-dependent harmonic or anharmonic traps [10] and to stochastic pumps for which the energy of each state (and potentially the barriers in between) are driven [72–74]. Paradigms for non-conservative driving are colloidal particles driven along static periodic potentials and colloidal particles in shear flow. Biophysical and biochemical

processes that are driven by unbalanced chemical reactions like the hydrolysis of nucleic acids fall in this class as well [75, 76].

Emphasizing this distinction leads to the question whether conservative or non-conservative driving leads to a lower cost for a given initial and final state. In a more technical formulation, the question is whether a time-dependent dynamics whose instantaneous stationary state is Boltzmann-Gibbs-like achieves already minimal entropy production or whether an additional non-conservative contribution, which at fixed control parameter would lead to a genuine non-equilibrium steady-state, can further decrease the cost. For systems with a continuous state space, i.e., for Langevin dynamics, it is known that the optimal protocol involves only conservative forces [25, 26, 28, 77]. Coming back to the example of a colloidal particle on a ring with periodic boundary conditions this result implies that there is nothing gained by allowing a non-conservative force to act on top of a time-dependent potential.

In this chapter, we address this question for systems with discrete states, i.e., for a master equation dynamics with time-dependent rates. We can build on the work of Muratore-Ginanneschi et al. [27] who formulated this optimization problem in terms of control theory without addressing the specific question we are interested in. Since they show that the optimization reduces to the Langevin problem in the continuum limit, one might even expect that the optimal protocol for a discrete state space can be achieved with conservative driving as well. In contrast to the continuous case, however, we will prove that the optimal driving is in fact non-conservative. Furthermore, we will show that for a broad class of systems all cycle affinities, defined precisely below as a quantitative measure of the "non-conservativeness" of the dynamics, remain bounded as a function of the number of states in a cycle during the whole process independent of its duration.

3.2 OPTIMAL CONTROL OF MARKOV JUMP PROCESSES

3.2.1 *Set-up*

We consider a discrete set of states $\{i\}$ of total number N . A transition between two states (i, j) occurs at a rate $k_{ij}(t)$, which is in general time-dependent. The probability $p_i(t)$ to find the system at time t in state i evolves according to the master-equation

$$\partial_t p_i(t) = \sum_{j \neq i} [k_{ji}(t)p_j(t) - k_{ij}(t)p_i(t)] \equiv - \sum_{j \neq i} j_{ij}(t) \quad (3.1)$$

with the net probability current $j_{ij}(t)$ through link (i, j) . We parameterize the transition rates as [27]

$$k_{ij}(t) = \kappa_{ij} e^{A_{ij}(t)/2} \quad (3.2)$$

with constant, symmetric part $\kappa_{ij} = \kappa_{ji}$, which sets the characteristic time-scale for the transition from state i to j , and time-dependent, antisymmetric $A_{ij}(t) = -A_{ji}(t)$. Throughout this chapter, we measure energies in units of a thermal energy and entropy in units of Boltzmann's constant.

Conservative driving implies that the ratio of forward and backward rates is given by the difference of time-dependent free energies $F_i(t)$ leading to

$$A_{ij}(t) = F_i(t) - F_j(t). \quad (3.3)$$

In contrast, for non-conservative driving $A_{ij}(t)$ cannot be written as a difference of state functions.

It will be convenient to transform the state densities as $\phi_i(t) \equiv \sqrt{p_i(t)}$ and to introduce the non-equilibrium driving function [27]

$$\varphi_{ij}(t) \equiv A_{ij}(t) + 2[\ln \phi_i(t) - \ln \phi_j(t)] , \quad (3.4)$$

which becomes for conservative driving

$$\varphi_{ij}(t) = B_i(t) - B_j(t) \quad \text{with} \quad B_i(t) \equiv F_i(t) + 2 \ln \phi_i(t). \quad (3.5)$$

In this representation, the current along link (i, j) transforms to

$$j_{ij}(t) = 2\kappa_{ij}\phi_i(t)\phi_j(t) \sinh \frac{\varphi_{ij}(t)}{2} \quad (3.6)$$

and the master equation (3.1) becomes

$$\partial_t \phi_i(t) = - \sum_{j \neq i} \kappa_{ij} \phi_j(t) \sinh \frac{\varphi_{ij}(t)}{2}. \quad (3.7)$$

The process that transforms the given initial density $\{\phi_i(0)\}$ to a given final one $\{\phi_i(T)\}$ in time T is optimal if it generates the least overall entropy production

$$\Delta S_{\text{tot}} \equiv \int_0^T dt \sigma(t) \quad (3.8)$$

with the entropy production rate [12]

$$\sigma(t) = \sum_{i \neq j} p_i(t) k_{ij}(t) \ln \frac{p_i(t) k_{ij}(t)}{p_j(t) k_{ji}(t)} = 2 \sum_{i < j} \kappa_{ij} \phi_i(t) \phi_j(t) \varphi_{ij}(t) \sinh \frac{\varphi_{ij}(t)}{2} . \quad (3.9)$$

3.2.2 Optimality of non-conservative driving

We first show that conservative driving does not lead to minimal entropy production. Assume that within this parameter space (3.5) we have found the optimal protocol $F_i^*(t)$ leading to $p_i^*(t)$ with currents $j_{ij}^*(t)$. For a unicyclic system, it is then clear that adding a time-dependent $\Delta(t)$ to the clockwise current will still satisfy the master equation (3.1) and the boundary conditions of a fixed initial and final density. Under the transformation

$$j_{ij}(t) \equiv j_{ij}^*(t) + \epsilon_{ij} \Delta(t) \quad (3.10)$$

with $\epsilon_{ij} = 1 = -\epsilon_{ji}$ for $i < j$ the entropy production rates $\sigma^*(t)$, respectively $\sigma(t)$, become by a Taylor-expansion

$$\sigma(t) - \sigma^*(t) = \Delta(t) 2 \sum_{i < j} \tanh \frac{B_i^*(t) - B_j^*(t)}{2} + \mathcal{O}(\Delta(t)^2) . \quad (3.11)$$

Since in general, the linear term will not vanish, see Appendix A.1, we get that the total entropy production found within conservative driving can be further decreased by adding a non-conservative term accounting for such a $\Delta(t)$. Specifically, we can choose $\Delta(t) = \text{const.} \neq 0$ such that

$$2\Delta \int_0^T dt \sum_{i < j} \tanh \frac{B_i^*(t) - B_j^*(t)}{2} < 0 . \quad (3.12)$$

This constitutes our first main result: In contrast to the continuous case, optimal protocols for Markov jump processes involve non-conservative driving, i.e., a genuine cycle affinity

$$\mathcal{A}_c(t) \equiv \sum_{(i,j) \in \mathcal{C}} A_{ij}(t) = \sum_{(i,j) \in \mathcal{C}} \varphi_{ij}(t) \quad (3.13)$$

for each cycle \mathcal{C} in the network. The above proof can indeed be extended trivially to multicyclic networks since a corresponding $\Delta(t)$ can be added to an arbitrary cycle in which case the summation in (3.11) is only over the directed links of this cycle.

3.2.3 Bound on the optimal cycle affinity

We next show that all cycle affinities $\mathcal{A}_c(t)$ are bounded by the number of states in each cycle for all times. To do so, we have to derive the Euler-Lagrange equations for the variational problem posed by minimizing the entropy production (3.8) under the constraints (3.7) which we add with Lagrangean multipliers $\{\eta_i(t)\}$ that ensure that the densities $\{\phi_i(t)\}$ satisfy the master equation. Thus, we minimize

$$\Delta S \equiv \int_0^T dt L[\{\phi(t), \varphi(t), \eta(t)\}] \quad (3.14)$$

for given $\{\phi_i(0)\}$ and $\{\phi_i(T)\}$ with Lagrange function

$$L(t) \equiv \sigma(t) + \sum_i \eta_i(t) [\partial_t \phi_i(t) + \sum_{j \neq i} \kappa_{ij} \phi_j(t) \sinh \frac{\varphi_{ij}(t)}{2}]. \quad (3.15)$$

From $\delta L / \delta \phi_i(t) = 0$, we get the equations of motion for the Lagrange multiplier

$$\partial_t \eta_i(t) = \sum_{j \neq i} \kappa_{ij} \sinh \frac{\varphi_{ij}(t)}{2} [2\phi_j(t)\varphi_{ij}(t) - \eta_j(t)]. \quad (3.16)$$

Variation with respect to the protocol $\varphi_{ij}(t)$ leads to

$$\eta_i(t)\phi_j(t) - \eta_j(t)\phi_i(t) = -4\phi_i(t)\phi_j(t) \left[\tanh \frac{\varphi_{ij}(t)}{2} + \frac{\varphi_{ij}(t)}{2} \right]. \quad (3.17)$$

By summing (3.17) over an arbitrary cycle with N_c states we get

$$0 = \sum_{i=1}^{N_c} [\eta_i(t)/\phi_i(t) - \eta_{i+1}(t)/\phi_{i+1}(t)] = -4 \sum_{i=1}^{N_c} \left[\tanh \frac{\varphi_{i,i+1}(t)}{2} + \frac{\varphi_{i,i+1}(t)}{2} \right] \quad (3.18)$$

where we relabeled the neighboring links $(i, j) \in \mathcal{C}$ as $(i, i+1)$. We now use this relation to find for the affinity

$$\mathcal{A}_c(t) = \sum_{i=1}^{N_c} \varphi_{i,i+1}(t) = -2 \sum_{i=1}^{N_c} \tanh \frac{\varphi_{i,i+1}(t)}{2} \quad (3.19)$$

and finally use $|\tanh(x)| \leq 1$ to obtain

$$|\mathcal{A}_c(t)| \leq 2N_c. \quad (3.20)$$

Thus for each cycle, the time-dependent affinity is bounded by the number of states within that cycle.

In fact, we can sharpen this bound further to

$$|\mathcal{A}_c(t)| \leq 2(N_c - 2). \quad (3.21)$$

which is our second main result. While the formal derivation of this improved bound as shown in Appendix A.2 is somewhat technical, its origin can be understood by the following consideration. Eqs. (3.19,3.20) require the affinity and hence the sum of the driving functions to be finite, thus, not all $\{\varphi_{ij}(t)\}$ are allowed to tend to, e.g., positive infinity at the same time which was the rational behind the weaker bound, Eq. (3.20). At least one driving function has to compensate this putative divergence by approaching negative infinity. The asymptotic behavior of the affinity is determined by Eq. (3.18), thus, for all $\varphi_{ij}(t) \rightarrow \pm\infty$ except one that tends to $\varphi_{kl}(t) \rightarrow \mp\infty$, the affinity approaches $\mathcal{A}_c(t) \rightarrow \mp 2(N_c - 2)$.

3.2.4 Configurations that tend to saturate the affinity bound

We now turn to numerics in order to explore how significant the improvement through non-conservative driving is and to check how strong the improved bound (3.21) is. For a three state system, i.e., $N_c = 3$, we sample arbitrary initial and final distributions and calculate for each pair of them the optimal protocol first for conservative and then for non-conservative

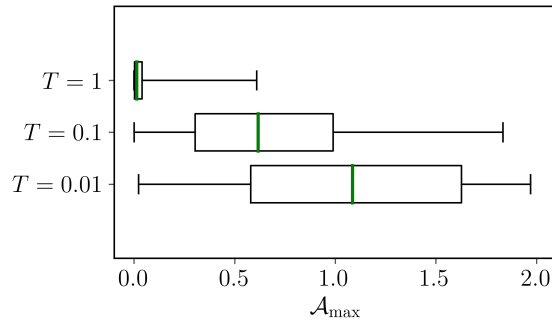


Figure 3.1: Influence of the allocated time T on the maximal affinity \mathcal{A}_{\max} for arbitrary sampled initial and final distributions. The edges of the boxes represent the first Q_1 (left) and third quartile Q_3 (right site). The whisker on the left represents the minimum value and on the right the maximum of the data. The thick green line displays the median of the data.

driving. We fix a basic time-scale by setting all symmetric prefactors $\kappa_{ij} = \kappa_{ji} = 1$. We find that the non-conservative driving leads to an only minute improvement. For a process transforming the state of the system within a time that is comparable to the intrinsic timescale, i.e., for $T = 1$, the advantage of non-conservative driving is on average only of the order of 10^{-5} with a maximal improvement of order 10^{-4} . Even for processes that are ten times faster, i.e., $T = 0.1$, on average this advantage raises only to 10^{-3} , respectively 10^{-2} for the maximum value.

The faster the process is, the larger is the maximum affinity applied in the optimal process as shown in Fig. (3.1). This reflects the fact that a non-equilibrium quantity like the cycle affinity should vanish as the quasi-static limit is approached, i.e. $T \rightarrow \infty$. While $\mathcal{A}_{\max} \equiv \max_{0 \leq t \leq T} |\mathcal{A}(t)|$ remains below the value of 2 as it should, there are combinations of initial and final densities for which the optimal affinity seems to reach this bound within about 2 percent. In Fig. (3.2), we show that the largest affinities are generated by those initial and final distributions that require to transport either the largest density, i.e., for which $\Delta p_i = p_i(0) - p_i(T)$ is approximately ± 1 for one pair of states, or for which $\Delta p_i \simeq 0$ for one state.

Comparing the configurations displayed in Fig. (3.2), we find that it becomes more difficult to obtain numerically convergent solutions the lower we set the allocated time T . Particularly, we find configurations which tend to transport the largest densities, $\Delta p_i \rightarrow \pm 1$, to be numerically unstable (black crosses). At present, it is unclear whether this is due to the numerical scheme, see Appendix A.3 and A.4, or whether there is a generic problem in the mathematical formulation, e.g., due to diverging derivatives of the driving functions or

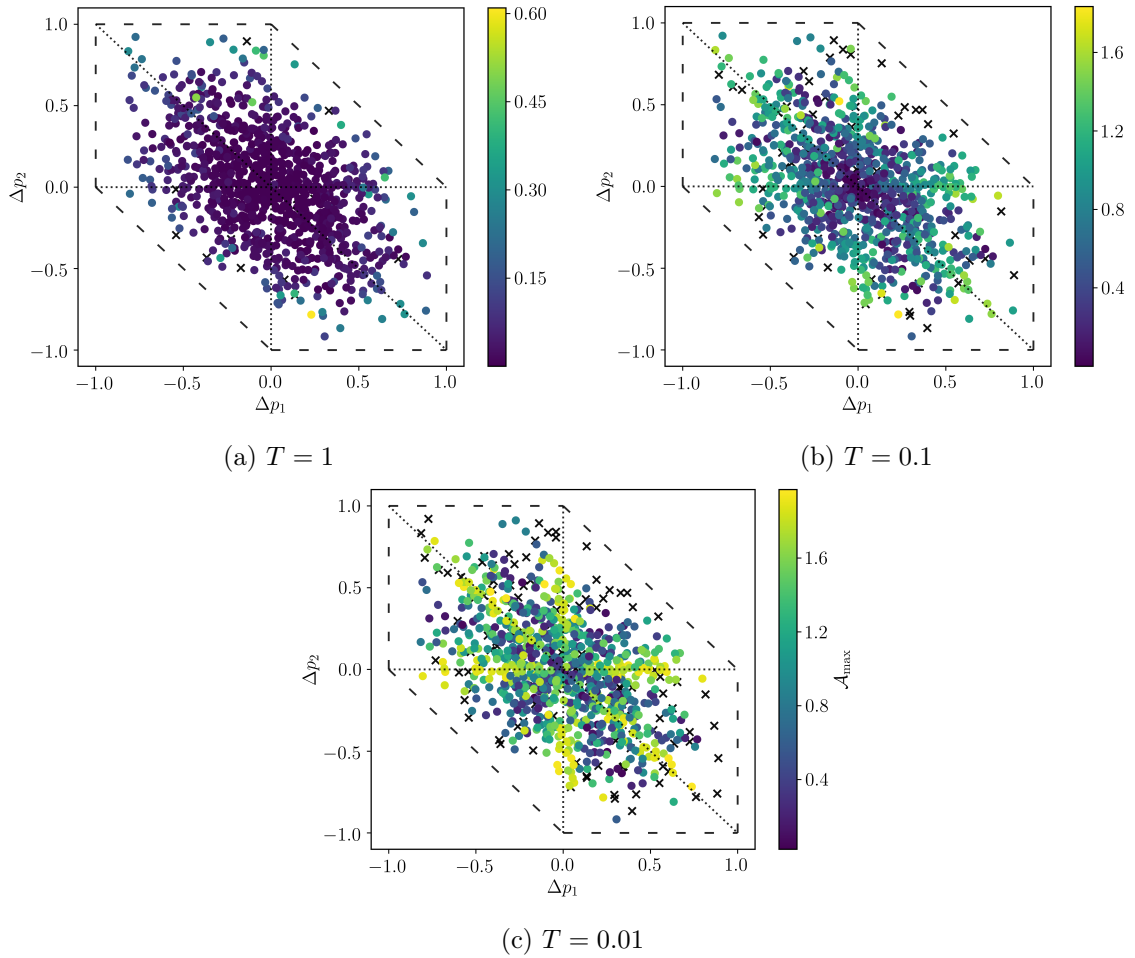


Figure 3.2: Influence of the system-parameters on the maximal affinity $\mathcal{A}_{\max} \equiv \max_{t \in [0, T]} |\mathcal{A}(t)|$ of arbitrary sampled configurations for different speeds T . $\Delta p_i = p_i(0) - p_i(T)$ displays the change in the state densities. The colorbar represents \mathcal{A}_{\max} . The dashed line is defined by $\Delta p_i = \pm 1$ for one i . The dotted line represents $\Delta p_i = 0$ for a i . Black crosses stand for configurations that failed to converge with our algorithm.

vanishing probabilities. Another question that remains open is whether there always exist a set of initial and final densities that saturate the bound of the affinity, Eq. (3.21), for a given time T . From our numerical findings we expect that this is the case for configurations that transport the maximal densities, i.e., for $\Delta p_i \simeq \pm 1$. The larger the allocated time T , the closer the transported densities need to be to ± 1 in order to saturate the bound.

3.2.5 Generalization to rates including a structural parameter

So far, with the parametrization (3.2), we have focused on a symmetric splitting of the driving over each forward and backward rate. In a more general setting, we now allow for a splitting that may be different for each link. We can then parametrize the rates as

$$\begin{aligned} k_{ij} &= \kappa_{ij} \exp(\alpha_{ij} A_{ij}) \\ k_{ji} &= \kappa_{ji} \exp[(1 - \alpha_{ij}) A_{ji}] \end{aligned} \quad (3.22)$$

with $\kappa_{ij} = \kappa_{ji}$ and one structural parameter for each link given by $0 < \alpha_{ij} = \alpha_{ji} < 1$. Following the derivation in the symmetric case from above, it is straightforward to show that the bound (3.20) becomes

$$-\sum_{i=1}^{N_c} \frac{1}{\alpha_{i,i+1}} \leq \mathcal{A}_c \leq \sum_{i=1}^{N_c} \frac{1}{1 - \alpha_{i,i+1}}, \quad (3.23)$$

see Appendix A.5 for a derivation. If $\alpha_i = 1/2$ for all i , we reproduce Eq. (3.20).

3.2.6 Recovering the optimal protocol for Langevin systems in the continuum limit

The more states a cycle has, the larger become our bounds. Naively extrapolating to a cycle with infinitely many states, one might conclude that in such a continuum limit the affinity could diverge. Such an expectation would be in contrast with the established result that for a Langevin dynamics conservative driving, i.e., zero affinity achieves optimality [25, 26]. We finally show that our approach reproduces this continuum limit correctly. Let dx denote a lattice spacing along a cycle. We relabel the driving function of adjacent states in a cycle from $\varphi_{i,i+1}$ to $\varphi_{x,x+dx}$. For small lattice spacing, the affinity becomes

$$\mathcal{A}_c(t) = \sum_{x \in \mathcal{C}} \varphi_{x,x+dx}(t) \approx \sum_{x \in \mathcal{C}} \varphi'_{x,x}(t) dx \approx \oint_{\mathcal{C}} \varphi'_{x,x}(t) dx \quad (3.24)$$

where the prime denotes a derivative with respect to x . Here, we have used that $\varphi_{x,x}(t) = 0$ due to the antisymmetry of $\varphi_{ij}(t)$. Thus, the affinity approaches the contour integral over the spatial derivative of the driving function $\varphi'_{x,x}(t)$ along the cycle. We can calculate

the limiting value of this integral by dividing Eq. (3.18) by -2 and a Taylor expansion, according to

$$0 = \sum_{x \in \mathcal{C}} \left[\varphi_{x,x+dx}(t) + 2 \tanh \frac{\varphi_{x,x+dx}(t)}{2} \right] \approx 2 \sum_{x \in \mathcal{C}} \varphi'_{x,x}(t) dx \approx 2 \oint_{\mathcal{C}} \varphi'_{x,x}(t) dx. \quad (3.25)$$

Thus, the cycle affinity indeed has to vanish in the continuum limit. This finding also generalizes to the non-symmetrical splitting of the rates, Eq. (3.22), see Appendix A.6.

3.3 CONCLUSION

In conclusion, we have proven that for discrete systems, optimal finite-time processes require non-conservative driving in marked contrast to the case of systems with continuous degrees of freedom. This result implies that with an optimal protocol for the Langevin dynamics, discretizing this solution will in general not guarantee optimality over the coarse-grained state space. Furthermore, driving a process, e.g., with unbalanced biochemical reactions, which necessarily imply non-vanishing affinity, can yield lower entropy production than by pumping the system through time-dependent modulations of energies and barriers, which amounts to conservative driving. For each cycle in a multicyclic network, the maximum affinity remains bounded throughout the process, even if the allocated time approaches zero. For driving that affects forward and backward rates symmetrically, the bound depends only on the number of states of a cycle. For a non-symmetric splitting, a structural parameter enters the bound. Open theoretical problems include a proof of the tightness of the improved bound, Eq. (3.21), for all T and a generalization of this improved bound to asymmetric splitting. For experiments, it remains a challenge to set up a system for which both types of driving, conservative and non-conservative one, can be implemented and quantitatively be compared with another at the same time.

COHERENCE OF OSCILLATIONS IN THE WEAK-NOISE LIMIT

4.1 INTRODUCTION

Oscillations are ubiquitous in living systems. The cell cycle [78], circadian rhythms [79, 80], glycolysis [81], and biochemical oscillations in general [82] represent a few examples for such periodic behavior. These models describe generic processes that are able to keep track of time, hence, to function as clocks. Typically, such biochemical clocks work in surroundings with large fluctuations. Thus, the question arises how these oscillations emerge and how they maintain their coherence.

On the macroscopic level, bifurcation theory is used to address these questions, i.e., to rationalize the dynamical behavior of deterministic chemical rate equations [48, 83]. A prominent example is Selkov's model for the self-sustained oscillations in glycolysis [49]. For microscopic systems, chemical master equations and Markov networks [37, 84, 85] are established tools to examine these oscillations [4, 45, 46, 86–90]. The latter lead to the notion of "Brownian clocks" [91, 92] and to central results like the thermodynamic uncertainty relation in stochastic thermodynamics [19, 93, 94], which links the precision of such clocks with the ultimate cost, i.e., the entropy production, see also [95]. The first correction of the macroscopic picture towards the microscopic scale can be determined through the weak-noise limit [45, 46]. On this mesoscopic scale, the master equation is approximated through a Kramers-Moyal expansion [37]. Thus, the behavior of the oscillations can be studied in the limit where the volume of the system becomes infinite. A recent approach uses large deviation theory to obtain the probability densities beyond the Gaussian approximation [96]. An alternative route to examine these oscillations is provided by the phase-reduction method [89, 97, 98].

The macroscopic theory is deterministic, hence, oscillations stay synchronized for all times. For phase diffusion and, thus, loss of coherence, randomness in the systems is needed. Cao and co-workers demonstrated for several stochastic models that the number of coherent oscillations increases with increasing entropy production rate [99]. A recent study conjectures a universal trade-off relation between this quantity and total entropy

production per period of oscillation [5]. The number of coherent oscillations is closely related to the quality factor which we will discuss in detail below. The latter has recently also been used as order parameter to study non-equilibrium phase transitions [90].

While the mesoscopic theory [45, 46] is rather involved in its general form, we simplify it by performing an explicit calculation for a one-dimensional Fokker-Planck dynamics. For the motion along a periodic ring, we derive an original, simple, analytical expression for the quality factor. Furthermore, we determine an upper bound on this quantity. This bound is the continuous version of a relation that has been conjectured for Markov networks in [4] and equal to the bound presented in [5] in the weak-noise limit. Moreover, we show that the number of coherent oscillations of a noisy limit cycle in two dimensions is also given by that of a one-dimensional Fokker-Planck system under the assumption that tangent and normal motion decouple in the weak-noise limit.

We illustrate our results through three numerical case studies examining a one-dimensional system subject to a periodic force, the noisy Stuart Landau oscillator also known as cubic normal form of a Hopf bifurcation, and the noisy rate equations of the Brusselator in two dimensions. The coherence resulting from the numerics agrees well with our analytical results both for the one-dimensional case and in two-dimensional systems with weak coupling between tangent and normal motion. Based on these numerical studies, we conjecture that the one-dimensional approximation is in general an upper bound for the two-dimensional quality factor.

This chapter is organized as follows. In Sec. 4.2, we discuss the quality factor as a quantitative measure for the coherence of noisy oscillations. Our central result, an explicit expression for the quality factor in one-dimensional Fokker-Planck systems is derived in Sec. 4.3.1. Using this form, we generalize the microscopic bound [4] to dynamics on a one-dimensional ring in Sec. 4.3.2. In Sec. 4.3.3, we derive the conjectured bound on the entropy production [5] for this one-dimensional system. We illustrate these results numerically in Sec. 4.3.4. In Sec. 4.4, we show that oscillations arising from a two-dimensional limit cycle can also be characterized by the one-dimensional expression for the quality factor in the limit of weak noise. We examine the noisy Stuart-Landau oscillator in Sec. 4.5.1 and discuss in detail the validity of the one-dimensional approximation in Sec. 4.5.2. As a generic example for a chemical reaction network, we numerically treat the Brusselator in Sec. 4.6 and conclude in Sec. 4.7.

4.2 COHERENCE OF OSCILLATIONS

A standard measure to describe the coherence of stochastic oscillations is the quality factor \mathcal{R} [4, 45, 46, 90, 100]. This quantity is related to the correlation function of an observable $O(t)$,

$$C_O(t) \equiv \langle O(t)O(0) \rangle , \quad (4.1)$$

which displays damped oscillations if $O(t)$ performs a noisy periodic motion. The quality factor,

$$\mathcal{R} \equiv \left| \frac{\text{Im}\lambda}{\text{Re}\lambda} \right| = \omega\tau , \quad (4.2)$$

is determined by the dominant eigenvalue

$$\lambda = -1/\tau + i\omega \quad (4.3)$$

of the corresponding dynamical equation. The larger \mathcal{R} is, the longer keeps the oscillator the coherence.

For unicyclic Markov networks, it has recently been conjectured that the quality factor is bounded by

$$\mathcal{R} \leq f(\mathcal{A}, N) \equiv \cot(\pi/N) \tanh(\mathcal{A}/2N) , \quad (4.4)$$

where N is the number of states. The affinity

$$\mathcal{A} \equiv \sum_{i=1}^N \ln \frac{k_i^+}{k_i^-} \quad (4.5)$$

is a function of the rates k_i^+ and k_i^- at which a transition from state i to $i \pm 1$ occurs and a measure for the non-equilibrium driving in the network. Eq. (4.4) is based on strong numerical evidence and covers in its most general form also multicyclic networks [4]. A further result relates the quality factor of an oscillator with the entropic cost to maintain the oscillation,

$$\Delta S_{\text{tot}} \geq 2\pi\mathcal{R} . \quad (4.6)$$

This bound is based on strong numerical evidence and has been conjectured for general Markov jump networks [5].

The quality factor for systems following a Fokker-Planck dynamics is obtained by a spectral decomposition of the Fokker-Planck operator [45, 46]. Thus, the number of coherent oscillations is also given by the dominant eigenvalue, Eq. (4.2). This expansion in the eigenbasis leads to a Hamilton-Jacobi equation with the Freidlin-Wentzell Hamiltonian respectively Onsagar-Machlup Lagrangian for the leading order term of the probability density in the weak-noise limit [45, 46, 100]. The quality factor is then obtained using techniques from Hamilton-Jacobi theory.

We next perform this eigenfunction expansion to find an analytical expression for the quality factor of one-dimensional systems in the weak-noise limit without explicitly using Hamilton-Jacobi theory.

4.3 ONE-DIMENSIONAL FOKKER-PLANCK SYSTEMS IN THE WEAK-NOISE LIMIT

4.3.1 *Quality factor*

Consider a single continuous degree of freedom $x(t)$, e.g., a particle or the concentration of a species on a one-dimensional ring of length $L > 0$. It is driven by a spatially periodic force $F(x) = F(x + L)$ and subject to a space-dependent diffusion $Q(x) = Q(x + L)$. We implement the weak noise explicitly through an external parameter $\Omega > 0$, which we assume to be large compared to all other system scales, i.e., $\Omega \gg 1$. The dynamics of such a system is then described by the following Fokker-Planck equation [45]

$$\partial_t p(x, t) = -\{\partial_x[F(x)p(x, t)] - \frac{1}{\Omega}\partial_x^2[Q(x)p(x, t)]\} \equiv \mathcal{L}_x p(x, t) , \quad (4.7)$$

where we assume that $Q(x) > 0$ for all x . \mathcal{L}_x denotes the Fokker-Planck operator. Additionally, we require that the force has a unique sign. The latter assumptions ensures that the dynamics has no rest position, which would destroy oscillations in the weak-noise limit. Without loss of generality, we assume $F(x)$ to be positive.

Following [45], we expand Eq. (4.7) to obtain the eigenvalues and thus, the quality factor. With the splitting ansatz, $p(x, t) = f(t)h(x)$, Eq. (4.7) becomes

$$\frac{df(t)/dt}{f(t)} = \frac{\mathcal{L}_x h(x)}{h(x)} \equiv \lambda . \quad (4.8)$$

The time dependence of the probability density is thus given by an exponential $f(t) \propto \exp(\lambda t)$.

In order to solve for the eigenvalues λ , we employ the ansatz $h(x) = \exp[-\Omega\phi(x)]$ [45]. Plugging this form into Eq. (4.8), we obtain an equation for $g(x) \equiv \phi'(x)$,

$$F(x)g(x) + Q(x)g(x)^2 + \frac{1}{\Omega^2}Q''(x) - \frac{1}{\Omega}[\lambda + F'(x) + 2Q'(x)g(x) + Q(x)g'(x)] = 0. \quad (4.9)$$

We solve this relation by expanding $g(x)$ in inverse powers of Ω , i.e.,

$$g(x) = g_0(x) + \frac{1}{\Omega}g_1(x) + \frac{1}{\Omega^2}g_2(x) + \mathcal{O}\left(\frac{1}{\Omega^3}\right), \quad \Omega \rightarrow \infty. \quad (4.10)$$

Comparing the coefficients, we find the following conditions. In $\mathcal{O}(1)$,

$$F(x)g_0(x) + Q(x)g_0(x)^2 = 0; \quad (4.11)$$

in $\mathcal{O}(1/\Omega)$,

$$-\lambda F(x)g_1(x) + 2Q(x)g_0(x)g_1(x) - F'(x) - Q(x)g_0'(x) - 2g_0(x)Q'(x) = 0; \quad (4.12)$$

and in $\mathcal{O}(1/\Omega^2)$,

$$F(x)g_2(x) + Q(x)[g_1(x)^2 + 2g_0(x)g_1(x)] - Q(x)g_1'(x) - 2g_1(x)Q'(x) + Q''(x) = 0. \quad (4.13)$$

There are two solutions for the $\mathcal{O}(1)$ constraint, i.e. $g_0(x) = 0$ and $\tilde{g}_0(x) = -F(x)/Q(x)$. We neglect the latter since this solution leads to a vanishing quality factor in the weak-noise limit, see Appendix B.1.

Solving the system of equations above, Eq. (4.11)-(4.13), we obtain the leading order terms for $g(x)$,

$$g_0(x) = 0, \quad (4.14)$$

$$g_1(x) = \frac{\lambda + F'(x)}{F(x)}, \quad (4.15)$$

and

$$g_2(x) = \frac{1}{F(x)^3}[-\lambda^2 Q(x) - 3\lambda Q(x)F'(x) - 2Q(x)F'(x)^2 + 2\lambda F(x)Q'(x) + 2F(x)F'(x)Q'(x) + F(x)Q(x)F''(x) - F(x)^2 Q''(x)]. \quad (4.16)$$

The periodicity, $p(x, t) = p(x + L, t)$, implies that $\phi(x) = \int^x g(u)du$ must satisfy

$$i2\pi k = \Omega \int_0^L dx g(x) = \Omega[\phi(L) - \phi(0)] \quad (4.17)$$

for an arbitrary $k \in \mathbb{Z}$. Plugging the perturbative solution $g(x)$, Eq. (4.10), into this relation, we can solve the quadratic equation for the eigenvalues as

$$\begin{aligned} \lambda_{\pm}^{(k)} = & \frac{\Omega}{2 \int_0^L Q(x)/F(x)^3 dx} \left\{ \int_0^L 1/F(x) dx - \frac{1}{\Omega} \int_0^L Q(x)F'(x)/F(x)^3 dx \right. \\ & \left. \pm \left[\left(\int_0^L 1/F(x) dx - \frac{1}{\Omega} \int_0^L Q(x)F'(x)/F(x)^3 dx \right)^2 - i8\pi k \int_0^L Q(x)/F(x)^3 dx / \Omega \right]^{\frac{1}{2}} \right\}. \end{aligned} \quad (4.18)$$

We find the well-behaved solution by a Taylor expansion for $\Omega \gg 1$ as

$$\begin{aligned} \lambda^{(k)} \equiv \lambda_-^{(k)} = & -(2\pi k)^2 \frac{1}{\Omega} \frac{\int_0^L Q(x)/F(x)^3 dx}{[\int_0^L 1/F(x) dx]^3} + \mathcal{O}\left(\frac{1}{\Omega^2}\right) \\ & + i 2\pi k \frac{1}{\int_0^L 1/F(x) dx} + i\mathcal{O}\left(\frac{1}{\Omega}\right). \end{aligned} \quad (4.19)$$

The corresponding eigenfunctions are given by

$$p^{(k)}(x, t) = \mathcal{N}^{(k)} \exp[\lambda^{(k)}t - \Omega \int^x g^{(k)}(u)du] \equiv \exp[\lambda^{(k)}t] h^{(k)}(x) \quad (4.20)$$

where $g^{(k)}(x)$ denotes the solution of Eq. (4.10) for the eigenvalue $\lambda^{(k)}$ and $h^{(k)}(x)$ the corresponding eigenfunction of the Fokker-Planck operator, Eq. (4.8).

The second solution for the eigenvalues is

$$\begin{aligned} \tilde{\lambda}^{(k)} \equiv \lambda_+^{(k)} \\ \approx \Omega \left[\int_0^L 1/F(x) dx \right] / \left[\int_0^L Q(x)/F(x)^3 dx \right] + \mathcal{O}(1) - i2\pi k / \int_0^L 1/F(x) dx + i\mathcal{O}\left(\frac{1}{\Omega}\right) \end{aligned} \quad (4.21)$$

which we can neglect since the $\tilde{\lambda}^{(k)}$ would lead to a vanishing number of oscillations in the weak-noise limit.

Thus, for a single continuous degree of freedom following a Fokker-Planck dynamics, Eq. (4.7), the quality factor is given by

$$\mathcal{R}_{\text{cont}} \equiv \left| \frac{\Im \lambda^{(1)}}{\Re \lambda^{(1)}} \right| = \frac{\Omega}{2\pi} \frac{\left(\int_0^L \frac{1}{F(x)} dx \right)^2}{\int_0^L \frac{Q(x)}{F(x)^3} dx} . \quad (4.22)$$

This transparent expression is the first main result of this chapter. In the next section, we discuss implications of this result for the microscopic bound, Eq. (4.4).

4.3.2 Bound on the quality factor

We first calculate a continuum limit of the bound on the quality factor, Eq. (4.4), and then use our main result, Eq. (4.22), to derive and prove the continuous version of this bound in the form

$$\mathcal{R}_{\text{cont}} \leq f_{\text{cont}} \equiv \frac{\Omega}{2\pi} \int_0^L \frac{F(x)}{Q(x)} dx . \quad (4.23)$$

We start by discretizing the Fokker-Planck equation (4.7) in space to obtain a master equation for a unicyclic network,

$$\partial_t p_i(t) = -(k_i^+ + k_i^-) p_i(t) + k_{i+1}^- p_{i+1} + k_{i-1}^+ p_{i-1}(t) , \quad (4.24)$$

where $p_i(t)$ denotes the probability to be in state i after time t and k_i^\pm are the associated transition rates. To this end, we use central differences to approximate the derivatives, i.e.,

$$\begin{aligned} f'(x) &\approx [f(x + \Delta x) - f(x - \Delta x)] / (2\Delta x) \quad \text{and} \\ f''(x) &\approx [f(x + \Delta x) - 2f(x) + f(x - \Delta x)] / \Delta x^2 . \end{aligned} \quad (4.25)$$

Comparing the result with Eq. (4.24), we get the rates

$$k_{x-\Delta x}^+ = \frac{F_{x-\Delta x}}{2\Delta x} + \frac{Q_{x-\Delta x}}{\Omega \Delta x^2} , \quad \text{and} \quad k_{x+\Delta x}^- = -\frac{F_{x+\Delta x}}{2\Delta x} + \frac{Q_{x+\Delta x}}{\Omega \Delta x^2} , \quad (4.26)$$

with $F_x \equiv F(x)$, $\Delta x \equiv L/N$, and relabeling of the states $i \rightarrow x = i\Delta x$.

The cycle affinity \mathcal{A} , Eq. (4.5), becomes by a Taylor expansion

$$\mathcal{A} = \sum_{x=1}^N \ln \frac{k_x^+}{k_x^-} = \Omega \sum_{x=1}^N \frac{F_x}{Q_x} \Delta x + \mathcal{O}(\Delta x^2) . \quad (4.27)$$

Thus, we find for the bound on the quality factor, Eq. (4.4), in the continuum limit, i.e., $N \gg 1$ respectively $\Delta x \ll 1$,

$$f = \cot \frac{\pi}{N} \tanh \frac{\mathcal{A}}{2N} \approx \frac{\Omega}{2\pi} \sum_{x=1}^N \frac{F_x}{Q_x} \Delta x \approx \frac{\Omega}{2\pi} \int_0^L \frac{F(x)}{Q(x)} dx \equiv f_{\text{cont}} . \quad (4.28)$$

The quality factor $\mathcal{R}_{\text{cont}}$ from Eq. (4.22) and f_{cont} can be related through a Cauchy Schwartz inequality,

$$\left(\int_0^L \frac{1}{F(x)} dx \right)^2 = \left(\int_0^L \sqrt{\frac{F(x)}{Q(x)}} \sqrt{\frac{Q(x)}{F(x)^3}} dx \right)^2 \leq \left(\int_0^L \frac{F(x)}{Q(x)} dx \right) \left(\int_0^L \frac{Q(x)}{F(x)^3} dx \right) . \quad (4.29)$$

Dividing both sides by $\int_0^L Q(x)/F(x)^3 dx$ leads to Eq. (4.23). Thus, we have proven the continuum version of the bound, Eq. (4.4), which has been conjectured in [4] for discrete unicyclic Markov networks. This is our second main result.

In the next section, we determine an expression for the entropy production in the weak-noise limit. With an analytical expression at hand, we proof the bound conjectured by Oberreiter and co-workers [5] for $\Omega \gg 1$.

4.3.3 Proof of entropic bound in the weak-noise limit

We derive an expression of the entropy production in the weak-noise limit, and then use inequality (4.23) to obtain a continuum version of the bound conjectured by Oberreiter and co-workers [5] in the form

$$\Delta S_{\text{tot}}[T] \geq 2\pi \mathcal{R}_{\text{cont}} . \quad (4.30)$$

As first step, we calculate the steady state distribution. Solving Eq. (4.9) for $\lambda = 0$, we obtain

$$p^s(x) \equiv \frac{N}{F(x)} \exp \left[-\frac{1}{\Omega} \frac{Q(x)}{F(x)} \partial_x \ln \frac{F(x)}{Q(x)} + \mathcal{O}\left(\frac{1}{\Omega^2}\right) \right] \quad (4.31)$$

with normalization constant

$$\frac{1}{N} \equiv \int dx \frac{1}{F(x)} \exp \left[-\frac{1}{\Omega} \frac{Q(x)}{F(x)} \partial_x \ln \frac{F(x)}{Q(x)} + \mathcal{O}\left(\frac{1}{\Omega^2}\right) \right] = \int dx \frac{1}{F(x)} + \mathcal{O}\left(\frac{1}{\Omega}\right). \quad (4.32)$$

Thus, we obtain the stationary probability current as

$$j^s(x) \equiv F(x)p^s(x) - \frac{1}{\Omega} \partial_x \left(Q(x)p^s(x) \right) = N + \mathcal{O}\left(\frac{1}{\Omega}\right). \quad (4.33)$$

In order to obtain the entropy production, we evaluate the following expression

$$\Omega \frac{j^s(x)^2}{Q(x)p^s(x)} = N\Omega \left[\frac{F(x)}{Q(x)} - \frac{1}{\Omega} \partial_x \left(\ln \frac{F(x)}{Q(x)} - \ln \frac{Q(x)}{F(x)} \right) + \mathcal{O}\left(\frac{1}{\Omega^2}\right) \right]. \quad (4.34)$$

This leads to

$$\begin{aligned} \sigma &\equiv \Omega \int dx \frac{j^s(x)^2}{Q(x)p^s(x)} = N\Omega \int dx \frac{F(x)}{Q(x)} + \mathcal{O}\left(\frac{1}{\Omega}\right) \\ &= \left(\Omega \int dx \frac{F(x)}{Q(x)} + \mathcal{O}\left(\frac{1}{\Omega}\right) \right) / \left(\int dx \frac{1}{F(x)} + \mathcal{O}\left(\frac{1}{\Omega}\right) \right) \end{aligned} \quad (4.35)$$

for $\Omega \gg 1$. In the first step we used Eq. (4.34) and Eq. (4.32) in the last step.

For the deterministic motion, the period of the oscillation is given by

$$T \equiv \int dx \frac{1}{F(x)}. \quad (4.36)$$

Using this definition, Eq. (4.28) and inequality Eq. (4.23), we obtain

$$T\sigma + \mathcal{O}\left(\frac{1}{\Omega}\right) = f_{\text{cont}} \geq 2\pi\mathcal{R}_{\text{cont}} + \mathcal{O}\left(\frac{1}{\Omega}\right). \quad (4.37)$$

Identifying the total entropy production per oscillation, i.e.,

$$\Delta S_{\text{tot}}[T] \equiv T\sigma, \quad (4.38)$$

we obtain Eq. (4.30). This constitutes our third main result.

4.3.4 A specific example

For an illustration, we consider a particle on a one-dimensional ring of length $L = 2\pi$. The particle experiences a periodic force $F_\varepsilon(x) \equiv 1 + \varepsilon \sin x$ with $-1 < \varepsilon < 1$. We keep the diffusivity constant, i.e., $Q(x) \equiv 1$. The dynamics is governed by the Langevin equation

$$\dot{x}(t) = F_\varepsilon(x(t)) + \sqrt{\frac{2}{\Omega}}\xi(t) \quad (4.39)$$

with $\langle \xi(t) \rangle = 0$ and $\langle \xi(t)\xi(t') \rangle = \delta(t - t')$. This equation is equivalent to a Fokker-Planck equation of the form of Eq. (4.7). Thus, we can apply the theory developed in the previous sections.

We keep the initial value constant, $x_0 = -\pi$, thus, the correlation function is proportional to the mean value of $x(t)$,

$$C_x(t) = \langle x(t) | x(0) = x_0 \rangle x_0 . \quad (4.40)$$

In the weak-noise limit, the deterministic solution for the mean value is given by

$$x_\infty(t) = -2 \arctan \left\{ \varepsilon - \sqrt{1 - \varepsilon^2} \tan \left[\frac{1}{2} t \sqrt{1 - \varepsilon^2} + \arctan \frac{\varepsilon + \tan(x_0/2)}{\sqrt{1 - \varepsilon^2}} \right] \right\} . \quad (4.41)$$

The quality factor for this system can be calculated analytically with Eq. (4.22) as

$$\mathcal{R}_{\text{cont}} = \Omega \frac{2(1 - \varepsilon^2)^{3/2}}{2 + \varepsilon^2} . \quad (4.42)$$

The bound, Eq. (4.28), is simply $f_{\text{cont}} = \Omega$.

As shown in Fig. 4.1a, we observe a numerical convergence towards the deterministic solution, Eq. (4.41) for increasing Ω , while the phase diffusion smears out the sharp edges the stronger the noise becomes. In this regime, we observe exponentially damped oscillations. From the numerically calculated correlation function, we obtain the frequency, the decay rate, and the quality factor \mathcal{R} as given by Eq. (4.2). The ratio \mathcal{R}/Ω is shown in Fig. 4.1b for various Ω as a function of ε . The numerical result for this one-dimensional system agrees very well with our analytical prediction. For vanishing ε , the bound, Eq. (4.28), is saturated as predicted by Eq. (4.42), while the quality factor tends to zero for

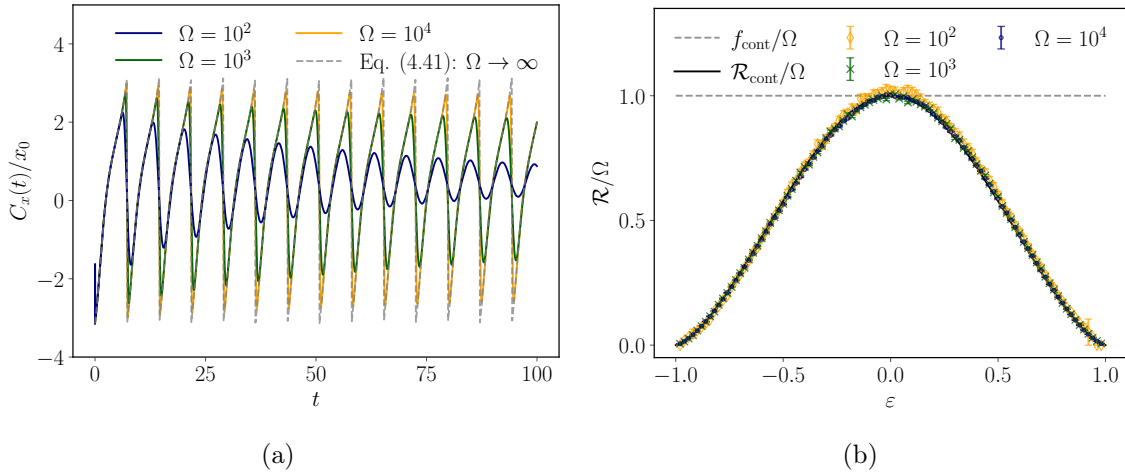


Figure 4.1: (a) Correlation function $C_x(t)/x_0$ for various Ω and $\varepsilon = -1/2$, $x_0 = -\pi$ for a particle on a ring. (b) Ratio \mathcal{R}/Ω as a function of ε . The continuous bound is the gray dashed line. The solid line represents the theoretical prediction for the quality factor, Eq. (4.42). We include error bars taking into account the fitting error.

$\varepsilon \rightarrow \pm 1$. This is due to the fact, that the force field, $F_\varepsilon(x) = 1 + \varepsilon \sin x$, establishes a root for $\varepsilon \approx \pm 1$, for which oscillations vanish.

In what follows, we turn to two-dimensional systems. We demonstrate analytically and numerically that the one-dimensional quality factor, Eq. (4.22), is also applicable to planar noisy oscillations for which a limit cycle emerging through a Hopf bifurcation is a prime example.

4.4 PLANAR OSCILLATIONS IN THE WEAK-NOISE LIMIT

Consider two continuous degrees of freedom $x(t)$ and $y(t)$. Their coupled dynamics is governed by an autonomous Langevin equation,

$$\frac{d}{dt} \begin{pmatrix} x(t) \\ y(t) \end{pmatrix} = \begin{pmatrix} F_x(x(t), y(t)) \\ F_y(x(t), y(t)) \end{pmatrix} + \frac{1}{\sqrt{\Omega}} C(x(t), y(t)) \begin{pmatrix} \xi_1(t) \\ \xi_2(t) \end{pmatrix} \quad (4.43)$$

where $\langle \xi_i(t) \rangle = 0$ and $\langle \xi_i(t) \xi_j(t') \rangle = \delta_{ij} \delta(t - t')$. The weak-noise limit is again given explicitly through the external parameter $\Omega \gg 1$. We denote the entries of the matrix characterizing the multiplicative noise as

$$C(x(t), y(t)) = \begin{pmatrix} c_{x,1}(x(t), y(t)) & c_{x,2}(x(t), y(t)) \\ c_{y,1}(x(t), y(t)) & c_{y,2}(x(t), y(t)) \end{pmatrix}. \quad (4.44)$$

We assume that the deterministic dynamics has a stable limit cycle, i.e., a closed curve in phase space which we denote as $\{\bar{x}, \bar{y}\}$. Along this curve, the vector-field $F(x, y) \equiv (F_x(x, y), F_y(x, y))$ has no root, thus, a non-vanishing norm

$$\|F(\bar{x}, \bar{y})\| > 0. \quad (4.45)$$

The norm $\|v\|$ of a vector $v = (v_x, v_y)$ is induced by the standard scalar-product in \mathbb{R}^2 ,

$$\|v\| \equiv \sqrt{v \cdot v} \equiv \sqrt{v_x^2 + v_y^2}. \quad (4.46)$$

Continuity of the vector field assures that Eq. (4.45) holds in a neighborhood of the limit cycle. Thus, we define the vector parallel to the force as

$$\hat{f}_{\parallel}(x, y) \equiv \begin{pmatrix} F_x(x, y) \\ F_y(x, y) \end{pmatrix} / \left\| \begin{pmatrix} F_x(x, y) \\ F_y(x, y) \end{pmatrix} \right\| \quad (4.47)$$

and the perpendicular one as

$$\hat{f}_{\perp}(x, y) \equiv \begin{pmatrix} F_y(x, y) \\ -F_x(x, y) \end{pmatrix} / \left\| \begin{pmatrix} F_x(x, y) \\ F_y(x, y) \end{pmatrix} \right\|. \quad (4.48)$$

We denote the projections along these directions as

$$s \equiv \hat{f}_{\parallel}(x, y) \cdot \begin{pmatrix} x \\ y \end{pmatrix} \quad \text{and} \quad s_{\perp} \equiv \hat{f}_{\perp}(x, y) \cdot \begin{pmatrix} x \\ y \end{pmatrix}. \quad (4.49)$$

In order to obtain the dynamics along a noisy limit cycle, we concentrate in the following on the parallel projection. The time-evolution is given by Ito's formula [38] and Eq. (4.43) as

$$\begin{aligned} \frac{d}{dt}s(t) &= \|F(x(t), y(t))\| + s_{\perp}(t)DF(x(t), y(t))\hat{f}_{\parallel}(x(t), y(t)) \cdot \hat{f}_{\perp}(x(t), y(t)) + \mathcal{O}\left(\frac{1}{\Omega}\right) \\ &+ \frac{1}{\sqrt{\Omega}}\hat{f}_{\parallel}(x(t), y(t)) \cdot C(x(t), y(t))\xi(t) \\ &+ \frac{1}{\sqrt{\Omega}}s_{\perp}(t)DF(x(t), y(t))\hat{f}_{\parallel}(x(t), y(t)) \cdot \hat{f}_{\perp}(x(t), y(t)) \cdot C(x(t), y(t))\xi(t). \end{aligned} \quad (4.50)$$

$DF(x, y)$ denotes the Jacobian matrix of the vector field $F(x, y)$. For brevity of notation, we write $x(t)$ or $y(t)$ in the equation above where we mean $x(t)$ and $y(t)$ parameterized in the new degrees of freedom, i.e., $x(t) = x(s(t), s_{\perp}(t))$ and similarly for $y(t)$.

In the vicinity of the limit cycle, the dominant direction is parallel to the force. Thus, we neglect the perpendicular component and set $s_{\perp}(t) = 0$ in Eq. (4.50) to obtain the following Langevin equation as a zeroth order Taylor expansion

$$\frac{d}{dt}s(t) \simeq F_{\parallel}(s(t)) + \frac{1}{\sqrt{\Omega}}C_{\parallel}(s(t)) \cdot \begin{pmatrix} \xi_1(t) \\ \xi_2(t) \end{pmatrix} \quad (4.51)$$

with the force

$$F_{\parallel}(s) \equiv \|F(x(s, 0), y(s, 0))\| \quad (4.52)$$

and the vector

$$C_{\parallel}(s) \equiv C^T(x(s, 0), y(s, 0)) \cdot \hat{f}_{\parallel}(x(s, 0), y(s, 0)) \equiv \begin{pmatrix} C_{\parallel,1}(s) \\ C_{\parallel,2}(s) \end{pmatrix}. \quad (4.53)$$

Hence, the diffusivity is given by

$$Q_{\parallel}(s) \equiv \frac{1}{2}[C_{\parallel,1}(s)^2 + C_{\parallel,2}(s)^2]. \quad (4.54)$$

The Ito-Langevin equation, Eq. (4.51), is equivalent to the Fokker-Planck equation

$$\partial_t p(s, t) = -\partial_s[F_{\parallel}(s)p(s, t)] + \frac{1}{\Omega}\partial_s^2[Q_{\parallel}(s)p(s, t)]. \quad (4.55)$$

We can now use the solution $p(s, t)$ to calculate the auto-correlation function of $x(t)$,

$$C_x(t) \equiv \langle x(t)x(0) \rangle , \quad (4.56)$$

along the noisy trajectory as

$$\begin{aligned} C_x(t) &= \int dx \int dy \int dx_0 \int dy_0 x x_0 p(x, y, t | x_0, y_0) p_0(x_0, y_0) \\ &\simeq \int ds \int ds_\perp \int ds_0 \int ds_{\perp,0} x(s, 0) x(s_0, 0) p(s, s_\perp, t | s_0, s_{\perp,0}) p_0(s_0, s_{\perp,0}) \\ &= \int ds \int ds_0 x(s, 0) x(s_0, 0) p(s, t | s_0) p_0(s_0) \\ &= \sum_{k \in \mathbb{Z}} \int ds \int ds_0 x(s) x(s_0) \exp(\lambda^{(k)} t) h^{(k)}(s | s_0) p_0(s_0) \\ &= C^{(0)} + C^{(1)} \cos(\Im \lambda^{(1)} t) \exp(\Re \lambda^{(1)} t) + \sum_{|k| \geq 2} C^{(k)} \exp(\lambda^{(k)} t) . \end{aligned} \quad (4.57)$$

In the second line, we neglect the $s_\perp(t)$ dependence of $x(t)$ to obtain the behavior parallel to the closed curve. The eigenvalues $\lambda^{(k)}$ and eigenfunctions $h^{(k)}(s | s_0)$ are the ones corresponding to the one-dimensional Fokker-Planck equation (4.55) and can be calculated as described above for the one-dimensional system, Sec. 4.3.1. The constants are given as

$$C^{(k)} \equiv \int ds \int ds_0 x(s) x(s_0) h^{(k)}(s | s_0) p_0(s_0) . \quad (4.58)$$

In the weak-noise limit, the coordinate $s(t)$ effectively becomes the arc-length. Hence, the integrals appearing in Eq. (4.19) can be evaluated according to

$$\int_{s(0)}^{s(T)} \frac{Q_{\parallel}(s)}{F_{\parallel}(s)^3} ds = \int_0^T \frac{Q_{\parallel}(\bar{x}(t), \bar{y}(t))}{F_{\parallel}(\bar{x}(t), \bar{y}(t))^3} \frac{ds}{dt} dt = \int_0^T \frac{Q_{\parallel}(\bar{x}(t), \bar{y}(t))}{F_{\parallel}(\bar{x}(t), \bar{y}(t))^2} dt . \quad (4.59)$$

The quality factor of a two-dimensional limit cycle oscillation is thus given by the one-dimensional expression, Eq. (4.22), in the weak-noise limit with $F_{\parallel}(s)$ and $Q_{\parallel}(s)$ as defined above, which is our fourth main result.

We note that the above argument is not restricted to planar oscillations. The basic idea, i.e., focusing on the parallel direction does not depend on the number of directions orthogonal to the trajectory. In a N -dimensional system, the degrees of freedom can be parameterized with one parallel direction $s(t)$ and $N - 1$ orthogonal directions, e.g.,

$x(t) = x(s(t), s_{\perp}^{(1)}(t), \dots, s_{\perp}^{(N-1)}(t))$, and approximated through $x(t) \approx x(s(t), 0, \dots, 0)$. Thus, the main result, Eq. (4.57), remains unchanged in this more general case.

The next two sections are devoted to applications. We first study the noisy Stuart-Landau oscillator and discuss the validity of the approximations made above. Then, we examine the thermodynamically consistent Brusselator as a generic model for a chemical clock.

4.5 CUBIC NORMAL FORM FOR A HOPF BIFURCATION

4.5.1 *Stuart-Landau oscillator*

The cubic normal form for a Hopf bifurcation [48, 100–105], often referred to as Stuart-Landau oscillator, is characterized by the following vector field in polar coordinates

$$\begin{aligned}\partial_t r &= \mu r - ar^3 \equiv F_r(r) \\ \partial_t \theta &= \omega + br^2 \equiv F_{\theta}(r, \theta) .\end{aligned}\tag{4.60}$$

When μ changes sign and $a > 0$, this field undergoes a Hopf bifurcation and a limit cycle with constant radius $r_0 \equiv \sqrt{\mu/a}$ emerges. We assume the matrix characterizing the noise to be constant,

$$C(x(t), y(t)) = \sqrt{2D} \begin{pmatrix} 1 & 0 \\ 0 & 1 \end{pmatrix} ,\tag{4.61}$$

with a free parameter $D > 0$.

The normal and tangent degrees of freedom for the closed curve in phase space are the radial deviation $\rho(t) \equiv r(t) - r_0$ and the angle $\theta(t)$, which compare to $s_{\perp}(t)$ and $s(t)$ from above, respectively. Following the procedure described in Sec. 4.4, we arrive at the Fokker-Planck equation for the angle

$$\partial_t p(\theta, t) = -\partial_{\theta}[\omega_0 p(\theta, t)] + \frac{aD}{\mu\Omega} \partial_{\theta}^2[p(\theta, t)] .\tag{4.62}$$

Thus, θ follows a free diffusion with constant drift, i.e.,

$$F_{\theta}(\theta) \equiv F_{\theta}(r_0, \theta) = \omega + b\mu/a \equiv \omega_0 \quad \text{and} \quad Q_{\theta}(\theta) = aD/\mu .\tag{4.63}$$

This definition originates from the zeroth order Taylor expansion of the angular force, Eq. (4.60), and Eq. (4.54). The solution of Eq. (4.62) is a Gaussian

$$p(\theta, t|\theta_0) = \frac{1}{\sqrt{4\pi tDa/(\Omega\mu)}} \exp \left[-\frac{1}{2} \frac{(\theta - \omega_0 t - \theta_0)^2}{2tDa/(\Omega\mu)} \right]. \quad (4.64)$$

For the initial condition $p_0(\theta_0) = \delta(\theta_0 - \theta(0))$, we carry out the Gaussian integrals and obtain

$$\begin{aligned} C_x(t) &= \frac{\mu}{a} \cos \theta(0) \int d\theta \cos \theta p(\theta, t|\theta_0) \\ &= \frac{\mu}{a} \cos \theta(0) \int d\theta \frac{1}{2} [\exp(i\theta) + \exp(-i\theta)] p(\theta, t|\theta_0) \\ &= \frac{\mu}{a} \cos \theta(0) \cos(\omega_0 t + \theta(0)) \exp[-(aD/\Omega\mu)t]. \end{aligned} \quad (4.65)$$

Thus, we find for the quality factor

$$\mathcal{R}^{2d} = \left| \frac{\omega_0}{aD/(\Omega\mu)} \right| = \left| \frac{\Omega}{D} \frac{\mu}{a} (\omega + b\mu/a) \right| = \mathcal{R}_{\text{cont}} \quad (4.66)$$

in agreement with what we get by putting Eq. (4.63) into the formula for a one-dimensional system, Eq. (4.22). Thus, we have analytically shown that the two-dimensional quality factor for the limit cycle oscillation is exactly given by the one-dimensional approximation. Furthermore, since $F_\theta(\theta)$ and $Q_\theta(\theta)$ are constant, $f_{\text{cont}} = \mathcal{R}_{\text{cont}}$.

In Fig. 4.2, we compare the quality factor obtained by a simulation of the Langevin dynamics and the analytical result from above. The parameters are chosen such that we obtain a decoupling of the angular and the radial motion, i.e., $|b| \ll 1$. Within this parameter range the numerically obtained quality factor agrees with the analytical one, Eq. (4.66). For $b = 1$, we see deviations from the theoretical value. This is due to the contribution of the radial motion to the diffusion of the angle [104] as we will show in the next section.

4.5.2 *Effective diffusion coefficient*

We explain the deviations from the analytical result, Eq. (4.66), and show how to expand the prediction into the regime where angular and radial motion are coupled. We start with the solution for the radial deviations $\rho(t) \equiv r(t) - r_0$ of the decoupled Stuart-Landau oscillator.

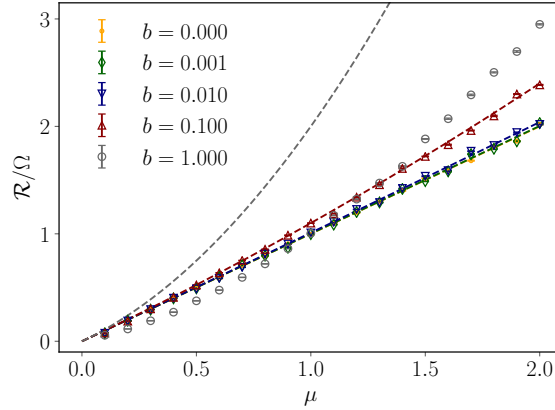


Figure 4.2: Quality factor for a two-dimensional limit cycle as a function of μ for different b with $\omega = a = 1$ and $\Omega = 10^3$. Dashed lines represent the theoretical prediction, Eq. (4.66).

In leading order for $\Omega \gg 1$, the Ito-Langevin equation is given by

$$\partial_t \rho(t) \approx \frac{D}{\Omega} \sqrt{\frac{a}{\mu}} - 2\mu\rho(t) + \frac{2D}{\sqrt{\Omega}} [\cos \theta(t)\xi_1(t) + \sin \theta(t)\xi_2(t)] \quad (4.67)$$

with the corresponding Fokker-Planck equation

$$\partial_t p(\rho, t) = \partial_\rho \left[\left(\frac{D}{\Omega} \sqrt{\frac{a}{\mu}} - 2\mu\rho \right) p(\rho, t) \right] + \frac{D}{\Omega} \partial_\rho^2 p(\rho, t). \quad (4.68)$$

Thus, the radial deviations follow an Ornstein-Uhlenbeck process with constant drift [104]. The mean is given by

$$\begin{aligned} \langle \rho(t) \rangle &= \rho_0 \exp(-2\mu t) + \frac{D}{2\Omega} \sqrt{\frac{a}{\mu^3}} [1 - \exp(-2\mu t)] \\ &\approx \rho_0 \exp(-2\mu t), \text{ for } \Omega \rightarrow \infty, \end{aligned} \quad (4.69)$$

with variance

$$\text{Var}[\rho(t)] = \frac{D}{2\Omega\mu} [1 - \exp(-4\mu t)] \approx 0, \text{ for } \Omega \rightarrow \infty. \quad (4.70)$$

The fluctuations of $\rho(t)$ are of order $\Omega^{-1/2}$ and hence, the coupling between ρ and θ needs to be included if the coupling strength

$$\partial_r F_\theta(r_0, \theta) = 2b \sqrt{\frac{\mu}{a}} \quad (4.71)$$

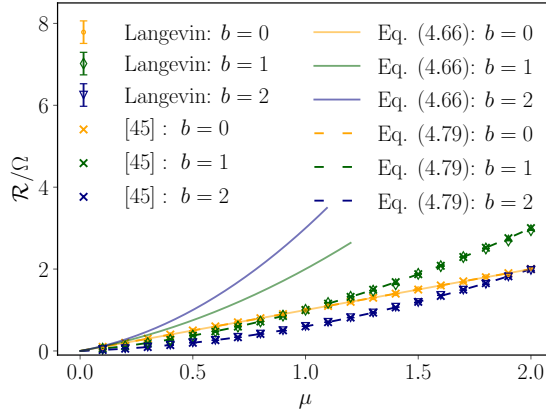


Figure 4.3: Quality factor \mathcal{R}/Ω of the cubic normal form as function of μ for various b . The extensivity-parameter is set to $\Omega = 10^3$ and $\omega = a = 1$. Solid lines represent the one-dimensional prediction, Eq. (4.66) and dashed lines the description with the effective diffusion coefficient, Eq. (4.79). Crosses are calculated with the scheme presented in [45].

is not negligible. Since this argument holds for any vector field that does not depend on θ in polar coordinates, the following holds beyond the cubic normal form of a Hopf bifurcation.

The dynamics of the coupled degrees of freedom is effectively given by the Langevin equations

$$\frac{d}{dt} \begin{pmatrix} \theta(t) \\ \rho(t) \end{pmatrix} = \begin{pmatrix} 0 & \kappa_1 \\ 0 & -\kappa_2 \end{pmatrix} \begin{pmatrix} \theta(t) \\ \rho(t) \end{pmatrix} + \begin{pmatrix} f_1 \\ f_2 \end{pmatrix} + \begin{pmatrix} \eta_1(t) \\ \eta_2(t) \end{pmatrix} \quad (4.72)$$

with Gaussian white noise $\langle \eta_\alpha(t) \rangle = 0$ and $\langle \eta_\alpha(t) \eta_\beta(t') \rangle = \sqrt{2D_\alpha} \delta_{\alpha,\beta} \delta(t - t')$. The κ_α , f_α and D_α are constants. The "effectively" should be understood such that the equation above leads to the same Fokker-Planck equation as the Langevin equation for $\rho(t)$ and $\theta(t)$ if one chooses the parameters correctly.

The equation for $\rho(t)$ has the solution presented in the beginning of this section. Therefore, we concentrate on $\theta(t)$ and calculate its variance in order to get the diffusion constant. A formal solution is given by

$$\begin{aligned} \theta(t) = & \theta_0 + \left(f_1 + \frac{\kappa_1}{\kappa_2} f_2 \right) t + \frac{\kappa_1}{\kappa_2} \left(\rho_0 - \frac{f_2}{\kappa_2} \right) \left(1 - e^{-\kappa_2 t} \right) \\ & + \int_0^t d\tau \eta_1(\tau) + \frac{\kappa_1}{\kappa_2} \int_0^t d\tau \eta_2(\tau) \left(1 - e^{-\kappa_2 t} e^{\kappa_2 \tau} \right) \end{aligned} \quad (4.73)$$

where the integrals are interpreted in the Ito sense and $\theta(0) \equiv \theta_0$ respectively $\rho(0) \equiv \rho_0$. The variance becomes

$$\langle \theta(t)^2 \rangle - \langle \theta(t) \rangle^2 = 2D_1 \left(1 + \frac{\kappa_1^2 D_2}{\kappa_2^2 D_1} \right) t + \frac{\kappa_1^2}{\kappa_2^3} D_2 \left(1 - e^{-2\kappa_2 t} - 4 + 4e^{-\kappa_2 t} \right). \quad (4.74)$$

We obtain the diffusion coefficient as

$$D_\theta \equiv \lim_{t \rightarrow \infty} \frac{\langle \theta(t)^2 \rangle - \langle \theta(t) \rangle^2}{2t} = \left(1 + \frac{\kappa_1^2 D_2}{\kappa_2^2 D_1} \right) D_1. \quad (4.75)$$

For the noisy Stuart-Landau oscillator, we identify the parameters as

$$D_1 = \frac{Da}{\Omega\mu}, D_2 = \frac{D}{\Omega}, \kappa_1 = 2b\sqrt{\frac{\mu}{a}}, \kappa_2 = 2\mu, f_1 = \omega + b\frac{\mu}{a} \equiv \omega_0, f_2 = \frac{D}{\Omega}\sqrt{\frac{a}{\mu}}. \quad (4.76)$$

Thus, the diffusion coefficients becomes

$$D_\theta = D_1 \left(1 + \frac{b^2}{a^2} \right) \quad (4.77)$$

and the mean angle is given by

$$\langle \theta(t) \rangle \approx \theta_0 + \frac{b}{\sqrt{\mu a}} \rho_0 + \left(\omega_0 + \frac{b D}{\mu \Omega} \right) t = \theta_0 + \frac{b}{\sqrt{\mu a}} \rho_0 + \omega_0 t + \mathcal{O}\left(\frac{1}{\Omega}\right) \quad (4.78)$$

in the limit of large times. Thus, for large t , the angular motion is effectively given by a diffusion with constant D_θ and drift ω_0 . According to the calculations in the previous section, the quality factor is then given in the weak-noise limit by

$$\tilde{\mathcal{R}}^{2d} = \frac{\omega_0}{D_\theta} = \frac{\mathcal{R}^{2d}}{1 + b^2/a^2}. \quad (4.79)$$

In Fig. 4.3, we show the quality factor obtained by integrating the Langevin equation, the one-dimensional prediction from the previous section, the effective theory introduced above and data calculated using the method presented in [45], see Appendix B.2 for a brief explanation. In contrast to the previous section, we consider a parameter range with non-negligible coupling between radial deviations and angular motion. As expected, the naive one-dimensional approximation fails to reproduce the quality factor of the underlying Langevin dynamics. Nevertheless, the effective description taking into account radial motion predicts the quality factor correctly and is in agreement with the full theory [45].

In conclusion, we have extended the validity of the approximations made in Sec. 4.4 to a class of systems in which the normal and tangent motion do not necessarily decouple. Moreover, the discussion presented above is not limited to the Stuart-Landau oscillator, it rather holds true for any vector field that does not depend on the angle. In the next section, we discuss an example for which the latter assumptions does not remain true.

4.6 BRUSSELATOR

A paradigmatic model for a chemical clock is the Brusselator [90, 106, 107],



The concentrations c_A and c_B of the chemical species A and B in the external bath are kept constant. Due to a difference in the chemical potential between A and B , i.e., $\Delta\mu \equiv \mu_B - \mu_A > 0$, the system is out of equilibrium and the number of the intermediate species X and Y can oscillate. Considering the reaction cycle which consumes a substrate B and generates a product A , the thermodynamic force associated with this cycle is

$$\mathcal{A} \equiv \Delta\mu = \ln \frac{c_B k_3^+ k_2^+ k_1^-}{c_A k_1^+ k_2^- k_3^-} \quad (4.81)$$

where k_i^\pm are the corresponding reaction rates. This equation is commonly known as local detailed balance condition [12].

Following [46], we obtain $F(x, y)$ and the diffusion matrix $Q(x, y)$ in the weak-noise limit as

$$\begin{aligned} F_x(x, y) &= c_A k_1^+ - k_1^- x + k_2^+ x^2 y - k_2^- x^3, \\ F_y(x, y) &= c_B k_3^+ - k_3^- y - k_2^+ x^2 y + k_2^- x^3, \\ Q_{x,x}(x, y) &= \frac{1}{2}(c_A k_1^+ + k_1^- x + k_2^+ x^2 y + k_2^- x^3), \\ Q_{y,y}(x, y) &= \frac{1}{2}(c_B k_3^+ + k_3^- y + k_2^+ x^2 y + k_2^- x^3), \\ Q_{x,y}(x, y) &= Q_{y,x}(x, y) = -\frac{1}{2}(k_2^+ x^2 y + k_2^- x^3), \end{aligned} \quad (4.82)$$

where $x \equiv n_X/\Omega$ and $y \equiv n_Y/\Omega$. Here, n_i denotes the number of molecules of species X or Y . The external parameter Ω represents the volume of the system.

We choose the noise matrix $C(x, y)$, Eq. (4.44), such that $Q(x, y) = \frac{1}{2}C(x, y)C(x, y)^T$, e.g.,

$$C(x, y) \equiv \sqrt{\frac{2}{Q_{x,x}(x, y)}} \begin{pmatrix} Q_{x,x}(x, y) & 0 \\ Q_{x,y}(x, y) & \sqrt{\det Q(x, y)} \end{pmatrix}. \quad (4.83)$$

Thus, the noisy rate equation for the Brusselator are of the form of Eq. (4.43) and we can apply the theory developed in Sec. 4.4.

The deterministic vector field

$$F(x, y) \equiv \begin{pmatrix} F_x(x, y) \\ F_y(x, y) \end{pmatrix} = \begin{pmatrix} c_A k_1^+ - k_1^- x + k_2^+ x^2 y - k_2^- x^3 \\ c_B k_3^+ - k_3^- y - k_2^+ x^2 y + k_2^- x^3 \end{pmatrix} \quad (4.84)$$

undergoes a Hopf bifurcation while increasing the chemical potential [90]. We obtain the emerging limit cycle by numerically solving the deterministic equation,

$$\frac{d}{dt} \begin{pmatrix} x(t) \\ y(t) \end{pmatrix} = \begin{pmatrix} F_x(x(t), y(t)) \\ F_y(x(t), y(t)) \end{pmatrix}. \quad (4.85)$$

Following the procedure from Sec. 4.4, we determine the force $F_{\parallel}(x, y)$ and diffusivity $Q_{\parallel}(x, y)$ and numerically obtain our estimate for the quality factor $\mathcal{R}_{\text{cont}}$.

In Fig. 4.4a, we compare our result with three sets of data; those from [90] as obtained by a Gillespie simulation of the Brusselator, from the algorithm of the full theory [45], see Appendix B.2, and from data obtained by a Langevin simulation with the force field $F(x, y)$ and matrix $C(x, y)$ described above. We find for all methods that the quality factor tends to zero in the vicinity of the bifurcation point $\Delta\mu_c \simeq 3.9$ [90] as expected. For $\Delta\mu$ significantly above $\Delta\mu_c$, the data obtained by a Langevin simulation and by the full theory agree, but there are deviations to the the data obtained through the Gillespie algorithm and our method. The variance in the Gillespie data is due to the fact that the number of coherent oscillations, thus the quality factor, scales around the bifurcation-point and away from the transition with an apparent exponent less than 1, i.e., $\mathcal{R} \propto \Omega^\alpha$ with $\alpha < 1$ [90]. Re-scaling the data with such an exponent leads to a better agreement with the other data sets, see Fig. 4.4b. While this procedure leads to consistency with the full theory, there is still a significant discrepancy to the method presented in Sec. 4.4.

The one-dimensional approximation of the quality factor overestimates the full dynamics of the Brusselator as shown in Fig. 4.4a. The bound, Eq. (4.23), is about a factor 2

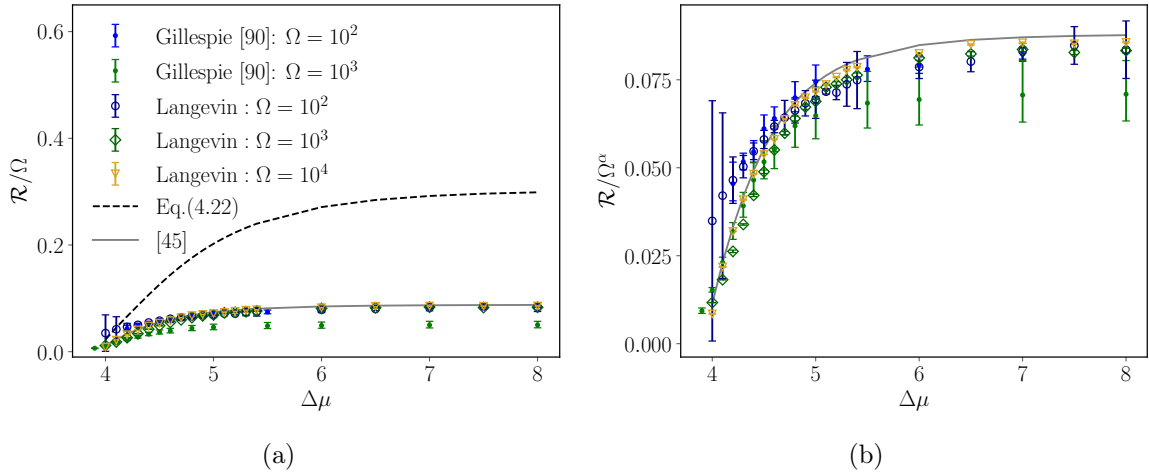


Figure 4.4: (a) Quality factor and (b) $\mathcal{R}/\Omega^\alpha$ of the Brusselator as function of the thermodynamic force $\Delta\mu$ for various Ω . The rates are chosen as $k_1^+ = k_3^+ = 0.1$, $k_1^- = k_2^+ = k_2^- = 1$, $c_A = 1$, and $c_B = 3$. The rate k_3^- is computed with the thermodynamic force $\Delta\mu$ and relation, Eq. (4.81). $\alpha = 0.99$ for the $\Omega = 100$ Gillespie data and $\alpha = 0.95$ for $\Omega = 10^3$. For all other methods, $\alpha = 1$ by theory. In (b) the prediction by Eq. (4.22) is not displayed in order to focus on the collapsed data.

to 3 times bigger than this continuous quality factor (data not shown). The significant discrepancy between the data obtained through Eq. (4.22) and for example by the algorithm [45] resembles the corresponding failure for the noisy Stuart-Landau oscillator, Sec. 4.5.2. There, we have analytically shown that the perpendicular motion amplifies the diffusion in the tangent direction. In particular, we have established an effective diffusion constant which sets the decay time of the correlation function. While this analytical treatment is not feasible anymore for the Brusselator due to an angular dependent limit cycle radius, we numerically calculate the frequency ω , Fig. 4.5a, and the coherence time τ , Fig. 4.5b, for all data sets except the one obtained by the Gillespie algorithm.

We find only small variations for the angular frequency. However, the decay time τ is overestimated by the one-dimensional expression, Eq. (4.19), while the remaining methods coincide. Thus, as in the strong coupling regime of the noisy Stuart-Landau oscillator, the diffusion constant for the tangential motion is larger than predicted by the one-dimensional approximation. In fact, this is a generic feature due to the stability of a limit cycle as we have seen in Sec. 4.5.2.

In summary, we have also found for the Brusselator that a coupling between normal and tangent motion leads to a reduced quality factor. Thus, the approximation we have presented in Sec. 4.4 can be understood as an effective upper bound on the coherence. For the generic model presented in Sec. 4.5.2, this upper bound is sharp.

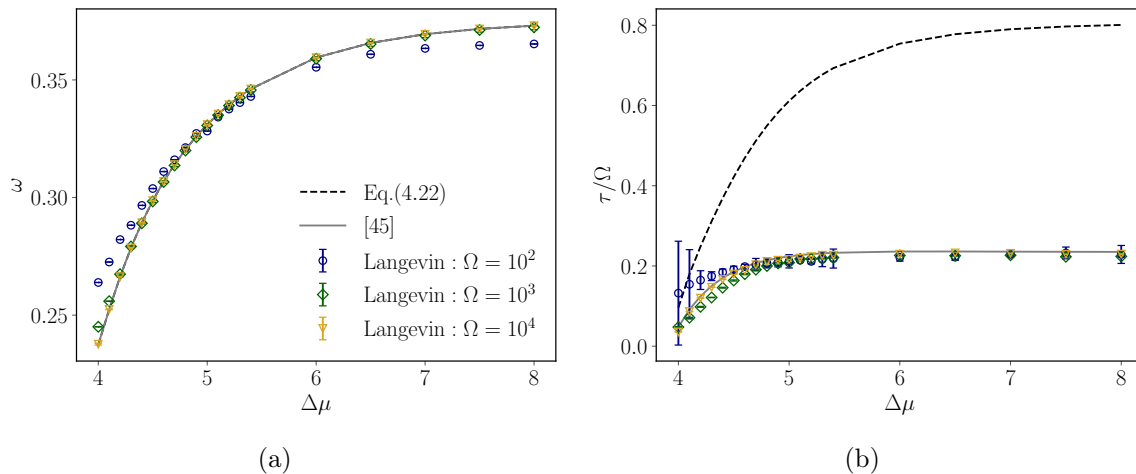


Figure 4.5: (a) Frequency ω and (b) decay time τ/Ω of the Brusselator as function of $\Delta\mu$ for various Ω . The rates are chosen as for Fig. 4.4.

4.7 DISCUSSION AND CONCLUSION

We have derived an analytical expression for the quality factor for an oscillator based on a one-dimensional Fokker-Planck dynamics, Eq. (4.22). This expression is obtained by a spectral decomposition of the Fokker-Planck operator as presented in [45, 46]. In contrast to these studies, we did not use the rather involved techniques of Hamilton-Jacobi theory but solved for the eigenvalues and eigenfunctions directly exploiting the weak-noise limit.

Furthermore, we have derived and proven a continuous version of the microscopic bound on the quality factor of a stochastic oscillator which has been conjectured in [4]. Based on numerical evidence, it has been suggested that the quality factor of a Markov network is bounded by the network topology and the force driving the system out of equilibrium. This continuous bound, Eq. (4.23), is tight, since it is derived through the Cauchy-Schwartz inequality. It is simply given by the integral of driving force over state-dependent diffusion coefficient. Furthermore, it turns out that this bound is in the weak-noise limit equivalent to the bound onto the entropy production presented in [5].

The one-dimensional quality factor also captures the behavior of a two-dimensional noisy oscillator. If the coupling of tangent and normal motion is negligible, this correspondence is exact. Moreover, even if the directions do not decouple, the quality factor for a broad class of oscillators can be obtained through an effective one-dimensional expression as we have analytically shown for the Stuart-Landau model as a generic example. The theoretical result is in agreement with data obtained by numerically integrating the corresponding Langevin equation. It also matches the numerical data resulting from the method introduced in [45].

This effective description breaks down for systems in which the two-dimensional motion does not decouple. As an example, we examined the Brusselator numerically and observed that the one-dimensional approximation leads to an overestimate in the decay time as we have also found for the Stuart-Landau oscillator. The full, rather involved method introduced in [45, 46] is in good agreement with data obtained by a Gillespie simulation and by integrating the corresponding chemical Langevin equation. Thus, based on the numerical and analytical findings, we suggest that the theory for the planar oscillations presented in our work is an upper bound on the quality factor of a two-dimensional noisy oscillator. Moreover, the calculations leading to a parametrization with the arc-length of a limit cycle are not limited to two dimensions but can be generalized to arbitrary dimensions.

In conclusion, we have presented a transparent formula for the quality factor of a noisy oscillator. In one dimension this expression is exact. For a broad class of two-dimensional systems, this expression can be adjusted to predict the correct coherence while for general two-dimensional oscillators, it should yield an upper bound. The method presented in this chapter provides an elementary approach to the coherence of a noisy clock. It is sufficient to find the limit cycle numerically and then integrate a function along it which is simpler than the numerically more challenging and sensitive techniques required for the full theory [45].

NONEQUILIBRIUM FLUCTUATIONS OF CHEMICAL REACTION NETWORKS AT CRITICALITY – THE SCHLÖGL MODEL AS PARADIGMATIC CASE

5.1 INTRODUCTION

Chemical reaction networks constitute a major paradigm for nonequilibrium systems. Due to their complexity, they offer a rich variety of non-trivial phenomena, thus, providing the chance to study nonequilibrium effects. In the macroscopic limit, chemical reaction networks can exhibit nonlinearities and bifurcations leading to phase transitions that occur out of equilibrium [83, 108–110].

With the development of stochastic thermodynamics [12] over the last decades, chemical reaction networks and their thermodynamic treatment gained significant interest [33, 34, 111–113]. Several case studies of thermodynamically consistent reaction networks have shown that a phase transition has immediate impact on nonequilibrium quantities such as the coherence of oscillations [90, 114] or the entropy production rate [115–127] and its fluctuations [90, 128]. From a mathematical perspective, large deviation theory turned out to be a useful tool to examine these phenomena [96, 127, 129–132]. As nonequilibrium phase transitions are not restricted to chemical systems, they can also be found in various biological [133–137] and active systems [138–145].

A common feature of chemical reaction networks exhibiting a phase transition is the presence of auto-catalytic reactions and chemostats. The latter provide a constant source of educt particles to the reaction channels, which, thus, are constantly consuming free energy. The flux and difference in chemical potentials of the respective particles are thus linked to the entropy production of the total system [12, 34].

So far, the focus has been on the mean behavior of physical observables like entropy production. Only a few studies have examined their fluctuations [127, 128] for example during a first order phase-transition [146, 147]. Fluctuations of the entropy production rate at a continuous phase transition have only been considered numerically in the context of biochemical oscillators [90]. Here, we examine nonequilibrium fluctuations during a continuous phase transition numerically as well as analytically.

We study the flux of particles consumed and produced in the reservoirs for the Schlögl model as a generic univariate system undergoing a continuous phase transition upon variation of a control parameter. Fluctuations of the fluxes are characterized by the associated diffusion coefficient. We numerically find that the particle flux is a continuous function of the control parameter. The diffusion coefficient displays critical behavior while varying a control parameter. We develop a theory that explains the continuous behavior of the particle flux and predicts scaling exponents for the diffusion coefficient in agreement with the numerically found ones.

This chapter is organized as follows. We introduce the model and discuss the different regimes in Sec. 5.2. In Sec. 5.3.1, we numerically determine the particle flux and the critical exponents for the scaling of the derivative of the flux in the monostable regime. Furthermore, we show how the diffusion coefficient scales with the control parameter and system size. The analytical prediction of scaling exponents for this pathway is presented in Sec. 5.3.2 and 5.3.3. For the transition into bistability, we numerically show that the flux depends continuously on the control parameters and that the associated diffusion coefficient of the reservoir particles also exhibits critical behavior in Sec. 5.4.1. In Sec. 5.4.2 and 5.4.3, we analytically describe the behavior of the particle flux and derive the critical exponents of the associated diffusion coefficient for the pitchfork bifurcation into coexistence. In Sec. 5.5, we transform into adopted coordinates and derive scaling forms for the particle flux and the diffusion coefficient. We conclude in Sec. 5.6.

5.2 SCHLÖGL MODEL

The reaction scheme which was first proposed by Schlögl [108, 116] consists of an autocatalytic reaction and a linear one,



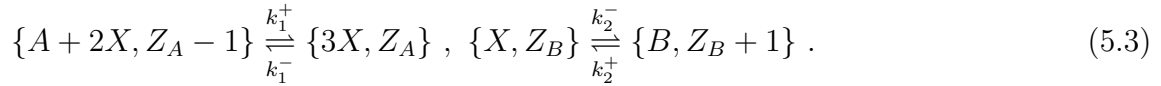
for species X in contact with an external reservoir of molecules A and B with fixed concentrations c_A , respectively c_B . The reactions take place in a volume Ω . Due to a difference in the chemical potential between A and B the system is out of equilibrium,

i.e., $\Delta\mu \equiv \mu_A - \mu_B > 0$. Considering the cycle in which one A is transformed to a B , the thermodynamic driving satisfies the local detailed balance condition [12]

$$e^{\beta\Delta\mu} = \frac{c_A k_1^+ k_2^-}{c_B k_1^- k_2^+}, \quad (5.2)$$

with inverse temperature β and molecular reaction rates k_i^\pm . We set $\beta = 1$ throughout the chapter, thus, measuring all energies in units of the thermal energy and entropy in the units of the Boltzmann constant.

We examine the number of produced respectively consumed molecules A and B in the reservoir by introducing random variables $Z_A(t)$ and $Z_B(t)$. Whenever a molecule A is produced, $Z_A(t)$ is decreased by one, whereas when a molecule B is produced, $Z_B(t)$ is increased by one leading to the following augmented reaction scheme



The mean flux entering and leaving the particle reservoirs is given by

$$J_B \equiv \lim_{t \rightarrow \infty} \frac{\langle Z_B(t) \rangle}{\Omega t} = J_A, \quad (5.4)$$

with fluctuations quantified by the diffusion coefficient

$$D_B \equiv \lim_{t \rightarrow \infty} \frac{\text{Var}[Z_B(t)]}{2\Omega t} = D_A, \quad (5.5)$$

where $\text{Var}[z] \equiv \langle z^2 \rangle - \langle z \rangle^2$. The equality between D_A and D_B has been proven in Ref. [128] using large deviation theory. Since the particle fluxes and their fluctuations are equal in both reservoirs, we consider in the rest of the chapter only particles of species B . All results are equally true for the particle flux of species A . Thus, we drop the index B for the mean values in the following.

The entropy production

$$\Delta S(t) = Z_A(t)\mu_A - Z_B(t)\mu_B \quad (5.6)$$

is proportional to the particle flux, thus, it exhibits the same fluctuations. The mean entropy production rate in the steady state is determined as

$$\sigma \equiv \lim_{t \rightarrow \infty} \frac{1}{t} \langle \Delta S(t) \rangle = \Omega J \Delta\mu. \quad (5.7)$$

In the thermodynamic limit, i.e., for $\Omega \rightarrow \infty$, the reaction scheme, Eq. (5.1), is described by the deterministic rate equation

$$\partial_t \hat{x}(t) = -k_1^- \hat{x}(t)^3 + c_A k_1^+ \hat{x}(t)^2 - k_2^- \hat{x}(t) + c_B k_2^+, \quad (5.8)$$

where $\hat{x}(t)$ denotes the mean concentration of species X at time t . We set $k_i^\pm = 1$ throughout the chapter which effectively corresponds to a rescaling of the parameters as

$$\begin{aligned} \tilde{c}_A &\equiv c_A k_1^+ / (k_1^- k_2^-)^{\frac{1}{2}}, & \tilde{c}_B &\equiv c_B (k_1^-)^{\frac{1}{2}} k_2^+ / (k_2^-)^{3/2}, \\ \tilde{\Omega} &\equiv \Omega (k_2^-)^{\frac{1}{2}} / (k_1^-)^{\frac{1}{2}}, & \tilde{t} &\equiv t k_2^- . \end{aligned} \quad (5.9)$$

Thus, the rate equation (5.8) depends only on the rescaled concentrations \tilde{c}_A and \tilde{c}_B . We drop the tilde in the following.

Depending on the choice of concentrations, Eq. (5.8) shows a different number of steady-states, see Fig. 5.1. The system exhibits a monostable phase (M) with a unique, stable fixed point of the dynamics, Eq. (5.8). The second phase is the cusp-like region with two stable fixed points and an unstable one in between (B). See Appendix C.1 for a derivation of the phase boundaries. Within the bistable region, there is a line denoted as coexistence line (C) along which the two stable fixed points correspond to the global minimum of the dynamics. Away from this line there exists only one global minimum. At the end of the cusp-like region where the coexistence line ends, there is a critical point with coordinates

$$c_A^{\text{crit}} \equiv \sqrt{3} \quad \text{and} \quad c_B^{\text{crit}} \equiv \sqrt{3}/9 . \quad (5.10)$$

From a thermodynamic perspective, there occur different phase transitions depending on the path chosen within the $c_A - c_B$ -plane. Crossing the coexistence line, the system undergoes a first order phase transition. While this transition has been the topic of several studies [116, 128, 146], we here consider two pathways through the critical point, i.e., the continuous phase transition. The first path corresponds to a constant thermodynamic driving

$$\Delta\mu_{\text{crit}} \equiv \ln 9 , \quad (5.11)$$

to which we refer as the critical line.

As second path, we consider the line which enters the cusp-like region tangential to its boundary and goes through the critical point, see the blue line in Fig. 5.1. Along that line, the system undergoes a pitchfork bifurcation.

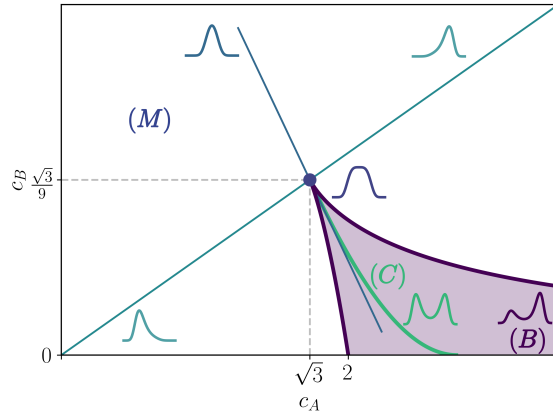


Figure 5.1: Phase diagram for the Schlögl model, Eq. (5.1). The monostable regime is denoted as (M) . The colored area is the bistable regime, (B) . (C) labels the coexistence line. Where the phase boundaries of the bistable region meet, the system exhibits a critical point (blue dot). The green line through the origin and this point is denoted critical line. The blue line is the tangential line into the coexistence area. For the specific areas, the typical shape of the steady-state probability distribution $p^s(x)$ is sketched.

5.3 ALONG THE CRITICAL LINE

We consider the line in the $c_A - c_B$ -plane parameterized as

$$c_B(c_A) \equiv c_A/9, \quad (5.12)$$

along which the concentration c_A and system-size Ω remain as control parameters.

5.3.1 Numerical data

Using Gillespie's direct method [35], we integrate the reaction scheme Eq. (5.1) numerically for various values of the control parameters. We determine $Z_B(t)$ according to Eq. (5.3) and calculate the mean flux J and diffusion coefficient D in the steady-state through Eq. (5.4), respectively (5.5). The results are shown in Fig. 5.2 and 5.3.

At the critical point, the mean flux J has a vertical tangential, i.e., a diverging first derivative with respect to the control parameter c_A , see Fig. 5.2b. Small deviations of the numerical derivative from the theoretical line are due to the non-uniform step-size while performing the numerical derivative. Shifting the c_A -axis in Fig. 5.2c, we extract a

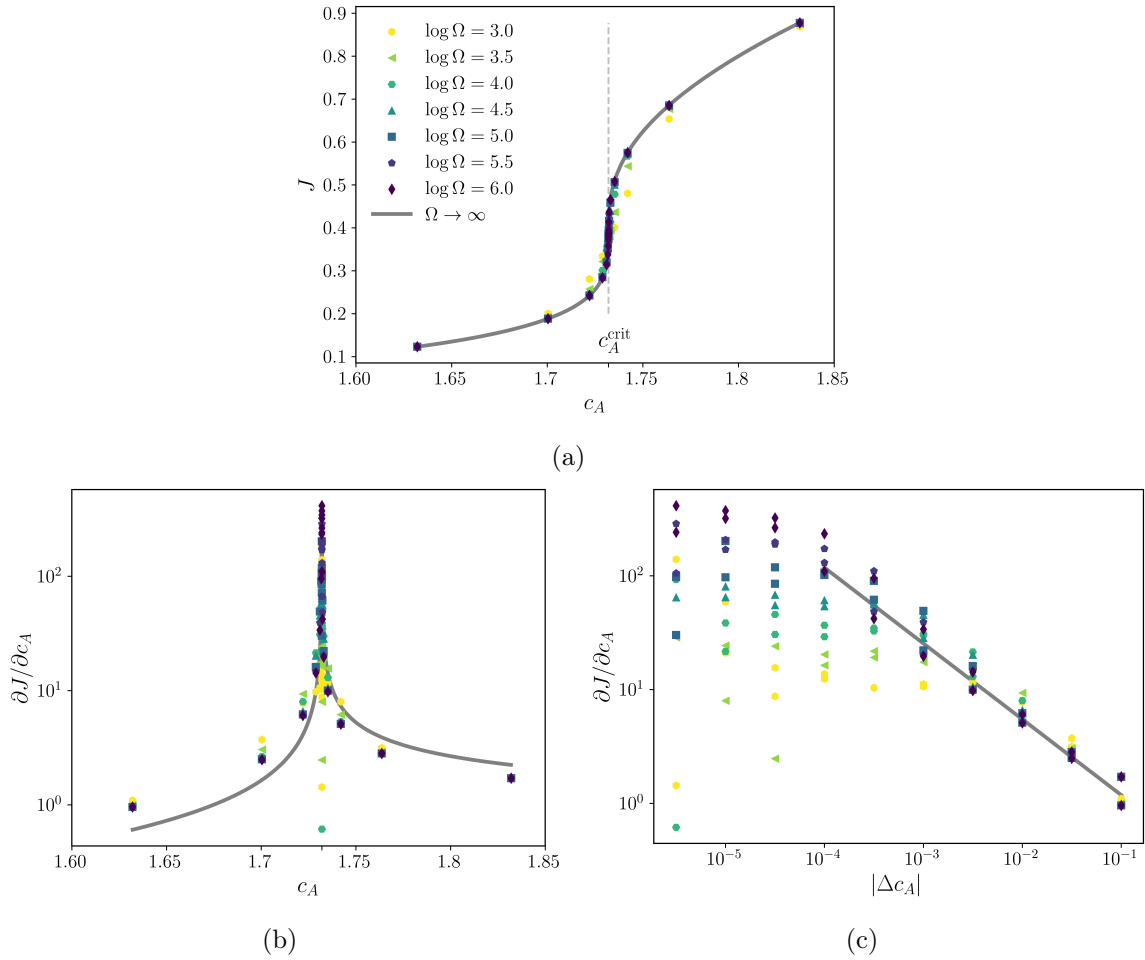


Figure 5.2: Mean flux J of the Schlögl model along the critical line. (a) J as function of the control parameter c_A for various system sizes Ω . (b) Numerical derivative of J with respect to the control parameter c_A . (c) Derivative of J as function of Δc_A . The concentration c_B is determined according to the local detailed balance condition, Eq. (5.2). A solid line represents the analytical prediction, Eq. (5.25), respectively Eq. (5.26).

power-law for the divergence in $\Delta c_A \equiv c_A - c_A^{\text{crit}}$ independent on the reaction volume Ω , i.e.,

$$\frac{\partial J}{\partial c_A} \propto |\Delta c_A|^{-\chi}, \quad \chi = 0.65 \pm 0.05. \quad (5.13)$$

We attribute the scattering of the derivative for $|\Delta c_A| \ll 1$ in Fig. 5.2c to the noisy numerical derivative on the logarithmic scale.

The diffusion coefficient D displays a pronounced peak around the critical value, see Fig. 5.3a. The maximum depends on the reaction volume Ω . Off the critical point, i.e., for

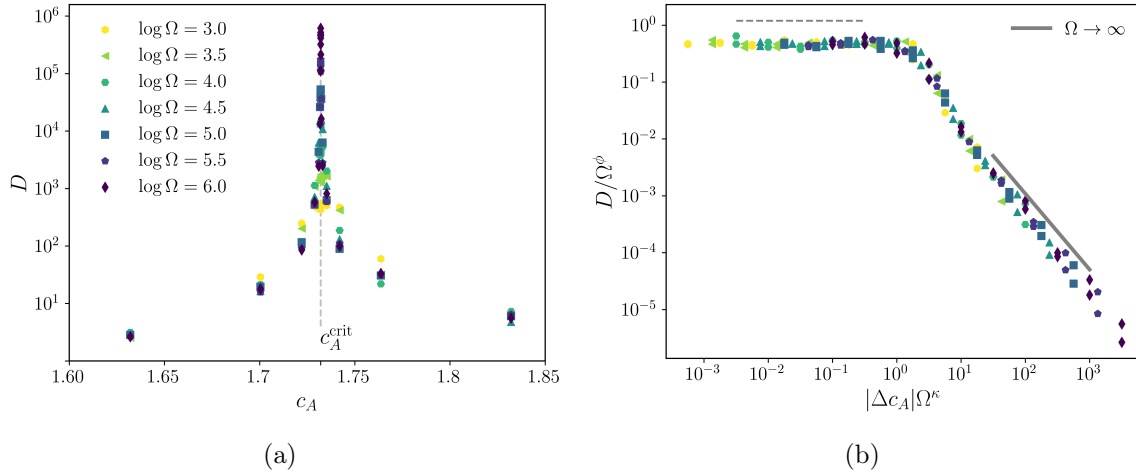


Figure 5.3: Diffusion coefficient D of the Schlögl model along the critical line. (a) D as function of the control parameter c_A for various system sizes Ω . (b) Scaling of D according to $D(\Delta c_A, \Omega) = \Omega^\phi \mathcal{D}(|\Delta c_A| \Omega^\kappa)$ with $c_A^{\text{crit}} = \sqrt{3}$, $\kappa = 0.75$ and $\phi = 1.00$. The concentration c_B is determined according to the local detailed balance condition, Eq. (5.2). The solid line represents the analytical prediction, Eq. (5.63).

$\Delta c_A \neq 0$, the value of D is independent of Ω . Furthermore, the data obey a scaling relation of the form

$$D = D(\Delta c_A, \Omega) = \Omega^\phi \mathcal{D}(|\Delta c_A| \Omega^\kappa) \quad (5.14)$$

as the collapse onto a master curve shows, see Fig. 5.3b. We determine the exponents as

$$\phi = 1.0 \pm 0.1 \quad \text{and} \quad \kappa = 0.75 \pm 0.05, \quad (5.15)$$

which results in a scaling function

$$\mathcal{D}(x) \propto \begin{cases} 1, & |x| \ll 1 \\ x^\varepsilon, & |x| \gg 1 \end{cases} \quad (5.16)$$

with

$$\varepsilon = -\phi/\kappa = -1.3 \pm 0.2. \quad (5.17)$$

The plateau for small values of $|\Delta c_A| \Omega^\kappa$ indicates a scaling of the critical value as $D^{\text{max}} \propto \Omega^\phi$ with ϕ given in Eq. (5.15). The power-law behavior with $-\phi/\kappa$ represents a scaling off the critical point with $D \propto \Omega^0$ consistent with the raw data, see Fig. 5.3a.

In the next two sections, we approximate the reaction scheme (5.3) through the rate equation and as a diffusion process to determine these exponents analytically.

5.3.2 Rate equation and mean flux

In the limit $\Omega \rightarrow \infty$, the mean concentration $\hat{x}(t)$ obeys the reaction rate equation

$$\partial_t \hat{x}(t) = -[\hat{x}(t) - 1/\sqrt{3}]^3 + \Delta c_A [\hat{x}(t)^2 + 1/9] . \quad (5.18)$$

The reaction scheme (5.1) has a unique fixed point x^* , thus, the rate equation approximates the system well in the limit of large reaction volume. Above the critical point, i.e., for $\Delta c_A > 0$, the fixed point is

$$\begin{aligned} x^*(\Delta c_A) = \Delta c_A/3 + [\Delta c_A^2 (\Delta c_A + 2\sqrt{3})]^{1/3}/3 \\ + [\Delta c_A (\Delta c_A^2 + 4\sqrt{3}\Delta c_A + 12)]^{1/3}/3 + 1/\sqrt{3} . \end{aligned} \quad (5.19)$$

For $-\sqrt{3} \leq \Delta c_A < 0$, we get

$$\begin{aligned} x^*(\Delta c_A) = \Delta c_A/3 + [-\Delta c_A (\Delta c_A + 2\sqrt{3})^2]^{2/3}/3 (\Delta c_A + 2\sqrt{3}) \\ - [-\Delta c_A (\Delta c_A + 2\sqrt{3})^2]^{1/3}/3 + 1/\sqrt{3} . \end{aligned} \quad (5.20)$$

For $|\Delta c_A| \ll 1$, we find

$$x^*(\Delta c_A) = 1/\sqrt{3} + \text{sign}(\Delta c_A) 2^{2/3} |\Delta c_A|^{1/3} / 3^{2/3} + 2^{1/3} |\Delta c_A|^{2/3} / 3^{5/6} + \mathcal{O}(|\Delta c_A|) . \quad (5.21)$$

Thus, for $\Delta c_A \rightarrow 0$, we get a continuous transition from one solution to the other, i.e.,

$$\lim_{\Delta c_A \downarrow 0} x^*(\Delta c_A) = \lim_{\Delta c_A \uparrow 0} x^*(\Delta c_A) = 1/\sqrt{3} . \quad (5.22)$$

The rate equation for the variable Z_B reads

$$\partial_t \hat{z}_B(t) = \hat{x}(t) - c_A/9 , \quad (5.23)$$

where $\hat{z}_B(t) \equiv \langle Z_B(t) \rangle / \Omega$ denotes the mean density of produced particles B up to time t . In the stationary state, we find

$$\hat{z}_B(t) = [x^*(\Delta c_A) - (\sqrt{3} + \Delta c_A)/9]t , \quad (5.24)$$

leading to a mean flux

$$J = J(\Delta c_A) \equiv x^*(\Delta c_A) - (\sqrt{3} + \Delta c_A)/9 \quad (5.25)$$

as a function of the control parameter. This expression together with Eqs. (5.19-5.20) gives the theoretical prediction of the mean flux along the critical line shown in Fig. 5.2. For the derivative of J we obtain the scaling law

$$\frac{\partial J}{\partial c_A}(\Delta c_A) = \frac{2^{2/3}}{3^{5/3}} |\Delta c_A|^{-2/3} \quad (5.26)$$

as displayed in Fig. 5.2c. Thus, we obtain the scaling exponent

$$\chi = 2/3 , \quad (5.27)$$

in agreement with the numerically derived one, Eq. (5.13).

5.3.3 Diffusion approximation and diffusion coefficient

5.3.3.1 Set-up

We approximate the augmented reaction scheme, Eq. (5.3), by Gillespie's chemical Langevin equation [40, 148] and van Kampen's system size expansion [37, 148]. The chemical Langevin equation for the number of molecules of species B reads

$$\partial_t Z_B(t) = W_2^+[n(t)] - W_2^-[n(t)] + \sqrt{W_2^+[n(t)] + W_2^-[n(t)]} \xi_B(t) , \quad (5.28)$$

with Gaussian white noise $\xi_B(t)$, i.e., $\langle \xi_B(t) \rangle = 0$ and $\langle \xi_B(t) \xi_B(t') \rangle = \delta(t-t')$. The $W_i^\pm[n(t)]$ are the propensity functions defined through Eq. (5.3) with the respective reaction direction, i.e.,

$$\begin{aligned} W_1^+(n) &\equiv c_A n(n-1)/\Omega , & W_1^-(n) &\equiv n(n-1)(n-2)/\Omega^2 , \\ W_2^+(n) &\equiv \Omega c_B & \text{and } W_2^-(n) &\equiv n , \end{aligned} \quad (5.29)$$

where we set $c_B = c_A/9$. Here, n denotes the number of molecules of species X .

In analogy to van Kampen's system size expansion [37, 148], we make the ansatz

$$\begin{pmatrix} n(t) \\ Z_B(t) \end{pmatrix} \equiv \Omega \begin{pmatrix} \hat{x}(t) \\ \hat{z}_B(t) \end{pmatrix} + \Omega^\mu \begin{pmatrix} x(t) \\ z_B(t) \end{pmatrix} \quad (5.30)$$

with a scaling exponent $0 < \mu < 1$. The idea of this approximation is to calculate the fluctuations of an observable around a macroscopic trajectory. Plugging the ansatz, Eq. (5.30), into the chemical Langevin equation (5.28) and dividing by Ω , we obtain after a Taylor expansion for $\Omega \gg 1$ in lowest order the mean field equation, i.e., the $\mathcal{O}(1)$ for $\Omega \rightarrow \infty$ leads to the rate equation (5.23).

The higher order terms can be rearranged as

$$\begin{aligned} \partial_t z_B(t) &= \{W_2^+ ' [\hat{x}(t)] - W_2^- ' [\hat{x}(t)]\} x(t) \\ &\quad + \Omega^{1/2-\mu} \sqrt{W_2^+ [\hat{x}(t)] + W_2^- [\hat{x}(t)]} + \mathcal{O}(\Omega^{\mu-1}) \xi_B(t) , \end{aligned} \quad (5.31)$$

where a prime denotes a derivative with respect to the argument. In order to obtain an equation for the fluctuations which is independent on Ω , we set $\mu = 1/2$. This exponent is consistent with van Kampen's linear noise approximation [37, 148]. Thus, with the dynamical equation above and the definition of D , Eq. (5.5), we find

$$\begin{aligned} D &= \frac{1}{2} \lim_{t \rightarrow \infty} \frac{1}{t} \int_0^t d\tau \int_0^t ds \{W_2^+ ' [\hat{x}(\tau)] - W_2^- ' [\hat{x}(\tau)]\} \{W_2^+ ' [\hat{x}(s)] - W_2^- ' [\hat{x}(s)]\} \langle x(\tau) x(s) \rangle \\ &\quad + \frac{1}{2} \lim_{t \rightarrow \infty} \frac{1}{t} \int_0^t ds \{W_2^+ [\hat{x}(s)] + W_2^- [\hat{x}(s)]\} \\ &\quad - \lim_{t \rightarrow \infty} \frac{1}{t} \int_0^t d\tau \int_0^t ds \{W_2^+ ' [\hat{x}(\tau)] - W_2^- ' [\hat{x}(\tau)]\} \sqrt{\frac{1}{2} \{W_2^+ [\hat{x}(s)] + W_2^- [\hat{x}(s)]\}} \langle x(\tau) \xi_B(s) \rangle . \end{aligned} \quad (5.32)$$

In order to obtain the diffusion coefficient D , we need to examine the dynamics of $\hat{x}(t)$ and $x(t)$, which is independent on $Z_B(t)$. Let $p(n, t)$ be the probability to have n molecules of species X at time t . Using the ansatz, Eq. (5.30), and the transformation rule for probability densities, we find for the density of the fluctuations

$$\pi(x, t) = \Omega^{1/2} p(\Omega \hat{x} + \Omega^{1/2} x, t) . \quad (5.33)$$

Following van Kampen's system-size expansion, we obtain the corresponding Fokker-Planck equation

$$\begin{aligned} \partial_t \pi(x, t) &= \frac{d}{dt} \Omega^{1/2} p[\Omega \hat{x}(t) + \Omega^{1/2} x, t] \\ &= \Omega^{1/2} \partial_x \left[\{ \partial_t \hat{x}(t) - \alpha_1[\hat{x}(t)] \} \pi(x, t) \right] - \partial_x \left[\alpha'_1[\hat{x}(t)] x \pi(x, t) + \mathcal{O}(\Omega^{-1/2}) \right] \\ &\quad + \frac{1}{2} \partial_x^2 \left[\alpha_2[\hat{x}(t)] \pi(x, t) + \mathcal{O}(\Omega^{-1/2}) \right] + \mathcal{O}(\Omega^{-1/2}) . \end{aligned} \quad (5.34)$$

The jump-moments are defined through

$$\lim_{\Omega \rightarrow \infty} \Omega \alpha_1(n/\Omega) \equiv \int dn' (n - n') W(n|n') \quad (5.35)$$

and

$$\lim_{\Omega \rightarrow \infty} \Omega \alpha_2(n/\Omega) \equiv \int dn' (n - n')^2 W(n|n') \quad (5.36)$$

The jump-rates $W(n|n')$ contain the propensity functions and are defined through Eq. (5.1) as

$$W(n|n') \equiv \delta_{n', n-1} [W_1^+(n) + W_2^+(n)] + \delta_{n', n+1} [W_1^-(n) + W_2^-(n)] . \quad (5.37)$$

$\delta_{i,j}$ denotes the Kronecker-delta.

The condition for the curly bracket in the second line of Eq. (5.34) to vanish determines the macroscopic law for the X species, i.e., the rate equation (5.18). As discussed above, this equation has a stable fixed point x^* , i.e., $\hat{x}(t) \rightarrow x^*$ for $t \rightarrow \infty$. Thus, the motion of $z_B(t)$ is in the long time limit equivalent to the following Langevin equation

$$\partial_t z_B(t) = (W_2^+ '[x^*] - W_2^- '[x^*]) x(t) + \sqrt{W_2^+[x^*] + W_2^-[x^*]} \xi_B(t) . \quad (5.38)$$

The diffusion coefficient, Eq. (5.32), reduces to

$$\begin{aligned} D &= (W_2^+ '[x^*] - W_2^- '[x^*])^2 \int_0^\infty dt \langle x(t)x(0) \rangle + \frac{1}{2} (W_2^+[x^*] + W_2^-[x^*]) \\ &\quad - \sqrt{\frac{1}{2} (W_2^+[x^*] + W_2^-[x^*])} (W_2^+ '[x^*] - W_2^- '[x^*]) \lim_{t \rightarrow \infty} \frac{1}{t} \int_0^t d\tau \int_0^\tau ds \langle x(\tau) \xi_B(s) \rangle . \end{aligned} \quad (5.39)$$

In the next paragraphs, we will examine the fluctuations $x(t)$ around the fixed point x^* both for $c_A = c_A^{\text{crit}}$, and for $c_A \neq c_A^{\text{crit}}$ in order to obtain an expression for the integral over the correlation function $\langle x(t)x(0) \rangle$ and $\langle x(\tau)\xi_B(s) \rangle$.

5.3.3.2 At the critical point

For $c_A = c_A^{\text{crit}} = \sqrt{3}$, the mean-field equation, Eq. (5.18), reduces to

$$\partial_t \hat{x}(t) = \alpha_1[\hat{x}(t)] = -[\hat{x}(t) - 1/\sqrt{3}]^3 . \quad (5.40)$$

We assume that the system has already relaxed into the stationary state of reaction scheme (5.1). This state corresponds to the fixed point $x^* \equiv 1/\sqrt{3}$. Thus, we can replace $\hat{x}(t) \rightarrow x^*$. The first and second derivative of the first jump moment vanishes at the critical point, compare Eq. (5.40). Following the strategy outlined above, we obtain for the probability density of the fluctuations

$$\partial_t \pi(x, t) = |\alpha_1'''(x^*)| \partial_x [x^3 \pi(x, t)] / 6\Omega + \alpha_2(x^*) \partial_x^2 \pi(x, t) / 2. \quad (5.41)$$

Thus, $x(t)$ corresponds to diffusive motion in a quartic potential

$$V(x) \equiv |\alpha_1'''(x^*)| x^4 / 24\Omega \quad (5.42)$$

with diffusion constant

$$D \equiv \alpha_2(x^*) / 2 . \quad (5.43)$$

This system is equivalently described by a self-adjoint Schrödinger-like operator [39]

$$L_x = D \partial_x^2 - V_S(x) \quad (5.44)$$

with

$$V_S(x) \equiv [V'(x)]^2 / 4D - V''(x) / 2 = |\alpha_1'''(x^*)|^2 x^6 / 72\alpha_2(x^*)\Omega^2 - |\alpha_1'''(x^*)| x^2 / 4\Omega . \quad (5.45)$$

The eigenvalues λ_n of this Schrödinger operator are real and nonnegative, i.e.,

$$L_x \psi_n(x) = -\lambda_n \psi_n(x) , \lambda_n \geq 0. \quad (5.46)$$

Moreover, they are equal to the eigenvalues of the Fokker-Planck operator defined through Eq. (5.41). The corresponding eigenfunctions $\psi_n(x)$ determine the propagator of Eq. (5.41) as

$$\pi(x, t|x', t') = e^{[V(x')-V(x)]/2D} \sum_n \psi_n(x)\psi_n(x')e^{-\lambda_n(t-t')} . \quad (5.47)$$

This results in

$$\int_0^\infty dt \langle x(t)x(0) \rangle = \sum_n C_n/\lambda_n , \quad (5.48)$$

with

$$C_n \equiv \int dx \int dx_0 x x_0 e^{[V(x_0)-V(x)]/2D} \psi_n(x)\psi_n(x_0)\pi^s(x_0) , \quad (5.49)$$

where $\pi^s(x_0)$ denotes the stationary solution of Eq. (5.41). The Ω -scaling of the correlation function, Eq. (5.48), is thus determined by the eigenvalues λ_n and C_n . We find their dependencies on Ω in two steps. First, we examine the operator L_x . We rescale the x variable according to

$$\tilde{x} \equiv \Omega^{-1/4}x , \quad (5.50)$$

where a tilde means that the variable does not depend on the reaction volume Ω . The Schrödinger operator transforms in this rescaled variable to

$$L_x = \tilde{L}_{\tilde{x}}/\sqrt{\Omega} . \quad (5.51)$$

The operator $\tilde{L}_{\tilde{x}}$ is self-adjoint and independent of the system-size Ω . Thus, its eigenvalues $\tilde{\lambda}_n$ and eigenfunctions $\tilde{\Psi}_n(\tilde{x})$ are also independent of Ω . These eigenvalues are connected to the ones of the Fokker-Planck operator as

$$\lambda_n = \tilde{\lambda}_n/\sqrt{\Omega} . \quad (5.52)$$

Furthermore, from the completeness relation, i.e.,

$$\delta_{n,m} = \int d\tilde{x} \int d\tilde{x}_0 \tilde{\Psi}_n(\tilde{x})\tilde{\Psi}_m(\tilde{x}_0) , \quad (5.53)$$

we obtain the eigenfunctions of the original Schrödinger operator, Eq. (5.44), as

$$\psi_n(x) \equiv \Omega^{-1/8} \tilde{\Psi}_n(\Omega^{-1/4}x) . \quad (5.54)$$

In the second step, we use these eigenfunctions to extract the scaling behavior of C_n , Eq. (5.49). Rescaling the integration variable according to Eq. (5.50), we obtain

$$C_n = \sqrt{\Omega} \int d\tilde{x} \int d\tilde{x}_0 \tilde{x}\tilde{x}_0 e^{[\tilde{V}(\tilde{x}_0) - \tilde{V}(\tilde{x})]/2D} \tilde{\Psi}_n(\tilde{x}) \tilde{\Psi}_n(\tilde{x}_0) \tilde{P}(\tilde{x}_0) \equiv \sqrt{\Omega} \tilde{C}_n . \quad (5.55)$$

With the scaling behavior of the eigenvalues, Eq. (5.52), and the constant C_n , Eq. (5.55), we obtain

$$(W_2^+ '[x^*] - W_2^- '[x^*])^2 \int_0^\infty dt \langle x(t)x(0) \rangle = \Omega (W_2^+ '[x^*] - W_2^- '[x^*])^2 \sum_n \tilde{C}_n / \tilde{\lambda}_n . \quad (5.56)$$

Thus, we have derived that the first term of Eq. (5.39) diverges linearly with the system-size Ω at the critical point.

We proceed by deriving a bound on the integral over $\langle x(\tau)\xi_B(s) \rangle$. We consider

$$\begin{aligned} 0 \leq \langle \{ \int_0^t d\tau [c_x x(\tau) \pm c_\xi \xi_B(\tau)] \}^2 \rangle &= c_x^2 \int_0^t d\tau \int_0^t ds \langle x(\tau)x(s) \rangle + c_\xi^2 \int_0^t d\tau \int_0^t ds \langle \xi_B(\tau)\xi_B(s) \rangle \\ &\quad \pm 2c_x c_\xi \int_0^t d\tau \int_0^t ds \langle x(\tau)\xi_B(s) \rangle , \end{aligned} \quad (5.57)$$

with arbitrary constants c_x and c_ξ . This leads to

$$\pm c_x c_\xi \int_0^t d\tau \int_0^t ds \langle x(\tau)\xi_B(s) \rangle \leq \frac{1}{2} \{ c_x^2 \int_0^t d\tau \int_0^t ds \langle x(\tau)x(s) \rangle + c_\xi^2 \int_0^t d\tau \int_0^t ds \langle \xi_B(\tau)\xi_B(s) \rangle \} . \quad (5.58)$$

Dividing both sides by t and taking the limit $t \rightarrow \infty$, we obtain

$$\pm c_x c_\xi \lim_{t \rightarrow \infty} \frac{1}{t} \int_0^t d\tau \int_0^t ds \langle x(\tau)\xi_B(s) \rangle \leq \frac{1}{2} \{ c_x^2 \int_0^\infty d\tau \langle x(\tau)x(0) \rangle + c_\xi^2 \} . \quad (5.59)$$

Using Eq. (5.56), we find that the integral over the correlation function $\langle x(\tau)\xi_B(s) \rangle$ grows at most linearly in the system-size Ω . Taking Eq. (5.56) and (5.59) into account, we, thus, have derived the divergence

$$D^{\text{crit}} \propto \Omega \quad (5.60)$$

for $\Omega \gg 1$.

We rationalize this result through the effect of critical slowing down [37, 38]. At the critical point, the inverse of the eigenvalues, Eq. (5.52), and, hence, the time-scales for relaxation of fluctuations grow with the system-size Ω which drives the divergence of the diffusion coefficient D .

We now determine the scaling of the diffusion coefficient as the critical point is approached.

5.3.3.3 Off the critical point

Moving away from the critical point, the macroscopic equation for the mean becomes

$$\partial_t \hat{x}(t) = \alpha_1[\hat{x}(t)] = -[\hat{x}(t) - 1/\sqrt{3}]^3 + \Delta c_A[\hat{x}(t)^2 + 1/9] . \quad (5.61)$$

This differential equation has a unique stable fixed point $x^* = x^*(\Delta c_A)$ with $\alpha_1(x^*) = 0$ and $\alpha_1'(x^*) < 0$, see Eq. (5.19) and (5.20). Thus, the linear noise approximation leads to the following Langevin equations

$$\begin{aligned} \partial_t x(t) &= -|\alpha_1'(x^*)|x(t) + \sqrt{c_A x^{*2} + x^{*3}}\xi_A(t) + \sqrt{c_A/9 + x^*}\xi_B(t) , \\ \partial_t z_B(t) &= -x(t) + \sqrt{c_A/9 + x^*}\xi_B(t) . \end{aligned} \quad (5.62)$$

For such a linear system, all integrals can be solved analytically, see Appendix C.2. We thus obtain the diffusion coefficient

$$D = 2^{1/3}|\Delta c_A|^{-4/3}/3^{5/6} = \mathcal{O}(1), \quad \text{for } \Omega \rightarrow \infty , \quad (5.63)$$

Comparing with the scaling ansatz, Eq. (5.16), we obtain $\varepsilon = -4/3$ and $\phi + \kappa\varepsilon = 0$. Furthermore, Eq. (5.60) yields $\phi = 1$. Thus, we conclude

$$\phi = 1, \quad \kappa = 3/4, \quad \text{and } \varepsilon = -4/3 , \quad (5.64)$$

which analytically explains the numerical findings shown in Fig. 5.3.

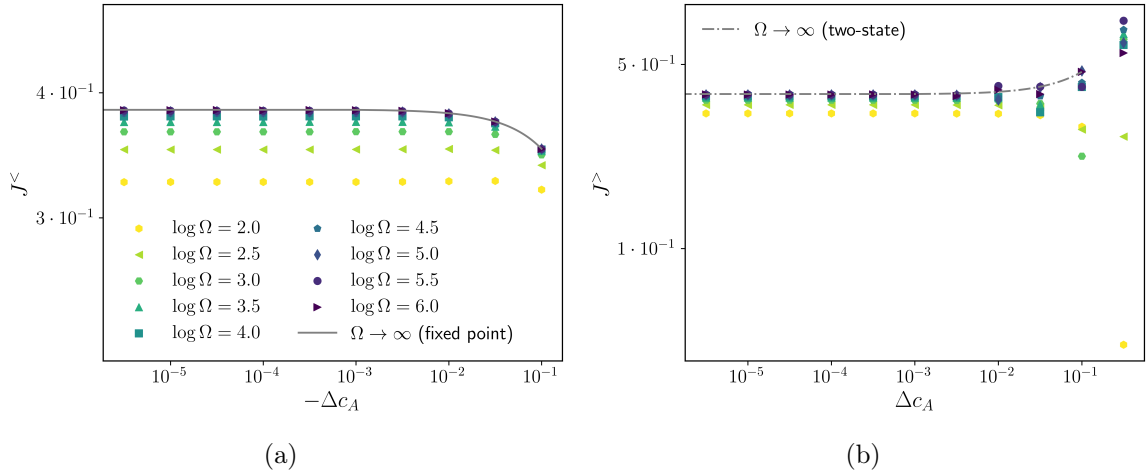


Figure 5.4: Mean flux J of the Schlögl model undergoing a pitchfork bifurcation for various system sizes Ω as function of the control parameter c_A (a) below and (b) above the critical point. The concentration c_B is determined according to Eq. (5.65). The solid line represents Eq. (5.75) and the dashed dotted line Eq. (5.89).

5.4 ALONG THE PITCHFORK BIFURCATION

We turn to the pathway along the pitchfork bifurcation, i.e., the line which enters the cusp-like region tangential to its boundary, see the blue line in Fig. 5.1. It is parameterized as

$$c_B(c_A) \equiv \sqrt{3}/9 - (c_A - \sqrt{3})/3 = \sqrt{3}/9 - \Delta c_A/3, \quad (5.65)$$

see Appendix C.1 for a derivation of the slope. Thus, Δc_A and Ω remain as free parameters of the reaction scheme Eq. (5.3).

5.4.1 Numerical data

We numerically integrate Eq. (5.3) using the stochastic sampling algorithm [35] while varying the control parameters. The particle flux J and diffusion coefficient D are determined according to Eqs. (5.4) and (5.5).

The diffusion coefficient increases with the concentration c_A showing two distinct regimes, Fig. 5.5a. Below the critical point, D does not depend on the system size Ω , whereas it

develops a dependence on Ω in the vicinity of c_A^{crit} and above. Rescaling the data according to

$$D = D(\Delta c_A, \Omega) = \Omega^\phi \mathcal{D}(|\Delta c_A| \Omega^\kappa) \quad (5.66)$$

leads to the collapse of the data onto a master curve, see Fig. 5.5b. We determine the exponents as

$$\phi = 1.0 \pm 0.1 \quad \text{and} \quad \kappa = 0.50 \pm 0.05 . \quad (5.67)$$

This results in a scaling function

$$\mathcal{D}^<(x) \propto \begin{cases} 1, & x \ll 1 \\ x^\varepsilon, & x \gg 1 \end{cases} \quad (5.68)$$

with

$$\varepsilon = -\phi/\kappa = -2.0 \pm 0.2 , \quad (5.69)$$

below the critical point. The plateau for small values of $|\Delta c_A| \Omega^\kappa$ indicates a scaling of the critical value as $D^{\text{max}} \propto \Omega^\phi$ with ϕ given in Eq. (5.67). The power-law behavior with $-\phi/\kappa$ below the critical point represents a scaling with $D \propto \Omega^0$ consistent with the raw data, see Fig. 5.5a.

In the supercritical regime, Fig. 5.5c, we find

$$\ln \mathcal{D}^>(x) \propto \begin{cases} 1, & x \ll 1 \\ x^{\tilde{\varepsilon}}, & x \gg 1 \end{cases} \quad (5.70)$$

with

$$\tilde{\varepsilon} = 1.5 \pm 0.5 . \quad (5.71)$$

We attribute the outliers above the critical point to the fact that we leave the coexistence line in this regime, see Fig. 5.1. We only consider a tangential to the coexistence line and not the fully, curved line. Furthermore, the linear dependence between $(|\Delta c_A \Omega^\kappa|)^{\tilde{\varepsilon}}$

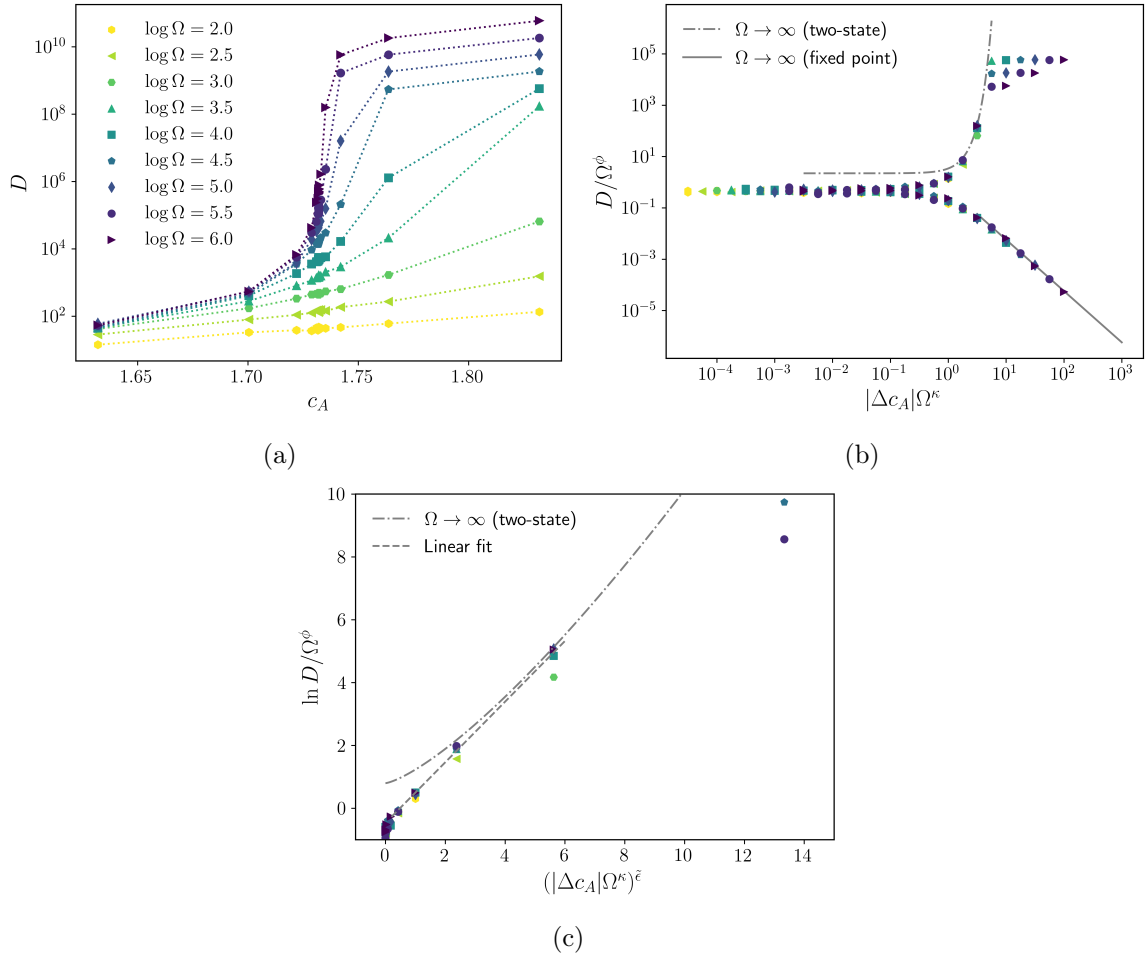


Figure 5.5: Diffusion coefficient D of the Schlögl model at the pitchfork bifurcation. (a) D as function of the control parameter c_A for various system sizes Ω . (b) Scaling of D according to $D(\Delta c_A, \Omega) = \Omega^\phi \mathcal{D}(|\Delta c_A| \Omega^\kappa)$ with $c_A^{\text{crit}} = \sqrt{3}$, $\kappa = 0.5$ and $\phi = 1.00$. (c) Logarithm of the re-scaled D above the critical point as function of $(|\Delta c_A \Omega^\kappa|)^{\tilde{\epsilon}}$ with $\tilde{\epsilon} = 1.5$. The concentration c_B is chosen as function of c_A , Eq. (5.65). The solid line represents the analytical result Eq. (5.77) and the dashed-dotted one Eq. (5.91).

and $\ln D/\Omega^\phi$ observed in Fig. 5.5c leads to our numerically obtained scaling function, Eq. (5.70).

In the next section, in order to obtain the scaling exponents analytically, we approximate the reaction scheme (5.3) below the critical point as in Sec. 5.3.2 and 5.3.3. Above c_A^{crit} , we can describe it as a two-state system.

5.4.2 *In the monostable regime and at the critical point*

The rate equation reads

$$\partial_t \hat{x}(t) = -\hat{x}(t)^3 + \hat{x}(t)^2(\sqrt{3} + \Delta c_A) - \hat{x}(t) + \sqrt{3}/9 - \Delta c_A/3 . \quad (5.72)$$

For $\Delta c_A < 0$, the only stable fixed point of this equation is

$$x^* \equiv x_0 \equiv 1/\sqrt{3} . \quad (5.73)$$

Thus, we find for the mean growth rate of particles B

$$\partial_t \hat{z}_B(t) = x_0 - (\sqrt{3}/9 - \Delta c_A/3) = 2\sqrt{3}/9 + \Delta c_A/3 . \quad (5.74)$$

The particle flux is hence given by

$$J^< = J^<(\Delta c_A) = 2\sqrt{3}/9 + \Delta c_A/3 . \quad (5.75)$$

In order to obtain the diffusion coefficient D , we employ the same technique as introduced in Sec. 5.3.3. Below the critical point, the chemical Langevin equation (5.62) becomes

$$\begin{aligned} \partial_t x(t) &= -2\sqrt{3}|\Delta c_A|x(t)/3 + \sqrt{4\sqrt{3}/9 + \Delta c_A/3}\xi_A(t) + \sqrt{4\sqrt{3}/9 - \Delta c_A/3}\xi_B(t) , \\ \partial_t z_B(t) &= -x(t) + \sqrt{4\sqrt{3}/9 - \Delta c_A/3}\xi_B(t) . \end{aligned} \quad (5.76)$$

Solving all integrals (see Appendix C.2), we obtain the diffusion coefficient in the monostable regime

$$D^< = 2\sqrt{3}|\Delta c_A|^{-2}/3 . \quad (5.77)$$

At the critical point, we have the same set-up as in Sec. 5.3.3. Thus, we obtain the divergence

$$D^{<, \text{crit}} \propto \Omega . \quad (5.78)$$

For the subcritical regime, we can summarize the scaling behavior of the diffusion coefficient D in the scaling form

$$D^< = \Omega^\phi \mathcal{D}^<(|\Delta c_A| \Omega^\kappa) \quad (5.79)$$

with

$$\phi = 1, \quad \text{and} \quad \kappa = 1/2 . \quad (5.80)$$

The scaling form is

$$\mathcal{D}^<(x) \propto \begin{cases} 1, & x \ll 1 \\ x^\varepsilon, & x \gg 1 \end{cases} \quad (5.81)$$

with exponent

$$\varepsilon = -\phi/\kappa = -2 . \quad (5.82)$$

Thus, approaching the critical point from below, we analytically find the same scaling exponents as obtained numerically.

5.4.3 Bistable regime and two-state approximation

We consider Eq. (5.65) for $\Delta c_A > 0$, i.e., in the bistable regime. Here, the steady state dynamics is given by two stable fixed points,

$$x_\pm(\Delta c_A) \equiv (2\sqrt{3} + 3\Delta c_A \pm [24\sqrt{3}\Delta c_A + 9\Delta c_A^2]^{1/2})/6 \approx 1/\sqrt{3} \pm \sqrt{2\Delta c_A}/3 , \quad (5.83)$$

that are separated by an unstable fixed point x_0 , Eq. (5.73). The system randomly jumps between these two steady states. In the following, we treat the system as a two-state system in order to obtain an estimate for the particle flux J and diffusion coefficient D [116, 128, 149].

In the limit of large system-sizes, $\Omega \gg 1$, the steady state solution of reaction scheme (5.1) is given by

$$p^s(x) = \mathcal{N} \exp[-\Omega\phi(x)] , \quad (5.84)$$

where we introduced the nonequilibrium potential

$$\phi(x) \equiv - \int_0^x du \ln \frac{c_A u^2 + c_B}{u^3 + u} . \quad (5.85)$$

The fixed points of Eq. (5.72) determine the extrema of this potential with a maximum at x_0 and minima at x_{\pm} .

The transition rates r_{\pm} from one minimum to the other are given by the potential barrier between the minima and their curvature as [116, 149]

$$r_{\pm} \equiv r_{x_{\pm} \rightarrow x_{\mp}} \equiv \frac{F(x_{\pm}) \sqrt{-\phi''(x_0) \phi''(x_{\pm})}}{2\pi\Omega} e^{-\Omega[\phi(x_0) - \phi(x_{\pm})]} , \quad (5.86)$$

where a prime denotes a derivative with respect to the argument. We have introduced $F(x) \equiv (\sqrt{3} + \Delta c_A)x^2 + \sqrt{3}/9 - \Delta c_A/3$ for brevity of notation. Furthermore, along the coexistence line, the minima are equivalent, i.e.,

$$\phi(x_+) = \phi(x_-) \quad \text{and} \quad \phi''(x_+) = \phi''(x_-) . \quad (5.87)$$

The probability p_{\pm} for the system to be in either of the minima is

$$p_{\pm} \equiv r_{\mp} / (r_+ + r_-) = 1/2 , \quad (5.88)$$

due to the symmetry of the problem.

Following Ref. [128], the particle flux is in leading order determined by

$$J^> \equiv p_- J^- + p_+ J^+ \approx 2/3\sqrt{3} + 5\Delta c_A/6 , \quad (5.89)$$

where J^{\pm} denotes the mean flux of species B caused through the respective minimum, i.e.,

$$J^{\pm} \equiv x_{\pm}(\Delta c_A) - c_B(\Delta c_A) . \quad (5.90)$$

The diffusion coefficient of the two-state model is given by

$$\begin{aligned} D^> &\equiv p_+ p_- (J^+ - J^-)^2 / (r_+ + r_-) + \mathcal{O}(\Omega) \\ &= \Omega \pi \exp(\sqrt{3}\Delta c_A^2 \Omega / 4) / \sqrt{2} + \mathcal{O}(\Omega) \equiv \Omega \mathcal{D}^> (|\Delta c_A| \Omega^{\frac{1}{2}}) . \end{aligned} \quad (5.91)$$

In the limit $\Delta c_A \rightarrow 0$, this expression leads to

$$D^{>,\text{crit}} \equiv D|_{\Delta c_A=0} = \mathcal{O}(\Omega) , \quad (5.92)$$

which is consistent with the result derived in the previous section, i.e., we obtain the scaling exponent

$$\phi = 1 . \quad (5.93)$$

Furthermore, $D^{>}/\Omega$ is a function of $|\Delta c_A|\Omega^{1/2}$, Eq. (5.91). Thus, we get the scaling exponent

$$\kappa = 1/2 , \quad (5.94)$$

which agrees with the one below the critical point. However, in the supercritical regime, we find an exponential behavior, Eq. (5.91), with exponent

$$\tilde{\varepsilon} = 2 , \quad (5.95)$$

which is consistent with the numerically obtained one, Eq. (5.70).

In summary, we have analytically derived the particle flux $J^{>}$, Eq. (5.89), which continuously extends the one obtained in the monostable regime $J^{<}$, Eq. (5.75), through the continuous phase transition following the tangential line into the bistable region, Eq. (5.65). Furthermore, approximating the system as a two-state one, we have obtained a theoretical prediction for the scaling of D , Eq. (5.91).

5.5 SCALING FORM

5.5.1 *General monostable pathway*

In order to obtain a general scaling form for the diffusion coefficient D , we consider a genuine line in the $c_A - c_B$ -plane through the critical point. For calculations it is convenient to use the following parameterization

$$c_B(\Delta c_A) \equiv \sqrt{3}/9 - (1/3 - \delta)\Delta c_A . \quad (5.96)$$

In the limit $\delta \rightarrow 0$, we recover the line along the pitchfork bifurcation, Eq. (5.65). Δc_A and δ remain as control parameters.

The rate equation reads

$$\partial_t \hat{x}(t) = -\hat{x}(t)^3 + \hat{x}(t)^2(\sqrt{3} + \Delta c_A) - \hat{x}(t) + \sqrt{3}/9 - (1/3 - \delta)\Delta c_A. \quad (5.97)$$

For $\delta \neq 0$, in the limit of $|\Delta c_A| \ll 1$, the fixed point of this equation is given by

$$x^*(\Delta c_A, \delta) \equiv 1/\sqrt{3} + \text{sign}(\Delta c_A \delta) |\Delta c_A \delta|^{1/3}. \quad (5.98)$$

Following the techniques introduced in Sec. 5.3.2, we obtain

$$J(\Delta c_A, \delta) \equiv 2\sqrt{3}/9 + \text{sign}(\Delta c_A \delta) |\Delta c_A \delta|^{1/3} + \mathcal{O}(\Delta c_A) \propto |\Delta c_A \delta|^{1/3}. \quad (5.99)$$

Thus, we find a continuous particle flux as function of $\Delta c_A \delta$.

Off the critical point, using the linear noise approximation introduced in Sec. 5.3.3, we obtain for the diffusion coefficient

$$D(\Delta c_A, \delta) = 8\sqrt{3} |\Delta c_A \delta|^{-4/3} / 27. \quad (5.100)$$

Right at the critical point, the diffusion coefficient is given by Eq. (5.60).

In summary, for any $\delta \neq 0$, we obtain the same scaling behavior for the particle flux and diffusion coefficient as along the critical line.

5.5.2 Change of coordinates

We change from the (c_A, c_B) -parameterization into a frame with the origin at the critical point. Furthermore, we consider the basis with direction parallel to the line along the pitchfork bifurcation and perpendicular to it, see Fig. 5.6.

We denote the deviations from the critical point along the c_A -axis as Δc_A and along the c_B -axis as $\Delta c_B \equiv c_B - c_B^{\text{crit}}$. In the direction along the pitchfork bifurcation, we label the deviations τ and into the perpendicular direction h , see Fig. 5.6. The coordinate transformation is given by

$$\begin{pmatrix} \Delta c_A \\ \Delta c_B \end{pmatrix} = \begin{pmatrix} 3/\sqrt{10} & 1/\sqrt{10} \\ -1/\sqrt{10} & 3/\sqrt{10} \end{pmatrix} \begin{pmatrix} \tau \\ h \end{pmatrix}. \quad (5.101)$$

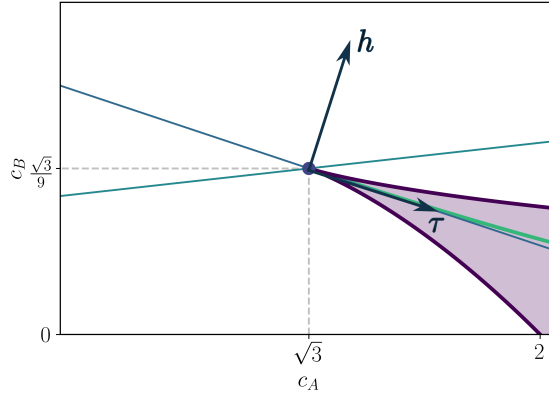


Figure 5.6: Phase-diagram of the Schlögl model, Eq. (5.1), with the coordinate-frame for the new variables (τ, h) .

For the line along the pitchfork bifurcation, Eq. (5.65), we obtain the parameterization

$$\tau = \sqrt{10}\Delta c_A/3, \quad \text{and} \quad h = 0. \quad (5.102)$$

For any other line through the critical point, Eq. (5.96), we find

$$\Delta c_A = (3\tau + h)/\sqrt{10} \quad \text{and} \quad \Delta c_B = 10h/(9\tau + 3h). \quad (5.103)$$

Thus, we get

$$\Delta c_A \delta = \sqrt{10}h/3, \quad (5.104)$$

which is independent of τ .

5.5.3 Scaling form for the particle flux

With the parameterization introduced in the previous section, Eq. (5.102) and (5.103), and the results for the particle fluxes, Eq. (5.75), (5.89) and (5.99), we find the following scaling form for the particle flux in the vicinity of the critical point

$$J(\tau, h) - J(0, 0) = \begin{cases} \tau/\sqrt{10}, & \tau < 0, \quad h = 0 \\ 5\sqrt{10}\tau/20, & \tau > 0, \quad h = 0 \\ 10^{1/6}\text{sign}(h)|h|^{1/3}/3^{1/3}, & h \neq 0 \end{cases}, \quad (5.105)$$

with $J(0, 0) \equiv 2\sqrt{3}/9$. For non-vanishing h , the derivative with respect to h scales as

$$\frac{\partial J(\tau, h)}{\partial h} \propto |h|^{-2/3}, \quad (5.106)$$

which agrees with the result obtained along the critical line, i.e., we recover the scaling exponent, Eq. (5.27).

5.5.4 Scaling form for the diffusion coefficient

Using the results of Sec. 5.5.2 and 5.4, we find the following scaling form for the diffusion coefficient

$$D = D(\Omega, \tau, h) = \Omega^\phi \mathcal{D}(\Omega^{\kappa_\tau} \tau, \Omega^{\kappa_h} h). \quad (5.107)$$

In the special case of $h = 0$, we have

$$D(\Omega, \tau, 0) = \Omega^\phi \mathcal{D}(\Omega^{\kappa_\tau} \tau, 0). \quad (5.108)$$

The scaling function is

$$\mathcal{D}(x, 0) \propto \begin{cases} 1, & |x| \ll 1 \\ (-x)^{\epsilon_\tau^<} , & x \ll -1 \\ \exp(4x^{\epsilon_\tau^>}/3), & x \gg 1 \end{cases} \quad (5.109)$$

with scaling exponents

$$\phi = 1, \quad \kappa_\tau = 1/2, \quad \text{and} \quad \epsilon_\tau^> = -\epsilon_\tau^< = 2. \quad (5.110)$$

For $h \neq 0$ and any τ , we obtain

$$\mathcal{D}(x, y) \propto \begin{cases} 1, & 0 < |y| \ll 1 \\ |y|^{\epsilon_h}, & |y| \gg 1 \end{cases}, \quad (5.111)$$

with critical exponents

$$\kappa_h = 3/4 \quad \text{and} \quad \epsilon_h = -4/3, \quad (5.112)$$

compare Sec. 5.3.3 and 5.5.1.

In summary, using the new coordinates (τ, h) , we have derived a scaling form for the diffusion coefficient D in the vicinity of the critical point, Eq. (5.107). The scaling functions for the two different regimes are given in Eq. (5.109) and (5.111) and the critical exponents in Eq. (5.110) and (5.112).

5.6 DISCUSSION AND CONCLUSION

We have numerically as well as analytically derived the scaling exponents of the thermodynamic flux and its associated diffusion coefficient for the univariate Schlögl model undergoing a continuous phase transitions. As representative path in phase space, we have considered the critical line, Eq. (5.12), along which the system exhibits critical scaling. Based on the rate equation, we have obtained the mean behavior of the particle flux, Sec. 5.3.2, which is in good agreement with the numerical found behavior, Sec. 5.3.1. Using the chemical Langevin equation and van Kampen's system-size expansion, we have analytically determined the critical exponents of the diffusion coefficient associated with the flux of the species in the reservoir.

For the second path, we have numerically shown that the system undergoes a continuous transition, Sec. 5.4.1. The fluctuations characterized through the associated diffusion coefficient diverge linearly in the system-size at the critical point. Furthermore, the diffusion coefficient obeys a scaling form, thus, indicating critical behavior. Using the techniques introduced in Sec. 5.3.2 and 5.3.3, we have obtained the scaling exponents in the monostable, subcritical regime, Sec. 5.4.2. Applying a two-state approximation, we have calculated the mean behavior of the particle flux and its diffusion coefficient in Sec. 5.4.3. We have obtained critical exponents that agree with the one of the subcritical regime. Furthermore, we have derived an exponential scaling function above the critical point which is consistent with previous results [128].

In Sec. 5.5, we have transformed to the variables parallel to the line along the pitchfork bifurcation and the direction perpendicular to it. Parameterizing the (c_A, c_B) -plane in those coordinates, we have derived a scaling form for the particle flux, Eq. (5.105), and the diffusion coefficient, Eq. (5.107), that summarizes the results of the previous sections.

In conclusion, we have examined the thermodynamic flux and its fluctuations in the vicinity of the critical point of the Schlögl model. We have analytically determined critical exponents based on the chemical Langevin equation, van Kampen's system size expansion and a two-state approximation. Furthermore, this work complements previous studies that

have considered the first order transition when crossing the coexistence line in Fig. 5.1 [128, 146]. Thus, our contribution completes the understanding of the thermodynamic treatment of the reaction scheme (5.1).

The critical behavior as derived here for the Schlögl model should be universal for any nonequilibrium reaction network with a critical point where a first-order transition between two stable dynamical phases terminates. A different universality class can be expected for more complex reaction schemes like the Brusselator [90, 106, 150–152] where a Hopf bifurcation separates an oscillatory regime described by a limit cycle from a monostable regime. We will apply the concepts derived here to this complementary paradigm of a nonequilibrium phase transition in the next chapter.

NONEQUILIBRIUM FLUCTUATIONS OF CHEMICAL REACTION NETWORKS AT CRITICALITY – THE BRUSSELATOR MODEL AS PARADIGMATIC CASE

6.1 INTRODUCTION

In the previous chapter, we have examined a univariate reaction scheme that undergoes a continuous phase transition. We have shown that the flux in a particle reservoir has a non-analytical derivative with respect to a control parameter. Furthermore, the associated diffusion coefficient diverges at the transition. A similar result has previously been reported for another system. Such fluxes and their fluctuations have been examined in Ref. [90] for a chemical reaction network undergoing a Hopf bifurcation. The authors have numerically found an effective exponent for the system-size scaling of these fluctuations but could not provide analytical insight. This lack of theoretical description is a primary motivation for this chapter.

We study the flux of particles consumed and produced in the reservoirs for the thermodynamically consistent Brusselator as paradigm for a Hopf bifurcation. Fluctuations of the fluxes are characterized by the associated diffusion coefficient. We numerically find a non-analytical behavior of the particle flux, i.e., we find a jump in the derivative of the flux with respect to the control parameter. Furthermore, we provide theoretical insight for the origin of this non-differentiable behavior using a mapping onto the cubic normal for Hopf bifurcations.

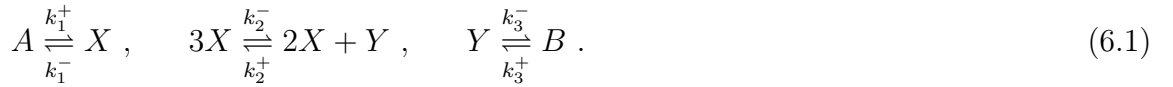
The diffusion coefficient displays critical behavior while varying a control parameter. We determine critical exponents and find that the diffusion coefficient discontinuously depends on the control parameter. Approximating the system through a chemical Langevin equation and van Kampen's system-size expansion, we obtain an equation of motion for the fluctuations which is not analytically treatable. Numerically integrating the CLE and the equations derived by van Kampen's system-size expansion, we determine which equation correctly approximates the non-analytical behavior of the diffusion coefficient.

This chapter is organized as follows. We introduce the thermodynamically consistent Brusselator model, particle flux and associated diffusion coefficient in Sec. 6.2. In Sec. 6.3,

we present our numerical results for the mean particle flux and the corresponding diffusion coefficient. The analytical understanding of the non-analytical particle flux is given in Sec. 6.4. In Sec. 6.5, we analytically examine the diffusion coefficient. We show where the techniques introduced in Chapter 5 fail to describe the system and which approximation should be used to study the diffusion coefficient. We conclude in Sec. 6.6.

6.2 THE THERMODYNAMIC CONSISTENT BRUSSELATOR MODEL

The reaction scheme of the thermodynamically consistent Brusselator model is given by

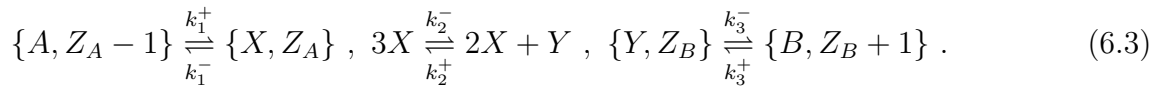


The species A and B in the external reservoir are kept at constant concentration c_A and c_B , respectively. Due to a difference in the chemical potential between A and B , i.e., $\Delta\mu \equiv \mu_B - \mu_A > 0$, the system is out of equilibrium and the intermediate species X and Y can oscillate. To ensure thermodynamic consistency, the nonequilibrium driving force fulfills the local detailed balance condition [12]

$$\beta\Delta\mu = \ln \frac{c_B k_3^+ k_2^+ k_1^-}{c_A k_1^+ k_2^- k_3^-} \quad (6.2)$$

with reaction rates k_i^\pm and inverse temperature β . We set $\beta = 1$ throughout this chapter, thus, measuring energies in units of the thermal energy and entropy in the units of the Boltzmann constant.

We introduce counting variables $Z_A(t)$ and $Z_B(t)$ in order to investigate the particle flux of the species in the reservoir and its fluctuations, compare Chapter 5. This leads to the following augmented reaction scheme,



The mean flux from the particle reservoir is given by

$$J_B \equiv \lim_{t \rightarrow \infty} \frac{\langle Z_B(t) \rangle}{\Omega t} = J_A, \quad (6.4)$$

with fluctuations quantified by the diffusion coefficient

$$D_B \equiv \lim_{t \rightarrow \infty} \frac{\text{Var}[Z_B(t)]}{2\Omega t} = D_A , \quad (6.5)$$

D_A and D_B are equal with a similar proof as for the Schlögl model using large deviation theory [128]. Thus, we discuss only particle species B . All results are equally true for chemostatted species A . We drop the index for the mean values in what follows.

The mean entropy production rate in the steady state is given by the particle flux J and the thermodynamic driving $\Delta\mu$,

$$\sigma \equiv \Omega J \Delta\mu . \quad (6.6)$$

In Ref. [90], the authors have found that the system undergoes a stochastic Hopf bifurcation while varying $\Delta\mu$. Furthermore, they found a continuous dependence of the thermodynamic flux J , hence, entropy production rate on the control parameter. Thus, the Hopf bifurcation is classified as a continuous phase transition.

A Hopf bifurcation is determined by the rate equations as discussed in Sec. 2.8.3. For the reaction scheme (6.1), the deterministic rate equations are given by

$$\begin{aligned} \frac{d}{dt} \begin{pmatrix} \hat{x}(t) \\ \hat{y}(t) \end{pmatrix} &= \begin{pmatrix} c_A k_1^+ + k_2^+ \hat{x}(t)^2 \hat{y}(t) - k_1^- \hat{x}(t) - k_2^- \hat{x}(t)^3 \\ c_B k_3^+ + k_2^- \hat{x}(t)^3 - k_3^- \hat{y}(t) - k_2^+ \hat{x}(t)^2 \hat{y}(t) \end{pmatrix} \\ &\equiv \begin{pmatrix} F_1[\hat{x}(t), \hat{y}(t)] \\ F_2[\hat{x}(t), \hat{y}(t)] \end{pmatrix} \equiv F[\hat{x}(t), \hat{y}(t)] , \end{aligned} \quad (6.7)$$

where $\hat{x}(t)$ and $\hat{y}(t)$ denote the mean particle concentration of species X and Y , respectively, at time t . We denote the stationary solution of the rate equations as $(x^*, y^*) = (x^*(\Delta\mu), y^*(\Delta\mu))$. The bifurcation is determined through the eigenvalues of the Jacobian matrix. We numerically find a vanishing real part of the eigenvalues for

$$\Delta\mu^{\text{crit}} \simeq 3.9303 , \quad (6.8)$$

which defines the bifurcation for the parameter-set considered in Ref. [90], see Table 6.1. Throughout this chapter, we keep all rates constant according to Ref. [90] except k_3^- which is determined by Eq. (6.2) as function of the control parameter $\Delta\mu$. Thus, the system-size Ω and $\Delta\mu$ remain as external parameters. We expect all results to hold for any other parameter-set for which the system undergoes a Hopf bifurcation.

k_1^+	k_3^+	k_1^-	k_2^+	k_2^-	c_A	c_B
0.1	0.1	1	1	1	1	3

Table 6.1: Reaction rates of the Brusselator model, Eq. (6.1), as presented in Ref. [90]. The rate k_3^- is determined by the local detailed balance condition, Eq. (6.2), as function of the control parameter $\Delta\mu$.

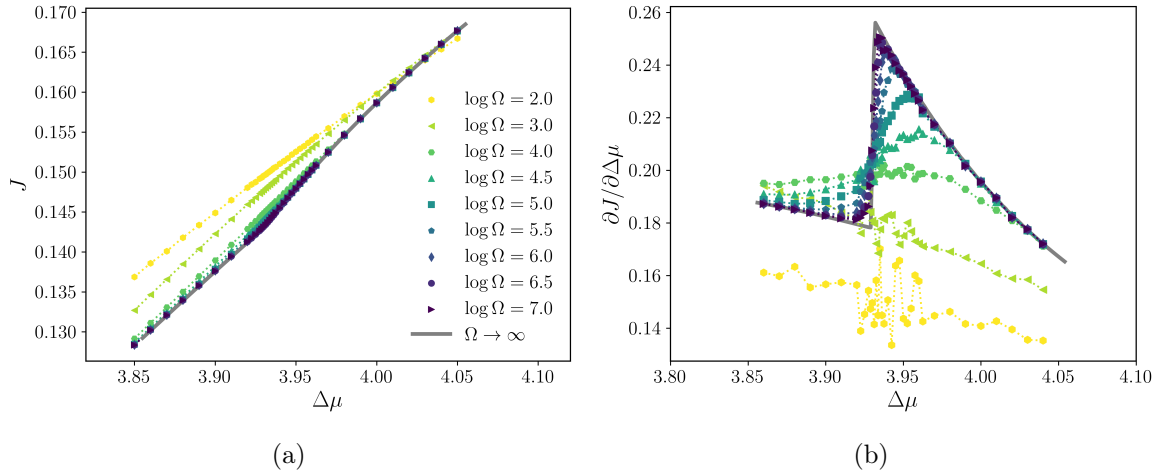


Figure 6.1: Numerical results for the mean flux J of the Brusselator model. (a) J as function of the control parameter $\Delta\mu$ for various system sizes Ω . (b) Derivative of the mean flux J with respect to the driving $\Delta\mu$.

In the next section, we examine the particle flux J and the associated diffusion coefficient D numerically while varying the control parameters.

6.3 NUMERICAL DATA

We numerically integrate reaction scheme Eq. (6.1) using Gillespie's direct method [35]. The particle flux J and D are determined according to Eq. (6.4) and (6.5). The results are shown in Fig. 6.1 and 6.2.

The mean flux depends continuously on the control parameter $\Delta\mu$, see Fig. 6.1a. For increasing Ω , we observe a convergence of J towards the result obtained when numerically integrating the rate equations (6.7) ($\Omega \rightarrow \infty$ line). In the vicinity of $\Delta\mu^{\text{crit}}$, the mean flux develops a kink while transitioning towards a different regime for $\Delta\mu > \Delta\mu^{\text{crit}}$. This kink is more apparent in the numerical derivative of J , see Fig. 6.1b. The derivative develops a jump around the bifurcation. The height of the jump saturates with increasing system-size Ω .

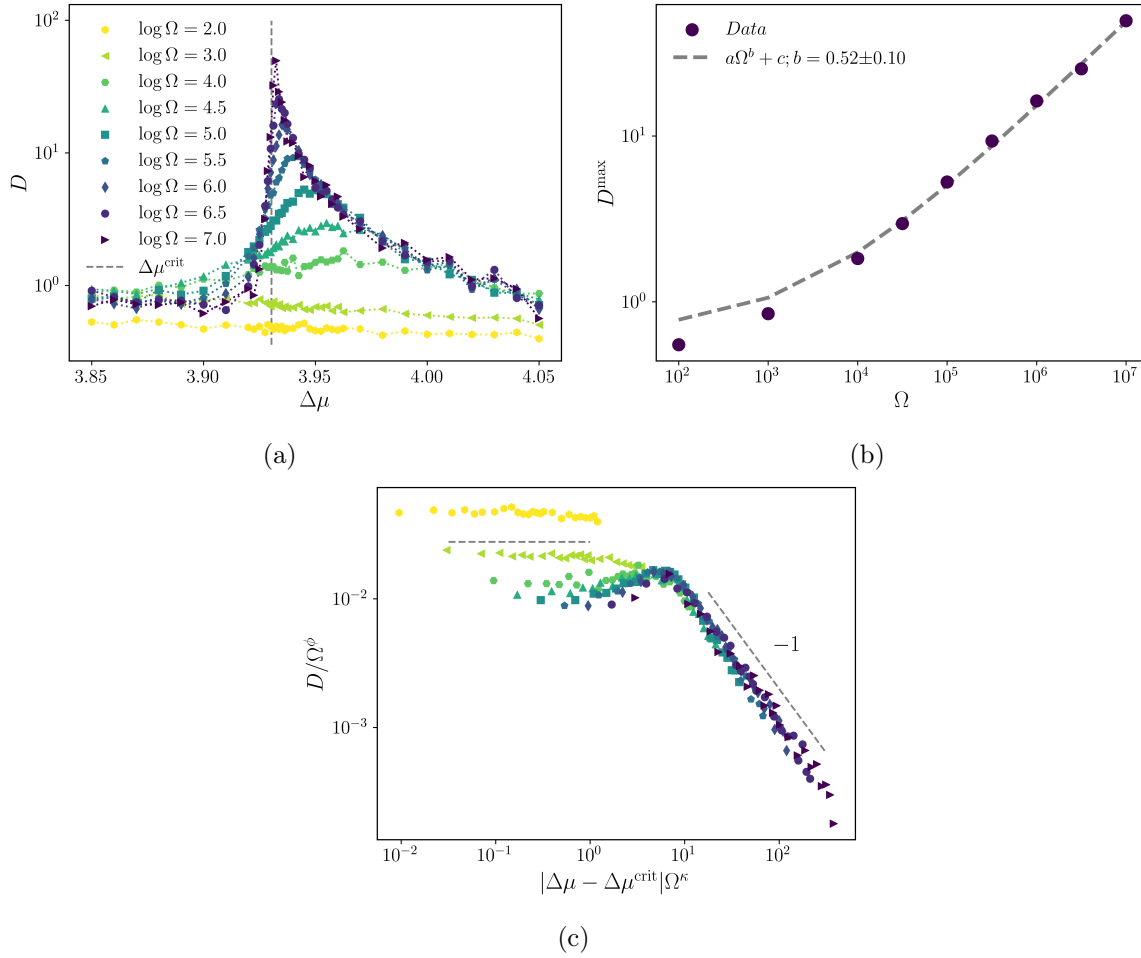


Figure 6.2: Numerical results for the fluctuations of the entropic flux. (a) Diffusion coefficient D as function of the control parameter $\Delta\mu$ for various system sizes Ω . (b) Maximal D as function of the system-size Ω . (c) Rescaled diffusion coefficient $D = \Omega^\phi \mathcal{D}(|\Delta\mu - \Delta\mu^{\text{crit}}|\Omega^\kappa)$ for data above the bifurcation with $\phi = \kappa = 0.5$.

The diffusion coefficient develops a pronounced peak around the bifurcation that depends on the system size, see Fig. 6.2. We find a power-law behavior

$$D^{\text{max}} \propto \Omega^\phi, \quad \phi = 0.52 \pm 0.10. \quad (6.9)$$

Above the bifurcation, D does not depend on the system-size. Furthermore, we find a smooth transition towards the bifurcation. In this regime, the data obey a scaling form

$$D(\Delta\mu, \Omega) = \Omega^\phi \mathcal{D}(|\Delta\mu - \Delta\mu^{\text{crit}}|\Omega^\kappa) \quad (6.10)$$

as the collapse onto a master curve shows, see Fig. 6.2c. The scaling exponent is determined as

$$\kappa = 0.5 \pm 0.1 . \quad (6.11)$$

Below the bifurcation, the diffusion coefficient D does not depend on Ω . Approaching the bifurcation from below, we find a discontinuous transition between the two regimes. With increasing system-size, D develops a jump. In contrast to the derivative of J discussed above, the height of the jump depends on the system-size, see Fig. 6.2b.

In summary, we have numerically found a continuous dependence of the particle flux J on the control parameter $\Delta\mu$. The derivative of this flux shows a system-size independent jump in the vicinity of the bifurcation. For the diffusion coefficient, we have found a power-law dependence on the system-size at the bifurcation and determined a scaling form while approaching the bifurcation from above. However, when coming from below, the diffusion coefficient develops a discontinuity with increasing system-size. This constitutes our first main result.

In the next section, we consider the rate equations in order to gain an analytical intuition for the dependence of the mean flux J on the control parameter $\Delta\mu$.

6.4 RATE EQUATION, MEAN FLUX AND NORMAL FORM MAPPING

6.4.1 Rate equation

The rate equation for the number of produced reservoir particles B is given by

$$\partial_t \hat{z}_B(t) = k_3^- \hat{y}(t) - c_B k_3^+ , \quad (6.12)$$

where $\hat{z}_B(t) \equiv \langle Z_B(t) \rangle / \Omega$ and $\hat{y}(t)$ obeys the rate equation (6.7). From Eq. (6.4), we obtain the particle flux

$$J = k_3^- \lim_{t \rightarrow \infty} \frac{1}{t} \int_0^t ds \hat{y}(s) - c_B k_3^+ . \quad (6.13)$$

Below the bifurcation, the dynamics of the system is determined by the fixed point (x^*, y^*) of Eq. (6.7). Thus, in the long-time limit, we can replace $\hat{y}(t) \rightarrow y^*$. This leads to

$$J = k_3^- y^* - c_B k_3^+ \equiv J^* \quad (6.14)$$

with $J^* = J^*(\Delta\mu)$. Above the bifurcation the system admits a stable limit cycle around the fixed point. Thus, we can parameterize the mean concentration as

$$\hat{y}(t) = y^* + \delta y(t) . \quad (6.15)$$

This leads to

$$J = k_3^- \lim_{t \rightarrow \infty} \frac{1}{t} \int_0^t ds \delta y(s) + J^* . \quad (6.16)$$

In summary, we find a mean flux

$$J - J^* = \begin{cases} 0 & , \Delta\mu < \Delta\mu^{\text{crit}} \\ k_3^- \lim_{t \rightarrow \infty} \frac{1}{t} \int_0^t ds \delta y(s) & , \Delta\mu > \Delta\mu^{\text{crit}} \end{cases} . \quad (6.17)$$

Shifting the numerically obtained flux by J^* , Eq. (6.14), we find good agreement of the data with relation (6.17), see Fig. 6.3. We observe a linear dependence on the control parameter in the vicinity but above the bifurcation. Below $\Delta\mu^{\text{crit}}$, however, we find a vanishing difference $J - J^*$.

In the next section, we use a normal form mapping in order to understand the contribution of $\delta y(t)$ to the flux.

6.4.2 Normal form mapping

We consider the rate equations (6.7) for the thermodynamically consistent Brusselator. We set the origin into the fixed point (x^*, y^*) of the rate equations,

$$\begin{pmatrix} \hat{x}(t) \\ \hat{y}(t) \end{pmatrix} = \begin{pmatrix} x^* + \delta x(t) \\ y^* + \delta y(t) \end{pmatrix} . \quad (6.18)$$

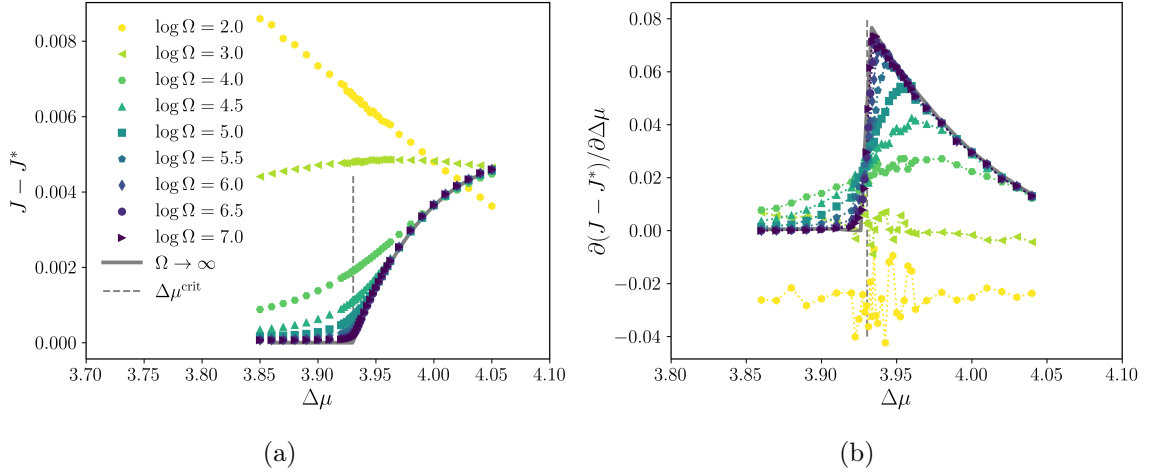


Figure 6.3: Mean flux shifted by the contribution due to the fixed point (a) as function of the control parameter $\Delta\mu$ and (b) its derivative with respect to $\Delta\mu$ for various system-sizes.

Thus, we get the following dynamical system

$$\partial_t \begin{pmatrix} \delta x(t) \\ \delta y(t) \end{pmatrix} = F[x^* + \delta x(t), y^* + \delta y(t)] \equiv \tilde{F}[\delta x(t), \delta y(t)] . \quad (6.19)$$

The fixed point of this vector-field is $(\delta x^*, \delta y^*) \equiv (0, 0)$. Furthermore, $\tilde{F}[\delta x, \delta y]$ undergoes a Hopf bifurcation upon variation of the control parameter $\Delta\mu$. Thus, we can map this vector-field to the cubic normal form for a Hopf bifurcation [48, 101, 153, 154]

$$F_{CNF}(\delta x, \delta y) \equiv \begin{pmatrix} \rho & -\omega \\ \omega & \rho \end{pmatrix} \begin{pmatrix} \delta x \\ \delta y \end{pmatrix} + (\delta x^2 + \delta y^2) \begin{pmatrix} a & -b \\ b & a \end{pmatrix} \begin{pmatrix} \delta x \\ \delta y \end{pmatrix} , \quad (6.20)$$

see also Eq. (2.156).

We briefly outline this normal form mapping following Ref. [153]. The first step is to apply a linear transformation U such that the differential evaluated at the origin becomes

$$D\tilde{F} \circ U(\delta x, \delta y) = \begin{pmatrix} \rho & -\omega \\ \omega & \rho \end{pmatrix} \begin{pmatrix} \delta x \\ \delta y \end{pmatrix} , \quad (6.21)$$

where the eigenvalues in the vicinity of the bifurcation are

$$\lambda_{\pm} = \rho \pm i\omega . \quad (6.22)$$

We note that $\rho = \rho(\Delta\mu)$ and $\omega = \omega(\Delta\mu)$ are functions of the control parameter.

The next step is to apply a series of quasi-linear transformations, i.e., functions of the form

$$f_k(\delta x, \delta y) \equiv \begin{pmatrix} \delta x \\ \delta y \end{pmatrix} + \begin{pmatrix} f_1^{(k)}(\delta x, \delta y) \\ f_2^{(k)}(\delta x, \delta y) \end{pmatrix} \equiv \begin{pmatrix} \delta x \\ \delta y \end{pmatrix} + f^{(k)}(\delta x, \delta y), \quad (6.23)$$

where $f^{(k)}(\delta x, \delta y)$ denotes a vector with component functions $f_i^{(k)}(\delta x, \delta y)$ that are homogeneous polynomials of order k , i.e., $f_i^{(k)}(0, 0) = 0$. Assuming that $|\delta x|, |\delta y| \ll 1$, the inverse transformation is in leading order

$$f_k^{-1}(\delta x, \delta y) = \begin{pmatrix} \delta x \\ \delta y \end{pmatrix} - f^{(k)}(\delta x, \delta y). \quad (6.24)$$

First, we apply a second order transformation of the form

$$f_2(\delta x, \delta y) \equiv \begin{pmatrix} \delta x \\ \delta y \end{pmatrix} + \begin{pmatrix} a_{2,0}\delta x^2 + a_{1,1}\delta x\delta y + a_{0,2}\delta y^2 \\ b_{2,0}\delta x^2 + b_{1,1}\delta x\delta y + b_{0,2}\delta y^2 \end{pmatrix}. \quad (6.25)$$

This transformation leaves the linear part unchanged. We can choose the free coefficients $a_{i,j}$ and $b_{i,j}$ such that the composition $\tilde{F} \circ f_2 \circ U(\delta x, \delta y)$ has no quadratic terms. Thus, the remaining vector-field has a linear part as given in Eq. (6.21) and arbitrary higher-order terms of at least order 3.

We further apply a third order transformation which leaves again the linear part unchanged and produces no quadratic terms. The free coefficients of this map can be chosen such that we obtain the cubic normal form after truncating all terms of order higher than three, i.e.,

$$\tilde{F} \circ f_3 \circ f_2 \circ U(\delta x, \delta y) = F_{CNF}(\delta x, \delta y) + \mathcal{O}(4). \quad (6.26)$$

Thus, the change of coordinates

$$\begin{pmatrix} \delta \tilde{x} \\ \delta \tilde{y} \end{pmatrix} \equiv f_3 \circ f_2 \circ U(\delta x, \delta y) \quad (6.27)$$

transforms $\tilde{F}(\delta x, \delta y)$ into the cubic normal form $F_{CNF}(\delta \tilde{x}, \delta \tilde{y})$.

In the oscillatory regime, the cubic normal form exhibits a stable limit cycle. The trajectory is parameterized as

$$\begin{pmatrix} \delta\tilde{x}(t) \\ \delta\tilde{y}(t) \end{pmatrix} = r_0 \begin{pmatrix} \cos(\omega_0 t) \\ \sin(\omega_0 t) \end{pmatrix}, \quad (6.28)$$

with limit cycle radius

$$r_0 \equiv \sqrt{\frac{\rho}{a}} \quad (6.29)$$

and angular frequency on the limit cycle

$$\omega_0 = \omega + br_0^2. \quad (6.30)$$

The back transformation of the oscillatory solution, Eq. (6.28), leads to

$$\delta y(t) = \delta\tilde{y}(t) + c_1 \delta\tilde{y}(t)^2 + c_2 \delta\tilde{x}(t) \delta\tilde{y}(t) + c_3 \delta\tilde{x}(t)^2 + \mathcal{O}(3), \quad (6.31)$$

with constants c_i that are determined through the coefficients $a_{i,j}$ and $b_{i,j}$ of the transformation $f_2(\delta x, \delta y)$. Using this expression, we find for the particle flux J in the oscillatory phase, Eq. (6.16),

$$J - J^* = k_3^- \lim_{t \rightarrow \infty} \frac{1}{t} \int_0^t ds \delta y(s) = k_3^- \frac{\rho}{a} \mathcal{C}_0, \quad (6.32)$$

where \mathcal{C}_0 contains all constants c_i and does not depend on the control parameter.

As last step, we identify the remaining dependencies on $\Delta\mu - \Delta\mu^{\text{crit}}$. The rate k_3^- is determined through the local detailed balance condition, Eq. (6.2). We find

$$k_3^- = k_3^-(\Delta\mu - \Delta\mu^{\text{crit}}) = \mathcal{O}(1) \quad (6.33)$$

for $\Delta\mu - \Delta\mu^{\text{crit}} \ll 1$. As ρ is the real part of the eigenvalue that determines the bifurcation, we necessarily have

$$\rho = \mathcal{O}(\Delta\mu - \Delta\mu^{\text{crit}}) \quad (6.34)$$

for $\Delta\mu - \Delta\mu^{\text{crit}} \ll 1$. Furthermore, we get

$$a = \mathcal{O}(1) \tag{6.35}$$

in the limit of vanishing $\Delta\mu - \Delta\mu^{\text{crit}}$ [154]. Thus, when approaching the bifurcation from above, the mean flux J depends linearly on the control parameter, i.e.,

$$J - J^* = \mathcal{C}(\Delta\mu - \Delta\mu^{\text{crit}}) , \tag{6.36}$$

with constant of proportionality \mathcal{C} .

In conclusion, we obtained the following behavior of the mean particle flux in the vicinity of the bifurcation,

$$J - J^* = \begin{cases} 0 & , \Delta\mu < \Delta\mu^{\text{crit}} \\ \mathcal{C}(\Delta\mu - \Delta\mu^{\text{crit}}) & , \Delta\mu > \Delta\mu^{\text{crit}} \end{cases} . \tag{6.37}$$

Thus, we find a continuous but non-differentiable transition between the two regimes which is in good agreement with the numerically found behavior, see Fig. 6.3. This manifests our second main result.

6.5 DISCONTINUOUS DIFFUSION COEFFICIENT

6.5.1 System-size expansion

6.5.1.1 Set-up

We turn to the diffusion coefficient D . Following the techniques developed in Chapter 5, we consider the ansatz

$$\begin{pmatrix} n_X(t) \\ n_Y(t) \\ Z_B(t) \end{pmatrix} = \Omega \begin{pmatrix} \hat{x}(t) \\ \hat{y}(t) \\ \hat{z}_B(t) \end{pmatrix} + \sqrt{\Omega} \begin{pmatrix} x(t) \\ y(t) \\ z_B(t) \end{pmatrix} , \tag{6.38}$$

where $n_X(t)$ denotes the number of molecules of species X up to time t , and $n_Y(t)$ of species Y , respectively.

Van Kampen's expansion leads in lowest order to the rate equations (6.7) and (6.12). The higher-order terms are equivalent to the following Langevin equations

$$\begin{aligned}
\partial_t x(t) &= \sqrt{\Omega} \left(F_1[\hat{x}(t) + x(t)/\sqrt{\Omega}, \hat{y}(t) + y(t)/\sqrt{\Omega}] - F_1[\hat{x}(t), \hat{y}(t)] \right) \\
&\quad + \sqrt{c_A k_1^+ + k_1^- \hat{x}(t)} \xi_A(t) + \sqrt{k_2^+ \hat{x}(t)^2 \hat{y}(t) + k_2^- \hat{x}(t)^3} \xi(t) , \\
\partial_t y(t) &= \sqrt{\Omega} \left(F_2[\hat{x}(t) + x(t)/\sqrt{\Omega}, \hat{y}(t) + y(t)/\sqrt{\Omega}] - F_2[\hat{x}(t), \hat{y}(t)] \right) \\
&\quad + \sqrt{k_2^+ \hat{x}(t)^2 \hat{y}(t) + k_2^- \hat{x}(t)^3} \xi(t) + \sqrt{c_B k_3^+ + k_3^- \hat{y}(t)} \xi_B(t) , \\
\partial_t z_B(t) &= -k_3^- y(t) + \sqrt{c_B k_3^+ + k_3^- \hat{y}(t)} \xi_B(t) .
\end{aligned} \tag{6.39}$$

Using ansatz Eq. (6.38) and the definition of D , Eq. (6.5), we obtain

$$\begin{aligned}
D &= (k_3^-)^2 \int_0^\infty dt \langle y(t) y(0) \rangle + \lim_{t \rightarrow \infty} \frac{1}{t} \int_0^t C_B(\hat{y}(s)) ds \\
&\quad - k_3^- \lim_{t \rightarrow \infty} \frac{1}{t} \int_0^t d\tau \int_0^\tau ds C_B(\hat{y}(s)) \langle y(\tau) \xi_B(s) \rangle ,
\end{aligned} \tag{6.40}$$

with $C_B(\hat{y}) \equiv \frac{1}{2}(c_B k_3^+ + k_3^- \hat{y})$.

In the next sections, we consider the above expression for D in the different regimes of the Brusselator model.

6.5.1.2 Fixed point regime

We assume that the rate equation (6.7) has a stable fixed point denoted as (x^*, y^*) . After a Taylor-expansion for $\Omega \gg 1$, the Langevin equations (6.39) become in leading order

$$\begin{aligned}
\partial_t x(t) &= DF(x^*, y^*)_{1,1} x(t) + DF(x^*, y^*)_{1,2} y(t) \\
&\quad + \sqrt{c_A k_1^+ + k_1^- x^*} \xi_A(t) + \sqrt{k_2^+ x^{*2} y^* + k_2^- x^{*3}} \xi(t) , \\
\partial_t y(t) &= DF(x^*, y^*)_{2,1} x(t) + DF(x^*, y^*)_{2,2} y(t) \\
&\quad + \sqrt{k_2^+ x^{*2} y^* + k_2^- x^{*3}} \xi(t) + \sqrt{c_B k_3^+ + k_3^- y^*} \xi_B(t) , \\
\partial_t z_B(t) &= -k_3^- y(t) + \sqrt{c_B k_3^+ + k_3^- y^*} \xi_B(t) ,
\end{aligned} \tag{6.41}$$

where $DF(x^*, y^*)_{i,j}$ denote the entries of the Jacobian matrix of vector-field $F(x, y)$ evaluated at the fixed point (x^*, y^*) . We obtain a linear system without any dependence on the system-size Ω . Furthermore, $x(t)$, $y(t)$ and $z_B(t)$ describe an Ornstein-Uhlenbeck process [38, 39], hence, are Gaussian variables.

For the diffusion coefficient, we find

$$D = (k_3^-)^2 \int_0^\infty dt \langle y(t)y(0) \rangle + C_3(y^*) - k_3^- C_3(y^*) \lim_{t \rightarrow \infty} \frac{1}{t} \int_0^t d\tau \int_0^\tau ds \langle y(\tau)\xi_B(s) \rangle . \quad (6.42)$$

As the fluctuations are described by a linear system, all integrals are in principle analytically solvable. However, since there is no analytical expression for the fixed point (x^*, y^*) , this leads only to a semi-analytically estimate of the diffusion coefficient, hence no analytical understanding of the observed behavior. A further possible route to take is to consider the ordinary differential equations for the moments. Using the fact that we consider Gaussian variables and Wick's theorem, we would obtain a closed system for the first and second moments. This approach, however, leads also to a numerical solution and not to an analytical understanding. Nevertheless, using Eq. (6.42), we find that D does not depend on the system-size Ω . This is consistent with the numerical data, see Fig. 6.2.

6.5.1.3 Oscillating phase

Above the bifurcation, the system exhibits limit cycle oscillations, i.e., the stable solution of the rate equations is time dependent. We denote this solution with $(x_0(t), y_0(t))$, i.e.,

$$\begin{pmatrix} x_0(t) \\ y_0(t) \end{pmatrix} \equiv \begin{pmatrix} x^* \\ y^* \end{pmatrix} + \begin{pmatrix} \delta x(t) \\ \delta y(t) \end{pmatrix} , \quad (6.43)$$

as introduced in Eq. (6.15). Using Eq. (6.39), we find

$$\begin{aligned} \partial_t x(t) &= DF[x_0(t), y_0(t)]_{1,1}x(t) + DF[x_0(t), y_0(t)]_{1,2}y(t) \\ &\quad + \sqrt{c_A k_1^+ + k_1^- x_0(t)} \xi_A(t) + \sqrt{k_2^+ x_0(t)^2 y_0(t) + k_2^- x_0(t)^3} \xi(t) , \\ \partial_t y(t) &= DF[x_0(t), y_0(t)]_{2,1}x(t) + DF[x_0(t), y_0(t)]_{2,2}y(t) \\ &\quad + \sqrt{k_2^+ x_0(t)^2 y_0(t) + k_2^- x_0(t)^3} \xi(t) + \sqrt{c_B k_3^+ + k_3^- y_0(t)} \xi_B(t) , \\ \partial_t z_B(t) &= -k_3^- y(t) + \sqrt{c_B k_3^+ + k_3^- y_0(t)} \xi_B(t) . \end{aligned} \quad (6.44)$$

This is a linear system without any Ω dependence. As before, $x(t)$, $y(t)$ and $z_B(t)$ are Gaussian variables. However, since there is no analytical expression for the limit cycle $(x_0(t), y_0(t))$, we again only find that the diffusion coefficient does not depend on Ω . This is consistent with the numerical data, see Fig. 6.2.

6.5.1.4 At the bifurcation

One of the conditions for a Hopf-bifurcation to take place is the constraint that the eigenvalues of the Jacobian matrix have a vanishing real part. Thus, at the bifurcation, the linear noise approximation as it has been used in the previous sections does not lead to a stationary solution of the fluctuations. As a consequence, we need to consider higher order terms in Ω .

At the bifurcation, the steady-state of the rate equations (6.7) is a fixed point. Thus, the vector-field for the $x(t)$ and $y(t)$ motion, Eq. (6.39), has the following form

$$\begin{aligned}\tilde{F}[x(t), y(t)] &\equiv \sqrt{\Omega} \left(F[x^* + x(t)/\sqrt{\Omega}, y^* + y(t)/\sqrt{\Omega}] - F[x^*, y^*] \right) \\ &= DF[x(t), y(t)] + \frac{1}{\sqrt{\Omega}} M[x(t), y(t)] + \frac{1}{\Omega} N[x(t), y(t)]\end{aligned}\quad (6.45)$$

with

$$DF[x, y] \equiv \begin{pmatrix} -(k_1^- + 3k_2^- x^{*2} - 2k_2^+ x^* y^*)x + k_2^+ x^{*2} y \\ (3k_2^- 2k_2^+ x^* y^* - 2k_2^+ x^* y^*)x - (k_3^- + k_2^+ x^{*2})y \end{pmatrix}, \quad (6.46)$$

$$M[x, y] \equiv \begin{pmatrix} -(3k_2^- x^* - k_2^+ y^*)x^2 + 2k_2^+ x^* x y \\ (3k_2^- x^* - k_2^+ y^*)x^2 - 2k_2^+ x^* x y \end{pmatrix}, \quad (6.47)$$

and

$$N[x, y] \equiv \begin{pmatrix} -k_2^- x^3 + k_2^+ x^2 y \\ k_2^- x^3 - k_2^+ x^2 y \end{pmatrix}. \quad (6.48)$$

We have dropped the dependence on the fixed point (x^*, y^*) in the above definitions.

The vector-field, Eq. (6.45), satisfies all requirements for a Hopf bifurcating field. Hence, we apply the normal form mapping discussed in Sec. 6.4. At the bifurcation, this leads to a normal form of the following form

$$\tilde{F}(x, y) \simeq \sqrt{\Omega} F_{CNF}(x/\sqrt{\Omega}, y/\sqrt{\Omega}), \quad (6.49)$$

i.e.,

$$\tilde{F}(x, y) \simeq \begin{pmatrix} 0 & -\omega \\ \omega & 0 \end{pmatrix} \begin{pmatrix} x \\ y \end{pmatrix} + \frac{1}{\Omega}(x^2 + y^2) \begin{pmatrix} a & -b \\ b & a \end{pmatrix} \begin{pmatrix} x \\ y \end{pmatrix}. \quad (6.50)$$

Comparing with the Langevin equation (6.39), we find

$$\partial_t \begin{pmatrix} u(t) \\ v(t) \end{pmatrix} = \sqrt{\Omega} F_{CNF}[u(t)/\sqrt{\Omega}, v(t)/\sqrt{\Omega}] + \begin{pmatrix} \sqrt{2D_1} & \sqrt{2D_2} & 0 \\ 0 & \sqrt{2D_2} & \sqrt{2D_3} \end{pmatrix} \begin{pmatrix} \zeta_1(t) \\ \zeta_2(t) \\ \zeta_3(t) \end{pmatrix} \quad (6.51)$$

where $u(t)$ and $v(t)$ are connected to $x(t)$ and $y(t)$ through the normal form mapping. The D_i are the diffusion constants of the Gaussian white noises with $\langle \zeta_i(t) \rangle = 0$ and $\langle \zeta_i(t) \zeta_j(t') \rangle = \delta_{ij} \delta(t - t')$. Due to the lack of radial symmetry of Eq. (6.51), we rely on numerical methods in order to investigate the properties of its solution.

6.5.2 Cubic normal form model

We consider Eq. (6.51) and

$$\partial_t z(t) = -v(t) + \sqrt{2D_3} \zeta_3(t). \quad (6.52)$$

We keep all parameters of the cubic normal form for a Hopf-bifurcation constant except for ρ which corresponds to the control parameter $\Delta\mu$. Thus, the external parameters are ρ , Ω , D_1 , D_2 and D_3 .

We numerically integrate Eq. (6.51) and (6.52) and determine the diffusion coefficient according to

$$D_z \equiv \Omega \lim_{t \rightarrow \infty} \frac{\text{Var}[z(t)]}{2t}. \quad (6.53)$$

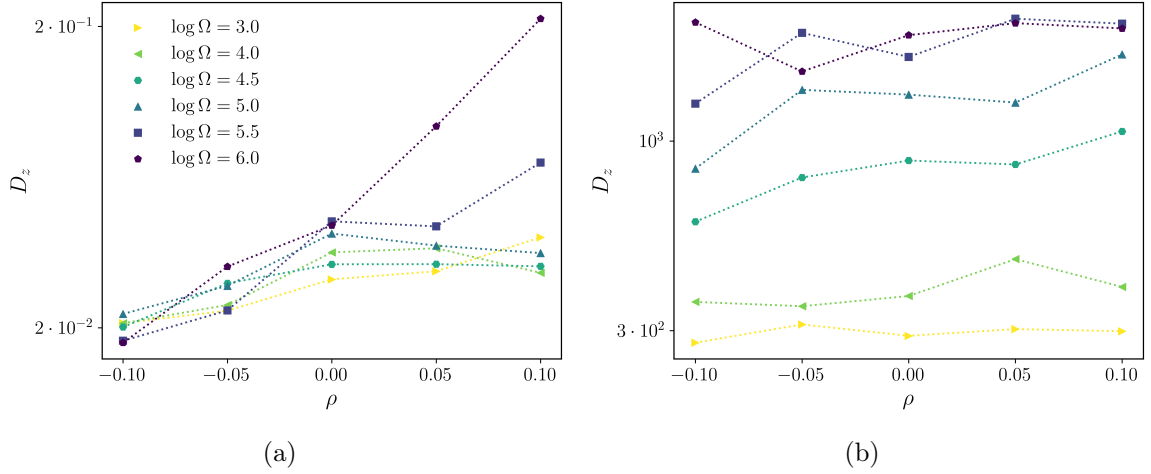


Figure 6.4: Diffusion coefficient D_z of the noisy cubic normal form for a Hopf bifurcation as a function of ρ for various D_1 , D_2 , D_3 and system-sizes Ω . The parameters are $a = b = \omega = 1$. (a) $D_1 = 10^{-3}$, $D_2 = 10^{-2}$, $D_3 = 10^{-3}$. (b) $D_1 = 10^2$, $D_2 = 10^3$, $D_3 = 10^{-2}$.

The results are shown in Fig. 6.4.

We find two characteristic scenarios depending on the set of diffusion constants D_1 , D_2 and D_3 . In Fig. 6.4a, we observe a ρ dependent D_z but it does not depend on Ω . The second scenario is characterized by a weak dependence on the system-size but none on the control parameter ρ , see Fig. 6.4b. We conclude that the system is not well described by Eq. (6.51) and (6.52) since it does not reproduce the key characteristics observed in the full model, i.e., Ω dependent diffusion coefficient at the bifurcation and discontinuous dependence on the control parameter ρ and correspondingly on $\Delta\mu$.

In order to understand this discrepancy, we numerically examine Eq. (6.39), i.e., the system before applying the normal form mapping.

6.5.3 Integration of van Kampen's approximation

We numerically integrate the rate equations, Eq. (6.7), in order to obtain a solution for $\hat{x}(t)$ and $\hat{y}(t)$. Using this solution, we integrate Eq. (6.39) and determine D according to Eq. (6.5), see Fig. 6.5.

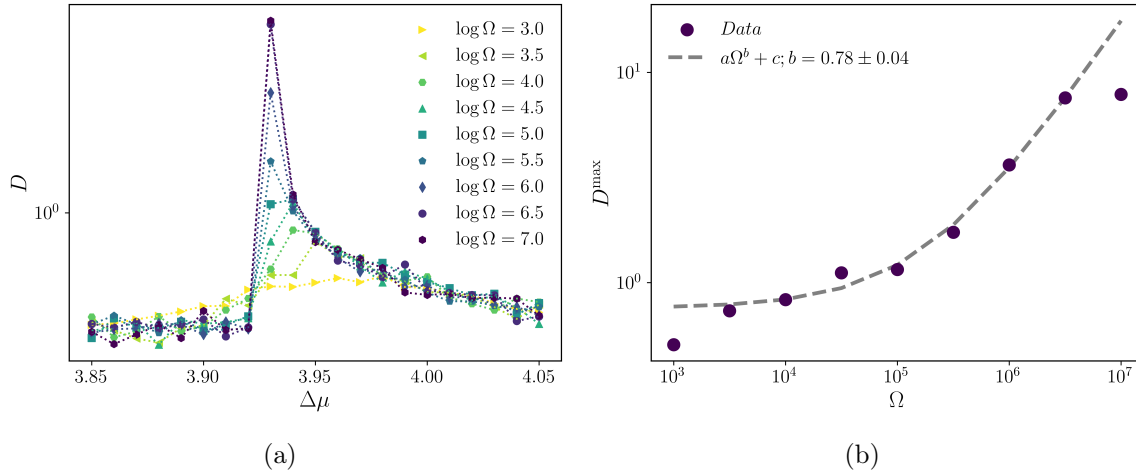


Figure 6.5: Fluctuations of the mean flux in the Brusselator model obtained by numerically solving the mean-field equations, Eq. (6.7), and the Langevin equation for the fluctuations, Eq. (6.39). (a) Diffusion coefficient D of the particle flux as function of the control parameter $\Delta\mu$ for various system sizes Ω . (b) Maximal D as function of the system-size Ω .

The diffusion coefficient D depends discontinuously on the control parameter $\Delta\mu$ with a jump in the vicinity of the bifurcation, see Fig. 6.5a. The maximum value depends on the system-size Ω , i.e.,

$$D^{\max} \propto \Omega^{\phi_{VK}} \quad \text{with} \quad \phi_{VK} = 0.78 \pm 0.04, \quad (6.54)$$

where the exponent is obtained through a fit, see Fig. 6.5b.

Thus, using ansatz Eq. (6.38), we find a discontinuous D as function of $\Delta\mu$. However, the scaling exponent of the maximum value is different than the one obtained through Gillespie's direct method, Eq. (6.9).

In the next section, we consider the full CLE in order to obtain D and compare with the data presented in Sec. 6.3.

6.5.4 Chemical Langevin equation

The chemical Langevin equation for the reaction scheme (6.3) reads

$$\begin{aligned}\partial_t \mathbf{x}(t) &= F_1[\mathbf{x}(t), \mathbf{y}(t)] + \frac{1}{\sqrt{\Omega}} \left(\sqrt{c_A k_1^+ + k_1^- \mathbf{x}(t)} \xi_A(t) + \sqrt{k_2^+ \mathbf{x}(t)^2 \mathbf{y}(t) + k_2^- \mathbf{x}(t)^3} \xi_0(t) \right), \\ \partial_t \mathbf{y}(t) &= F_2[\mathbf{x}(t), \mathbf{y}(t)] + \frac{1}{\sqrt{\Omega}} \left(\sqrt{k_2^+ \mathbf{x}(t)^2 \mathbf{y}(t) + k_2^- \mathbf{x}(t)^3} \xi_0(t) + \sqrt{c_B k_3^+ + k_3^- \mathbf{y}(t)} \xi_B(t) \right), \\ \partial_t \mathbf{z}_B(t) &= k_3^+ c_B - k_3^- \mathbf{y}(t) + \frac{1}{\sqrt{\Omega}} \sqrt{c_B k_3^+ + k_3^- \mathbf{y}(t)} \xi_B(t),\end{aligned}\tag{6.55}$$

where $\mathbf{x}(t) \equiv n_X(t)/\Omega$ denotes the density of particles of species X at time t , analogously for $\mathbf{y}(t)$ and $\mathbf{z}_B(t)$. $F_i[\mathbf{x}, \mathbf{y}]$ is defined in Eq. (6.7) and $\xi_i(t)$ denotes Gaussian-white noise, i.e., $\langle \xi_i(t) \rangle = 0$ and $\langle \xi_i(t) \xi_j(t') \rangle = \delta_{ij} \delta(t - t')$. We numerically integrate Eq. (6.55) and determine the diffusion coefficient D according to Eq. (6.5), see Fig. 6.6.

We obtain a diffusion coefficient that displays a jump at the bifurcation $\Delta\mu^{\text{crit}}$, see Fig. 6.6a. The maximal value of D scales as

$$D^{\text{max}} \propto \Omega^{\phi_{CLE}}, \quad \phi_{CLE} = 0.49 \pm 0.01 .\tag{6.56}$$

Thus, the data obtained by numerically solving the CLE (6.55) shows the same behavior as the one obtained by using Gillespie's direct method, compare Sec. 6.3.

6.5.5 Discussion of the different approximations

We have approximated the reaction scheme (6.3) using van Kampen's system-size expansion in order to obtain an analytical understanding of the diffusion coefficient D . This ansatz has led to Eq. (6.39). Since there are no analytical expressions for the fixed point (x^*, y^*) nor the limit cycle $(x_0(t), y_0(t))$, we have only extracted the Ω scaling of D for the regimes above and below the bifurcation. However, at the bifurcation, we were not able to analytically extract any scaling behavior due to the complexity of the vector-field, Eq. (6.45).

We have further approximated the vector-field, Eq. (6.45), using a normal form mapping, see Sec. 6.5.2. We have numerically found that the resulting equations fail to reproduce the non-analytical behavior of D . We attribute this to the non-systematic truncation during the normal form mapping.

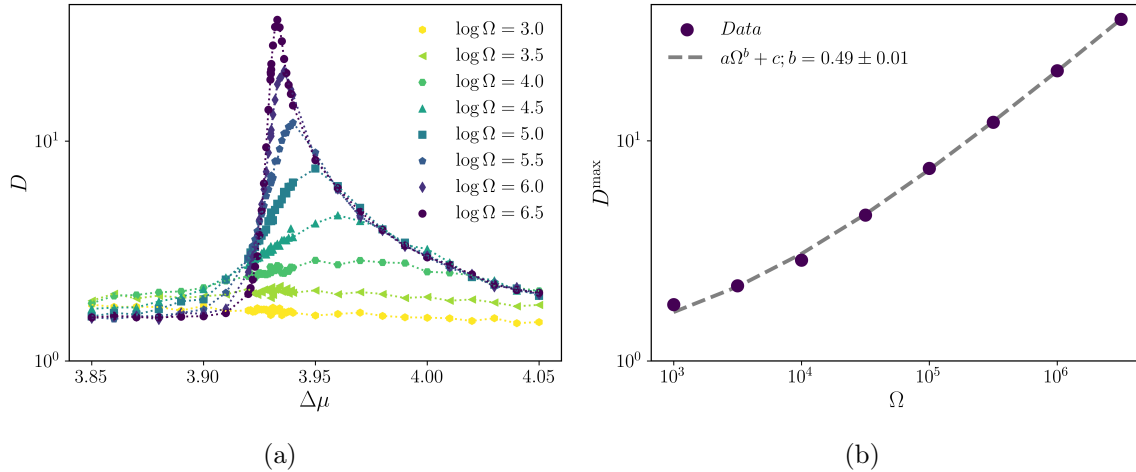


Figure 6.6: Fluctuations of the mean flux in the Brusselator model obtained by numerically integrating the chemical Langevin equation (6.55). (a) D as function of the control parameter $\Delta\mu$ for various system sizes Ω . (b) Maximal D as function of the system-size Ω .

Using the rate equations (6.7) and the Langevin equation for the fluctuations around it, Eq. (6.39), we have numerically obtained a discontinuous diffusion coefficient D but with a wrong scaling exponent for the maximal value. Nevertheless, we conclude that this approach should be sufficient to understand the non-analytical behavior of D . However, we were not able to extract this information from the corresponding equations, thus, leaving it as an open question.

In the last step, we numerically solved the CLE (6.55) and recovered all characteristic behaviors, i.e., a discontinuous D as function of $\Delta\mu$ and a scaling exponent for the maximal value of D that is consistent with Eq. (6.9). This is due to the fact that the chemical Langevin equation approximates the reaction scheme (6.3) exactly in the limit of $\Omega \gg 1$. In this limit, both leap conditions can always be satisfied, see Sec. 2.7.3. However, due to the multiplicative noise of Eq. (6.55), we leave the analytical extraction of the scaling exponents as an open problem.

In conclusion, the equations obtained when using van Kampen's system-size expansion are sufficient in order to understand the discontinuous dependence of the diffusion coefficient on the thermodynamic driving $\Delta\mu$. However, in order to find the correct scaling exponents, the CLE should be considered.

6.6 CONCLUSION

We have examined the thermodynamic consistent Brusselator model, Eq. (6.1), during a Hopf bifurcation. Using the stochastic sampling algorithm, we have numerically shown a continuous dependence of the mean particle flux of reservoir species on the control parameter $\Delta\mu$, see Sec. 6.3. In the vicinity of the bifurcation, this flux develops a kink which leads to a jump in the derivative. This non-differentiable behavior is also found in the solution of the rate equations. Thus, the maximum value of the derivative saturates for growing system-size. These findings are consistent with a previous study [90].

In Sec. 6.4, we have used bifurcation theory and the mapping onto normal forms to theoretically explain this non-differentiable dependence. We have argued that the particle flux consists of two contributions. One is due to the system being in the fixed point. In the oscillatory phase, there is an additional term due to the periodic motion around the fixed point that depends in leading order linear on the control parameter.

Furthermore, we have numerically shown that the diffusion coefficient displays critical behavior when approaching the bifurcation from above, i.e., satisfies a scaling relation, Eq. (6.10), and obtained critical exponents. In the vicinity of the bifurcation, the diffusion coefficient develops a pronounced peak that depends on the system-size. We have obtained a scaling exponent for the maximum value which does not agree with Ref. [90]. However, we reproduce their result when considering system-sizes up to $\Omega = 10^{4.5}$. Approaching the bifurcation from below, the diffusion coefficient develops a discontinuous dependence on $\Delta\mu$ for increasing system-size. This discontinuous behavior is novel and has not been reported before.

In order to understand the diffusion coefficient analytically, we applied the techniques which we have developed in Chapter 5. We have confirmed the system-size independence off the bifurcation. However, due to the lack of an analytical expression for the fixed point and the limit cycle, we were not able to obtain scaling exponents with respect to the thermodynamic driving.

In the vicinity of the bifurcation, we have derived an expression for the vector-field, Eq. (6.45), that we could not further simplify. Using numerical integration, we have shown that the naive application of a normal form mapping does not lead to an equation that captures the complex behavior of the diffusion coefficient, see Sec. 6.5.2. Further numerical integration has been performed using van Kampen's ansatz, Eq. (6.38), and the corresponding equations of motion in Sec. 6.5.3. We have shown that the vector-field, Eq. (6.45), leads to a discontinuous diffusion coefficient with respect to the thermodynamic

driving but to a system-size dependence with an exponent that is off. In Sec. 6.5.4, we have numerically integrated the chemical Langevin equation corresponding to the reaction scheme (6.1). We have found a discontinuous dependence on the thermodynamic driving and on the system-size which is consistent with the one presented in Sec. 6.3.

In contrast to the Schlögl model discussed in Chapter 5, the Brusselator model exhibits a fixed point and a dynamical, oscillatory phase. For the Schlögl model, we have considered a continuous transition with a singular, critical point. However, the Jacobian matrix of the Brusselator model does not become singular at the bifurcation. Furthermore, we have noise terms that are not homogeneous in space. Due to these two facts, we were not able to analytically derive scaling exponents for the Brusselator model or to explain the apparent discontinuity in the diffusion coefficient. Nevertheless, numerical simulations have shown that the vector-field, Eq. (6.45), leads to an discontinuous diffusion coefficient and that the chemical Langevin equation (6.55) reproduces the correct system-size scaling.

In summary, we have numerically found a jump in the derivative of the thermodynamic flux and have theoretically explained this behavior. Furthermore, we have numerically found novel phenomena in the fluctuations of this flux, i.e., a discontinuous dependence of the diffusion coefficient on the control parameter and a scaling exponent for the system-size dependence of the maximum value. The analytical explanation of this behavior is left as an open problem.

CONCLUDING REMARKS

Over the last decades, stochastic thermodynamics has emerged as a fruitful field of research. The novel, dynamical approach towards statistical physics led to a reinterpretation of well established results and concepts such as entropy and the second law. Furthermore, the comprehensive framework of stochastic thermodynamics allows the treatment of systems in thermal equilibrium as well as of those that are out of equilibrium, i.e., constantly producing entropy. Thus, this approach is extending the overall applicability of thermodynamics to living, active or biological systems.

In this thesis, we have examined several nonlinear phenomena in stochastic thermodynamics. In Chapter 3, we have considered the optimization of a finite-time transformation of a system from a given initial to a final state for a minimal entropic cost. This optimization problem has been topic of several studies on continuous state space [24–26, 28, 77]. For the analogous problem on discrete state space, the governing equations have been derived and it has been shown that it reduces to the continuous one in the appropriate limit [27]. However, a characterization of the optimal protocol was still missing. We have proven that the optimal protocols realizing a transformation at lowest entropic cost are in general non-conservative, i.e., include an external driving which is not given by differences of state variables. This is in contrast to systems with continuous state space where the optimal transformation is given by conservative forces [25]. Subsequent studies have been working towards a unification of the optimization problem regarding different underlying state spaces and dynamics [29, 30], thus, putting our result into a broader perspective from an information geometrical point of view.

In Chapter 4, we have turned to the phenomenon of coherent oscillations. We have discussed the question of how "good" a stochastic oscillator can keep its period, hence, its precision. For a one-dimensional motion along a ring, we have derived a novel, analytical expression for the quality factor as a measure for an oscillator to maintain its coherence. Using this expression, we have derived and proven a continuous version of the bound on the quality factor for Markov jump processes conjectured in Ref. [4]. This bound has only recently been proven by Ohga and co-workers [50]. For a particle on a ring, we have further shown that this bound reduces to the one conjectured by Oberreiter and co-workers [5] in

the limit of weak noise, i.e., that the quality factor of a noisy oscillator sets a lower bound on the total entropy produced during one period. Thus, we provide the first and up to now only analytical attempt towards proving this bound.

As biochemical oscillators include at least two different species, we have considered planar oscillators in the subsequent sections. We have developed a theory that projects a two-dimensional oscillator onto an effective one-dimensional motion along the arc-length, thus, allowing the application of the quality factor obtained for a one-dimensional system. We have further studied the validity of this projection method considering the noisy Stuart-Landau oscillator and the Brusselator model. For both models, we have observed a discrepancy when comparing to a theory based on Hamilton-Jacobi theory [45, 46]. However, for the noisy Stuart-Landau oscillator, we have extended our theory in order to capture the full dynamics of the system. Thus, we derived an exact expression for the quality factor of a broad class of planar oscillators. The derived formula only includes quantities known from the equation of motion and does not rely on Hamilton-Jacobi-theory in contrast to the full expression derived in Ref. [45]. Thus, we have provided simple, intuitive insights into the coherence of a noisy oscillator.

A prime example for a noisy oscillator is a chemical reaction network undergoing a Hopf bifurcation or, in terms of stochastic thermodynamics, a system undergoing a continuous phase transition. Before we have examined a noisy Hopf bifurcation in Chapter 6, we have considered the Schlögl model undergoing a continuous phase transitions in Chapter 5. Upon variation of the concentration of a chemostatted species, this system exhibits various transitions. A first order phase transition is characterized by a discontinuous entropy production and thermodynamic flux, respectively, with respect to the control parameter. While this transition and the fluctuations of the thermodynamic flux have been topic of several studies [128, 146], we have focused on paths through the critical point. We have numerically as well as analytically shown that the system undergoes a continuous phase transition. Furthermore, we have numerically found that the associated diffusion coefficient of the thermodynamic flux diverges at the critical point and have determined scaling exponents. In both cases, we have observed critical power-law behavior. Using the chemical Langevin equation and van Kampen's system-size expansion, we have developed a theory in order to analytically obtain the scaling exponents for the diffusion coefficient in the monostable regime. In the bistable regime, we have used an approximation as two-state system in order to analytically understand the critical behavior. In all cases, we have found good agreement between the numerical and analytical results. All in all, our discussion of

the Schlögl model complements the studies that examined the first order transition. Thus, we have completed the thermodynamic understanding of the univariate Schlögl model.

In Chapter 6, we have considered the thermodynamically consistent Brusselator model as a paradigm for a system undergoing a Hopf bifurcation. We have numerically obtained a continuous thermodynamic flux and its discontinuous derivative with respect to a control parameter. Furthermore, at the bifurcation, we have found a diverging diffusion coefficient characterizing the fluctuations of this flux. These results are consistent with a previous study [90]. However, considering system-sizes bigger than in Ref. [90], we have numerically found a discontinuous behavior of the diffusion coefficient with respect to the control parameter below the bifurcation. Above the bifurcation, we have obtained scaling exponents for the diffusion coefficient and found a collapse onto a master-curve. At the bifurcation, the diffusion coefficient diverges with the system-size. However, we have obtained a different scaling exponent than reported in Ref. [90] but recovered the previous result in the limit of small system-sizes.

Using a mapping to the normal form for a Hopf bifurcation, we have analytically derived the non-differentiable behavior of the thermodynamic flux. Applying the methods developed for the Schlögl model, we have derived an expression for the diffusion coefficient that is not analytically treatable. We have numerically shown that a further simplification would not reproduce the observed behavior of the fluctuations. Numerically integrating the rate equations for the mean concentrations and the Langevin equations for their fluctuations, we have shown that the procedure based on van Kampen's system-size expansion reproduces the discontinuity correctly but leads to a different system-size exponent for the divergence of the diffusion coefficient at the bifurcation. However, numerical simulation have shown that the chemical Langevin equation reproduces the behavior of the diffusion coefficient in the vicinity of the critical point. In conclusion, we have analytically derived the jump in the derivative of the thermodynamic flux and numerically observed a discontinuous diffusion coefficient with respect to a control parameter. Due to the theoretically non-treatable expression for the diffusion coefficient, we have left the analytical determination of the scaling exponents and derivation of the discontinuity as an open problem.

In summary, we have considered various nonequilibrium phenomena that arise due to nonlinearities or are intrinsically nonlinear. Using optimal control theory, we have studied the entropic cost of transforming a system from a given initial to a final state in finite time. Furthermore, we have examined the change in the typical behavior of a system while undergoing a phase transition upon variation of an external control parameter. The typical

behavior is captured by an appropriate order parameter such as the thermodynamic flux or for instance the quality factor.

Possible future work could incorporate recent developments regarding large deviation theory for chemical reaction networks [130] or systems undergoing a phase transition [132] in order to examine the fluctuations during a Hopf bifurcation. As the path along the Hopf bifurcation in the Brusselator corresponds to the pathway into coexistence in the Schlögl model, it would be interesting to study the fluctuations of the thermodynamic flux along other pathways that, for instance, corresponds to the critical line of the Schlögl model. Since the system would be monostable along that line, we expect our formalism based on the CLE and van Kampen's system-size expansion to be applicable. However, due to the high dimensionality of the configuration space of the Brusselator, it will be challenging to find an appropriate path. Nevertheless, since the critical behavior of an equilibrium system depends on its dimension, it would be intriguing to study this question for the corresponding nonequilibrium situation.

OPTIMALITY OF NON-CONSERVATIVE DRIVING FOR
FINITE-TIME PROCESSES WITH DISCRETE STATES

A.1 COMMENT ON EQ. (3.11) OF THE MAIN TEXT

In this section, we show that the linear term in Eq. (3.11) of the main text does not vanish, i.e.,

$$\sum_{i=1}^N \tanh \left[\frac{B_i(t) - B_{i+1}(t)}{2} \right] \neq 0, \quad (\text{A.1})$$

from which we can conclude that a non-zero affinity is optimal, in general. In order to understand the implications of a vanishing right hand side of the above relation, it is instructive to consider a network of three states. Requiring the sum in Eq. (A.1) to vanish implies for such a set-up

$$\tanh \frac{B_1(t) - B_2(t)}{2} + \tanh \frac{B_2(t) - B_3(t)}{2} + \tanh \frac{B_3(t) - B_1(t)}{2} = 0. \quad (\text{A.2})$$

This expression simplifies with $\tanh(\alpha + \beta) = \frac{\tanh(\alpha) + \tanh(\beta)}{1 + \tanh(\alpha)\tanh(\beta)}$ to

$$\left(\tanh \frac{B_1(t)}{2} - \tanh \frac{B_2(t)}{2} \right) \left(\tanh \frac{B_2(t)}{2} - \tanh \frac{B_3(t)}{2} \right) \left(\tanh \frac{B_3(t)}{2} - \tanh \frac{B_1(t)}{2} \right) = 0 \quad (\text{A.3})$$

Thus, the solutions are characterized by

1. $B_1(t) = B_2(t)$
 2. $B_1(t) = B_3(t)$
 3. $B_2(t) = B_3(t)$
- (A.4)

We now consider the second case, i.e., $B_1(t) = B_3(t)$. This equality implies that the current $j_{13}(t) = 2\kappa_{13}\phi_1(t)\phi_3(t)\sinh\{[B_1(t) - B_3(t)]/2\} = 0$ is zero for all times, hence, there is effectively no link between state 1 and 3. Furthermore, this equality has consequences for the master equation as well

$$\begin{aligned}\partial_t\phi_1(t) &= -\kappa_{12}\phi_2(t)\sinh\frac{B_1(t) - B_2(t)}{2} \\ \partial_t\phi_2(t) &= \dots \\ \partial_t\phi_3(t) &= -\kappa_{23}\phi_2(t)\sinh\frac{B_1(t) - B_2(t)}{2}.\end{aligned}\tag{A.5}$$

Combining the equations for $\phi_1(t)$ and $\phi_3(t)$, we obtain

$$\partial_t[\phi_1(t)/\kappa_{12} - \phi_3(t)/\kappa_{23}] = 0.\tag{A.6}$$

This results in

$$\phi_1(t)/\kappa_{12} - \phi_3(t)/\kappa_{23} = \text{const}.\tag{A.7}$$

for all times $0 \leq t \leq T$. Since $\phi_1(0/T) = \sqrt{p_1^{0/T}}$ and $\phi_3(0/T) = \sqrt{p_3^{0/T}}$ are the boundary values that we can choose arbitrarily and the densities $\{\phi_i(t)\}$ are continuous for $0 \leq t \leq T$, the assumption of a vanishing right hand side in Eq. (A.1) is in general wrong.

A.2 IMPROVED BOUND FOR SYMMETRIC RATES

We proof Eq. (3.21) of the main text, i.e.,

$$|\mathcal{A}(t)| \leq 2(N - 2), \quad \forall t \in [0, T]\tag{A.8}$$

where here $N \geq 3$ denotes the number of states of a cycle \mathcal{C} in the network, $\mathcal{A}(t)$ the associated affinity and T the total duration of the process. The key-idea of the proof is to ask for which affinities a solution can exist. For convenience we relabel the driving functions of adjacent states along a cycle as

$$x_i \equiv \varphi_{i,i-1}(t)\tag{A.9}$$

for arbitrary but fixed $0 \leq t \leq T$. Thus, Eq. (3.18) from the main text becomes

$$0 = \sum_{i=1}^N \left(x_i + 2 \tanh \frac{x_i}{2} \right) \quad (\text{A.10})$$

and the affinity along the cycle reads

$$\mathcal{A} = \sum_{i=1}^N x_i . \quad (\text{A.11})$$

A possible solution to the variational problem has to satisfy both of these relations. We can thus write the first relation as

$$\mathcal{A} = -2 \sum_{i=1}^N \tanh \frac{x_i}{2} \equiv F_N(x_1, \dots, x_N) . \quad (\text{A.12})$$

Let us now reparameterize the solution-space as

$$(x_1, \dots, x_{k-1}, x_k, x_{k+1}, \dots, x_N) \rightarrow (x_1, \dots, x_{k-1}, \mathcal{A} - \sum_{i \neq k} x_i, x_{k+1}, \dots, x_N) \quad (\text{A.13})$$

using Eq. (A.11). This reflects that we are only interested in solutions that are on the \mathcal{A} -hyperplane for a given affinity. We now look for the maximum respectively minimum value of

$$f_{N-1}(x_1, \dots, x_{k-1}, x_{k+1}, \dots, x_N; \mathcal{A}) \equiv F_N(x_1, \dots, x_{k-1}, \mathcal{A} - \sum_{i \neq k} x_i, x_{k+1}, \dots, x_N) \quad (\text{A.14})$$

which has to be at least \mathcal{A} for a solution to exist. Be $L \gg 1$ arbitrary and $x \equiv (x_1, \dots, x_{k-1}, x_{k+1}, \dots, x_N) \in (-L, L)^{N-1}$.

A.2.1 Local extrema

At first, we consider the local maxima and minima. Setting the derivative of f_{N-1} with respect to x_i ($i \neq k$) to zero gives

$$\frac{1}{\cosh^2 \frac{\mathcal{A} - \sum_{i \neq k} x_i^*}{2}} - \frac{1}{\cosh^2 \frac{x_i^*}{2}} = 0 . \quad (\text{A.15})$$

Thus, we find for all local extrema x^*

$$\cosh \frac{x_i^*}{2} = \cosh \frac{\mathcal{A} - \sum_{i \neq k} x_i^*}{2} \quad (\text{A.16})$$

and the extreme-values are parameterized as

$$\begin{aligned} f_{N-1}^* &\equiv f_{N-1}(x^*; \mathcal{A}) \\ &= -\frac{2}{\cosh \frac{\mathcal{A} - \sum_{i \neq k} x_i^*}{2}} \left[\sum_{i \neq k} \sinh \frac{x_i^*}{2} + \sinh \frac{\mathcal{A} - \sum_{i \neq k} x_i^*}{2} \right]. \end{aligned} \quad (\text{A.17})$$

This expression simplifies with $\sinh(x) = \sigma(x)\sqrt{\cosh^2(x) - 1}$ and Eq. (A.16) to

$$f_{N-1}^* = -2 \left| \tanh \frac{x_k^*}{2} \right| \sum_i \sigma(x_i^*) = 2 \left| \tanh \frac{x_k^*}{2} \right| \{N_- - N_+\}. \quad (\text{A.18})$$

Here, $x_k^* \equiv \mathcal{A} - \sum_{i \neq k} x_i^*$, N_{\pm} is the number of positive respectively negative x_i^* and σ denotes the sign-function. We now distinguish between positive and negative affinities.

A.2.1.1 Positive affinity

Let us assume $\mathcal{A} > 0$. We want to examine when a solution to Eq. (A.12) can exist for positive affinity, hence we need to find an upper bound for f_{N-1}^* . The local extrema are elements of the \mathcal{A} -hyperplane, therefore we find

$$0 < \mathcal{A} = \sum_i x_i^*. \quad (\text{A.19})$$

Thus, at least one of the $\{x_i^*\}$ needs to be positive, i.e. $N_+ \geq 1$. Since the number of states in the cycle satisfies $N = N_+ + N_-$, the number of negative x_i^* is bounded by $N_- \leq N - 1$.

We can now bound the extreme value from above as

$$f_{N-1}^* = 2 \left| \tanh \frac{x_k^*}{2} \right| \{N_- - N_+\} \leq 2 \left| \tanh \frac{x_k^*}{2} \right| \{N - 1 - 1\} \leq 2(N - 2) \quad (\text{A.20})$$

where we used $|\tanh(x)| \leq 1$ in the last step. Thus, the affinity must necessarily satisfy

$$\mathcal{A} \leq 2(N - 2) \quad (\text{A.21})$$

for a possible solution inside $(-L, L)^{N-1}$ and $\mathcal{A} > 0$.

A.2.1.2 *Negative affinity*

Let us assume $\mathcal{A} < 0$. We now need to find a lower bound on f_{N-1}^* in order to make a statement about existence of a solution to Eq. (A.12). A negative affinity implies

$$\sum_i x_i^* < 0. \tag{A.22}$$

Thus, the number of negative x_i^* is now bounded from below $N_- \geq 1$ and therefore $N_+ \leq N - 1$. The minimum value is hence

$$f_{N-1}^* \geq -2(N - 2). \tag{A.23}$$

Therefore, the affinity needs to be bounded from below as

$$\mathcal{A} \geq -2(N - 2) \tag{A.24}$$

by the same reasoning as in the previous section.

In total, we find that the affinity needs to satisfy

$$|\mathcal{A}| \leq 2(N - 2) \tag{A.25}$$

to obtain a solution inside $(-L, L)^{N-1}$. To make the proof complete, we examine the behavior on the boundary $\partial(-L, L)^{N-1}$.

A.2.2 *Extrema on the boundary*

We claim that Eq. (A.25) also holds on the boundary and prove it by induction.

A.2.2.1 *Initial Step: $N = 3$*

We calculate the bounds explicitly for $N = 3$. x_3 is parameterized as $x_3 = \mathcal{A} - x_1 - x_2$ and $\partial(-L, L)^2$ as 4 lines and 4 points, see Fig. A.1.

1. $x_1 = -L$ & $x_2 \in (-L, L)$:

We find a local extremum at

$$x_2^- = \frac{\mathcal{A} + L}{2} \tag{A.26}$$

with value

$$f_2(-L, x_2^-) = -2 \left[2 \tanh \frac{L + \mathcal{A}}{2} - \tanh \frac{L}{2} \right] \geq -2 \quad (\text{A.27})$$

2. $x_1 = +L$ & $x_2 \in (-L, L)$:

We find a local extremum at

$$x_2^+ = \frac{\mathcal{A} - L}{2} \quad (\text{A.28})$$

with value

$$f_2(L, x_2^+) = 2 \left[2 \tanh \frac{L - \mathcal{A}}{2} - \tanh \frac{L}{2} \right] \leq 2 \quad (\text{A.29})$$

3. $x_1 \in (-L, L)$ & $x_2 = -L$:

We find a local extremum at

$$x_1^- = \frac{\mathcal{A} + L}{2} \quad (\text{A.30})$$

with value

$$f_2(x_1^-, -L) = -2 \left[2 \tanh \frac{L + \mathcal{A}}{2} - \tanh \frac{L}{2} \right] \geq -2 \quad (\text{A.31})$$

4. $x_1 \in (-L, L)$ & $x_2 = +L$:

We find a local extremum at

$$x_1^+ = \frac{\mathcal{A} - L}{2} \quad (\text{A.32})$$

with value

$$f_2(x_1^+, L) = 2 \left[2 \tanh \frac{L - \mathcal{A}}{2} - \tanh \frac{L}{2} \right] \leq 2 \quad (\text{A.33})$$

5. $x_1 = L$ & $x_2 = L$:

$$f_2(L, L) = -2 \left[2 \tanh \frac{L}{2} - \tanh \frac{2L - \mathcal{A}}{2} \right] \geq -2 \quad (\text{A.34})$$

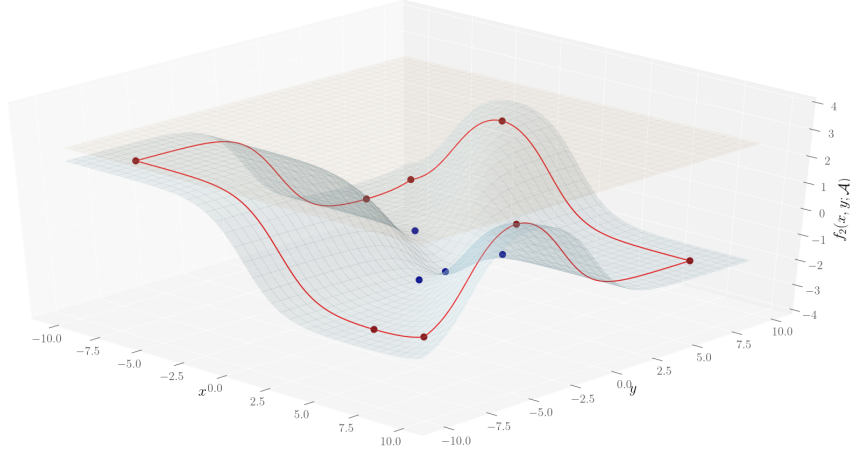


Figure A.1: Illustration of the explicit calculations for the 3 state system. The blue graph is $f_2(x_1, x_2; \mathcal{A})$ and the red surface is $\mathcal{A} = x_1 + x_2 + x_3$. The thick red line represents f_2 along the boundary $\partial(-L, L)^2$. The red dots display the 8 boundary-points discussed in the text. Blue dots represent the local extrema inside $(-L, L)^2$. In this example we set $\mathcal{A} = 2.5$ and $L = 8$, thus, there's no intersection between the \mathcal{A} -plane and the graph of f_2 .

6. $x_1 = -L$ & $x_2 = -L$:

$$f_2(-L, -L) = 2 \left[2 \tanh \frac{L}{2} - \tanh \frac{2L - \mathcal{A}}{2} \right] \leq 2 \quad (\text{A.35})$$

7. $x_1 = -L$ & $x_2 = L$:

$$\begin{aligned} f_2(-L, L) &= -2 \tanh \frac{\mathcal{A}}{2} \\ |f_2(-L, L)| &\leq 2 \end{aligned} \quad (\text{A.36})$$

8. $x_1 = L$ & $x_2 = -L$:

$$\begin{aligned} f_2(L, -L) &= -2 \tanh \frac{\mathcal{A}}{2} \\ |f_2(L, -L)| &\leq 2 \end{aligned} \quad (\text{A.37})$$

Thus, we find on $\partial(-L, L)^2$ that

$$|f_2(x_1, x_2)| \leq 2 = 2(N - 2) \quad (\text{A.38})$$

for $N = 3$.

A.2.2.2 Inductive step

Let us assume that for an arbitrary $N \geq 3$

$$|F_N(x_1, \dots, x_N)| \leq 2(N - 2) . \quad (\text{A.39})$$

holds true. Let $k \in \{1, 2, \dots, N + 1\}$ be arbitrary and set $x_k = \pm L$. Let us now write

$$\begin{aligned} F_{N+1}(x_1, \dots, x_{k-1}, \pm L, x_{k+1}, \dots, x_{N+1}) &= -2 \sum_{i \neq k} \tanh \frac{x_i}{2} \mp 2 \tanh \frac{L}{2} \\ &= F_N(x_1, \dots, x_{k-1}, x_{k+1}, \dots, x_{N+1}) \mp 2 \tanh \frac{L}{2} . \end{aligned} \quad (\text{A.40})$$

Thus, we find by assumptions and using $|\tanh x| \leq 1$

$$\begin{aligned} \left| F_{N+1}(x_1, \dots, x_{k-1}, \pm L, x_{k+1}, \dots, x_{N+1}) \right| &\leq \left| F_N(x_1, \dots, x_{k-1}, x_{k+1}, \dots, x_{N+1}) \right| + 2 \left| \tanh \frac{L}{2} \right| \\ &\leq 2(N - 2) + 2 = 2(N - 1) . \end{aligned} \quad (\text{A.41})$$

This completes the proof by induction since k is arbitrary,

A.2.3 Concluding remark

We specified the length L of the $N - 1$ -cube as arbitrary large. In fact, we need to be more precise for all statements to be true. In order to include all local extrema, we need $L > \max_i |x_i^*|$. We suppressed this conditions since we are interested in the limit $L \rightarrow \infty$ and by definition, setting the derivative zero will find only finite x_i^* . Moreover, all arguments in the explicit calculations for $N = 3$ are only true for $L > |\mathcal{A}|$ which again can be neglected since we already know that $|\mathcal{A}| \leq 2N < \infty$ and we examine $L \rightarrow \infty$. The important fact is that all derived bounds are independent on $L \gg 1$.

A.3 NUMERICAL SCHEME

In this section, we describe the numerical scheme that we implemented in Python to solve the Euler-Lagrange equations, Eq. (3.7,3.16,3.17) in the main text. The imposed boundary value problem is of the following form:

$$\begin{aligned}\partial_t \phi_i(t) &= f_i(\{\phi_i(t)\}, \{\eta_i(t)\}, \{\varphi_{ij}(t)\}) \\ \partial_t \eta_i(t) &= g_i(\{\phi_i(t)\}, \{\eta_i(t)\}, \{\varphi_{ij}(t)\}) \\ 0 &= r_{ij}(\{\phi_i(t)\}, \{\eta_i(t)\}, \{\varphi_{ij}(t)\})\end{aligned}\tag{A.42}$$

with given boundary values $\{\phi_i(0) = \sqrt{p_i^0}\}$ and $\{\phi_i(T) = \sqrt{p_i^T}\}$. The relation above is a system of ordinary differential equations coupled with a non-linear, algebraic constrain. For the concrete set-up, the algebraic equation is given through the variation with respect to $\{\varphi_{ij}(t)\}$

$$r_{ij}(t) = \eta_i(t)\phi_j(t) - \eta_j(t)\phi_i(t) + 4\phi_i(t)\phi_j(t) \left[\tanh \frac{\varphi_{ij}(t)}{2} + \frac{\varphi_{ij}(t)}{2} \right].\tag{A.43}$$

We solve Eq. (A.42) using a shooting method [155, chapter 87] where we treat the $\{\eta_i(0)\}$ as free shooting-parameter. The numerical scheme can be summarized as follows:

1. Make an initial guess for $\{\eta_i(0)\}$
2. Solve Eq. (A.43) for $\{\varphi_{ij}(0)\}$ with given $\{\phi_i(0)\}$ and $\{\eta_i(0)\}$.
3. Calculate

$$\begin{pmatrix} \{\phi_i(t + \Delta t)\} \\ \{\eta_i(t + \Delta t)\} \end{pmatrix} \approx \text{G-2}(\{\phi_i(t)\}, \{\eta_i(t)\}, \{\varphi_{ij}(t)\})$$

4. Update $\{\varphi_{ij}(t + \Delta t)\}$ by solving $0 = r_{ij}(\{\phi_i(t + \Delta t)\}, \{\eta_i(t + \Delta t)\}, \{\varphi_{ij}(t + \Delta t)\})$.
5. Repeat step 3 and 4 until T is reached.
6. Compare the numerically obtained values for $\{\phi_i(T)\}$ with the given ones $\{\phi_i^T \equiv \sqrt{p_i^T}\}$:
 - If $\phi_i(T) \approx \phi_i^T$ within a tolerance of Δt , accept the solution.
 - If $|\phi_i(T) - \phi_i^T| > \Delta t$ for at least one i , start from 1 with another initial guess.

We used the implicit 2-step Gauß-scheme (G-2) [155, chapter 78] to integrate the ODE-part of Eq. (A.42) and the SciPy-root function to solve Eq. (A.43). For updating the initial guess for $\{\eta_i(0)\}$ we also used the root function of SciPy. We iterated this scheme up to 20 times to find convergent solutions. The step size was chosen as $\Delta t = T/n$ where we kept $n = 10000$ constant.

A.4 RANDOMLY GENERATED CONFIGURATIONS

We now describe how we generated the random set of initial and final distributions. In order to obtain uniformly distributed densities from the allowed parameter-ranges of the 3 states system, we used the following parametrization [156, Eq. (1)]

$$\begin{pmatrix} p_1 \\ p_2 \\ p_3 \end{pmatrix} (u, v) = (1 - \sqrt{u}) \vec{e}_1 + \sqrt{u}(1 - v) \vec{e}_2 + v\sqrt{u} \vec{e}_3 \quad (\text{A.44})$$

with \vec{e}_i the unit-vector in the i -th direction, see Fig. A.2. Choosing u, v uniformly distributed between 0 and 1 results in the vector $\vec{p} = (p_1, p_2, p_3)^T$ to be uniformly distributed over the surface area of the triangle of allowed state densities.

We generated 999 configurations. We could not find a numerically stable solution for 13 configuration for an allocated time $T = 1$, not for 61 for $T = 0.1$ and not for 112 for $T = 0.01$.

A.5 AFFINITY BOUND FOR NONSYMMETRICAL SPLITTING

We determine the equivalent of the bound, Eq. (3.20), on the affinity for the case of a nonsymmetrical splitting of the jump-rates, i.e., for

$$\begin{aligned} k_{ij}(t) &= \kappa_{ij} \exp(\alpha_{ij} A_{ij}(t)) \\ k_{ji}(t) &= \kappa_{ji} \exp[(1 - \alpha_{ij}) A_{ji}(t)] \end{aligned} \quad (\text{A.45})$$

with $\kappa_{ij} = \kappa_{ji} = \text{const.}$ and $0 < \alpha_{ij} = \alpha_{ji} < 1$.

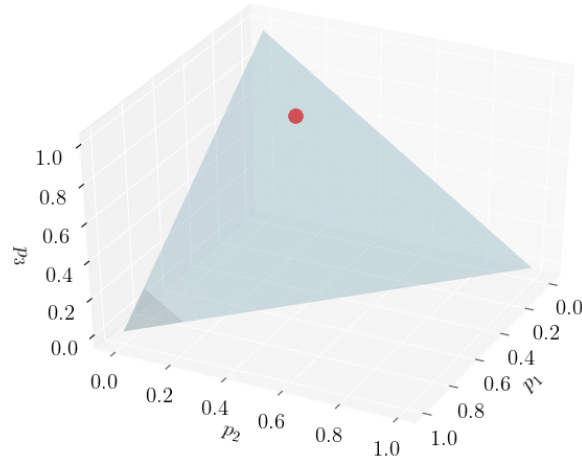


Figure A.2: Random point (red dot) in the allowed region of the probabilities-phase space, which is defined by the the constrains $0 < p_i < 1$ and $\sum_i p_i = 1$ (blue area).

The Lagrange-function is given by

$$\begin{aligned}
 L(t) = & \sum_{i \neq j} p_i(t) \kappa_{ij} \exp[\alpha_{ij} A_{ij}(t)] \ln \left\{ \frac{p_i(t)}{p_j(t)} \exp[A_{ij}(t)] \right\} \\
 & + \sum_i \eta_i(t) \left\{ \partial_t p_i(t) - \sum_{j \neq i} [\kappa_{ji} \exp((1 - \alpha_{ij}) A_{ji}(t)) p_j(t) - \kappa_{ij} \exp(\alpha_{ij} A_{ij}(t)) p_i(t)] \right\} .
 \end{aligned} \tag{A.46}$$

To find an expression for a cycle affinity, we need to evaluate the variation with respect to $A_{ij}(t)$. From $\delta L / \delta A_{ij}(t) = 0$ ($i < j$) we find

$$A_{ij}(t) = - \ln \frac{p_i(t)}{p_j(t)} - \eta_i(t) + \eta_j(t) - \frac{p_i(t) \exp[A_{ij}(t)] - p_j(t)}{\alpha_{ij} \exp[A_{ij}(t)] p_i(t) + (1 - \alpha_{ij}) p_j(t)} . \tag{A.47}$$

We sum this relation over an arbitrary cycle \mathcal{C} in the network, to find for the corresponding affinity

$$\mathcal{A}_c(t) \equiv \sum_{(i,j) \in \mathcal{C}} A_{ij}(t) = - \sum_{(i,j) \in \mathcal{C}} \frac{p_i(t) \exp[A_{ij}(t)] - p_j(t)}{\alpha_{ij} \exp[A_{ij}(t)] p_i(t) + (1 - \alpha_{ij}) p_j(t)} . \tag{A.48}$$

This relation simplifies to

$$\begin{aligned} \mathcal{A}_c(t) = & - \sum_{(i,j) \in \mathcal{C}} \frac{1}{\alpha_{ij} + (1 - \alpha_{ij}) \exp[-A_{ij}(t)] p_j(t)/p_i(t)} \\ & + \sum_{(i,j) \in \mathcal{C}} \frac{1}{\alpha_{ij} \exp[A_{ij}(t)] p_i(t)/p_j(t) + (1 - \alpha_{ij})} . \end{aligned} \quad (\text{A.49})$$

Since all terms in the denominator are positive, we use $1/(a+b) \leq 1/a$ for $a, b > 0$ to derive the bound, Eq. (3.23), on the cycle affinity

$$- \sum_{(i,j) \in \mathcal{C}} \frac{1}{\alpha_{ij}} \leq \mathcal{A}_c(t) \leq \sum_{(i,j) \in \mathcal{C}} \frac{1}{1 - \alpha_{ij}} . \quad (\text{A.50})$$

Alternatively, we can rewrite Eq. (A.49) as

$$\mathcal{A}_c(t) = -2 \sum_{(i,j) \in \mathcal{C}} \frac{\tanh \frac{\varphi_{ij}(t)}{2}}{1 - (1 - 2\alpha_{ij}) \tanh \frac{\varphi_{ij}(t)}{2}} \quad (\text{A.51})$$

with $\varphi_{ij}(t) = A_{ij}(t) + \ln p_i(t) - \ln p_j(t)$, which is a direct generalization of the symmetric case, Eq. (3.19), described in the main text. Eq. (A.50) follows from the monotonic behavior in $\varphi_{ij}(t)$ of the summands for given α_{ij} .

A.6 CONTINUUM LIMIT FOR NONSYMMETRICAL SPLITTING

We derive the continuum limit of a cycle affinity for rates parameterized as Eq. (A.45). Relabeling adjacent states in a cycle from (i, j) to $(x, x + dx)$ with a lattice spacing dx leads to

$$\mathcal{A}_c(t) = \sum_{x \in \mathcal{C}} A_{x, x+dx}(t) . \quad (\text{A.52})$$

In the limit $dx \rightarrow 0$ we find by a Taylor-expansion

$$\mathcal{A}_c(t) \approx \sum_{x \in \mathcal{C}} A'_{x,x}(t) dx \approx \oint_{\mathcal{C}} A'_{x,x}(t) dx \quad (\text{A.53})$$

where the prime denotes a spatial derivative. The limit value of this contour integral is dictated by a Taylor-expansion of Eq. (A.48) for small dx

$$\mathcal{A}_c(t) \approx \sum_{x \in \mathcal{C}} \frac{p'_x(t)}{p_x(t)} dx - \sum_{x \in \mathcal{C}} A'_{x,x}(t) dx \approx \oint_{\mathcal{C}} d \log p_x(t) - \oint_{\mathcal{C}} A'_{x,x}(t) dx . \quad (\text{A.54})$$

We now combine this relation with Eq. (A.53) to obtain

$$\mathcal{A}_c(t) \approx \frac{1}{2} \oint_{\mathcal{C}} d \log p_x(t) = 0 . \quad (\text{A.55})$$

In the last step, we have used that the closed contour integral over a total differential vanishes.

COHERENCE OF OSCILLATIONS IN THE WEAK-NOISE LIMIT

B.1 IRRELEVANCE OF THE SECOND SOLUTION OF THE ONE-DIMENSIONAL FOKKER-PLANCK SYSTEM

We follow the calculations of Sec. 4.3.1 in the main text and calculate the eigenvalues for the second solution of Eq. (4.11),

$$\tilde{g}(x) = -\frac{F(x)}{Q(x)} + \frac{1}{\Omega} \left(-\frac{\lambda}{F(x)} + \frac{Q'(x)}{Q(x)} \right) + \mathcal{O}\left(\frac{1}{\Omega^2}\right). \quad (\text{B.1})$$

From Eq. (4.17), we obtain the eigenvalues

$$\tilde{\lambda}^{(k)} \approx -i 2\pi k \frac{1}{\int_0^L 1/F(x) dx} - \Omega \frac{\int_0^L F(x)/Q(x) dx}{\int_0^L 1/F(x) dx}. \quad (\text{B.2})$$

The resulting quality factor would be given as

$$\tilde{\mathcal{R}} = \left| \frac{\Im \tilde{\lambda}^{(1)}}{\Re \tilde{\lambda}^{(1)}} \right| = \mathcal{O}\left(\frac{1}{\Omega}\right), \text{ for } \Omega \rightarrow \infty. \quad (\text{B.3})$$

Thus, this second solution, Eq. (B.1), does not contribute to oscillations in the weak-noise limit.

B.2 METHOD INTRODUCED IN [45]

In this Appendix, we briefly discuss the numerical scheme to obtain the quality factor according to [45]. For theoretical background we refer to the original publication [45], see also [46, 86].

As first step, one obtains the limit cycle by numerically integrating the deterministic equation of motion, i.e.,

$$\frac{d}{dt} \begin{pmatrix} x(t) \\ y(t) \end{pmatrix} = \begin{pmatrix} F_x(x(t), y(t)) \\ F_y(x(t), y(t)) \end{pmatrix} . \quad (\text{B.4})$$

We label this periodic solution $(\bar{x}(t), \bar{y}(t))$. The period T can be obtained from the numerical data, for instance, by estimating the distance of adjacent maxima.

The next step is to calculate the eigenvectors of the fundamental matrix

$$M(T) = \begin{pmatrix} M_{11}(T) & M_{12}(T) \\ M_{21}(T) & M_{22}(T) \end{pmatrix} \quad (\text{B.5})$$

at time T . In order to do so, one has to solve the following system of differential equations for $0 \leq t \leq T$,

$$\begin{cases} \frac{d}{dt} M(t) = DF(\bar{x}(t), \bar{y}(t)) M(t) \\ M(0) = \mathcal{I} \end{cases} \quad (\text{B.6})$$

with the two-dimensional unity matrix \mathcal{I} and the Jacobian matrix $DF(\bar{x}(t), \bar{y}(t))$ evaluated along the limit cycle. The solution $M(T)$ has an eigenvalue $\Lambda_1 = 1$ with right eigenvector

$$e_1 \equiv F(\bar{x}(T), \bar{y}(T)) , \quad (\text{B.7})$$

which reflects the stability of the periodic solution. The corresponding left eigenvector is denoted by f_1 , i.e.,

$$M(T)^T f_1 = f_1 . \quad (\text{B.8})$$

This eigenvector is chosen such that

$$f_1 \cdot e_1 = 1 , \quad (\text{B.9})$$

where we used the standard scalar product as in the main text. The second eigenvalue Λ_2 with $|\Lambda_2| < 1$ and eigenvectors e_2 respectively f_2 can be ignored.

Deviations from the limit cycle evolve during one period according to the following system of differential equations,

$$\left\{ \begin{array}{l} \frac{d}{dt} \begin{pmatrix} \delta x(t) \\ \delta y(t) \end{pmatrix} = \begin{pmatrix} \partial_x F_x(\bar{x}(t), \bar{y}(t)) & \partial_x F_y(\bar{x}(t), \bar{y}(t)) \\ \partial_y F_x(\bar{x}(t), \bar{y}(t)) & \partial_y F_y(\bar{x}(t), \bar{y}(t)) \end{pmatrix} \begin{pmatrix} \delta x(t) \\ \delta y(t) \end{pmatrix} \\ \frac{d}{dt} \begin{pmatrix} \delta p_x(t) \\ \delta p_y(t) \end{pmatrix} = - \begin{pmatrix} \partial_x F_x(\bar{x}(t), \bar{y}(t)) & \partial_x F_y(\bar{x}(t), \bar{y}(t)) \\ \partial_y F_x(\bar{x}(t), \bar{y}(t)) & \partial_y F_y(\bar{x}(t), \bar{y}(t)) \end{pmatrix}^T \begin{pmatrix} \delta p_x(t) \\ \delta p_y(t) \end{pmatrix} \end{array} \right. , \quad \begin{pmatrix} \delta x(0) \\ \delta y(0) \end{pmatrix} = \begin{pmatrix} 0 \\ 0 \end{pmatrix} \\ \begin{pmatrix} \delta p_x(0) \\ \delta p_y(0) \end{pmatrix} = \begin{pmatrix} f_{1,x} \\ f_{1,y} \end{pmatrix} . \quad (\text{B.10})$$

As a last step, the solution

$$\delta X(T) \equiv \begin{pmatrix} \delta x(T) \\ \delta y(T) \end{pmatrix} \quad (\text{B.11})$$

determines the quality factor as

$$\mathcal{R} \equiv \Omega \frac{T^2}{\pi |f_1 \cdot \delta X(T)|} . \quad (\text{B.12})$$

NONEQUILIBRIUM FLUCTUATIONS OF CHEMICAL
REACTION NETWORKS AT CRITICALITY – THE SCHLÖGL
MODEL AS PARADIGMATIC CASE

C.1 PHASE DIAGRAM IN THE $c_A - c_B$ -PLANE

We derive the phase diagram, Fig. 5.1. The right hand side of the rate-equation (5.8) is a cubic polynomial. The number of roots, i.e., fixed points, is determined by the cubic discriminant

$$\Delta \equiv -4 + c_A^2 + 18c_Ac_B - 4c_A^3c_B - 27c_B^2 . \quad (\text{C.1})$$

For $\Delta > 0$, the polynomial has three distinct real roots, whereas for $\Delta < 0$, there is only one real root. The limiting case of $\Delta = 0$ gives the phase boundary where we find at least one double root. Thus, setting $\Delta = 0$ and solving for c_B , we obtain the boundary curves of the cusp-like region

$$c_B^\pm(c_A) \equiv [9c_A - 2c_A^3 \pm (c_A^2 - 3)^{3/2}]/27 . \quad (\text{C.2})$$

At the critical point, both solution meet, i.e.,

$$c_B^\pm(c_A \rightarrow c_A^{\text{crit}}) = \sqrt{3}/9 , \quad (\text{C.3})$$

with the same slope

$$\frac{\partial c_B^\pm}{\partial c_A}(c_A^{\text{crit}}) = -1/3 . \quad (\text{C.4})$$

This is the slope of the blue line, Fig. 5.1, considered in Sec. 5.4.

In the regime with two stable fixed points, x_{\pm} , see Sec. 5.4, there exists a line in phase space which is denoted as coexistence line. This line is defined through the condition that the nonequilibrium potential, Eq. (5.85), has two global minima, i.e.,

$$\phi(x_+) = \phi(x_-) . \quad (\text{C.5})$$

Since the potential and the two minima depend on the concentrations c_A and c_B , above relation defines the coexistence line as a parametric curve in the $c_A - c_B$ -plane.

C.2 DIFFUSION COEFFICIENT IN LINEAR SYSTEM

Consider a system that is described by the following Langevin equation

$$\begin{aligned} \partial_t x(t) &= -Kx(t) + \sqrt{2\Delta_A}\xi_A(t) + \sqrt{2\Delta_B}\xi_B(t) \\ \partial_t z(t) &= -x(t) + \sqrt{2\Delta_B}\xi_B(t) , \end{aligned} \quad (\text{C.6})$$

with $K, \Delta_A, \Delta_B > 0$ and Gaussian white noise $\xi_i(t)$, i.e., $\langle \xi_i(t) \rangle = 0$ and $\langle \xi_i(t)\xi_j(t') \rangle = \delta_{ij}\delta(t-t')$. The diffusion coefficient,

$$D \equiv \lim_{t \rightarrow \infty} \frac{\text{Var}[z(t)]}{2t} , \quad (\text{C.7})$$

can be obtained explicitly as follows.

The x -fluctuations describe an Ornstein-Uhlenbeck process [38, 39] with solution

$$x(t) = \exp(-Kt) \int_0^t d\tau \exp(K\tau) \sum_{\rho=A,B} \sqrt{2\Delta_\rho} \xi_\rho(\tau) . \quad (\text{C.8})$$

A solution for $z(t)$ is given by

$$z(t) = - \int_0^t d\tau x(\tau) + \sqrt{2\Delta_B} \int_0^t d\tau \xi_B(\tau) . \quad (\text{C.9})$$

With

$$\langle x(\tau)x(\tau') \rangle = (\Delta_A + \Delta_B)(e^{-K|\tau-\tau'|} - e^{-K(\tau+\tau')})/K \quad (\text{C.10})$$

and

$$\langle x(\tau)\xi_B(\tau') \rangle = \sqrt{2\Delta_B} \exp[-K(\tau - \tau')] \theta(\tau - \tau') , \quad (\text{C.11})$$

where $\theta(x) = 1$ for $x > 0$ and $\theta(x) = 0$ elsewhere, we get

$$D = \Delta_B(1 - 1/K)^2 + \Delta_A/K^2 . \quad (\text{C.12})$$

Identifying the coefficients as

$$K = |\alpha'_1(x^*)|, \quad \Delta_A = (\sqrt{3} + \Delta c_A)x^{*2} + x^{*3} \quad \text{and} \quad \Delta_B = (\sqrt{3} + \Delta c_A)/9 + x^* , \quad (\text{C.13})$$

where $x^* = x^*(\Delta c_A)$ is given in Eq. (5.21) and $\alpha_1(x)$ in Eq. (5.61), we obtain Eq. (5.63) after a Taylor-expansion for $|\Delta c_A| \ll 1$.

Respectively, identifying the coefficients as

$$K = |\alpha'_1(x_0)|, \quad \Delta_A = (\sqrt{3} + \Delta c_A)x_0^2 + x_0^3 \quad \text{and} \quad \Delta_B = (\sqrt{3}/9 - \Delta c_A/3) + x_0 , \quad (\text{C.14})$$

where $x_0 = 1/\sqrt{3}$ is given in Eq. (5.73) and $\alpha_1(x)$ through the right hand side of the rate-equation (5.72), we obtain Eq. (5.77).

The following coefficients

$$K = |\alpha'_1(x^*)|, \quad \Delta_A = (\sqrt{3} + \Delta c_A)x^{*2} + x^{*3} \quad \text{and} \quad \Delta_B = \sqrt{3}/9 - (1/3 - \delta)\Delta c_A + x^* , \quad (\text{C.15})$$

where $x^* = x^*(\Delta c_A \delta)$ is given in Eq. (5.98) and $\alpha_1(x)$ through the right hand side of Eq. (5.97), lead to Eq. (5.100).

BIBLIOGRAPHY

- [1] Remlein, B. & Seifert, U. *Optimality of nonconservative driving for finite-time processes with discrete states*. *Phys. Rev. E* **103**, L050105 (2021).
- [2] Remlein, B., Weissmann, V. & Seifert, U. *Coherence of oscillations in the weak-noise limit*. *Phys. Rev. E* **105**, 064101 (2022).
- [3] Remlein, B. & Seifert, U. *Nonequilibrium fluctuations of chemical reaction networks at criticality: The Schlögl model as paradigmatic case*. arXiv: **2402.13168** (2024).
- [4] Barato, A. C. & Seifert, U. *Coherence of biochemical oscillations is bounded by driving force and network topology*. *Phys. Rev. E* **95**, 062409 (2017).
- [5] Oberreiter, L., Seifert, U. & Barato, A. C. *Universal minimal cost of coherent biochemical oscillations*. *Phys. Rev. E* **106**, 014106 (2022).
- [6] Carnot, S. *Réflexions Sur la Puissance Motrice du Feu* (Vrin, 1978).
- [7] Boltzmann, L. *Über die mechanische Bedeutung des zweiten Hauptsatzes der Wärmetheorie*. *Wiener Berichte*. **53**, 195–220 (1866).
- [8] Gibbs, J. *Elementary Principles in Statistical Mechanics* (Charles Scribner's sons, 1902).
- [9] Ritort, F. *Single-molecule experiments in biological physics: methods and applications*. *Journal of Physics: Condensed Matter* **18**, R531 (2006).
- [10] Ciliberto, S. *Experiments in Stochastic Thermodynamics: Short History and Perspectives*. *Phys. Rev. X* **7**, 021051 (2017).
- [11] Einstein, A. *Über die von der molekularkinetischen Theorie der Wärme geforderte Bewegung von in ruhenden Flüssigkeiten suspendierten Teilchen*. *Annalen der Physik* **322**, 549–560 (1905).
- [12] Seifert, U. *Stochastic thermodynamics, fluctuation theorems and molecular machines*. *Reports on Progress in Physics* **75**, 126001 (2012).
- [13] Peliti, L. & Pigolotti, S. *Stochastic Thermodynamics: An Introduction* (Princeton University Press, Princeton, New Jersey, 2021).
- [14] Sekimoto, K. *Stochastic Energetics* (Springer, Heidelberg, 2010).

- [15] Seifert, U. *Entropy Production along a Stochastic Trajectory and an Integral Fluctuation Theorem*. *Phys. Rev. Lett.* **95**, 040602 (2005).
- [16] Jarzynski, C. *Nonequilibrium Equality for Free Energy Differences*. *Phys. Rev. Lett.* **78**, 2690–2693 (1997).
- [17] Crooks, G. E. *Entropy production fluctuation theorem and the nonequilibrium work relation for free energy differences*. *Phys. Rev. E* **60**, 2721–2726 (1999).
- [18] Seifert, U. *Fluctuation theorem for birth–death or chemical master equations with time-dependent rates*. *Journal of Physics A: Mathematical and General* **37**, L517 (2004).
- [19] Barato, A. C. & Seifert, U. *Thermodynamic Uncertainty Relation for Biomolecular Processes*. *Phys. Rev. Lett.* **114**, 158101 (2015).
- [20] Horowitz, J. M. & Gingrich, T. R. *Proof of the finite-time thermodynamic uncertainty relation for steady-state currents*. *Phys. Rev. E* **96**, 020103 (2017).
- [21] Seifert, U. *Stochastic thermodynamics: From principles to the cost of precision*. *Physica A: Statistical Mechanics and its Applications* **504**. Lecture Notes of the 14th International Summer School on Fundamental Problems in Statistical Physics, 176–191 (2018).
- [22] Seifert, U. *From Stochastic Thermodynamics to Thermodynamic Inference*. *Annual Review of Condensed Matter Physics* **10**, 171–192 (2019).
- [23] Andresen, B. *Current Trends in Finite-Time Thermodynamics*. *Angewandte Chemie International Edition* **50**, 2690–2704 (2011).
- [24] Schmiedl, T. & Seifert, U. *Optimal Finite-Time Processes In Stochastic Thermodynamics*. *Phys. Rev. Lett.* **98**, 108301 (2007).
- [25] Aurell, E., Mejía-Monasterio, C. & Muratore-Ginanneschi, P. *Optimal Protocols and Optimal Transport in Stochastic Thermodynamics*. *Phys. Rev. Lett.* **106**, 250601 (2011).
- [26] Aurell, E., Gawedzki, K., Mejía-Monasterio, C., Mohayaei, R. & Muratore-Ginanneschi, P. *Refined second law of thermodynamics for fast random processes*. *Journal of Statistical Physics* **147**, 487–505 (2012).
- [27] Muratore-Ginanneschi, P., Mejía-Monasterio, C. & Peliti, L. *Heat release by controlled continuous-time Markov jump processes*. *Journal of Statistical Physics* **150**, 181–203 (2013).

- [28] Dechant, A. & Sakurai, Y. *Thermodynamic interpretation of Wasserstein distance*. arXiv: **1912.08405** (2019).
- [29] Dechant, A. *Minimum entropy production, detailed balance and Wasserstein distance for continuous-time Markov processes*. *Journal of Physics A: Mathematical and Theoretical* **55**, 094001 (2022).
- [30] Van Vu, T. & Saito, K. *Thermodynamic Unification of Optimal Transport: Thermodynamic Uncertainty Relation, Minimum Dissipation, and Thermodynamic Speed Limits*. *Phys. Rev. X* **13**, 011013 (2023).
- [31] Evans, L. *Partial Differential Equations* (American Mathematical Society, Providence, Rhode Island, 1998).
- [32] Gaspard, P. *Fluctuation theorem for nonequilibrium reactions*. *The Journal of Chemical Physics* **120**, 8898–8905 (2004).
- [33] Schmiedl, T. & Seifert, U. *Stochastic thermodynamics of chemical reaction networks*. *The Journal of Chemical Physics* **126**, 044101 (2007).
- [34] Rao, R. & Esposito, M. *Nonequilibrium Thermodynamics of Chemical Reaction Networks: Wisdom from Stochastic Thermodynamics*. *Phys. Rev. X* **6**, 041064 (2016).
- [35] Gillespie, D. T. *Exact Stochastic Simulation of Coupled Chemical Reactions*. *The Journal of Physical Chemistry* **81**, 2340–2361 (1977).
- [36] Touchette, H. *Introduction to dynamical large deviations of Markov processes*. *Physica A: Statistical Mechanics and its Applications* **504**. Lecture Notes of the 14th International Summer School on Fundamental Problems in Statistical Physics, 5–19 (2018).
- [37] van Kampen, N. G. *Stochastic Processes in Physics and Chemistry* (North-Holland, Amsterdam, 1981).
- [38] Gardiner, C. *Handbook of Stochastic Methods* 3rd (Springer-Verlag, Berlin, 2004).
- [39] Risken, H. *The Fokker-Planck Equation* 2nd (Springer-Verlag, Berlin, 1989).
- [40] Gillespie, D. T. *The chemical Langevin equation*. *The Journal of Chemical Physics* **113**, 297–306 (2000).
- [41] Gillespie, D. T. *Deterministic Limit of Stochastic Chemical Kinetics*. *The Journal of Physical Chemistry B* **113**, 1640–1644 (2009).

- [42] Touchette, H. *The large deviation approach to statistical mechanics. Physics Reports* **478**, 1–69 (2009).
- [43] Bressloff, P. *Stochastic Processes in Cell Biology* (Springer International Publishing, Cham, 2014).
- [44] Qian, H. & Ge, H. *Stochastic Chemical Reaction Systems in Biology* (Springer Nature, Cham, 2021).
- [45] Gaspard, P. *Trace Formula for Noisy Flows. Journal of Statistical Physics* **106**, 57–96 (2002).
- [46] Gaspard, P. *The correlation time of mesoscopic chemical clocks. The Journal of Chemical Physics* **117**, 8905–8916 (2002).
- [47] Schwabl, F. *Statistische Mechanik* (Springer-Verlag, Berlin Heidelberg New York, 2000).
- [48] Strogatz, S. H. *Nonlinear Dynamics and Chaos: With Applications to Physics, Biology, Chemistry and Engineering* (Perseus Books Group, Reading, Massachusetts, 2000).
- [49] Selkov, E. E. *Self-Oscillations in Glycolysis 1. A Simple Kinetic Model. European Journal of Biochemistry* **4**, 79–86 (1968).
- [50] Ohga, N., Ito, S. & Kolchinsky, A. *Thermodynamic Bound on the Asymmetry of Cross-Correlations. Phys. Rev. Lett.* **131**, 077101 (2023).
- [51] Sekimoto, K. & Sasa, S. *Complementarity Relation for Irreversible Process Derived from Stochastic Energetics. Journal of the Physical Society of Japan* **66**, 3326 (1997).
- [52] Schmiedl, T. & Seifert, U. *Efficiency at maximum power: An analytically solvable model for stochastic heat engines. Europhysics Letters* **81**, 20003 (2007).
- [53] Fu, R., Taghvaei, A., Chen, Y. & Georgiou, T. T. *Maximal power output of a stochastic thermodynamic engine. Automatica* **123**, 109366 (2021).
- [54] Esposito, M., Kawai, R., Lindenberg, K. & den Broeck, C. V. *Finite-time thermodynamics for a single-level quantum dot. Europhysics Letters* **89**, 20003 (2010).
- [55] Diana, G., Bagci, G. B. & Esposito, M. *Finite-time erasing of information stored in fermionic bits. Phys. Rev. E* **87**, 012111 (2013).
- [56] Zulkowski, P. R. & DeWeese, M. R. *Optimal finite-time erasure of a classical bit. Phys. Rev. E* **89**, 052140 (2014).

- [57] Crooks, G. E. & Jarzynski, C. *Work distribution for the adiabatic compression of a dilute and interacting classical gas. Phys. Rev. E* **75**, 021116 (2007).
- [58] Sivak, D. A. & Crooks, G. E. *Thermodynamic Metrics and Optimal Paths. Phys. Rev. Lett.* **108**, 190602 (2012).
- [59] Zulkowski, P. R., Sivak, D. A., Crooks, G. E. & DeWeese, M. R. *Geometry of thermodynamic control. Phys. Rev. E* **86**, 041148 (2012).
- [60] Muratore-Ginanneschi, P. *On the use of stochastic differential geometry for non-equilibrium thermodynamic modeling and control. Journal of Physics A: Mathematical and Theoretical* **46**, 275002 (2013).
- [61] Zulkowski, P. R. & DeWeese, M. R. *Optimal control of overdamped systems. Phys. Rev. E* **92**, 032117 (2015).
- [62] Sivak, D. A. & Crooks, G. E. *Thermodynamic geometry of minimum-dissipation driven barrier crossing. Phys. Rev. E* **94**, 052106 (2016).
- [63] Deffner, S. & Bonança, M. V. S. *Thermodynamic control — An old paradigm with new applications. Europhysics Letters* **131**, 20001 (2020).
- [64] Shiraishi, N., Funo, K. & Saito, K. *Speed Limit for Classical Stochastic Processes. Phys. Rev. Lett.* **121**, 070601 (2018).
- [65] Bérut, A., Arakelyan, A., Petrosyan, A., Ciliberto, S., Dillenschneider, R. & Lutz, E. *Experimental verification of Landauer’s principle linking information and thermodynamics. Nature* **483**, 187–189 (2012).
- [66] Jun, Y., Gavrilov, M. & Bechhoefer, J. *High-Precision Test of Landauer’s Principle in a Feedback Trap. Phys. Rev. Lett.* **113**, 190601 (2014).
- [67] Proesmans, K., Ehrich, J. & Bechhoefer, J. *Finite-Time Landauer Principle. Phys. Rev. Lett.* **125**, 100602 (2020).
- [68] Proesmans, K., Ehrich, J. & Bechhoefer, J. *Optimal finite-time bit erasure under full control. Phys. Rev. E* **102**, 032105 (2020).
- [69] Proesmans, K. & Bechhoefer, J. *Erasing a majority-logic bit. Europhysics Letters* **133**, 30002 (2021).
- [70] Woodside, M. T. & Block, S. M. *Reconstructing folding energy landscapes by single-molecule force spectroscopy. Annual Review of Biophysics* **43**, 19–39 (2014).

- [71] Camunas-Soler, J., Ribezzi-Crivellari, M. & Ritort, F. *Elastic Properties of Nucleic Acids by Single-Molecule Force Spectroscopy. Annual Review of Biophysics* **45**, 65–84 (2016).
- [72] Sinitsyn, N. A. & Nemenman, I. *The Berry phase and the pump flux in stochastic chemical kinetics. Europhysics Letters* **77**, 58001 (2007).
- [73] Rahav, S., Horowitz, J. & Jarzynski, C. *Directed Flow in Nonadiabatic Stochastic Pumps. Phys. Rev. Lett.* **101**, 140602 (2008).
- [74] Chernyak, V. Y. & Sinitsyn, N. A. *Pumping Restriction Theorem for Stochastic Networks. Phys. Rev. Lett.* **101**, 160601 (2008).
- [75] Fang, X., Kruse, K., Lu, T. & Wang, J. *Nonequilibrium physics in biology. Rev. Mod. Phys.* **91**, 045004 (2019).
- [76] Mugnai, M. L., Hyeon, C., Hinczewski, M. & Thirumalai, D. *Theoretical perspectives on biological machines. Rev. Mod. Phys.* **92**, 025001 (2020).
- [77] Gawedzki, K. *Fluctuation Relations in Stochastic Thermodynamics. arXiv: 1308.1518* (2013).
- [78] Ferrell, J., Tsai, T.-C. & Yang, Q. *Modeling the Cell Cycle: Why Do Certain Circuits Oscillate? Cell* **144**, 874–885 (2011).
- [79] Nakajima, M., Imai, K., Ito, H., Nishiwaki, T., Y., M., Iwasaki, H., Oyama, T. & Kondo, T. *Reconstitution of circadian oscillation of cyanobacterial KaiC phosphorylation in vitro. Science* **308**, 414 (2005).
- [80] Dong, G. & Golden, S. S. *How a cyanobacterium tells time. Current opinion in microbiology* **11**, 541–546 (2008).
- [81] Goldbeter, A. *Modelling biochemical oscillations and cellular rhythms. Current Science* **73**, 933–939 (1997).
- [82] Novák, B. & Tyson, J. J. *Design principles of biochemical oscillators. Nature Reviews Molecular Cell Biology* **144**, 874–885 (2008).
- [83] Nicolis, G. & Malek-Mansour, M. *Nonequilibrium Phase Transitions and Chemical Reactions. Progress of Theoretical Physics Supplement* **64**, 249–268 (1978).
- [84] McQuarrie, D. A. *Stochastic Approach to Chemical Kinetics. Journal of Applied Probability* **4**, 413–478 (1967).
- [85] Weber, M. F. & Frey, E. *Master equations and the theory of stochastic path integrals. Reports on Progress in Physics* **80**, 046601 (2017).

- [86] Gonze, D., Halloy, J. & Gaspard, P. *Biochemical clocks and molecular noise: Theoretical study of robustness factors. Journal of Chemical Physics* **116**, 10997–11010 (2002).
- [87] Qian, H. *Open-System Nonequilibrium Steady State: Statistical Thermodynamics, Fluctuations, and Chemical Oscillations. The Journal of Physical Chemistry B* **110**, 15063–15074 (2006).
- [88] Morelli, L. G. & Jülicher, F. *Precision of Genetic Oscillators and Clocks. Phys. Rev. Lett.* **98**, 228101 (2007).
- [89] d'Eysmond, T., Simone, A. D. & Naef, F. *Analysis of precision in chemical oscillators: implications for circadian clocks. Physical Biology* **10**, 056005 (2013).
- [90] Nguyen, B., Seifert, U. & Barato, A. C. *Phase transition in thermodynamically consistent biochemical oscillators. Journal of Chemical Physics* **149**, 045101 (2018).
- [91] Barato, A. C. & Seifert, U. *Cost and Precision of Brownian Clocks. Phys. Rev. X* **6**, 041053 (2016).
- [92] Potvin-Trottier, L., Lord, N. D., Vinnicombe, G. & Paulsson, J. *Synchronous long-term oscillations in a synthetic gene circuit. Nature* **538**, 514–517 (2016).
- [93] Gingrich, T. R., Horowitz, J. M., Perunov, N. & England, J. L. *Dissipation Bounds All Steady-State Current Fluctuations. Phys. Rev. Lett.* **116**, 120601 (2016).
- [94] Horowitz, J. M. & Gingrich, T. R. *Thermodynamic uncertainty relations constrain non-equilibrium fluctuations. Nature Physics* **16**, 15–20 (2020).
- [95] Pietzonka, P. *Classical Pendulum Clocks Break the Thermodynamic Uncertainty Relation. Phys. Rev. Lett.* **128**, 130606 (2022).
- [96] Freitas, N., Falasco, G. & Esposito, M. *Linear response in large deviations theory: a method to compute non-equilibrium distributions. New Journal of Physics* **23**, 093003 (2021).
- [97] Yoshimura, K. & Arai, K. *Phase Reduction of Stochastic Limit Cycle Oscillators. Phys. Rev. Lett.* **101**, 154101 (2008).
- [98] Teramae, J.-n., Nakao, H. & Ermentrout, G. B. *Stochastic Phase Reduction for a General Class of Noisy Limit Cycle Oscillators. Phys. Rev. Lett.* **102**, 194102 (2009).
- [99] Cao, Y., Wang, H., Ouyang, Q. & Tu, Y. *The free-energy cost of accurate biochemical oscillations. Nature Physics* **11**, 772–778 (2015).

- [100] Bagheri, S. *Effects of weak noise on oscillating flows: Linking quality factor, Floquet modes, and Koopman spectrum*. *Physics of Fluids* **26**, 094104 (2014).
- [101] Wiggins, S. *Introduction to applied nonlinear dynamical systems and chaos 2.*, corr. printing (Springer, New York; Berlin; Heidelberg, 1990).
- [102] Frey, E. & Brauns, F. *Self-organisation of Protein Patterns*. arXiv: 2012.01797 (2020).
- [103] Xiao, T. J., Ma, J., Hou, Z. H. & Xin, H. *Effects of internal noise in mesoscopic chemical systems near Hopf bifurcation*. *New J. Phys.* **9**, 403 (2007).
- [104] Louca, S. *Stable limit cycles perturbed by noise*. arXiv: 1506.00756 (2018).
- [105] Tantet, A., Chekroun, M. D., Neelin, J. D. & Dijkstra, H. A. *Ruelle–Pollicott Resonances of Stochastic Systems in Reduced State Space. Part III: Application to the Cane–Zebiak Model of the El Niño–Southern Oscillation*. *Journal of Statistical Physics* **179**, 1449–1474 (2020).
- [106] Lefever, R., Nicolis, G. & Borckmans, P. *The brusselator: it does oscillate all the same*. *J. Chem. Soc., Faraday Trans. 1* **84**, 1013–1023 (1988).
- [107] Andrieux, D. & Gaspard, P. *Fluctuation theorem and mesoscopic chemical clocks*. *The Journal of Chemical Physics* **128**, 154506 (2008).
- [108] Schlögl, F. *Chemical reaction models for non-equilibrium phase transitions*. *Zeitschrift für Physik* **253**, 147–161 (1972).
- [109] Matheson, I., Walls, D. F. & Gardiner, C. W. *Stochastic models of firstorder nonequilibrium phase transitions in chemical reactions*. *Journal of Statistical Physics* **12**, 21–34 (1975).
- [110] Schnakenberg, J. *Network theory of microscopic and macroscopic behavior of master equation systems*. *Rev. Mod. Phys.* **48**, 571 (1976).
- [111] Beard, D. A., Babson, E., Curtis, E. & Qian, H. *Thermodynamic constraints for biochemical networks*. *Journal of Theoretical Biology* **228**, 327–333 (2004).
- [112] Qian, H. & Beard, D. A. *Thermodynamics of stoichiometric biochemical networks in living systems far from equilibrium*. *Biophys. Chem.* **114**, 213 (2005).
- [113] Esposito, M. *Open questions on nonequilibrium thermodynamics of chemical reaction networks*. *Communications Chemistry* **3**, 107 (2020).

- [114] Fritz, J. H., Nguyen, B. & Seifert, U. *Stochastic thermodynamics of chemical reactions coupled to finite reservoirs: A case study for the Brusselator. The Journal of Chemical Physics* **152**, 235101 (2020).
- [115] Crochik, L. & Tomé, T. *Entropy production in the majority-vote model. Phys. Rev. E* **72**, 057103 (2005).
- [116] Vellela, M. & Qian, H. *Stochastic dynamics and non-equilibrium thermodynamics of a bistable chemical system: the Schlögl model revisited. Journal of The Royal Society Interface* **6**, 925–940 (2009).
- [117] Andrae, B., Cremer, J., Reichenbach, T. & Frey, E. *Entropy Production of Cyclic Population Dynamics. Phys. Rev. Lett.* **104**, 218102 (2010).
- [118] Rao, T., Xiao, T. & Hou, Z. *Entropy production in a mesoscopic chemical reaction system with oscillatory and excitable dynamics. The Journal of Chemical Physics* **134**, 214112 (2011).
- [119] Tomé, T. & de Oliveira, M. J. *Entropy Production in Nonequilibrium Systems at Stationary States. Phys. Rev. Lett.* **108**, 020601 (2012).
- [120] Zhang, Y. & Barato, A. C. *Critical behavior of entropy production and learning rate: Ising model with an oscillating field. Journal of Statistical Mechanics: Theory and Experiment* **2016**, 113207 (2016).
- [121] Shim, P.-S., Chun, H.-M. & Noh, J. D. *Macroscopic time-reversal symmetry breaking at a nonequilibrium phase transition. Phys. Rev. E* **93**, 012113 (2016).
- [122] Noa, C. E. F., Harunari, P. E., de Oliveira, M. J. & Fiore, C. E. *Entropy production as a tool for characterizing nonequilibrium phase transitions. Phys. Rev. E* **100**, 012104 (2019).
- [123] Herpich, T. & Esposito, M. *Universality in driven Potts models. Phys. Rev. E* **99**, 022135 (2019).
- [124] Rana, S. & Barato, A. C. *Precision and dissipation of a stochastic Turing pattern. Phys. Rev. E* **102**, 032135 (2020).
- [125] Goes, B. O., Fiore, C. E. & Landi, G. T. *Quantum features of entropy production in driven-dissipative transitions. Phys. Rev. Res.* **2**, 013136 (2020).
- [126] Seara, D., Machta, B. & Murrell, M. *Irreversibility in dynamical phases and transitions. Nature Communications* **12**, 392 (2021).

- [127] Fiore, C. E., Harunari, P. E., Noa, C. E. F. & Landi, G. T. *Current fluctuations in nonequilibrium discontinuous phase transitions*. *Phys. Rev. E* **104**, 064123 (2021).
- [128] Nguyen, B. & Seifert, U. *Exponential volume dependence of entropy-current fluctuations at first-order phase transitions in chemical reaction networks*. *Phys. Rev. E* **102**, 022101 (2020).
- [129] Ge, H. & Qian, H. *Non-equilibrium phase transition in mesoscopic biochemical systems: from stochastic to nonlinear dynamics and beyond*. *Journal of The Royal Society Interface* **8**, 107–116 (2010).
- [130] Lazarescu, A., Cossetto, T., Falasco, G. & Esposito, M. *Large deviations and dynamical phase transitions in stochastic chemical networks*. *The Journal of Chemical Physics* **151**, 064117 (2019).
- [131] Jack, R. L. *Ergodicity and large deviations in physical systems with stochastic dynamics*. *The European Physical Journal B* **93**, 74 (2020).
- [132] Guislain, L. & Bertin, E. *Nonequilibrium Phase Transition to Temporal Oscillations in Mean-Field Spin Models*. *Phys. Rev. Lett.* **130**, 207102 (2023).
- [133] Heussinger, C. & Frey, E. *Floppy Modes and Nonaffine Deformations in Random Fiber Networks*. *Phys. Rev. Lett.* **97**, 105501 (2006).
- [134] Broedersz, C. P., Mao, X., Lubensky, T. C. & MacKintosh, F. C. *Criticality and isostaticity in fibre networks*. *Nature Physics* **7**, 983–988 (2011).
- [135] Broedersz, C. P. & MacKintosh, F. C. *Modeling semiflexible polymer networks*. *Rev. Mod. Phys.* **86**, 995–1036 (2014).
- [136] Bi, D., Lopez, J. H., Schwarz, J. M. & Manning, M. L. *A density-independent rigidity transition in biological tissues*. *Nature Physics* **11**, 1074–1079 (2015).
- [137] Gnesotto, F. S., Remlein, B. M. & Broedersz, C. P. *Nonequilibrium dynamics of isostatic spring networks*. *Phys. Rev. E* **100**, 013002 (2019).
- [138] Buttinoni, I., Bialké, J., Kümmel, F., Löwen, H., Bechinger, C. & Speck, T. *Dynamical Clustering and Phase Separation in Suspensions of Self-Propelled Colloidal Particles*. *Phys. Rev. Lett.* **110**, 238301 (2013).
- [139] Wittkowski, R., Tiribocchi, A., Stenhammar, J., Allen, R. J., Marenduzzo, D. & Cates, M. E. *Scalar φ^4 field theory for active-particle phase separation*. *Nature Communications* **5**, 4351 (2014).

- [140] Huber, L., Suzuki, R., Krüger, T., Frey, E. & Bausch, A. R. *Emergence of coexisting ordered states in active matter systems. Science* **361**, 255–258 (2018).
- [141] Gompper, G. *et al.* *The 2020 motile active matter roadmap. Journal of Physics: Condensed Matter* **32**, 193001 (2020).
- [142] Gopal, A., Roldán, É. & Ruffo, S. *Energetics of critical oscillators in active bacterial baths. Journal of Physics A: Mathematical and Theoretical* **54**, 164001 (2021).
- [143] Markovich, T., Fodor, E., Tjhung, E. & Cates, M. E. *Thermodynamics of Active Field Theories: Energetic Cost of Coupling to Reservoirs. Phys. Rev. X* **11**, 021057 (2021).
- [144] Fodor, E., Jack, R. L. & Cates, M. E. *Irreversibility and Biased Ensembles in Active Matter: Insights from Stochastic Thermodynamics. Annual Review of Condensed Matter Physics* **13**, 215–238 (2022).
- [145] Speck, T. *Critical behavior of active Brownian particles: Connection to field theories. Phys. Rev. E* **105**, 064601 (2022).
- [146] Ge, H. & Qian, H. *Thermodynamic Limit of a Nonequilibrium Steady State: Maxwell-Type Construction for a Bistable Biochemical System. Phys. Rev. Lett.* **103**, 148103 (2009).
- [147] Iwata, M. & Sasa, S.-i. *Theoretical analysis for critical fluctuations of relaxation trajectory near a saddle-node bifurcation. Phys. Rev. E* **82**, 011127 (2010).
- [148] Horowitz, J. M. *Diffusion approximations to the chemical master equation only have a consistent stochastic thermodynamics at chemical equilibrium. The Journal of Chemical Physics* **143**, 044111 (2015).
- [149] Hänggi, P., Grabert, H., Talkner, P. & Thomas, H. *Bistable systems: Master equation versus Fokker-Planck modeling. Phys. Rev. A* **29**, 371–378 (1984).
- [150] Prigogine, I. & Lefever, R. *Symmetry Breaking Instabilities in Dissipative Systems. II. Journal of Chemical Physics* **48**, 1695 (1968).
- [151] Schnakenberg, J. *Simple chemical reaction systems with limit cycle behaviour. Journal of Theoretical Biology* **81**, 389–400 (1979).
- [152] Qian, H., Saffarian, S. & Elson, E. L. *Concentration fluctuations in a mesoscopic oscillating chemical reaction system. Proceedings of the National Academy of Sciences* **99**, 10376–10381 (2002).

- [153] Crawford, J. D. *Introduction to bifurcation theory. Rev. Mod. Phys.* **63**, 991–1037 (1991).
- [154] Guckenheimer, J. & Holmes, P. *Nonlinear oscillations, dynamical systems, and bifurcations of vector fields* Corr. 7. printing (Springer, New York; Berlin; Heidelberg, 2002).
- [155] Hanke-Bourgeois, M. 3., aktualisierte Auflage (Vieweg+Teubner, Wiesbaden, 2009).
- [156] Osada, R., Funkhouser, T., Chazelle, B. & Dobkin, D. *Shape Distributions. ACM Transactions on Graphics* **21**, 807–832 (2002).

LIST OF FIGURES

Figure 2.1	Coarse-graining of microstates	6
Figure 2.2	Trajectory over mesostates	7
Figure 2.3	Schematic partition of the supersystem	9
Figure 2.4	Brownian particle in a harmonic trap	16
Figure 2.5	Reaction tank of a closed CRN	21
Figure 2.6	Reaction tank with chemostat	24
Figure 2.7	Closed paths in one-dimensional CRN	25
Figure 2.8	Path along the $\rho = 0$ -line	40
Figure 2.9	Characteristics of a pitchfork bifurcation	41
Figure 2.10	Characteristics of a Hopf bifurcation	43
Figure 3.1	Influence of the allocated time T on the maximal affinity \mathcal{A}_{\max}	53
Figure 3.2	Influence of the system-parameters on the maximal affinity \mathcal{A}_{\max}	54
Figure 4.1	A specific example	67
Figure 4.2	Quality factor for a two-dimensional limit cycle	73
Figure 4.3	Quality factor of the cubic normal form of a Hopf bifurcation	74
Figure 4.4	Quality factor of the Brusselator	78
Figure 4.5	Frequency and decay time of the Brusselator	79
Figure 5.1	Phase diagram for the Schlögl model	85
Figure 5.2	Mean flux J of the Schlögl model along the critical line	86
Figure 5.3	Diffusion coefficient D of the Schlögl model along the critical line	87
Figure 5.4	Mean flux J of the Schlögl model undergoing a pitchfork bifurcation	96
Figure 5.5	Diffusion coefficient D of the Schlögl model at the pitchfork bifurcation	98
Figure 5.6	New variables for the Schlögl model	104
Figure 6.1	Mean flux J of the Brusselator model	112
Figure 6.2	Fluctuations of the entropic flux in the Brusselator	113
Figure 6.3	Mean flux shifted by the contribution due to the fixed point of the Brusselator	116

Figure 6.4	Diffusion coefficient D_z of the noisy cubic normal form for a Hopf bifurcation	124
Figure 6.5	Fluctuations of the mean flux in the Brusselator model due to van Kampen's expansion	125
Figure 6.6	Fluctuations of the mean flux in the Brusselator model obtained by integrating the CLE	127
Figure A.1	Illustration of the explicit calculations for the 3 state system	141
Figure A.2	Allowed region of probabilities-phase space	145

LIST OF TABLES

Table 6.1	Reaction rates of the Brusselator taken from Ref. [90]	112
-----------	--	-----

ACRONYMS

NESS nonequilibrium steady-state.

CRN chemical reaction network.

CLE chemical Langevin equation.

TUR thermodynamic uncertainty relation.

ERKLÄRUNG

Die eingereichte Dissertation mit dem Titel „Nonlinear phenomena in stochastic thermodynamics – From optimal protocols to criticality“ stellt meine eigenständig erbrachte Leistung dar.

Ich habe ausschließlich die angegebenen Quellen und Hilfsmittel benutzt. Wörtlich oder inhaltlich aus anderen Werken übernommene Angaben habe ich als solche kenntlich gemacht.

Die Richtigkeit der hier getätigten Angaben bestätige ich und versichere, nach bestem Wissen die Wahrheit erklärt zu haben.

Stuttgart, den 28. Februar 2024

Benedikt Remlein

ERKLÄRUNG ZUR ÜBEREINSTIMMUNG DER DIGITALEN
VERSION MIT DER VORGELEGTEN PRINTVERSION DER
DISSERTATION

Hiermit erkläre ich, Benedikt Remlein, geboren am 21. Juni 1991, dass das von mir eingereichte pdf-Dokument zur Dissertation mit dem Thema „Nonlinear phenomena in stochastic thermodynamics – From optimal protocols to criticality“ in Inhalt und Wortlaut der ebenfalls eingereichten Printversion meiner Dissertationsschrift entspricht.

Stuttgart, den 28. Februar 2024

Benedikt Remlein

WISSENSCHAFTLICHER WERDEGANG

2016 Bachelor of Science Physik, Johannes-Gutenberg Universität Mainz

Abschlussarbeit zum Thema „Simulation von nichtlinearen eindimensionalen Ketten mit verschiedenen Integratoren“ mit Prof. Dr. Friederike Schmid und Prof. Dr. Thorsten Raasch.

2016 Bachelor of Science Mathematik, Johannes-Gutenberg Universität Mainz

Abschlussarbeit zum Thema „Simulation von nichtlinearen eindimensionalen Ketten mit verschiedenen Integratoren“ mit Prof. Dr. Thorsten Raasch und Prof. Dr. Friederike Schmid.

2019 Master of Science Theoretische und Mathematische Physik, Ludwig-Maximilians-Universität München und Technische Universität München

Abschlussarbeit zum Thema „Non-equilibrium criticality in isostatic spring networks“ mit Prof. Dr. Chase Broedersz.

DANKSAGUNG

An dieser Stelle möchte ich mich herzlich bei denjenigen bedanken, die mich während meines Studiums und meiner Promotion begleitet und unterstützt haben.

Zuerst möchte ich mich bei Herrn Prof. Dr. Udo Seifert für die Betreuung während meiner Promotion bedanken. Durch hilfreiche Diskussionen und Denkanstöße konnte ich viel lernen und mich stets weiterentwickeln.

Bei Prof. Dr. Thomas Speck bedanke ich mich für die Anfertigung des Zweitgutachtens und bei Herrn Prof. Dr. Ronny Nawrodt für die Übernahme des Prüfungsvorsitzes.

Ich bedanke mich bei allen ehemaligen und aktuellen Kollegen am Institut für die angenehme und entspannte Atmosphäre. Besonderer Dank geht an meinen ehemaligen Adminkollegen Dr. Timur Koyuk, welcher mich in die Serverstrukturen des Instituts eingeführt hat. Die vielen Online-Sitzungen haben Abwechslung in die Eintönigkeit der Pandemie gebracht. Ebenso bedanke ich mich bei meinen Adminkollegen Julius Degünther und Benjamin Ertel für die freundliche und erfolgreiche Zusammenarbeit. Für die konstruktive Zusammenarbeit mit Volker Weissmann im Rahmen seiner Masterarbeit bin ich dankbar.

Ein besonderer Dank gebührt Frau Anja Steinhauser, die mir durch ihre freundliche und professionelle Art sehr geholfen hat, mich an einer neuen Universität zurechtzufinden, und mich geschickt durch den Dschungel der Bürokratie geleitet hat. Zudem danke ich Frau Claudia Heydorn, die diese Aufgaben kompetent weiterführt.

Bei Julius Degünther bedanke ich mich für das Korrekturlesen dieser Arbeit.

Meiner Familie und allen Freunden, welche die verschiedenen Etappen des Studiums und der Promotion mit mir gegangen sind, sowie ganz besonders Shioru Morikawa danke ich sehr. Ohne euren Rückhalt und Hilfe hätte ich diesen Weg nicht beschreiten können. Danke!